Engineering Materials

Annelise Kopp Alves *Editor*

Environmental Applications of Nanomaterials

Springer

Engineering Materials

This series provides topical information on innovative, structural and functional materials and composites with applications in optical, electrical, mechanical, civil, aeronautical, medical, bio- and nano-engineering. The individual volumes are complete, comprehensive monographs covering the structure, properties, manufacturing process and applications of these materials. This multidisciplinary series is devoted to professionals, students and all those interested in the latest developments in the Materials Science field, that look for a carefully selected collection of high quality review articles on their respective field of expertise.

Indexed at Compendex (2021)

More information about this series at http://www.springer.com/series/4288

Annelise Kopp Alves
Editor

Environmental Applications of Nanomaterials

Springer

Editor
Annelise Kopp Alves
Escola de Engenharia
Universidade Federal do Rio Grande do Sul
Porto Alegre, Rio Grande do Sul, Brazil

ISSN 1612-1317 ISSN 1868-1212 (electronic)
Engineering Materials
ISBN 978-3-030-86821-5 ISBN 978-3-030-86822-2 (eBook)
https://doi.org/10.1007/978-3-030-86822-2

This Springer imprint is published by the registered company Springer Nature Switzerland AG
The registered company address is: Gewerbestrasse 11, 6330 Cham, Switzerland

Preface

This book contains an overview of synthesis, characterization, and applications of nanomaterials specially focused on the environmental context. Based on an extensive state-of-the-art literature survey and the results obtained by our research group during the past years, this book presents novel techniques and special applications of classical and modern nanomaterials.

This book is aimed at students, researchers, and engineers who seek general scientific knowledge about nanomaterials with an application-oriented environmental research topic.

The following chapters present the general aspects of synthesis and characterization of different nanomaterials applied to environmental research: spinel cobalt ferrites (Chapter "Synthesis, Properties, and Applications of Spinel Cobalt Ferrites"); wastewater treatment (Chapter "Wastewater Treatment Using Nanomaterials"); photochromism and photocatalysis (Chapter "Photochromic Nanomaterials with Photocatalytic Application"); carbon nanotubes for gas sensing (Chapter "Carbon Nanotubes for Gas Sensing"); renewable energy applications (Chapter "Titanium Dioxide Nanomaterials for Renewable Energy Applications"); catalysts for biomass gasification (Chapter "Nanostructured Catalysts for Biomass Gasification"); bio-oil from biomass pyrolysis (Chapter "Nanomaterials to Improve Bio-Oil from Biomass Pyrolysis: State-Of-Art and Challenges"); iron-based materials for Fenton reaction (Chapter "Iron-Based Nanomaterials for Fenton Reaction"); fuel production (Chapter "Nanomaterials for Fuel Production"); light-harvesting and water splitting techniques (Chapter "Photoelectrochemical Performance of Doped and Undoped TiO_2 Nanotubes for Light-Harvesting and Water Splitting Techniques: Systematic Review and Meta-Analysis"); CNT/TiO_2 hybrid materials (Chapter "CNT/TiO_2 Hybrid Nanostructured Materials: Synthesis, Properties and Applications"); zero-valent iron (Chapter "Nanostructured Zero-Valent Iron: From

Synthesis to Application"); nanosensors in forensic sciences (Chapter "Nanosensors in Forensic Sciences"); and perovskite nanomaterials (Chapter "Perovskite Nanomaterials: Properties and Applications").

Porto Alegre, Brazil
July 2021

Annelise Kopp Alves

Contents

Synthesis, Properties, and Applications of Spinel Cobalt Ferrites

Luis Eduardo Caldeira

Abstract Materials composed of metal oxide nanoparticles have been the subject of much interest due to their unique properties. Among them, spinel cobalt ferrite ($CoFe_2O_4$) stands out, a well-known magnetic material with excellent structural and magnetic properties. However, despite the efforts, there is still much uncertainty regarding the effects of different synthesis methods and the most diverse parameters on the properties of cobalt ferrite nanoparticles (CFNPs). This chapter presents the essential aspects of these materials. The main synthesis methods are described. Furthermore, the structural and magnetic properties are detailed. Finally, an overview of the wide range of applications of CFNPs is presented, ranging from the industrial area, both in traditional fields and in new technologies, to employment in biomedicine.

Keywords Nanoparticles · Spinel · Cobalt ferrite · $CoFe_2O_4$

Abbreviation

CFNPs cobalt ferrite nanoparticles

1 Introduction

Ferrites are non-metallic and magnetic materials widely studied today. They are considered ancient materials due to their applications [1]. These materials are formed by iron oxide (Fe_2O_3) as the main constituent and one or more transition metals—like manganese, iron, cobalt, nickel, and copper. One of the main characteristics that make them stand out among other magnetic materials is the simultaneous presentation of ferromagnetic or ferrimagnetic properties and insulating characteristics [2].

L. E. Caldeira (✉)
Universidade Federal do Rio Grande do Sul, Porto Alegre, Brazil

A. Kopp Alves (ed.), *Environmental Applications of Nanomaterials*, Engineering Materials, https://doi.org/10.1007/978-3-030-86822-2_1

Magnetite—iron oxide II and III or Fe_3O_4—a non-metallic solid found in nature, is a ferrite that exhibits magnetic behavior. This mineral is the oldest magnetic material known to our civilization, possibly used before iron [3]. Centuries later, the first primary technical application of magnetite occurred in the manufacture of compasses. From that period to the present day, several scientific advances in discovering similar materials in nature. Thus, there was an outbreak of ferrite production of synthetic form aimed at maximizing the physical and magnetic properties.

Ferrites are classified as ceramic materials. They have dark gray or black coloring—usually in powder, thin-film, or solid pressed, which is very hard and brittle [4]. Several factors can modify and improve the properties of ferrites. Preparation methods, synthesis parameters, stoichiometric proportions of the precursors, the precursors themselves, and their characteristics, among others, are some of these factors [5, 6]. The methods of preparing ferrites, presented below, significantly influence the structural properties, directly affecting them in their microstructural and morphological aspects [7]. Furthermore, the metallic cation selection intensely contributes to an excellent response to properties due to each of these ions [8]. Therefore, the correct selection of the synthesis of ferrites and the cation to be incorporated, be it divalent or trivalent, is essential for obtaining ferrites with excellent final properties.

Particularly, cobalt ferrite ($CoFe_2O_4$) has attracted significant interest from researchers due to its promising results in different characterizations [9]. The great asset of this type of ferrite certainly comes from its magnetic behavior associated with high chemical stability and good thermal and structural properties [10]. In terms of magnetization, in addition to presenting exciting results of remanence and saturation, cobalt ferrite has high coercivity, something that differs from other types of ferrite [11, 12]. Furthermore, concerning the material structure, this ferrite has a crystalline, homogeneous, and with a high degree of purity microstructure [13].

The applications of cobalt ferrites nanoparticles (CFNPs) will be presented at the end of this chapter. Nevertheless, it worth notice that there is considerable growth in the applications of these materials, ranging from use in the processing of electronic signals [14] to insertion in the field of biomedicine [15, 16]. The wide range of shapes and sizes, the continuous advance in research to improve properties, and manufacturing cost–benefit make ferrites attractive materials for conventional and innovative applications.

2 Synthesis Methods

Cobalt ferrite nanoparticles (CFNPs) can be obtained through different synthesis methods. In terms of purity, morphology, and stability, the high quality of the products is directly related to the synthesis selection [17]. In general, nanoparticle preparation techniques are categorized into two approaches [18, 19], as shown in Fig. 1. The "bottom-up" approach provides the widest variety of methods in which the formation of nanoparticles takes place through the chemical combination of ions.

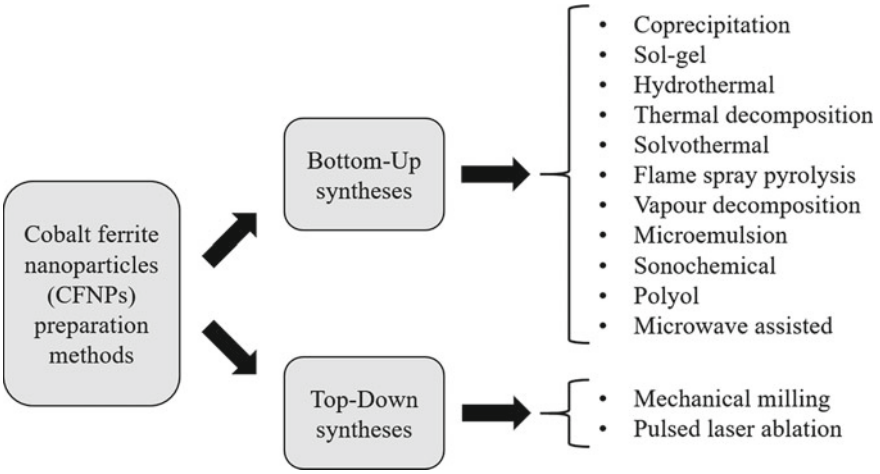

Fig. 1 Typical synthesis methods for CFNPs for the bottom-up and top-down approaches

The methods that operate in this way and produce cobalt ferrites nanoparticles are coprecipitation, thermal decomposition, sol–gel, hydrothermal, solvothermal, flame spray pyrolysis, vapor decomposition, microemulsion, sonochemical, polyol, and microwave-assisted.

In a "top-down" approach, nanoparticles are obtained by spraying the materials. Cobalt ferrites can be obtained, in this approach, by mechanical milling and pulsed laser ablation methods. The "bottom-up" methods have been preferred, mainly due to the formation of nanoparticles with high homogeneity and also the use of low treatment temperatures. Many of these synthesis methods are reported in the literature [20–27], both in experimental and review articles. The main aspects of the most used techniques will be presented.

2.1 Coprecipitation

The coprecipitation method can be named one of the most used techniques for producing cobalt ferrite nanoparticles. It is a simple and easy synthesis to be performed and presents uniform nanoparticles in morphology and size [28]. In a coprecipitation method, the divalent (Co^{2+}) and trivalent (Fe^{3+}) metallic ions—this, in general, in the form of soluble salts—are mixed under agitation in an aqueous solution in a molar ratio of 1:2, respectively. The experiment is typically carried out in an alkaline medium. This method requires strict pH control through an adjustment with a solution of ammonium or sodium hydroxide being added to the mixture. An adequate pH is essential for obtaining high-quality nanoparticles. The solution is then subjected to an agitation that does not necessarily require the use of thermal energy. However, in general, CFNPs obtained by coprecipitation have a low crystallinity. In

this case, the application of heat in a subsequent thermal treatment or even during mixing becomes interesting to obtain cobalt ferrite nanoparticles with a better degree of crystallinity [29, 30].

2.2 Sol–gel

Sol–gel synthesis is one of the simplest, easy-to-perform, and low-cost methods for obtaining CFNPs. In addition to these characteristics, this route allows the definition of several synthesis parameters, such as stoichiometry, size, shape, and degree of agglomeration, in addition to having a significant contribution from the structural properties of ferrites [31, 32]. The process parameters used in a sol–gel synthesis have been reported in the literature as being of great importance in the arrangement of cations in the spinel structure of cobalt ferrites [33].

There is not just one path to carry out a sol–gel synthesis. The citrate–nitrate method stands out due to its simplicity and versatility regarding the sol–gel methods used to produce cobalt ferrites. The process involves combining inorganic nitrates with citric acid ($C_6H_8O_7$), an organic compound. Some parameters such as reaction temperature and ambient humidity can vary from synthesis to synthesis. Excessive or insufficient drying times and a very high or very low treatment temperature can modify the structure of the produced ferrites [34]. For example, in spinel nanoparticles, additional heat treatment with a more comprehensive condensation is necessary to obtain higher crystallinity structures [35]. This subsequent treatment at a higher temperature can be directly related to improvements in the final quality of the products.

2.3 Hydrothermal

The hydrothermal synthesis consists of dissolutions carried out separately and in the mixture of divalent (Co^{2+}) and trivalent (Fe^{3+}) transition metal salts, in a molar ratio of 1:2, respectively. This mixture is set into continuous vigorous stirring so that the solution is homogenized. During stirring, organic solvents such as ethylene glycol or ethanol are added. The next step consists of heating under high pressure in an autoclave. Heating parameters such as temperature and heating time must be defined according to the desired properties and characteristics of the CFNPs. One of the advantages of the hydrothermal technique is the possibility of the large-scale production of nanoparticles. Reasonable dimensional control, shape, and size distribution—can also be achieved with this technique. Such control is reached by mixing solvents and controlling reaction parameters such as temperature, time, and pressure [36, 37].

2.4 Thermal Decomposition

Synthesis by thermal decomposition is known as a method in which the system is perfectly under control. In this technique, cobalt ferrite nanoparticles are obtained through the thermal decomposition of organometallic precursors in the presence of organic solvents and surfactants. The particle size of materials synthesized with this method is much smaller than that of particles synthesized by other conventional methods, such as the coprecipitation method [38]. It is one of the most employable methods in the industry, due to its simplicity of execution and because of the possibility of large-scale production, with morphology, size, and quality control. Such highlights also arise due to the permission to control synthesis parameters, such as temperature and ratio between precursors [21, 39].

2.5 Solvothermal

CFNPs can also be obtained by solvothermal synthesis, in which aqueous or non-aqueous solvents are used. This technique stands out due to the facile, environmentally, and economically alternative approach to prepare ferrite nanomaterials [40]. Several experimental factors can be fitted in this synthesis. These include reaction temperature and time, solvent, surfactant, and precursor materials. The solvothermal method is considered a synthesis with a low-cost and straightforward reaction that allows products with desirable dimensions and easy control [41].

3 General Properties of CFNPs

There is a growth in researches related to more advanced techniques for the synthesis of cobalt ferrites. At the same time, there is a considerable advance in property characterization techniques for the most diverse applications. Thus, studies in the cobalt ferrite nanoparticles field gained a significant boost. Among the variables studied, it is possible to highlight the different processing methods and their parameters, variations in stoichiometry, and additives. These variables are the main parameters evaluated in nanoparticles of spinel cobalt ferrites.

The synthesis of magnetic materials, especially cobalt ferrites, has been of interest for a long time. Researches indicate that the conditions of preparation, processing and methods of obtaining these materials contribute to determining their physical, structural, morphological, and magnetic properties [42, 43]. In the following subsections, the essential topics of the structure and magnetism of CFNPs will be presented.

3.1 Structure

Cobalt ferrite belongs to the spinel space group (MFe_2O_4)—where M refers to the transition metal, in our case, the cobalt (Co)—due to its crystalline structure [44]. Most ferrites crystallize in the structures of this group. Bragg and Nishikawa independently reported, for the first time, a crystal structure of the spinel group [45, 46]. This structure belongs to the space group $Fd\bar{3}m$, no. 227 of the International Crystallography Tables [47].

In a spinel structure, whatever it may be, the oxygen anions O^{2-} are accommodated, forming a face-centered cubic structure (fcc). There are two interstitial positions: the tetrahedral and octahedral sites, surrounded by four and six oxygen ions, respectively. The crystal structures of the normal and inverse spinels can be seen in Fig. 2, represented by fcc lattices of the $MgAl_2O_4$ and $MgGa_2O_4$ minerals, respectively.

The allocation of cations between the tetrahedral and octahedral interstitial positions is directly related to the classification of the spinel structure, which can be of the normal, inverse, or mixed type [48]. The obtaining of ferrites with superior properties and increasingly diverse applications are due to different synthesis cations [49]. There is a correlation between the preferential distributions of each metallic cation in interstitial sites, which lead to improvements in the final properties of spinel ferrites [50]. A crystal structure with normal spinel is composed of divalent cations (A^{2+}) occupying tetrahedral positions and trivalent cations (B^{3+}) occupying octahedral positions. This spinel can be represented as $(A^{2+})_{tet}(B_2{}^{3+})_{oct}O_4$ [51].

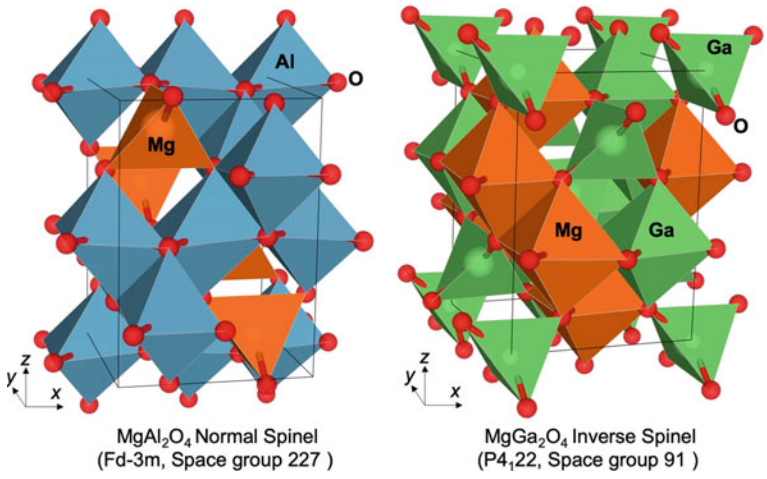

Fig. 2 Normal and inverse spinel structures. Solid black lines represent the unit cell. Octahedral and tetrahedral sites are also identified by the coordination polyhedra in both cases. (Adapted and reprinted with permission from Pilania et al. [52])

In an inverted spinel structure, divalent cations (A^{2+}) occupy octahedral positions, and trivalent cations (B^{3+}) occupy both tetrahedral and octahedral positions. Thus, the inverted spinel arrangement can be represented as $(B^{3+})_{tet}(A^{2+}B^{3+})_{oct}O_4$. However, there is a natural preference for some cations for tetrahedral or octahedral positions, depending on the ferrite transition metal. This definition can thus cause an inversion of the structure of the spinel. Furthermore, different methods of synthesis and fabrication of ferrites can alter the structure of the spinel [53].

Several ferrites have an intermediate structure to those presented. It is the case of a mixed spinel, with a chemical formula known as $(A_{1-x}{}^{2+}B_x{}^{3+})_{tet}(A_x{}^{2+}B_{2-x}{}^{3+})_{oct}O_4$, with x defining the degree of inversion of the spinel. Most ferrites have some degree of inversion. However, some exhibit a spinel with a strong tendency to a normal structure ($x \approx 0$) and others to an inverted structure ($x \approx 1$). Intermediate values at 0 and 1 represent ferrites with a mixed spinel structure [54].

In general, cobalt ferrite exhibits a mixed crystalline structure, i.e., it has crystallization characteristics of both normal spinel and inverted spinel. Both divalent (Co^{2+}) and trivalent (Fe^{3+}) metal ions fill such sites. The chemical formula of this structure is known as $(Co_{1-x}{}^{2+}Fe_x{}^{3+})_{tet}(Co_x{}^{2+}Fe_{2-x}{}^{3+})_{oct}O_4$, where x is the spinel inversion degree. It is known that there is a predominant tendency for inverse spinel, with an x value close to 1 [55]. The antiparallel alignment of spins between the cations present in the tetrahedral and octahedral sites causes the important ferrimagnetism presented by cobalt ferrites [56]. For this reason, the occupation of these interstitial positions is crucial in determining the material's magnetic properties. This characteristic, allied with a strong magnetocrystalline anisotropy presentation, is among the decisive factors for choosing this type of ferrite among other spinels for the most diverse applications [57].

3.2 Magnetic Behavior

In general, magnetic domains have dimensions of microscopic order. Each domain can be represented by a single magnetization vector, which symbolizes the sum of all magnetic moments per unit of volume. A grain of a polycrystalline material usually consists of more than one domain, which is generally separated from the others by walls. Defects such as dislocations and vacancies probably generate these domain walls in their vicinity and originate in the grain boundaries. In external magnetic fields, the walls can leave their positions and be moved in the material. The change in magnetization direction from a domain to its neighbor occurs gradually, indicating a correlation of several factors—such as energy, crystallographic and geometric—with the domain wall thickness [58, 59].

In a geometric approach, the larger the particle size, the greater the probability of forming several magnetic domains—or multidomains—since there is a higher incidence of defects [60]. On the other hand, the smaller the particle size, as in the case of nanoparticles, there is a significant drop in energy stability through the formation of domains, with the formation of a single domain configuration [61].

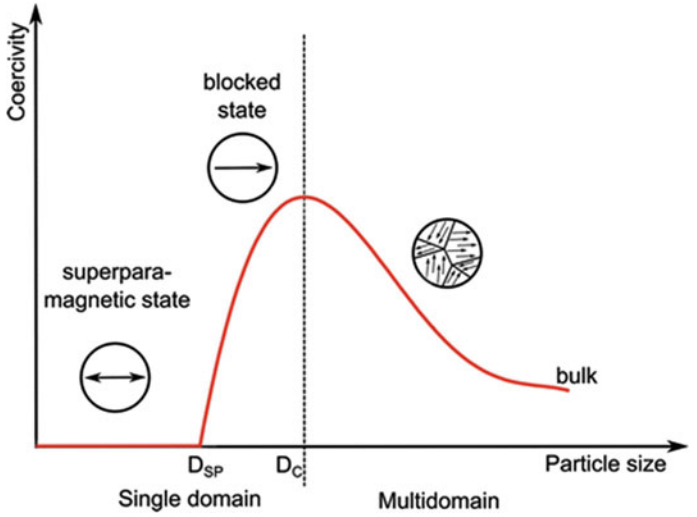

Fig. 3 Dependence of the coercivity on the size of a magnetic nanoparticle. (Reprinted with permission from Witte et al. [64])

When there is this formation, the particle is considered to be magnetized throughout its volume. There is a limit to which the particle size must be increased to adopt this single-domain configuration. If this size is reduced below a critical value, the particle ceases to present a stable monodomain appearance to a superparamagnetic characteristic without a magnetic field. It occurs due to the change from an orientation state to a relaxed state due to the thermal energy overcoming the anisotropy barrier [62].

There is, then, a direct relationship between the size of a particle and its magnetic behavior, which can be divided into three regimes: multidomain, single domain, or superparamagnetic. Figure 3 shows the dependence of the coercivity on the size of a magnetic nanoparticle. In multidomain nanoparticles, the magnetic moment vectors do not necessarily point in the same direction. However, they do point to random directions with different magnitudes, which is why they end up partially canceling themselves. There is a maximum coercivity value when the particle size is reduced until it has only a single magnetic domain in its volume (particle size named as D_C). Particle size values bigger than D_C refer to a multidomain regime, just as a reduction in size leads to a drop in coercivity. When this coercivity vanishes—at a particle size D_{SP}—the particle magnetically presents itself as superparamagnetic [63].

In practical terms, each material, depending on its composition, morphology, and structural organization, has particular dimensions that define its magnetic behavior concerning domains. There is a critical particle size that limits the material from being in a multidomain or monodomain region. Alternatively, it limits to define if it presents itself as superparamagnetic or ferrimagnetic. It is correct to say that structural, chemical, and physical properties, which are attractive in practical terms,

are directly linked to the preparation of nanoparticles with adequate dimensions and methods of preparation.

Depending on how liquid magnetic moments are oriented in the domains, magnetism can divide materials into different categories: diamagnetic, paramagnetic, ferromagnetic, antiferromagnetic, and ferrimagnetic. Nanoparticles of spinel cobalt ferrites present a ferrimagnetism behavior. In ferrimagnetic compounds, the resulting momentum originates from incomplete cancellation between the ions. This resulting moment would be smaller than the resulting moment of materials that, by chance, present ferromagnetic behavior. However, when these materials are spinel ferrites, in particular cobalt ferrites, there is a simultaneous behavior of ferrimagnetism with an insulating response [65]. These two properties combined make this material interesting for innovative applications, ranging from the industrial and technological to the medical area [66]. Applications of this class of materials will be covered later in this chapter.

Two essential variables when analyzing magnetic behavior are related to magnetization (M) and magnetic field (H). Magnetization (M) refers to the vector sum of all magnetizations of all domains of a material. The intensity of each vector is by the volumetric fraction of each domain. A change in shape and dimension of the domains occurs when there is an application of a magnetic field (H). It happens due to the movement of its walls [63].

Magnetic hysteresis can be evaluated using M versus H curves. The irreversible magnetizations of a sample are measured due to applying positive and negative cycles of magnetic fields. Figure 4 shows an example of a typical hysteresis curve for magnetic materials such as ferrites. Initially, an initial magnetization appears

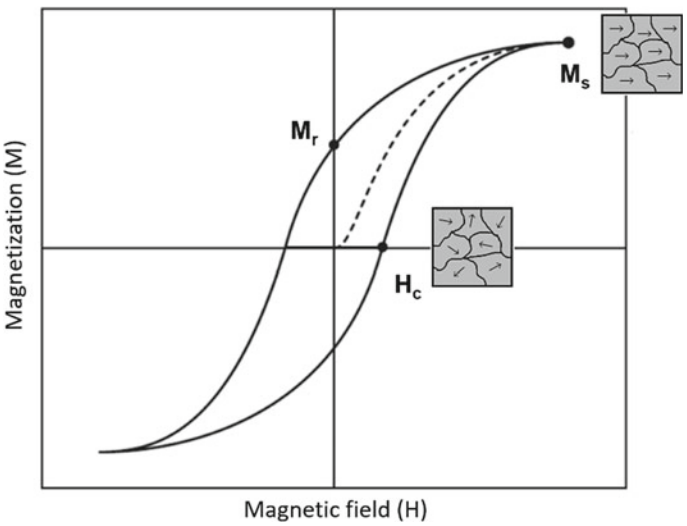

Fig. 4 Magnetization (M) curve versus magnetic field (H) with the parameters of coercivity (Hc), saturation (Ms), and remanence (Mr) representing a hysteresis cycle of a magnetic material

(dashed line) as a magnetic field (H) is applied until it reaches a saturation point. The domains are all aligned and oriented in the direction of the field. After reaching this point, the structure changes irreversibly. The curve enters a loop in which the previous points will no longer be repeated in the analysis.

The saturation magnetization (Ms), the remanent magnetization (Mr), and the coercive field (Hc) are essential parameters to be extracted from this curve, as they characterize the magnetic behavior of a given material. The saturation magnetization (Ms)—or just saturation—is the maximum value that magnetization (M) can reach regardless of the applied field. This value is reached when the maximum magnetic moments of the material align with the external field. Remanent magnetization (Mr)—or remanence—is the magnetization exhibited by the material in the absence of an external field. After the curve enters a loop, the material does not recover a demagnetized state without a field. The remanence is the value corresponding to the magnetization remaining in the material when a field is removed. The intensity of the external magnetic field necessary to completely demagnetize a sample, that is, to completely nullify its net magnetism after it has been brought to saturation (Ms), refers to the coercivity or coercive field (Hc) [59].

Ferromagnetic or ferrimagnetic materials, such as cobalt ferrites, can be classified into two categories because of their difficulty in demagnetizing. The shape of the curves, especially the area within a hysteresis cycle, plays an important role in this classification. This area represents the loss of magnetic energy for each volumetric unit of the sample for each magnetization-demagnetization cycle. Due to the size of this area within the hysteresis curve, magnetic materials can be divided into soft or hard. In soft material cycles, domain walls move quickly, relatively low energy losses occur.

Consequently, small hysteresis cycles are generated. In this case, materials have low coercivity and quickly lose their magnetization. On the other hand, the domain walls move with more difficulty in hard materials, requiring more intense magnetic fields (high coercivities) for the complete demagnetization of the sample. Thus, higher hysteresis loops appear. For the latter case, magnetization is said to be permanent [62]. In general, with hard or soft magnetism—with strong or weak intensities—most ferrites have a magnetism that is easy to reverse.

4 Applications

Much of the research related to ferrite took place after the 1950s, thanks to expanding technology in different fields. Ferrites are considered better magnetic materials compared to pure metals due to their high resistivity [67], low production cost [68], easy manufacturing, and superior magnetizing properties [69]. More specifically, cobalt ferrites have been standing out as a material with great potential for many applications. These applications range from the industrial area [70], both in traditional fields and new technologies, to employment in the medical field [71]. Cobalt ferrites are widely used in permanent magnets [72], recording media [73], transformers

[74], inductors [75], energy conversion [76], magnetic fluids [77], high-performance devices interference suppression [78], among many others.

According to the areas mentioned above, applications in the industrial field can be used in magnetic sensors used for temperature control, such as microwave absorbent materials, permanent magnets, electronic components, and storage devices, high-density recording, magnetic recording media, rotation filters, catalysts, chemical sensors, among others [70, 78]. In the medical field, cobalt ferrites have great potential for contrast enhancers in magnetic resonance images, enabling the observation of metastatic cancer cells. In addition, they can be used as biosensors in localized drug delivery, hyperthermia treatments, and tissue repair [71].

New research points to the great prominence of CFNPs as anode material in lithium-ion batteries, replacing graphite. In terms of specific capacity, cobalt ferrite shows an increase of up to three times compared to the material used today, something exciting when the use of high-capacity batteries becomes more and more necessary and indispensable [79].

This chapter brought up the concepts of cobalt ferrite nanoparticles, with details of the available synthesis methods. In addition, the general properties of CFNPs were detailed, in particular the structural and magnetic behavior. Finally, a wide range of applications was presented. The topics discussed allowed a complete understanding of $CoFe_2O_4$ nanoparticles, showing that these materials hold great promise for future applications as advanced magnetic materials.

References

1. Ziarkowska, W., Nowicki, M., Charubin, T.: Magnetic Moment Measurement Stand 178–185 (2020). https://doi.org/10.1007/978-3-030-29993-4_23.
2. Lüders, U., Bibes, M., Bouzehouane, K., Jacquet, E., Contour, J.-P., Fusil, S., Bobo, J.-F., Fontcuberta, J., Barthélémy, A., Fert, A.: Spin filtering through ferrimagnetic NiFe2O4 tunnel barriers. Appl. Phys. Lett. **88**, 82505 (2006). https://doi.org/10.1063/1.2172647
3. Fairweather, A., Roberts, F.F., Welch, A.J.E.: Ferrites. Rep. Prog. Phys. **15**, 306 (1952). https://doi.org/10.1088/0034-4885/15/1/306
4. Sugimoto, M.: The past, present, and future of ferrites. J. Am. Ceram. Soc. **82**, 269–280 (1999). https://doi.org/10.1111/j.1551-2916.1999.tb20058.x
5. Jauhar, S., Kaur, J., Goyal, A., Singhal, S.: Tuning the properties of cobalt ferrite: a road towards diverse applications. RSC Adv. **6**, 97694–97719 (2016). https://doi.org/10.1039/C6RA21224G
6. Sharifi Dehsari, H., Asadi, K.: Impact of stoichiometry and size on the magnetic properties of cobalt ferrite nanoparticles. J. Phys. Chem. C. **122**, 29106–29121 (2018). https://doi.org/10.1021/acs.jpcc.8b09276
7. Jacob, B., Kumar, A., Pant, R., Singh, S., Mohammed, E.M.: Influence of preparation method on structural and magnetic properties of nickel ferrite nanoparticles. Bull. Mater. Sci. **34**, 1345–1350 (2011). https://doi.org/10.1007/s12034-011-0326-7
8. Bakhshi, H., Vahdati, N., Sedghi, A., Mozharivskyj, Y.: Comparison of the effect of nickel and cobalt cations addition on the structural and magnetic properties of manganese-zinc ferrite nanoparticles. J. Magn. Magn. Mater. **474**, 56–62 (2019). https://doi.org/10.1016/j.jmmm.2018.10.146

9. Gul, I.H., Maqsood, A.: Structural, magnetic and electrical properties of cobalt ferrites prepared by the sol–gel route. J. Alloys Compd. **465**, 227–231 (2008). https://doi.org/10.1016/j.jallcom.2007.11.006
10. Ajroudi, L., Mliki, N., Bessais, L., Madigou, V., Villain, S., Leroux, C.: Magnetic, electric and thermal properties of cobalt ferrite nanoparticles. Mater. Res. Bull. **59**, 49–58 (2014). https://doi.org/10.1016/j.materresbull.2014.06.029
11. Chagas, E., Ponce, A., Prado, R., Silva, G., Bettini, J., Baggio-Saitovitch, E.: Thermal effect on magnetic parameters of high-coercivity cobalt ferrite. J. Appl. Phys. **116**, 0333901 (2014). https://doi.org/10.1063/1.4890033
12. Pillai, V., Shah, D.O.: Synthesis of high-coercivity cobalt ferrite particles using water-in-oil microemulsions. J. Magn. Magn. Mater. **163**, 243–248 (1996). https://doi.org/10.1016/S0304-8853(96)00280-6
13. Sajjia, M., Oubaha, M., Hasanuzzaman, M., Olabi, A.G.: Developments of cobalt ferrite nanoparticles prepared by the sol-gel process. Ceram. Int. **40**, 1147–1154 (2014). https://doi.org/10.1016/j.ceramint.2013.06.116
14. Harris, V.G., Geiler, A., Chen, Y., Yoon, S.D., Wu, M., Yang, A., Chen, Z., He, P., Parimi, P.V., Zuo, X., Patton, C.E., Abe, M., Acher, O., Vittoria, C.: Recent advances in processing and applications of microwave ferrites. J. Magn. Magn. Mater. **321**, 2035–2047 (2009). https://doi.org/10.1016/j.jmmm.2009.01.004
15. Issa, B., Obaidat, I.M., Albiss, B.A., Haik, Y.: Magnetic nanoparticles: surface effects and properties related to biomedicine applications. Int. J. Mol. Sci. **14**, 21266–21305 (2013). https://doi.org/10.3390/ijms141121266
16. Roca, A.G., Costo, R., Rebolledo, A.F., Veintemillas-Verdaguer, S., Tartaj, P., González-Carreño, T., Morales, M.P., Serna, C.J.: Progress in the preparation of magnetic nanoparticles for applications in biomedicine. J. Phys. D. Appl. Phys. **42**, 224002 (2009). https://doi.org/10.1088/0022-3727/42/22/224002
17. Gyergyek, S., Makovec, D., Kodre, A., Arčon, I., Jagodič, M., Drofenik, M.: Influence of synthesis method on structural and magnetic properties of cobalt ferrite nanoparticles. J. Nanoparticle Res. **12**, 1263–1273 (2010). https://doi.org/10.1007/s11051-009-9833-5
18. Khan, F.A.: Synthesis of nanomaterials: methods & technology. In: Khan, F.A., (ed.) Application Nanomaterials Human Health, pp. 15–21. Springer, Singapore, Singapore (2020). https://doi.org/10.1007/978-981-15-4802-4_2
19. Mohamed, A.E.-M.A., Mohamed, M.A.: Nanoparticles: magnetism and applications. In: Abd-Elsalam, K.A., Mohamed, M.A., Prasad, R. (eds.), Magnetic Nanostructures Environment Agriculture Application, pp. 1–12. Springer International Publishing, Cham, (2019). https://doi.org/10.1007/978-3-030-16439-3_1
20. Kurian, M., Thankachan, S., Nair, D.S., Babu, A.E.K.A., Thomas, A., Krishna, B.K.T.: Structural, magnetic, and acidic properties of cobalt ferrite nanoparticles synthesised by wet chemical methods. J. Adv. Ceram. **4**, 199–205 (2015). https://doi.org/10.1007/s40145-015-0149-x
21. Tomar, D., Jeevanandam, P.: Synthesis of cobalt ferrite nanoparticles with different morphologies via thermal decomposition approach and studies on their magnetic properties. J. Alloys Compd. **843**, 155815 (2020). https://doi.org/10.1016/j.jallcom.2020.155815
22. Allaedini, G., Tasirin, S.M., Aminayi, P.: Magnetic properties of cobalt ferrite synthesized by hydrothermal method. Int. Nano Lett. **5**, 183–186 (2015). https://doi.org/10.1007/s40089-015-0153-8
23. Kalam, A., Al-Sehemi, A.G., Assiri, M., Du, G., Ahmad, T., Ahmad, I., Pannipara, M.: Modified solvothermal synthesis of cobalt ferrite (CoFe2O4) magnetic nanoparticles photocatalysts for degradation of methylene blue with H2O2/visible light. Results Phys. **8**, 1046–1053 (2018). https://doi.org/10.1016/j.rinp.2018.01.045
24. Shatrova, N., Yudin, A., Levina, V., Dzidziguri, E., Kuznetsov, D., Perov, N., Issi, J.-P.: Elaboration characterization and magnetic properties of cobalt nanoparticles synthesized by ultrasonic spray pyrolysis followed by hydrogen reduction. Mater. Res. Bull. **86**, 80–87 (2017). https://doi.org/10.1016/j.materresbull.2016.10.010

25. Manova, E., Kunev, B., Paneva, D., Mitov, I., Petrov, L., Estournès, C., D'Orléan, C., Rehspringer, J.-L., Kurmoo, M.: Mechano-synthesis, characterization, and magnetic properties of nanoparticles of cobalt ferrite, CoFe 2 O 4. Chem. Mater. **16**, 5689–5696 (2004). https://doi.org/10.1021/cm049189u
26. Mahdikhah, V., Ataie, A., Babaei, A., Sheibani, S., Yang, C.W.O., Abkenar, S.K.: Control of structural and magnetic characteristics of cobalt ferrite by post-calcination mechanical milling. J. Phys. Chem. Solids. **134**, 286–294 (2019). https://doi.org/10.1016/j.jpcs.2019.06.018
27. Waag, F., Gökce, B., Kalapu, C., Bendt, G., Salamon, S., Landers, J., Hagemann, U., Heidelmann, M., Schulz, S., Wende, H., Hartmann, N., Behrens, M., Barcikowski, S.: Adjusting the catalytic properties of cobalt ferrite nanoparticles by pulsed laser fragmentation in water with defined energy dose. Sci. Rep. **7**, 13161 (2017). https://doi.org/10.1038/s41598-017-13333-z
28. Samavati, A., Ismail, A.F.: Antibacterial properties of copper-substituted cobalt ferrite nanoparticles synthesized by co-precipitation method. Particuology **30**, 158–163 (2017). https://doi.org/10.1016/j.partic.2016.06.003
29. Houshiar, M., Zebhi, F., Razi, Z.J., Alidoust, A., Askari, Z.: Synthesis of cobalt ferrite (CoFe2O4) nanoparticles using combustion, coprecipitation, and precipitation methods: a comparison study of size, structural, and magnetic properties. J. Magn. Magn. Mater. **371**, 43–48 (2014). https://doi.org/10.1016/j.jmmm.2014.06.059
30. Gul, I.H., Maqsood, A., Naeem, M., Ashiq, M.N.: Optical, magnetic and electrical investigation of cobalt ferrite nanoparticles synthesized by co-precipitation route. J. Alloys Compd. **507**, 201–206 (2010). https://doi.org/10.1016/j.jallcom.2010.07.155
31. Caldeira, L.E., Guaglianoni, W.C., Venturini, J., Arcaro, S., Bergmann, C.P., Bragança, S.R.: Sintering-dependent mechanical and magnetic properties of spinel cobalt ferrite (CoFe2O4) ceramics prepared via sol-gel synthesis. Ceram. Int. **46**, 2465–2472 (2020). https://doi.org/10.1016/j.ceramint.2019.09.240
32. Erhardt, C.S., Caldeira, L.E., Venturini, J., Bragança, S.R., Bergmann, C.P.: Sucrose as a sol-gel synthesis additive for tuning spinel inversion and improving the magnetic properties of CoFe2O4 nanoparticles. Ceram. Int. (2020). https://doi.org/10.1016/j.ceramint.2020.02.044
33. Vlazan, P., Stoia, M.: Structural and magnetic properties of CoFe2O4 nanopowders, prepared using a modified Pechini method. Ceram. Int. **44**, 530–536 (2018). https://doi.org/10.1016/j.ceramint.2017.09.207
34. Calvo-de la Rosa, J., Segarra, M.: Optimization of the synthesis of copper ferrite nanoparticles by a Polymer-Assisted Sol-Gel Method. ACS Omega **4**, 18289–18298 (2019). https://doi.org/10.1021/acsomega.9b02295
35. Shirsath, S., Wang, D., Jadhav, S., Mane, M., Li, S.: Ferrites Obtained by Sol–Gel Method (2017). https://doi.org/10.1007/978-3-319-19454-7_125-3
36. Zhao, L., Zhang, H., Xing, Y., Song, S., Yu, S., Shi, W., Guo, X., Yang, J., Lei, Y., Cao, F.: Studies on the magnetism of cobalt ferrite nanocrystals synthesized by hydrothermal method. J. Solid State Chem. **181**, 245–252 (2008). https://doi.org/10.1016/j.jssc.2007.10.034
37. Zhang, Y., Liu, Y., Fei, C., Yang, Z., Lu, Z., Xiong, R., Yin, D., Shi, J.: The temperature dependence of magnetic properties for cobalt ferrite nanoparticles by the hydrothermal method. J. Appl. Phys. **108**, 84312 (2010). https://doi.org/10.1063/1.3499289
38. Monfared, A.H., Zamanian, A., Beygzadeh, M., Sharifi, I., Mozafari, M.: A rapid and efficient thermal decomposition approach for the synthesis of manganese-zinc/oleylamine core/shell ferrite nanoparticles. J. Alloys Compd. **693**, 1090–1095 (2017). https://doi.org/10.1016/j.jallcom.2016.09.253
39. Herrera, A.P., Polo-Corrales, L., Chavez, E., Cabarcas-Bolivar, J., Uwakweh, O.N.C., Rinaldi, C.: Influence of aging time of oleate precursor on the magnetic relaxation of cobalt ferrite nanoparticles synthesized by the thermal decomposition method. J. Magn. Magn. Mater. **328**, 41–52 (2013). https://doi.org/10.1016/j.jmmm.2012.09.069
40. Ma, J., Zhao, J., Li, W., Zhang, S., Tian, Z., Basov, S.: Preparation of cobalt ferrite nanoparticles via a novel solvothermal approach using divalent iron salt as precursors. Mater. Res. Bull. **48**, 214–217 (2013). https://doi.org/10.1016/j.materresbull.2012.09.072

41. Vázquez-Vázquez, C., Lovelle, M., Mateo, C., López-Quintela, M.A., Buján-Núñez, M.C., Serantes, D., Baldomir, D., Rivas, J.: Magnetocaloric effect and size-dependent study of the magnetic properties of cobalt ferrite nanoparticles prepared by solvothermal synthesis. Phys. Status Solidi. **205**, 1358–1362 (2008). https://doi.org/10.1002/pssa.200778128
42. Fernandes de Medeiros, I.A., Lopes-Moriyama, A.L., de Souza, C.P.: Effect of synthesis parameters on the size of cobalt ferrite crystallite. Ceram. Int. **43**, 3962–3969 (2017). https://doi.org/10.1016/j.ceramint.2016.10.105
43. Khandekar, M.S., Kambale, R.C., Patil, J.Y., Kolekar, Y.D., Suryavanshi, S.S.: Effect of calcination temperature on the structural and electrical properties of cobalt ferrite synthesized by combustion method. J. Alloys Compd. **509**, 1861–1865 (2011). https://doi.org/10.1016/j.jallcom.2010.10.073
44. Tolani, S.C., Golhar, A.R., Rewatkar, K.G.: A review of morphological, structural behaviour and technological applications of ferrites. AIP Conf. Proc. **2104**, 30032 (2019). https://doi.org/10.1063/1.5100459
45. Nishikawa, S.: Structure of Some Crystals of Spinel Group, Tokyo Sugaku-Buturigakkwai Kizi Dai 2 Ki. **8**, 199–209_1 (1915). https://doi.org/10.11429/ptmps1907.8.7_199
46. Bragg, W.H.: The structure of the spinel group of crystals, London, Edinburgh Dublin. Philos. Mag. J. Sci. **30**, 305–315 (1915). https://doi.org/10.1080/14786440808635400
47. Pauling, L.: International Tables for X-ray Crystallography. Volume I. Symmetry Groups edited by Henry N.F.M., Lonsdale K.: Acta Crystallogr. **7**, 304–304 (1954). https://doi.org/10.1107/S0365110X54000874
48. Harris, V.G., Koon, N.C., Williams, C.M., Zhang, Q., Abe, M., Kirkland, J.P., McKeown, D.A.: Direct measurement of octahedral and tetrahedral site environments in NiZn-ferrites. IEEE Trans. Magn. **31**, 3473–3475 (1995). https://doi.org/10.1109/20.489540
49. Urusov, V.S.: Interaction of cations on octahedral and tetrahedral sites in simple spinels. Phys. Chem. Miner. **9**, 1–5 (1983). https://doi.org/10.1007/BF00309461
50. Li, J., Yuan, H., Li, G., Liu, Y., Leng, J.: Cation distribution dependence of magnetic properties of sol–gel prepared MnFe2O4 spinel ferrite nanoparticles. J. Magn. Magn. Mater. **322**, 3396–3400 (2010). https://doi.org/10.1016/j.jmmm.2010.06.035
51. Mathew, D.S., Juang, R.S.: An overview of the structure and magnetism of spinel ferrite nanoparticles and their synthesis in microemulsions. Chem. Eng. J. **129**, 51–65 (2007). https://doi.org/10.1016/j.cej.2006.11.001
52. Pilania, G., Kocevski, V., Valdez, J.A., Kreller, C.R., Uberuaga, B.P.: Prediction of structure and cation ordering in an ordered normal-inverse double spinel. Commun. Mater. **1**, 84 (2020). https://doi.org/10.1038/s43246-020-00082-2
53. Tatarchuk, T., Bououdina, M., Judith Vijaya, J., John Kennedy, L.: Spinel ferrite nanoparticles: synthesis, crystal structure, properties, and perspective applications BT—nanophysics, nanomaterials, interface studies, and applications. In: Fesenko, O., Yatsenko, L. (eds.), pp. 305–325. Springer International Publishing, Cham (2017)
54. Zaki, H.M., Dawoud, H.A.: Far-infrared spectra for copper–zinc mixed ferrites. Phys. B Condens. Matter. **405**, 4476–4479 (2010). https://doi.org/10.1016/j.physb.2010.08.018
55. Gore, S.K., Jadhav, S.S., Jadhav, V.V., Patange, S.M., Naushad, M., Mane, R.S., Kim, K.H.: The structural and magnetic properties of dual phase cobalt ferrite. Sci. Rep. **7**, 2524 (2017). https://doi.org/10.1038/s41598-017-02784-z
56. Rani, B.J., Ravina, M., Saravanakumar, B., Ravi, G., Ganesh, V., Ravichandran, S., Yuvakkumar, R.: Ferrimagnetism in cobalt ferrite (CoFe2O4) nanoparticles. Nano-Struct. & Nano-Objects **14**, 84–91 (2018). https://doi.org/10.1016/j.nanoso.2018.01.012
57. Rondinone, A.J., Samia, A.C.S., Zhang, Z.J.: Characterizing the magnetic anisotropy constant of spinel cobalt ferrite nanoparticles. Appl. Phys. Lett. **76**, 3624–3626 (2000). https://doi.org/10.1063/1.126727
58. Spaldin, N.A.: Magnetic materials: fundamentals and applications. Cambridge University Press (2010)
59. Diep, H.T.: Theory of Magnetism. World Scientific (2014)

60. Li, Q., Kartikowati, C.W., Horie, S., Ogi, T., Iwaki, T., Okuyama, K.: Correlation between particle size/domain structure and magnetic properties of highly crystalline Fe3O4 nanoparticles. Sci. Rep. **7**, 9894 (2017). https://doi.org/10.1038/s41598-017-09897-5
61. Brunsman, E.M., Scott, J.H., Majetich, S.A., McHenry, M.E., Huang, M.-Q.: Magnetic properties of monodomain Nd-Fe-B-C nanoparticles. J. Appl. Phys. **79**, 5293–5295 (1996). https://doi.org/10.1063/1.361355
62. Callister, W.D., Rethwisch, D.G.: Materials Science and Engineering. John wiley & sons, NY (2011)
63. Dunlop, D.J., Özdemir, Ö.: Rock Magnetism: Fundamentals and Frontiers. Cambridge University Press (2001)
64. Witte, K., Grüttner, C., Bodnar, W., Burkel, E.: Magnetic Nanoparticles for Biomedical Applications. In: Bhushan, B. (ed.) Encyclopedia Nanotechnology, pp. 1842–1850. Springer Netherlands, Dordrecht (2016). https://doi.org/10.1007/978-94-017-9780-1_100952
65. Rani, B.J., Ravina, M., Saravanakumar, B., Ravi, G., Ganesh, V., Ravichandran, S., Yuvakkumar, R.: Ferrimagnetism in cobalt ferrite (CoFe2O4) nanoparticles. Nano-Struct. Nano-Objects. **14**, 84–91 (2018). https://doi.org/10.1016/j.nanoso.2018.01.012
66. De Biasi, R.S., De Souza Lopes, R.D.: Magnetocrystalline anisotropy of NiCoFe2O4 nanoparticles. Ceram. Int. **42**, 9315–9318 (2016). https://doi.org/10.1016/j.ceramint.2016.02.141
67. Verma, A., Goel, T.C., Mendiratta, R.G., Gupta, R.G.: High-resistivity nickel–zinc ferrites by the citrate precursor method. J. Magn. Magn. Mater. **192**, 271–276 (1999). https://doi.org/10.1016/S0304-8853(98)00592-7
68. Zampiva, R.Y.S., Kaufmann, C.G., Alves, A.K., Bergmann, C.P.: Influence of the fuel composition and the fuel/oxidizer ratio on the combustion solution synthesis of MgFe2O4 catalyst nanoparticles. FME Trans. **46**, 157–164 (2018). https://doi.org/10.5937/fmet1802157Z
69. Kamali, S., Pouryazdan, M., Ghafari, M., Itou, M., Rahman, M., Stroeve, P., Hahn, H., Sakurai, Y.: Magnetization and stability study of a cobalt-ferrite-based ferrofluid. J. Magn. Magn. Mater. **404**, 143–147 (2016). https://doi.org/10.1016/j.jmmm.2015.12.007
70. Kazemi, M., Ghobadi, M., Mirzaie, A.: Cobalt ferrite nanoparticles (CoFe2O4 MNPs) as catalyst and support: magnetically recoverable nanocatalysts in organic synthesis. Nanotechnol. Rev. **7**, 43–68 (2018). https://doi.org/10.1515/ntrev-2017-0138
71. Srinivasan, S.Y., Paknikar, K.M., Bodas, D., Gajbhiye, V.: Applications of cobalt ferrite nanoparticles in biomedical nanotechnology. Nanomedicine **13**, 1221–1238 (2018). https://doi.org/10.2217/nnm-2017-0379
72. López-Ortega, A., Lottini, E., de Fernandez, C.J., Sangregorio, C.: Exploring the magnetic properties of cobalt-ferrite nanoparticles for the development of a rare-earth-free permanent magnet. Chem. Mater. **27**, 4048–4056 (2015)
73. Shu, C., Qiao, H.: Tuning magnetic properties of magnetic recording media cobalt ferrite nanoparticles by co-precipitation method. In: 2009 Symp. Photonics Optoelectron., pp. 1–4. IEEE (2009)
74. Srinivasamurthy, K.M., Angadi, J.V., Kubrin, S.P., Matteppanavar, S., Sarychev, D.A., Kumar, P.M., Azale, H.W., Rudraswamy B.: Tuning of ferrimagnetic nature and hyperfine interaction of Ni2+ doped cobalt ferrite nanoparticles for power transformer applications. Ceram. Int. **44**, 9194–9203 (2018). https://doi.or/10.1016/j.ceramint.2018.02.129
75. Geng, L.D., Yan, Y., Priya, S., Wang, Y.U.: Computational study of cobalt-modified nickel-ferrite/PZT magnetoelectric composites for voltage tunable inductor applications. Acta Mater. **166**, 493–502 (2019)
76. Alshehri, S.M., Alhabarah, A.N., Ahmed, J., Naushad, M., Ahamad, T.: An efficient and cost-effective tri-functional electrocatalyst based on cobalt ferrite embedded nitrogen doped carbon. J. Colloid Interface Sci. **514**, 1–9 (2018)
77. Soler, M.A.G., Lima, E.C.D., da Silva, S.W., Melo, T.F.O., Pimenta, A.C.M., Sinnecker, J.P., Azevedo, R.B., Garg, V.K., Oliveira, A.C., Novak, M.A.: Aging investigation of cobalt ferrite nanoparticles in low pH magnetic fluid. Langmuir **23**, 9611–9617 (2007)

78. Ismail, M.M., Rafeeq, S.N., Sulaiman, J.M.A., Mandal, A.: Electromagnetic interference shielding and microwave absorption properties of cobalt ferrite CoFe 2 O 4/polyaniline composite. Appl. Phys. A. **124**, 1–12 (2018)
79. Dun, C., Xi, G., Heng, X., Zhang, Y., Liu, Y., Xing, X.: Comparative study on the magnetostrictive property of cobalt ferrite synthesized by different methods from spent Li-ion batteries. Ceram. Int. **45**, 8539–8545 (2019). https://doi.org/10.1016/j.ceramint.2019.01.170

Wastewater Treatment Using Nanomaterials

Allan Ramone de Araujo Scharnberg and Fabrício Ravanello

Abstract Wastewater treatment efficiency is paramount in seeking a more sustainable future. However, due to exponential population growth and accelerated industrial development in the last century, it has been increasingly challenging to maintain drinking water resources available to the population. Among several tertiary wastewater treatment technologies, this chapter focus on Adsorption and Photocatalysis processes. The recent advances achieved mainly for nanomaterials development, both adsorbents, and photocatalysts, are addressed. According to the overall literature, both photodegradation and adsorption presented remarkable results related to wastewater treatment. The results achieved by photodegradation and adsorption technics show that it is possible to mineralize toxic compounds or even recover several types of toxic materials from aqueous effluents without the need for an excessively complex system.

Keywords Wastewater · Adsorption · Photocatalysis · Magnetic nanoparticles

1 Introduction

Water is probably the unique natural resource related to human civilization, from agricultural and industrial development to cultural values ingrained in our societies. Water is also fundamental to all known kinds of life. Therefore, humankind must sustain this resource available for future generations.

Since the last century, mainly due to exponential population growth and accelerated industrial development, it has been increasingly challenging to maintain drinking water resources available to the population. Liu et al. [1] pinpoints that, each year, 3.2 million people worldwide die because of water-related issues (unsafe water, inadequate hygiene, and poor sanitation).

Chemicals from industrial discharge and agricultural input materials are the primary water contamination sources. Besides the organic effluent generated by the

A. R. de Araujo Scharnberg (✉) · F. Ravanello
Universidade Federal do Rio Grande do Sul, Porto Alegre, Brazil

A. Kopp Alves (ed.), *Environmental Applications of Nanomaterials*, Engineering Materials, https://doi.org/10.1007/978-3-030-86822-2_2

sewage of urban areas, many hazardous wastes as textile dyes, resins, pharmaceutical wastes, mining effluents, pesticides, herbicides, and phenolic compounds can pollute water [2]. Thus, due to its undesirable health and environmental effects, water pollution is one of the main international political concerns.

Wastewater treatment technologies are usually arranged as primary, secondary, and tertiary treatment steps. Primary treatment (screening, comminution, grit removal, and sedimentation) removes materials that float or that are readily settled by gravity. Secondary treatment (biological processes) removes soluble organic matter and suspended solids. Tertiary treatment (advanced treatment technologies) can produce high-quality effluent for discharge or reuse [3]. Each kind of wastewater and discharge legislation will require specific advanced treatment.

Therefore, tertiary treatment techniques can be designed to remove specific pollutants that escape the secondary treatment step, as Emergent Contaminants (ECs), which present recalcitrant nature and/or toxicity to the microorganisms, for example [4]. Rout et al. [4] point to the main employed tertiary treatment technics: oxidation processes (ozonation, UV treatment, chlorination, photocatalysis) and sorption (activated carbon, biochar, carbon nanotubes, clay minerals).

From this perspective, this chapter focus on two important tertiary wastewater treatment technologies: Adsorption and Photocatalysis. The recent advances achieved mainly for nanomaterials development, both adsorbents, and photocatalysts, are addressed.

2 Wastewater Treatment Technologies Applying Nanomaterials

2.1 Adsorption

Water pollution is a recurrent problem on a global scale. The toxicity of some contaminants found in the water bodies is dangerous for human health and the environment. Thus, its removal efficiency involves complex mechanisms to achieve high efficiency. At the same time, the increase in the possible reuse of such materials widely applied in industry is an important parameter that enables the maintenance of a sustainable environment [5]. Other important parameters to be considered in such a project are low cost and easy operation. At the same time, it is known that metal-based nanomaterials have an excellent capacity to absorb toxic heavy metals from water [6]. Also, iron is a significant source of raw material for iron oxide synthesis, i.e., Fe_3O_4 nanoparticles (a low-cost material). From this point of view, the adsorption technique currently meets such requirements [5, 7–9]. The adsorption mechanism's basis is related to the type of molecular forces acting over the surface atoms of the adsorbent material. Since the adsorbent has a porous structure, the solute is collected and concentrated over the porous surface through intermolecular forces, most commonly electrostatic interaction [10, 11], chemisorption [11, 12], or physisorption.

Following the idea of sustainable thinking, Xue et al. [13] produced a novel adsorbent applying humic acid (HA) and Fe_3O_4 nanoparticles as a composite (HA-O/Fe_3O_4), which presented significant results of Adsorption. Magnetic nanoparticles are well-known materials with remarkable adsorption capacity. However, its stability is compromised over acid media, for example, when applied in a solution with heavy metal ions like Pb (II), Cu (II), Cd (II), and Ni (II). In order to increase its stability, an association with humic acid was tested by forming a colloid. Figure 1 illustrates the increased adsorption capacity and stability of Fe_3O_4 with surface-adsorbed HA. As shown in the diagram, the material can be collected with an image due to the magnetic nature of the composite and reused, maintaining its effectiveness for 4 cycles, as seen in Fig. 2.

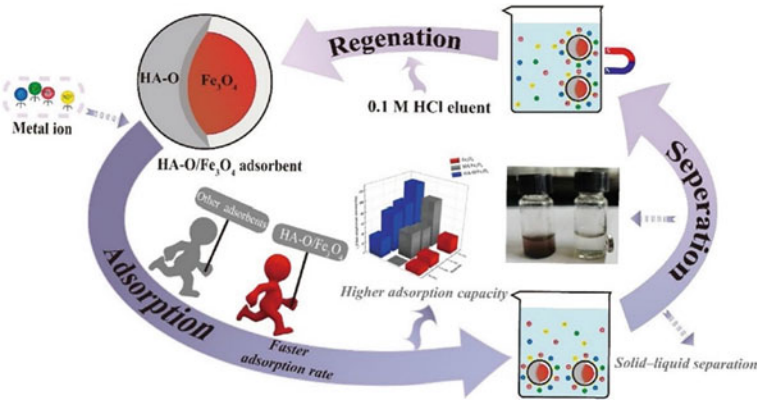

Fig. 1 Template of the adsorption process from application to reuse. Reprinted from Xue et al. [13]. Copyright 2021, with permission from Elsevier

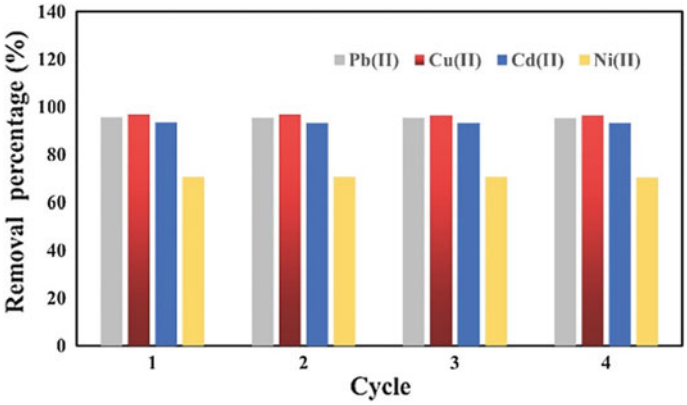

Fig. 2 Overall results on removal efficiency of HA-O/Fe_3O_4. Reprinted from Xue et al. [13]. Copyright 2021, with permission from Elsevier

Table 1 Maximum adsorption capacity (mg g^{-1})

Adsorbent	q_{max} (mg g^{-1})				Reference
	Pb(II)	Cu(II)	Cd(II)	Ni(II)	
HA-O/Fe_3O_4	111.10	76.90	71.42	33.33	[13]
Fe_3O_4	29.0	-	18.60	11.30	[13–15]

The primary adsorption mechanism is formed by condensed aromatic rings and oxygen functional groups randomly distributed. The presence of carboxyl and phenolic groups sets the mechanism as electrostatic Adsorption [13]. Table 1 shows the adsorption capacity of HA-O/Fe_3O_4, comparing the results without the presence of HA.

The literature reports the effective Adsorption of another toxic material U(VI), using Fe_3O_4 nanoparticles [16–18]. Zhang et al. [18] synthesized iron oxide coated with humic acid derived from lignite (LHA-coated Fe_3O_4) as a pathway to preventing aggregation due to the magnetic nature of the nanoparticles. In this study, a maximum adsorption capacity of 68.7 mg g^{-1} was obtained. In this case, lignite was used to prevent. Pan et al. [19] obtained an enhancement of maximum Adsorption applying different types of organic acids, thus preventing the aggregation and reaching 103 mg g^{-1}.

2.2 Photocatalysis

2.2.1 Introduction

This section presents a review of the photocatalysis technique applied to wastewater treatment. The involved mechanisms are presented focusing on the desirable semiconductors features to enhance the process efficiency, mainly the semiconductor bandgap energy (E_g) related to the sunlight absorption capacity and, hence, photocatalytic efficiency. Subsequently, the recent advances achieved in nanostructured photocatalyst research are presented.

2.2.2 Photocatalysis Mechanism

Photosynthesis is the primarily responsible energy entry into the biosphere. Through this process, life transforms sunlight into chemical energy and thus sustains the entire global flora. However, the natural photosynthesis mechanism is not yet fully understood. Therefore, developing an artificial system capable of directly using sunlight, as photosynthesis does, would be an excellent achievement for the whole scientific community [20].

The idea of using solar energy was initially presented in 1912 as *"The photochemistry of the future"* by Ciamician [21]. Meanwhile, in 1972, an important discovery was made in this field: *"Electrochemical photolysis of water at a semiconductor electrode*" by Honda and Fujishima [22]. This publication was noticeable as the beginning of a new era in heterogeneous photocatalysis, reporting the discovery of photocatalytic water oxidation on a TiO_2 electrode under UV light. Since then, extensive research on apparatus and semiconductor materials was performed to understand the fundamental mechanisms and enhance photocatalytic efficiency [2].

Nowadays, heterogeneous photocatalysis is a well-known Advanced Oxidative Process (AOP), which consists of hydroxyl free radicals generation, highly oxidizing, capable of mineralizing organic pollutants to non-toxic forms, such as CO_2 and H_2O. The great advantage of AOPs is that pollutants are destroyed (mineralized) instead of transferred from one phase to another, which makes them an effective alternative for effluent treatment [23].

Therefore, heterogeneous photocatalysis is catalysis driven by light. It involves redox reactions induced by radiation on the surface of mineral semiconductors, used as catalysts. These semiconducting catalysts must present charge transport characteristics, light absorption properties, and an electronic structure characterized by an empty conduction band and a filled valence band [24].

As reported by Kisch [25], the process starts on a semiconductor photocatalyst when a photoexcited electron is promoted from the filled valence band (VB) to its empty conduction band (CB). When the incident photon energy ($h\nu$) is equal to or greater than the semiconductor bandgap, it happens. Thus, an electron/hole pair ($e^-_{cb} + h^+_{vb}$) is formed. The e^-_{cb} is adsorbed by O_2 forming $O_2{}^{\circ -}$. The oxidation process starts when electron holes (h^+_{vb}) split the water molecule. Interacting with H^+ generated ion, $O_2{}^{\circ -}$ create hydroperoxyl radicals ($HO_2{}^{\circ}$), as shown in Eqs. 1–4.

$$\text{Photocatalyst} + \text{light} = \text{Photocatalyst}\left(e^-_{cb} + h^-_{vb}\right) \tag{1}$$

$$\text{Photocatalyst}\left(e^-_{cb}\right) + O_2 = \text{Photocatalyst} + O_2^{\circ -} \tag{2}$$

$$\text{Photocatalyst}\left(h^+_{vb}\right) + H_2O = \text{Photocatalyst} + H^+ + OH^- \tag{3}$$

$$O_2^{\circ -} + H^+ = HO_2^{\circ} \tag{4}$$

Hydroperoxyl radicals have scavenging properties, adsorbing electrons. This is very important to prevent electron/hole pair recombination. The generated holes have a high potential to oxidize organic matter and combine with all reactive oxygen species (ROS), as demonstrated by Eqs. 5–7.

$$HO_2^{\circ} + HO_2^{\circ} = H_2O_2 + O_2 \tag{5}$$

$$H_2O_2 + O_2^{\circ -} = OH^{\circ} + OH^- + O_2 \tag{6}$$

$$h^{+}_{vb} + \text{ROS} + \text{organic pollutant} = \text{degradation products} \quad (7)$$

Figure 3 illustrates the photocatalytic mechanism of organic pollutants degradation, simplified as follows: wastewater → photocatalyst/O_2/hν > E_g → degradation metabolites → CO_2 + H_2O + mineral acid [20].

The semiconductor material is the most important part of this system. Some photocatalyst desired properties are: high photoactive; the possibility of using visible and/or near-UV light; chemically and biologically inertness; cost-effective; non-toxic and stable toward photo corrosion [2]. An electron–hole pair is created when the incident photon (hν) presents energy equal to or higher than the semiconductor bandgap (E_g). As electron–hole pairs are required to start the photocatalytic process, low bandgap energy is critical for an efficient photocatalyst [27, 28].

As shown in Fig. 4, part of solar irradiation is dispersed or absorbed as it reaches the atmosphere. Chemical substances absorb specific wavelengths, altering the amount of light of those frequencies that reach the earth's surface [29]. ASTM G-173 [30] quantify the energy amount that hits the surface in each wavelength (W m^{-2} nm^{-1}). Therefore, the photocatalyst band gap energy (E_g, eV) can be related to its equivalent wavelength value (λg), which is the minimum required energy for semiconductor activation related to the solar spectrum ($E_g = 1240/\lambda g$). Thus, it is possible to estimate the maximum wavelength that still contains enough energy to generate electron/hole pairs in the semiconductor. Hence, estimate the percentage of the solar spectrum that it can use, i.e., its solar energy usage capacity [31].

Therefore, semiconductors with low bandgap energy can be more efficient. In addition, the smaller the bandgap of the material, the greater the number of photons

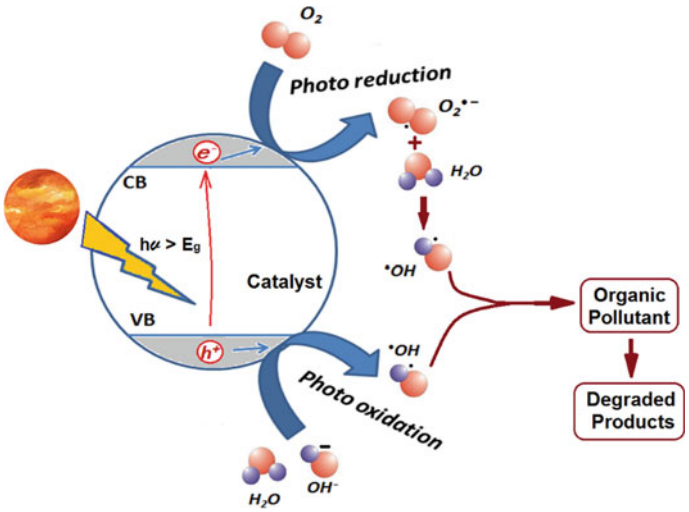

Fig. 3 Organic pollutants photocatalytic degradation mechanism. Adapted and reprinted from Kumar et al. [26]. Copyright 2017, with permission from Elsevier

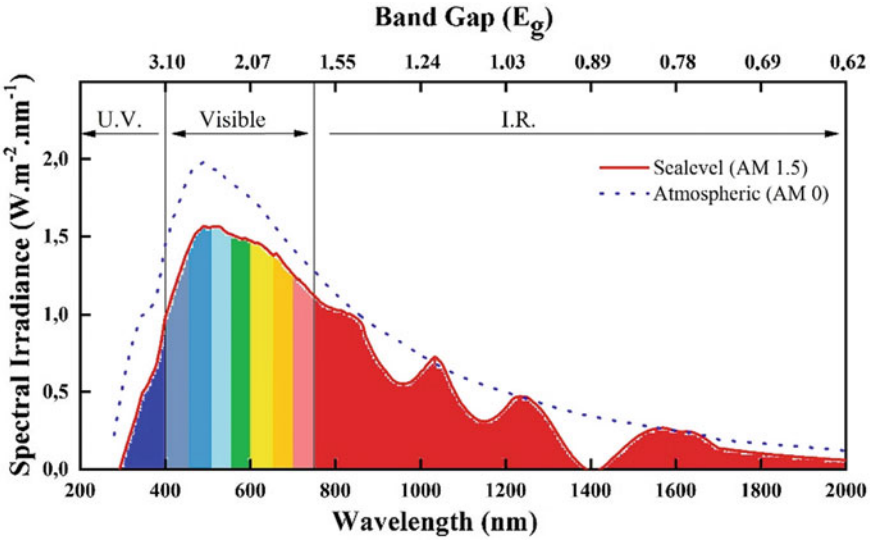

Fig. 4 Solar irradiance (W m^{-2}) as a function of wavelength (200–2000 nm) before atmospheric filter (AM 0) and at sea level (AM 1.5). Arranged using data from ASTM standard G-173–03 Top X presents each wavelength equivalent band gap energy (E_g). Reproduced with permission of [30]

with the specific energy to activate it [32]. For example, titanium dioxide (TiO_2) was the first and is one of the most studied photocatalysts due to its high chemical stability, relatively low cost, and highly oxidizing photogenerated holes [24]. However, the TiO_2 band gap is 3–3.2 eV [23], thus requiring wavelengths shorter than 384 nm for electron/hole photogeneration, availing less than 7% of the solar spectrum and generating extra costs with UV lamp need.

Several materials and their various combinations have been studied as a photocatalyst, the most common being: TiO_2, CdS, ZnO, WO_3, ZnS, BiO_3, to use visible solar irradiation GaAs, and Fe_2O_3 [33]. Recently, significant new materials and combinations such as mixed nanostructured oxide semiconductors based on bismuth [27, 34], and MnO_2 based photocatalysts [35] have been developed.

Some methods for improving semiconductor photocatalytic activity are composite systems, metal ion dopants, nonmetal doping, and dye sensitization [2]. Recently, a significant effort has been made in the nanostructured materials area to synthesize photocatalysts in the nanoscale (1–100 nm) that can present improved catalysts features, as shown in the next topic.

2.2.3 Nanostructured Photocatalysts

Saravanan et al. [2] report that, in comparison with bulk materials, nanomaterials have a large surface area and a small size, which can provide better efficiency in superficial reactions, as photocatalysis. A higher catalytic activity can be accomplished because

nanocatalysts present much more surface atoms than bulk materials, increasing their surface/volume ratio, hence the number of active sites and interfacial charge carriers. In addition, photocatalytic redox reaction also occurs on the photocatalysts surface, so the bigger surface area of nanostructured photocatalysts can meaningly enhance the photocatalytic wastewater treatment efficiency.

Despite its high bandgap energy (~3.2 eV), titanium dioxide (TiO_2) was the first and is the most employed and studied photocatalyst semiconductor, mainly due to its stability in extreme situations, extraordinary photocatalytic productivity, and even suitable band edge capabilities [36]. D'Amato et al. [37] studied modified TiO_2 nanoparticles surface with ascorbic acid. The obtained nanophotocatalyst (55–80 nm) showed a bandgap energy (Eg) reduction to 2.87neV and presented good results when applied in photodegradation of Alizarin Red S in water solutions, even under visible light, which cannot be performed employing the commercial catalyst. Assayehegn et al. [38] studied the effect of nitrogen-doped titania (N/TiO_2) nanomaterials to photodegrade Methylene Blue under visible light irradiation. The obtained nanophotocatalyst (1:1 N/Ti, 42% Anatase, 58% Rutile, 14–18 nm, 2.91 eV) showed photodegradation kinetics of 0.033 min^{-1} (17 times faster than undoped TiO_2) and an efficiency up to 97%. The improvement was attributed to the higher surface area, light absorption capacity, and lower bandgap energy achieved by the synergistic effect of N-doping.

Using scattered photocatalysts in solution is the most efficient way as its whole area can react while receiving irradiation. However, there are some concerns about using dispersed nanoparticles in photocatalysis, mainly that it requires a recovery step to separate the catalyst from treated water after the photodegradation process. For example, Scharnberg et al. [23] evaluated Rhodamine B (RhB) degradation using TiO_2 nanoparticles (15 nm; 60 m^{-2} g^{-1}) supported by a dip-coating process under porous ceramics previously produced incorporating glass and organic wastes [39]. Although the nanoparticle's reactive area has been reduced, satisfactory results were obtained, and the photocatalyst could be easily taken from treated water with the ceramic plates. It was even possible to reuse the nanocatalyst.

In the same way, Rangel et al. [40] studied a foam glass decorated with zinc oxide (ZnO) nanoparticles (3.18 eV; 75 nm) in Rhodamine B photodegradation. The results were satisfactory and similar to those obtained using nanostructured ZnO suspension. Still, the use of a support for the semiconductor facilitated its recovery and eliminated a filtration step.

Another alternative for catalyst recovery was introduced by the development of magnetic nanophotocatalysts (MNPCs). These semiconductors separation can be easily performed applying an external magnetic field, what can provide a more efficient and even environmentally friendly photocatalysis wastewater treatment process. Gómez-Pastora et al. [41] list synthesis routes, catalytic performance, and magnetic recovery step of several MNPCs. Magnetic photocatalysts present a composite core–shell structure, attaching semiconductors and magnetic nanomaterials. The core provides its magnetic behavior and is composed of magnetic elements, usually iron, nickel, cobalt, and oxides (Fe_3O_4, Υ-Fe_2O_3, $CoFe_2O_4$, Ni_3Fe). The shell is

composed of photocatalytic materials. TiO_2 is the coating material most widely studied; however, ZnO, AgBr, BiOCl, and others are applied as well [41].

Fisli et al. [42] prepared Fe_3O_4/TiO_2 nanocomposites by heteroagglomeration. The magnetic nanophotocatalyst (100 nm; 63.5 m^2g^{-1}) presented superparamagnetic characteristics (21.5 emu g^{-1}). Due to iron oxide in composite (non-active), the photocatalytic activity (92%) was lower than using pure TiO_2. However, the composite was easily recovered by applying an external magnetic field in a slurry-type reactor. Rezaei-Vahidian et al. [43] evaluated the degradation of P-Nitrophenol (PNP) by photocatalysis employing magnetic titania nanoparticles ($Fe_3O_4@SiO_2@TiO_2$), with 22 nm, as shown in Fig. 5. The results showed a degradation rate of up to 90 and 69% of PNP mineralization. The nanophotocatalyst was recovered from the treated solution using a magnetic field and recycled five times. Recycling presented a low decline in degradation efficiency (90 to 82%). The decline was attributed to the loss of a small part of the photocatalyst in each run.

Beyond the improvements achieved with the study of traditional nanostructured photocatalysts, significant advances using new semiconductor nanomaterials have been accomplished. Bencina et al. [44] synthesized Bi–Fe–Nb–O pyrochlore nanoparticles (40 nm) by coprecipitation method. The semiconductor (Fig. 6) exhibits narrow bandgap energy (1.9 eV), hence an intense visible light absorption and high visible-light photocatalytic activity. Using 0.1 g of nanoparticles, 75 ml of methyl orange (14 $mg.L^{-1}$) was photodegrade in 4 h under visible light. However, preliminary, the semiconductor suspension in pure water did not induce the reaction. An alternative found was adding peroxide hydrogen to the solution that can interact with the photoinduced electrons and preventing charge recombination, allowing the photogenerated electron holes to be available to react.

Carbon-based nanomaterials compose another family of promising photocatalysts, mainly due to their large surface area, abundance, and relatively low cost. The

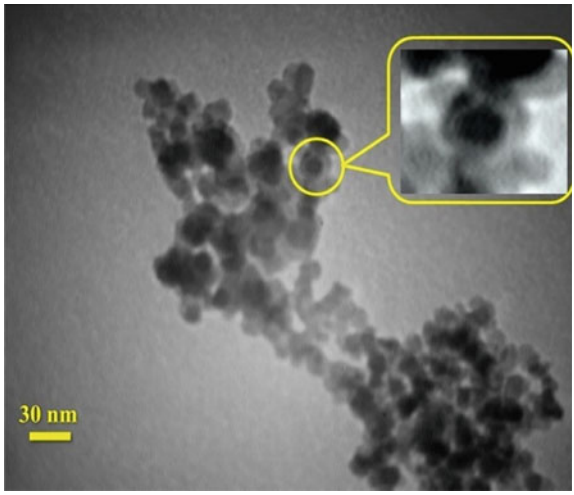

Fig. 5 Transmission Electron Microscopy (TEM) image of $Fe_3O_4@SiO_2@TiO_2$ nanoparticles. Reprinted with permission from Rezaei-Vahidian et al. [43]. Copyright 2017 Elsevier

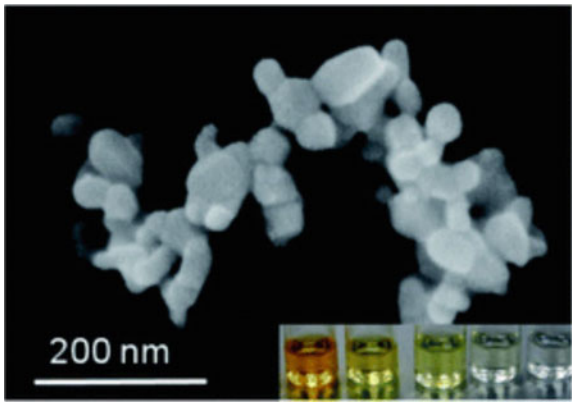

Fig. 6 Scanning Electron Microscopy (SEM) image of Bi-Fe-Nb–O nanoparticles and methyl orange photodegradation as a function of time. Reprinted with permission from Bencina et al. [44]. Copyright 2014 The Royal Society of Chemistry

most studied carbonaceous photocatalysts include Carbon Quantum Dots (CQDs), smaller than 10 nm; Carbon Nanotubes (CNTs), which can have its proprieties enhanced by doping photocatalysts; Graphene Oxide (GO) and Reduced Graphene Oxide (RGO), with reduced bandgap energy due to their high light absorption capacity; and Activated Carbon (AC), with large surface area and porosity [45]. Graphitic carbon nitride (g-C_3N_4) is considered one of the most promising photocatalysts being investigated, even relatively recent (2009), due to its good stability, easy method of preparation, and easy band gap handling. Much progress has been made on g-C_3N_4-based photocatalysts. Cao et al. [46] report methods of nanostructured pristine g-C_3N_4 synthesis, the preparation of g-C_3N_4-based semiconductor composites (g-C_3N_4/TiO_2; g-C_3N_4/ZnO; g-C_3N_4/WO_3; g-C_3N_4/Fe_2O_3; etc.), and versatile bandgap engineering through atomic level doping (Cu^{2+}, Fe^{3+}, Mn^{3+}, Ni^{3+}, Co^{3+}).

Wang et al. [47] studied g-C_3N_4/Bi_2WO_6 nanosheets (60 nm) to degrade Methylene Blue throw photocatalysis. The results showed a photocatalytic activity 68.9% higher than using pure Bi_2WO_6. The enhancement was attributed to the rapid photoinduced charge separation on the composite surface. In addition, the photogenerated electron-holes on the catalyst could be transferred to the highest occupied molecular orbital of C_3N_4, reducing the recombination effect. Ghanbari et al. [48] evaluated Copper Iodide decorated g-C_3N_4 nanosheets (CuI/g-C_3N_4) to photocatalytic organic pollutant removal under visible light. With a bandgap of 2.8 eV, the nanocomposite showed higher photocatalytic performance than the pure C_3N_4 and CuI and presented satisfactory results degrading various organic dyes. Besides, CuI/g-C_3N_4 nanosheets could be successfully reused without loss of photocatalytic activity.

Niobium-based photocatalysts have received attention due to their desirable catalyst features like non-toxicity, good stability, facile recycling, and availability. Dos Santos et al. [49] pinpoints Nb_2O_5 nanoparticles as potential photocatalysts in wastewater treatment due to their innocuous character. Complete decolorization of a methyl orange solution (15 mg L^{-1}) was achieved in only 40 min of treatment. After several cycles, Nb_2O_5 nanoparticles presented the same efficiency rate. Dai et al. [50] developed a nano-fibriform C-modified niobium pentoxide (F–C/Nb_2O_5), forming

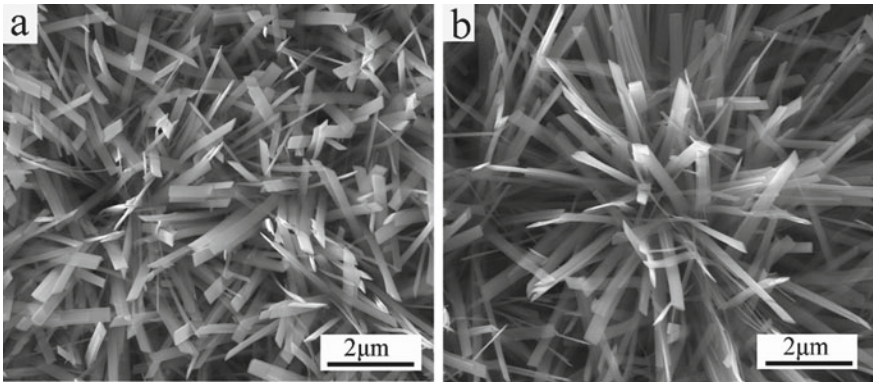

Fig. 7 Field Emission Scanning Electron Microscopy (FESEM) image of **a** Nb_2O_5 annealed in air and **b** N-Nb_2O_5 annealed in NH_3. Reprinted with permission from Hu and Liu [51]. Copyright 2017 Elsevier

a three-dimensional nanorod structure (30 nm) by vacuum induced self-assembly method. The nanophotocatalyst exhibited a surface area of 52 m^2g^{-1} and a bandgap of 3.01 eV, able to operate under visible light. Rhodamine B (pH < 3) degradation results showed an efficiency 2.4 higher than ordinary C/Nb_2O_5 under visible light, even after cycling five times.

Hu and Liu [51] developed nitrogen-doped niobium pentoxide nanobelt quasi-arrays (N-Nb_2O_5) by hydrothermal reaction followed by annealing in NH_3 atmosphere on metal Nb foil. The doped nanocatalyst (Fig. 7) presented bandgap energy of 2.4 eV, while the conventional Nb_2O_5 is 3.4 eV. Furthermore, its structure is quasi 1D, hence provides a large surface area, light irradiation, and contact with pollutant molecules, showing high photocatalytic performance. Furthermore, while conventional Nb_2O_5 nanobelt presented a weak photocatalytic activity under visible light photodegrading Methyl Blue (10%), the N-Nb_2O_5 samples presented a significant enhancement (40%). This phenomenon is explained by the middle gap formed by the doped N atoms, which accelerates the electrons/holes pairs production under visible light, which is impossible using conventional Nb_2O_5 (3.4 eV). Thus, N-Nb_2O_5 nanobelt was considered a promising candidate for wastewater treatment under visible light.

The development of a functional and effective photocatalytic wastewater treatment system without requiring external energy (under visible light) will represent an excellent achievement for society. As described so far, much advance has been made in nanophotocatalysts research. However, to overthrow the bottleneck imposed by light absorption capacity, it is paramount to develop a photocatalyst that joins features as good stability under a wide range of pH; non-toxic; easily available; not expensive; low bandgap energy; low electron–hole recombination rate, and the possibility of reuse.

3 Conclusions

According to the overall results, both photodegradation and Adsorption presented remarkable results related to water treatment reported in the literature. It can be seen that the two techniques are in agreement with sustainable development. There is a constant concern and increasing attention of the scientific community due to the mechanism's effectiveness. The results achieved by photodegradation and adsorption technics show that it is possible to mineralize toxic compounds or even recover several types of toxic materials from aqueous effluents without the need for an excessively complex system. The synthesis of magnetic nanoparticles is a widespread and studied process, making it extremely precise, thus ensuring its high applicability. Photocatalysts have been investigated at least since 1972. However, in the scope of both areas, some studies focused on toxicity and adsorption mechanism understanding are still required to ensure the most suitable way of using these technologies on an industrial scale.

References

1. Liu, L., Johnson, H.L., Cousens, S., Perin, J., Scott, S., Lawn, J.E., Rudan, I., Campbell, H., Cibulskis, R., Li, M., Mathers, C., Black, R.E.: Global, regional, and national causes of child mortality: An updated systematic analysis for 2010 with time trends since 2000. Lancet **379**(9832), 2151–2161 (2012)
2. Saravanan, R., Gracia, F., Stephen, A: Basic principles, mechanism, and challenges of photocatalysis. In: Nanocomposites for Visible Light-induced Photocatalysis, p. 19–40. Springer Series (2017)
3. Metcalf e Eddy, Wastewater Engineering: Treatment and Reus. Boston, MA, McGraw-Hill, (2003)
4. Rout, P.R., Zhang, T.C., Bhunia, P., Surampalli, R.Y.: Treatment technologies for emerging contaminants in wastewater treatment plants: A review. Sci. Total Environ. **753**, 141990 (2021)
5. Zhou, W., Deng, J., Qin, Z., Huang, R., Wang, Y., Tong, S.: Construction of MoS_2 nanoarrays and MoO_3 nanobelts: two efficient adsorbents for removal of Pb(II), Au(III) and Methylene Blue. J. Environ. Sci. **111**, 38–50 (2022)
6. Guo, R., Jiao, T., Li, R., Chen, Y., Guo, W., Zhang, L., Zhou, J., Zhang, Q., Peng, Q.: Sandwiched Fe3O4/Carboxylate graphene oxide nanostructures constructed by layer-by-layer assembly for highly efficient and magnetically recyclable dye removal ACS sustain. Chem. Eng. **6**(1), 1279–1288 (2018)
7. Zheng, H., Jia, J., Li, Z., Jia, Q.: Bifunctional magnetic supramolecular-organic framework: a nanoprobe for simultaneous enrichment of glycosylated and phosphorylated peptides. Anal. Chem. **92**(3), 2680–2689 (2020)
8. Mariosi, F.R., Venturini, J., da Cas Viegas, A., Bergmann, C.P.: Lanthanum-doped spinel cobalt ferrite ($CoFe_2O_4$) nanoparticles for environmental applications. Ceram. Int. **46**(3), 2772–2779 (2020)
9. Venturini, J.: Application of Ferrite Nanoparticles in Wastewater Treatment. In: Nanomaterials for Eco-friendly Applications, p. 141–151. A. Kopp Alves, Org. Cham, Springer International Publishing (2019)
10. Gupta, V.K., Moradi, O., Tyagi, I., Agarwal, S., Sadegh, H., Shahryari-Ghoshekandi, R., Makhlouf, A.S.H., Goodarzi, M., Garshasbi, A.: Study on the removal of heavy metal ions

from industry waste by carbon nanotubes: Effect of the surface modification: a review. Crit. Rev. Environ. Sci. Technol. **46**(2), 93–118 (2016)
11. Sadegh, H., Ali, G.A.M., Gupta, V.K., Makhlouf, A.S.H., Shahryari-ghoshekandi, R., Nadagouda, M.N., Sillanpää, M., Megiel, E.: The role of nanomaterials as effective adsorbents and their applications in wastewater treatment. J. Nanostruct. Chem. **7**(1), 1–14 (2017)
12. Sadegh, H., Zare, K., Maazinejad, B., Shahryari-Ghoshekandi, R., Tyagi, I., Agarwal, S., Gupta, V.K.: Synthesis of MWCNT-COOH-Cysteamine composite and its application for dye removal. J. Mol. Liq. **215**(March), 221–228 (2016)
13. Xue, S., Xiao, Y., Wang, G., Fan, J., Wan, K., He, Q., Gao, M., Miao, Z.: Adsorption of heavy metals in water by modifying Fe3O4 nanoparticles with oxidized humic acid. Colloids Surf. A Physicochem. Eng. Asp. **616**(1), 126333 (2021)
14. Nassar, N.N.: Rapid removal and recovery of Pb(II) from wastewater by magnetic nanoadsorbents. J. Hazard. Mater. **184**(1), 538–546 (2010)
15. Nassar, N.N.: Kinetics, equilibrium and thermodynamic studies on the adsorptive removal of nickel, cadmium and cobalt from wastewater by superparamagnetic iron oxide nanoadsorbents. Can. J. Chem. Eng. **90**(5), 1231–1238 (2012)
16. Huber, F., Schild, D., Vitova, T., Rothe, J., Kirsch, R., Schäfer, T.: U(VI) removal kinetics in presence of synthetic magnetite nanoparticles. Geochim. Cosmochim. Acta **96**, 154–173 (2012)
17. Crane, R.A., Dickinson, M., Popescu, I.C., Scott, T.B.: Magnetite and zero-valent iron nanoparticles for the remediation of uranium contaminated environmental water. Water Res. **45**(9), 2931–2942 (2011)
18. Zhang, Y., Fein, J.B., Li, Y., Yu, Q., Zu, B., Zheng, C.: U(VI) adsorption to Fe_3O_4 nanoparticles coated with lignite humic acid: Experimental measurements and surface complexation modeling. Colloids Surf. A Physicochem. Eng. Asp. **614**, 126150 (2021)
19. Pan, Z., Li, W., Fortner, J.D., Giammar, D.E.: Measurement and surface complexation modeling of U(VI) adsorption to engineered iron oxide nanoparticles. Environ. Sci. & Technol. **51**(16), 9219–9226 (2017)
20. Colmenares, J.C., Luque, R.: Heterogeneous photocatalytic nanomaterials: prospects and challenges in selective transformations of biomass-derived compounds. Chem. Soc. Rev. **43**(3), 765–778 (2014)
21. Ciamician, G.: MODERN civilization is the daughter of coal, for this offers to mankind the solar. Science (80-) **XXXVI**, 926 (1912)
22. Fujishima, A., Honda, K.: Electrochemical photolysis of water at a semiconductor electrode. Nature **238**(5358), 37–38 (1972)
23. de Araujo Scharnberg A.R., de Loreto, A.C., Wermuth, T.B., Alves A.K., Arcaro, S., dos Santos, P.A.M., de Rodriguez A.A.L.: Porous ceramic supported TiO2 nanoparticles: Enhanced photocatalytic activity for Rhodamine B degradation. Boletín la Soc. Española Cerámica y Vidr **59**(6), 230–238 (2020)
24. Fujishima, A., Rao, T., Tryk, D.: Titanium dioxide photocatalysis. J. Photochem. Photobiol. C Photochem. Rev. **1**, 1–21 (2000)
25. Kisch, H.: Semiconductor photocatalysis—Mechanistic and synthetic aspects. Angew. Chemie.—Int. Ed. **52**(3), 812–847 (2013)
26. Kumar, A.A., Rajini, A., Venkatathri, N.: Synthesis and characterization of magnetically separable porous titanium silicate nanocomposite catalyst for environmental applications. Mater. Today Proc. **4**(1), 19–24 (2017)
27. Araujo Scharnberg, A.R., Carvalho de Loreto, A., Kopp Alves, A.: Optical and structural characterization of $Bi_2Fe_xNbO_7$ nanoparticles for environmental applications. Emerg. Sci. J. **4**(1), 11–17 (2020)
28. de Scharnberg, A.R.A., Berutti, F., Alves, A.: Visible-light Bi-Fe-Nb-O photoanodes for solar-light driven hydrogen production. Environ. Technol. (2020)
29. Lean, J.: Evolution of the Sun's Spectral Irradiance Since the Maunder Minimum (2000)

30. A.S.T.M. International: ASTM G173–03(2012). Standard Tables for Reference Solar Spectral Irradiances: Direct Normal and Hemispherical on 37° Tilted Surface (2012)
31. Scharnberg, A., Pavlovic, A., Alves, A.: Synthesis of Bi2FeXNbO7 films applied as a catalyst for hydrogen production using visible-light photo-electrolysis. IOP Conf. Ser. Mater. Sci. Eng. **659**(1), 012081 (2019)
32. Valant, M., Bencina, M., Fanetti, M.: Visible-light photoactivity of Bi-pyrochlores with high Fe contents. Acta Chim. Slov. **61**(3), 447–452 (2014)
33. Kabra, K., Chaudhary, R., Sawhney, R.L.: Treatment of hazardous organic and inorganic compounds through aqueous-phase photocatalysis: a review. Ind. Eng. Chem. Res. **43**(24), 7683–7696 (2004)
34. Ropero-Vega, J.L., Meléndez, A.M., Pedraza-Avella, J.A., Candal, R.J., Niño-Gómez, M.E.: Mixed oxide semiconductors based on bismuth for photoelectrochemical applications. J. Solid State Electrochem. **18**(7), 1963–1971 (2014)
35. Chiam, S.L., Pung, S.Y., Yeoh, F.Y.: Recent developments in MnO_2-based photocatalysts for organic dye removal: a review. Environ. Sci. Pollut. Res. **27**(6), 5759–5778 (2020)
36. Tahir, M.B., Iqbal, T., Rafique, M., Rafique, M.S., Nawaz, T., Sagir, M.: Nanomaterials for photocatalysis. In: Nanotechnology and Photocatalysis for Environmental Applications, pp 65–76. Elsevier Inc (2020)
37. D'Amato, C.A., Giovannetti, R., Zannotti, M., Rommozzi, E., Minicucci, M., Gunnella, R., Di Cicco, A.: Band gap implications on Nano-TiO2 surface modification with ascorbic acid for visible light-active polypropylene coated photocatalyst. Nanomaterials **8**(8), 599 (2018)
38. Assayehegn, E., Solaiappan, A., Chebude, Y., Alemayehu, E.: Fabrication of tunable anatase/rutile heterojunction N/TiO_2 nanophotocatalyst for enhanced visible light degradation activity. Appl. Surf. Sci. **515**, 145966 (2020)
39. Scharnberg, A.R.A., Priebbnow, A.V., Arcaro, S., Da Silva, R.M., Dos Santos, P.A.M., Basegio, T.M., Rodriguez, A.A.L.: Evaluation of the addition of soda-lime glass and yerba mate wastes in ceramic matrix. Cerâmica **65**, 63–69 (2019)
40. Rangel, E.M., de Melo, C.C.N., Machado, F.M.: Ceramic foam decorated with ZnO for photodegradation of Rhodamine B dye. Boletín la Soc Española Cerámica y Vidr. **58**(3), 134–140 (2019)
41. Gómez-Pastora, J., Dominguez, S., Bringas, E., Rivero, M.J., Ortiz, I., Dionysiou, D.D.: Review and perspectives on the use of magnetic nanophotocatalysts (MNPCs) in water treatment. Chem. Eng. J. **310**, 407–427 (2017)
42. Fisli, A., Saridewi, R., Dewi, S.H., Gunlazuardi, J.: Preparation and characterization of Fe_3O_4/TiO_2 composites by heteroagglomeration. Adv. Mater. Res. **626**, 131–137 (2013)
43. Rezaei-Vahidian, H., Zarei, A.R., Soleymani, A.R.: Degradation of nitro-aromatic explosives using recyclable magnetic photocatalyst: catalyst synthesis and process optimization. J. Hazard. Mater. **325**, 310–318 (2017)
44. Bencina, M., Valant, M., Pitcher, M.W., Fanetti, M.: Intensive visible-light photoactivity of Bi- and Fe-containing pyrochlore nanoparticles. Nanoscale **6**(2), 745–748 (2014)
45. Tahir, M. B., Khalid, N. R., Rafique, M., Iqbal, T., Rafique, M. S., Ahmed A.: Carbonaceous nanomaterials as photocatalysts. In: Nanotechnology and Photocatalysis for Environmental Applications, pp. 97–117. Elsevier Inc. (2020)
46. Cao, S., Low, J., Yu, J., Jaroniec, M.: Polymeric photocatalysts based on graphitic carbon nitride. Adv. Mater. **27**(13), 2150–2176 (2015)
47. Wang, Y., Bai, X., Pan, C., He, J., Zhu, Y.: Enhancement of photocatalytic activity of Bi_2WO_6 hybridized with graphite-like C_3N_4. J. Mater. Chem. **22**(23), 11568–11573 (2012)
48. Ghanbari, M., Salavati-Niasari, M.: Copper iodide decorated graphitic carbon nitride sheets with enhanced visible-light response for photocatalytic organic pollutant removal and antibacterial activities. Ecotoxicol. Environ. Saf. **208**, 111712 (2021)
49. Dos Santos, A.J., Batista, L.M.B., Martínez-Huitle, C.A., de Alves, A.P.M., Garcia-Segura, S.: Niobium oxide catalysts as emerging material for textile wastewater reuse: Photocatalytic decolorization of azo dyes. Catalysts **9**(12), 1070 (2019)

50. Dai, Q., Yuan, B., Guo, M., Zhang, K., Chen, X., Song, Z., Nguyen, T.T., Wang, X., Lin, S., Fan, J., Li, Y., Liu, H., Guo, Z.: A novel nano-fibriform C- modified niobium pentoxide by using cellulose templates with highly visible-light photocatalytic performance. Ceram. Int. **46**(9), 13210–13218 (2020)
51. Hu, B., Liu, Y.: Nitrogen-doped Nb_2O_5 nanobelt quasi-arrays for visible light photocatalysis. J. Alloys Compd. **635**, 1–4 (2015)

Photochromic Nanomaterials with Photocatalytic Application

Luana Góes Soares and Annelise Kopp Alves

Abstract Heterogeneous photocatalysis is part of Advanced Oxidative Processes (POA's), using semiconductors as catalysts, usually TiO_2. The activation of this semiconductor occurs when exposed to solar or artificial radiation. It is extensively used for the most diverse applications due to its effectiveness in decomposing pollutants in water, air, bacteria, cancer cells, and in the degradation of toxic organic compounds. However, the absorption capacity occurs preferentially in the UV region of the electromagnetic spectrum, and only 3–4% of the solar spectrum can be used to activate it for photocatalysis. Aiming to expand the region of sunlight absorption, several studies have already been carried out, and one of the alternatives is the doping of TiO_2 with transition metals, such as WO_3. Within this context, the use of TiO_2 nanofibers synthesized by electrospinning and doped with WO_3 as photocatalysts is inserted. Because they present a greater photoactivity, as they have a high surface area, they prevent the recombination of the electron/gap pair and reduce the rearrangement speed. It is believed that there is a synchrony between the photochromic and photocatalytic properties of titanium and tungsten oxide nanofibers, which directly contribute to the photocatalytic efficiency of the materials, allowing the transfer of charges between TiO_2 and WO_3.

Keywords Titanium dioxide · Tungsten trioxide · Nanofiber · Photocatalysis · Photochromic

Abbreviations

a*	Red/green color coordinate chromatic
b*	Blue/yellow chromatic coordinate
CIE-Lab	Commission International Lighting-Colour Space L*a*b
EDX	Energy Dispersion X-ray Spectroscopy
L%	Luminosity

L. G. Soares (✉) · A. K. Alves
Universidade Federal do Rio Grande do Sul, Porto Alegre, Brazil

A. Kopp Alves (ed.), *Environmental Applications of Nanomaterials*, Engineering Materials, https://doi.org/10.1007/978-3-030-86822-2_3

POA's	Advanced oxidative processes
SEM	Scanning electron microscopy
TEM	Transmission electron microscopy
UV	Ultraviolet light
XRD	X-ray diffraction

1 Introduction

Physical, chemical, biological, and hybrid techniques can be used to synthesize different types of nanomaterials, which are in the form of colloids, agglomerates, powders, tubes, rods, wires, thin films, among others. The technique to be used varies depending on the material of interest and the type of nanomaterial [1].

The characterization of optical properties in nanomaterials depends on how these materials interact when light is incident. Because when light falls on a material, one or more optical phenomena can occur, and they are: reflection, transmission, and absorption. Other factors that affect a material's optical response are the photon energy, or wavelength of light, the technique to be used to obtain the material in question and the type of substrate to be used [2].

It is also worth remembering that many optical properties, such as those that initiate color activity, are related to electronic absorption and emission processes due to impurities and other punctual defects [3].

Photochromism was first observed in 1963 in tungsten oxide. This effect becomes visible when a material is subjected to some type of electromagnetic radiation, which can be UV, visible light, or infrared. Photochromic alterations are reversible and vary according to the chemical environment, the irradiation conditions under which the material is submitted, the characteristics and composition of the material. Morphology and crystallinity, for example, are properties that will directly influence the photochromic alteration capacity of the material in question [2, 4].

The application of photochromic materials occurs in the most diverse branches of the industry. It includes contact lenses and eyeglasses, in sensors, in smart windows, in high-density memory devices, non-emitting displays, photoswitches, etc. To explain photochromism, several mechanisms are recommended; the most recognized are the formation of color centers by O_2 vacancies, double insertion of ions and electrons, and small-polaron [5].

Although tungsten oxide is the transition metal with the largest optical absorbance variations, other metal oxides have also been used to analyze this effect, such as molybdenum, vanadium, and titanium oxides [2].

Generally, for the perception of this phenomenon, oxides in the form of powders and thin films are used when irradiated in vacuum, in air, in alcohols and aldehydes, or in a hydrogen atmosphere, which can be crystalline, amorphous oxides, or oxides of different compositions [2]. To measure color differences, colorimeters or spectrophotometers are used. These types of equipment have sensors responsible

for determining the reflected or transmitted light and analyze the optical properties of materials by associating them with one of the existing color systems, usually the CIELab [6, 7].

The synthesis, photochromic characterization, and application of nanofibers in heterogeneous photocatalysis will be covered in this chapter.

2 TiO_2

Titanium dioxide (TiO_2) has three allotropic crystalline forms: anatase (tetragonal), rutile (tetragonal), and brookite (orthorhombic) [9]. The anatase and rutile forms are most frequently used in photocatalytic applications. The main differences between the TiO_2 polymorphs are the lengths and the angles of the Ti–O bonds, and how the TiO_6 octahedra are arranged in the formation of the crystallographic network. Figure 1 shows the three crystal structures under which TiO_2 appears.

TiO_2 has been used in both environmental and commercial applications. Some examples include water remediation, photocatalysis, rechargeable batteries, supercapacitors, sensor devices, as an opacifying agent in paints, plastics, textiles, and cosmetics, as coatings, antibacterial agent, for self-cleaning surfaces, H_2 production from water, in food additives, such as an ultraviolet absorber, among others. It is generally chosen to be used in the aforementioned applications because it has the following characteristics: low toxicity, insoluble in water, photostable, can be immobilized on solids, it has high stability and low cost [8].

Even with a high bandgap value (3.0–3.2 eV), TiO_2 is a semiconductor extensively used in heterogeneous photocatalysis. However, there are some restrictions encountered when using it: recombination of the generated electron–hole pair, the high speed of rearrangement of H_2 and O_2 in water, and the absorption capacity of TiO_2 occur preferentially in the UV region of the electromagnetic spectrum, thus, only 3–4% of the solar spectrum can be used to activate the TiO_2 for photocatalysis [8].

Aiming at solving these restrictions, several studies have already been carried out, and some alternatives are: the doping of TiO_2 with non-metallic elements and transition metals (WO_3, Mo, Mn, Fe, Ni, Co, etc.), and the synthesis of nanostructures: nanotubes, nanowires, nanorods, nanobelts, nanofibers, among others [10, 11]. Figures 2, 3 and 4 show images of different TiO_2 nanostructures.

3 TiO_2 Nanofibers

Fibers are one-dimensional nanostructures, widely used in the most diverse applications, as they have properties such as flexibility, optical properties, and the ability to interact with other areas of science, in addition to exhibiting properties superior to those of their respective micrometric fibers. Furthermore, they also demonstrate

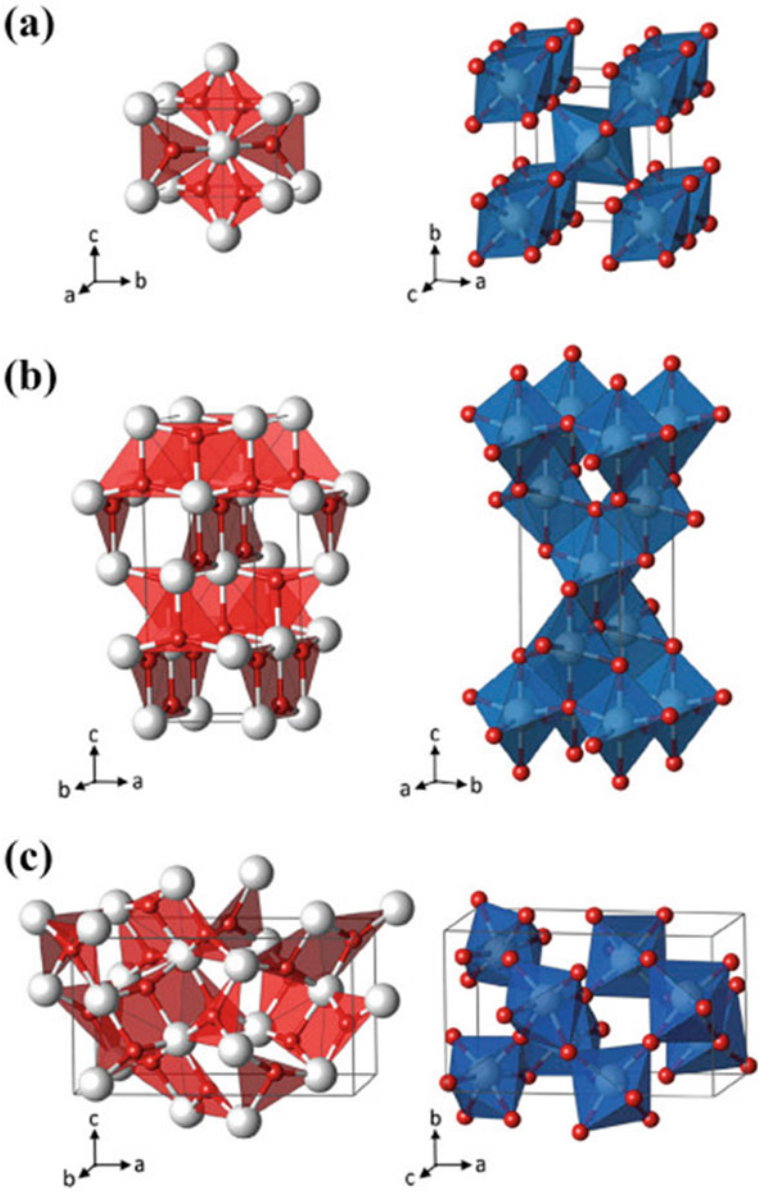

Fig. 1 Polymorphic structures of TiO_2 **a** rutile, **b** anatase and **c** brookite. Reproduced with permission from Ref. [8]

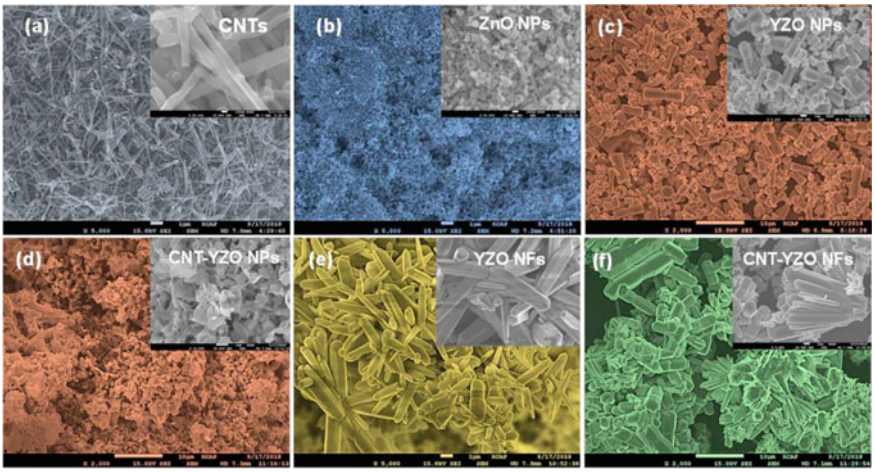

Fig. 2 SEM images of nanoparticles and nanoflowers with different compositions. Reproduced with permission of Sharma et al. [12]

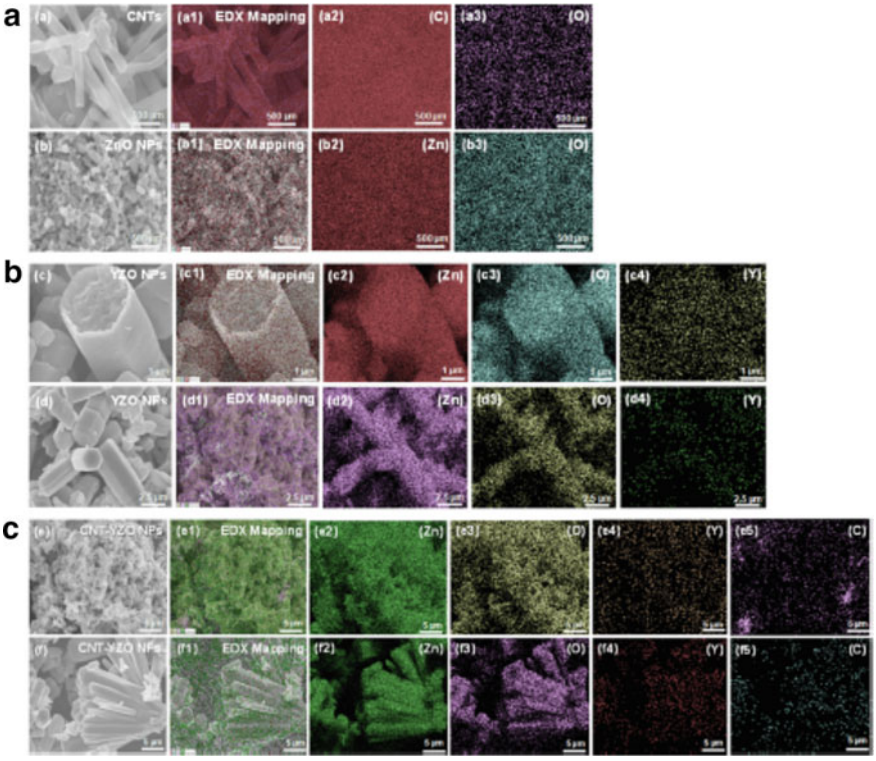

Fig. 3 **a** EDX mapping CNTs and ZnO NPs, **b** YZO NPs and NFs, **c** CNT-ZnO NPs and NFs. Reproduced with permission of Sharma et al. [12]

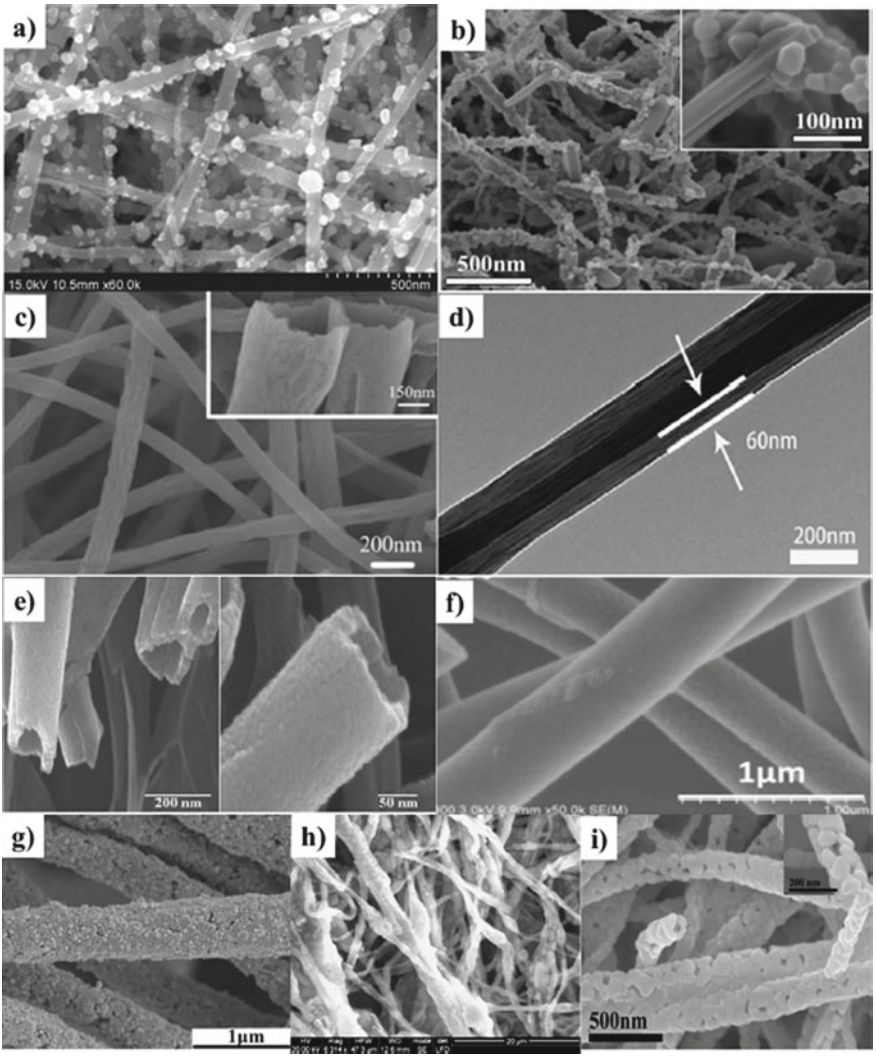

Fig. 4 SEM images of electrospun fibers of **a** CdS/TiO_2 on PVP; **b** V_2O_5/TiO_2 on PVP; **c** Ag-TiO_2 nanotubes on PVP; **d** core-sheath TiO_2-SiO_2 on PVA; **e** hollow TiO_2 on PVP; **f** SiO_2-TiO_2 calcined at 700 °C; **g** TiO_2 on PMMA; **h** TiO_2 on PAN; **i** graphene oxide wrapped TiO_2 on PVP. Reproduced with permission of Pasini et al. [11]

greater photoactivity when used in catalytic reactions; for example, the reaction rate increases as the diameter of the catalyst fibers decreases since active sites are also linked to the increase in their surface area. In this way, it is feasible to increase the system's reactivity without causing adversities, such as agglomeration/aggregation of particles [13, 14].

Fibers can be formed through solutions that contain inorganic, non-metallic oxides or non-oxides, with a polycrystalline, semi-crystalline, or amorphous structure. Ceramic fibers are mostly intended for applications that require oxidative stability and high resistance at high temperatures, such as in structural materials for ceramic (CMC) and metallic (CMM) composites [13, 14].

Ceramic oxides and non-oxides that can be used are: SiO_2, Al_2O_3, $BaTiO_3$, TiO_2, ZrO_2, CuO, ZnO, NiO, mullite, hydroxyapatite, ferrites (Co, Ni), $NiZnFe_2O_4$, rare-earth ferrites (Yb, Gd, Sm, La), NiO–SnO_2, $CeO_2.Y_2O_3$, WO_3, SiC and others [13–15].

In this context, most of the works published in the last ten years report the electrospinning method as the main technique for obtaining fibers/nanofibers from different types of materials.

Pasini et al. [11] describe in their work a review involving the synthesis of TiO_2 nanofibers by electrospinning to be used as semiconductors in heterogeneous photocatalysis. These nanofibers will be used in wastewater treatment. The photocatalytic tests were carried out by monitoring the degradation of dyes such as CR, MB, MO, RB5 and RhB at a concentration of 10 to 20 mg L^{-1}. Under ultraviolet light (50–800 W) at variable times (60–240 min). In general, nanofibers showed good stability and could be reused in at least three more cyclic experiments. The best results were obtained in pharmaceutical degradation, where removal reached 80%. Degradation of other organic contaminants has reached; 70% for phenol, 50% for 4-nitrophenol, and 50% for paraquat herbicide, respectively.

Çinar et al. [16] describe in his work the synthesis of CuO-TiO_2 p-n heterostructures. They manufactured CuO particles hydrothermally and by electrospinning TiO_2 fibers for application in the photocatalytic degradation of water pollutants, such as methylene blue and 4-nitrophenol. The results of the photocatalytic tests indicated that the degradation efficiency was influenced by the amount of CuO particles in the samples. Among all the compositions studied, samples with 1.25 and 0.5% by weight of CuO exhibited greater photoactivity under UV illumination, about 3.3 times greater than pure TiO_2. Under visible illumination, approximately 3.75 times higher compared to pure TiO_2, respectively. The photoactivity improves compared to pure fibers, a consequence of the fiber/particle architecture, the ability to capture light, and the efficiency in charge separation, provided by the staggered band structure and p-n junctions of the heterostructured samples. According to these authors [15, 16], the results obtained are promising, as the nanofibers synthesized by electrospinning showed photocatalytic efficiency in the degradation of wastewater pollutants.

4 WO_3

WO_3 is an n-type semiconductor with several polymorphic forms: triclinic, monoclinic, hexagonal, orthorhombic, and tetragonal. Tungsten can also be found in the form of tungstates. Several semiconductor materials have been used to study

photochromism; some examples include GaAs, WO_3, TiO_2, CdSe, and ZnO, among others [17].

When studying the photochromic effect, WO_3 presents of all chromogenic the greatest variations in optical absorbance, which makes this oxide the most used for research [2, 4]. Many researchers have studied alterations in the structure and stoichiometry of hexagonal and monoclinic tungsten oxide in the oxidized or reduced form, where it was observed that the oxidized form had a greater photocatalytic activity than the reduced form [18]. Characteristics such as surface area, crystallite size and morphology are some parameters that affect the photochromic properties of the material [18, 19]. Some of its applications include photocatalytic processes, gas sensors, electrochromic devices, solar cells, among others [19–21]. They can be applied in powder or immobilized [18]. Several methods are suggested to synthesize WO_3, such as chemical vapor deposition, sol–gel, electrospinning, sputtering, electron beam, thermal evaporation, among others [18, 19].

Tungsten trioxide nanomaterials comprise nanowires, nanotubes, nanofibers, nanorods, and nanofilms, which provide excellent morphology for electro-functional devices. The synthesis of these WO_3 nanostructures has shown promising results such as high density with diameters around 300 nm, electrochemical efficiency close to 2.0 mA/cm^2, good photoactivity, and remarkable morphology in the most diverse applications [19].

The first information about color changes in materials was described in 1953 when it was discovered that WO_3 is bluish in the presence of 0.1 M H_2SO_4. But only in 1969, studies involving photochromism in WO_3 gained visibility. Since then, almost all studies in this area have been carried out on films containing WO_3 and, less frequently, films made from other oxides, such as V_2O_5 and TiO_2 [2].

The works carried out by the authors below confirm the use of WO_3 in photochromic and photocatalytic characterizations because regardless of the technique used for its synthesis and the type of sample obtained, the optical effectiveness and photocatalytic activity increase.

In their work, Pan et al. [22] report the synthesis of WO_3 films prepared on TiO_2 substrates, obtained through a sodium tungsten precursor, using the hydrothermal method. The results showed that the increase in the concentrations of precursors increases the optical absorption capacity, improving their photochromic properties.

Soares et al. [23] describe in their work the obtainment of thin films containing TiO_2, TiO_2/WO_3, and $TiO_2/Na_2WO_4.2H_2O$ fibers, where their optical and photocatalytic properties were correlated by the occurrence of phenomena similar. As a result, tungsten-doped TiO_2 thin films demonstrated increased photocatalytic efficiency in the degradation of 125 mL of a 20 ppm solution of the methyl orange dye. Furthermore, they simultaneously exhibited the greatest photochromic effects, as these samples demonstrated the highest reflectance values when the incidence of light. A consequence of an existing synchronization between the chemical and physical properties of TiO_2 and WO_3.

The synthesis, characterization, properties, and photocatalytic application of TiO_2 and TiO_2/WO_3 nanofibers by electrospinning will be covered in this chapter.

Also emphasizing the correlation between photochromism and heterogeneous photocatalysis.

5 Preparation, Synthesis, and Characterization of TiO_2 and TiO_2/WO_3 Nanofibers

5.1 Electrospinning

A method for obtaining nanofibers was proposed by Alves et al. [24]. The synthesis of nanofibers through this technique consists primarily in the preparation of solutions containing the precursors of TiO_2 and tungsten (H_2WO_4). Once the preparation is complete, a plastic syringe is loaded with 5 mL of each precursor solution. Then a stainless steel hypodermic (capillary) needle (1 mm in diameter) is connected to the high voltage source. A rotating cylindrical collector, where the nanofibers are deposited, is covered with a sheet of aluminum foil and is located at a distance of 12 cm from the capillary tip. A voltage of 13.5 kV is used between the capillary and the collector. An infusion pump performs the flow control of each precursor solution (1.8 mL/h). Nanofibers were collected every 30 min for 4 h for each formulation. After the synthesis of the nanofibers, an electric oven is used to perform the heat treatment on the samples. The temperatures used vary between 650 and 800 °C, with a 1 h tide level and a heating rate of 1.4 °C/min.

5.2 Morphology

The surfaces of the TiO_2 and TiO_2/WO_3 samples synthesized by electrospinning are shown in Fig. 5. The SEM images (Fig. 5a, b) showed the formation of continuous nanofibers, with a similar microstructure. Its appearance resembles thin, long, and scruffy sticks. Considering the TEM images in Fig. 5c, d, the TiO_2 nanofibers seem to be constituted by an agglomerate of interconnected particles. TiO_2/WO_3 nanofibers, on the other hand, demonstrate that they have several interconnected grains in their structure, with sizes larger than those observed for TiO_2 nanofibers. This suggests that during heat treatment, the higher the calcination temperature, the smaller the diameter of the nanofibers and the larger the size of the grains that make them up. The diameter of the TiO_2 nanofibers ranged between 330 and 150 nm (Table 1). The TiO_2/WO_3 nanofibers had a diameter that ranged between 600 and 280 nm. The increase observed in the diameter of TiO_2/WO_3 nanofibers when compared to TiO_2 samples is possibly due to the presence of agglomerates containing crystals of WO_3. Similar images and observations were also obtained by Nguyen et al. [25] when they synthesized nanofibers by the electrospinning process.

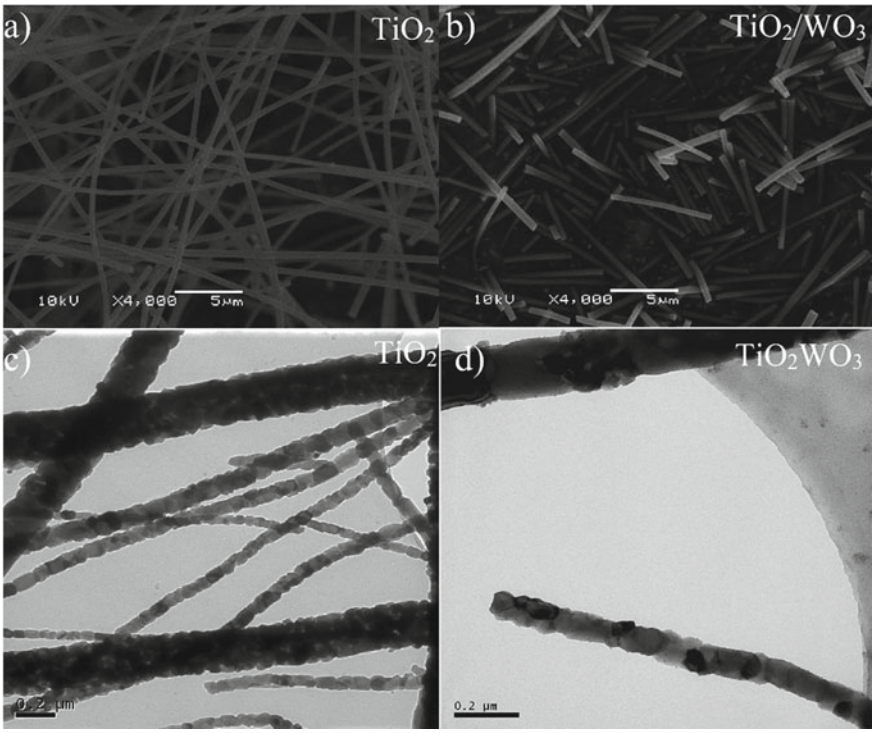

Fig. 5 SEM **a**, **b** and TEM **c**, **d** images of TiO_2 and TiO_2/WO_3 nanofibers synthesized by electrospinning

Table 1 Diameter and surface area of nanofibers synthesized by electrospinning

Nanofibers (°C)	Diameter (nm)	Surface área (m^2/g)
TiO_2—650	330	26.6
TiO_2—700	230	29.8
TiO_2—750	210	33.6
TiO_2—800	150	40.8
TiO_2/WO_3—650	600	45.6
TiO_2/WO_3—700	450	57.2
TiO_2/WO_3—750	320	60.5
TiO_2/WO_3—800	280	88.5

5.3 Crystallinity and Phases Present in Nanofibers

Table 2 shows the crystallite size of the TiO_2 and TiO_2WO_3 nanofibers that were calculated from X-ray diffraction and with the help of the WinFit® software.

Table 2 Crystallite size values of TiO_2 and TiO_2/WO_3 nanofibers synthesized by electrospinning

Nanofibers (°C)	Crystallite size (nm)
TiO_2—650	16.45
TiO_2—700	12.76
TiO_2—750	9.38
TiO_2—800	5.65
TiO_2/WO_3—650	43.0
TiO_2/WO_3—700	41.8
TiO_2/WO_3—750	38.2
TiO_2/WO_3—800	35.0

TiO_2/WO_3 nanofibers (650 °C) had the largest crystallite size (43 nm). In all formulations, the crystallite size was gradually reduced as the heat treatment temperature to which the nanofibers were subjected increased. The samples containing tungsten had crystallite size above 20 nm, probably due to the presence of WO_3.

Figure 6a, b shows the XRD of TiO_2 and TiO_2/WO_3 nanofibers. For the TiO_2 samples treated up to a temperature of 700 °C, only the presence of the crystalline phase anatase (JCPDS 01-078-2486) was identified, with the first characteristic peak at $2\theta = 25.271°$. In samples submitted to temperatures above 750 °C, the anatase and rutile phases were identified (JCPDS 01-077-0442), the latter with the first characteristic peak at approximately $2\theta = 27.294°$. This phase transformation of TiO_2 occurs as a consequence of the increase in the sintering temperature. TiO_2/WO_3 nanofibers treated up to a temperature of 650 °C exhibited the anatase and brookite phases for TiO_2 (JCPDS 01-075-1582), with characteristic peaks at $2\theta = 25.271°$ and 25.425°, respectively. In addition to the anatase and brookite phases, nanofibers treated from 700 °C exhibited the rutile phase (JCPDS 01-077-0442) for TiO_2, the latter with the first characteristic peak at $2\theta = 27.294°$. WO_3 showed peaks characteristic of the orthorhombic phase (JCPDS 00-032-1393), with the initial value at approximately $2\theta = 23°$. Similar result was reported by Nguyen et al. [25]. They observed intensive peaks for WO_3 at $2\theta = 23.04$ compatible with the orthorhombic phase.

5.4 Photocatalytic Activity

Various dyes such as; Rhodamine B, methyl orange, and methylene blue, among others, are frequently used in photocatalytic tests. Methyl orange is an anionic, synthetic dye, belonging to the azo group, has $-N = N-$ bonds in its structure. It was often chosen for monitoring photodegradation tests as it provides high stability to the photochemical and degradation processes [26].

The photodegradation test takes place in a photocatalytic reactor. By following the decolorization of 125 mL of a 20 ppm solution of the methyl orange dye with time (intervals of 15 min), the photocatalytic efficiency of TiO_2-P25 and nanofibers

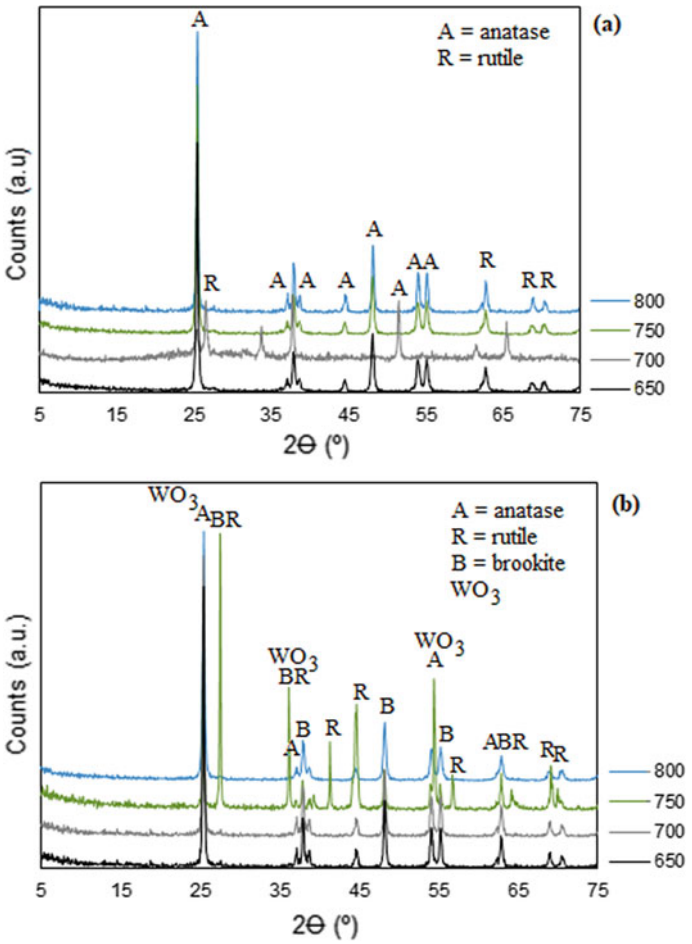

Fig. 6 X-ray diffractograms of **a** TiO_2 and **b** TiO_2/WO_3 nanofibers synthesized by electrospinning and heat trated at different temperatures

TiO_2 and TiO_2/WO_3 is obtained by following the color change. Before starting the photocatalytic tests, the nanofibers were dispersed in the dye solution using an ultrasound, in the dark, for 20 min for initial adsorption of the dye on the surface of the samples.

Among the results obtained, TiO_2/WO_3 nanofibers (800 °C) were the most efficient in the degradation of the methyl orange dye. They showed 90% degradation in 90 min of exposure to UV-A radiation, that is, they did not need 135 min of exposure to UV-A radiation to degrade the dye. These results suggest the existence of a relationship between temperature and surface area. For, samples sintered at higher temperatures (800 °C) had a greater surface area (88.5 m^2/g) when compared to TiO_2 nanofibers (800 °C), which had a surface area of 40.8 m^2/g. Another factor

that contributed to the performance of this sample is the presence of the tungsten precursor (H_2WO_4), which, associated with the bandgap reduction, increased the number of O_2 vacancies in the TiO_2 crystal structure. Thus, it is possible to state that the joint action of these factors gave TiO_2 phase stability structure, responsible for the increase in photoactivity and conductivity for the oxygen ion. The rise in the heat treatment temperature allowed the O_2 vacancies to acquire the mobility needed to move to a disordered state in the anionic sub-network [28]. Some of these results were also observed by Bharti et al. [29] they observed that the best results were obtained by samples that had an increase in the number of O_2 vacancies and a reduction in the bandgap. They concluded that the association of these factors produces samples with good optical properties, making them promising candidates for electrode applications [29].

6 Optical Properties

Optical properties refer to the reaction that a material expresses when subjected to electromagnetic radiation, more specifically, visible light [30]. Transmission, absorption, and reflection phenomena are associated with colorimetry and occur when light falls on the surface of a material.

Transparent materials are capable of transmitting light with little absorption and reflection. On the other hand, translucent materials transmit light in a diffuse way, dispersed inside the material. And finally, opaque materials do not allow visible light to be transmitted. For example, metals are opaque along the visible spectrum, electrical insulators can be transparent, and semiconductors are transparent or opaque [30].

6.1 Bandgap Energy

For example, various optical properties, those that give rise to color, are brought about by electronic absorption and emission processes. The absorption of a photon can occur with the promotion of an electron from Bv to Bc. For this to happen in semiconductor materials, it is necessary that the electron excited in the Bv has an energy value greater than or equal to the bandgap, being able to surpass it. Thus, generating a hole in Bv and an electron in Bc [3, 30].

Materials that have a bandgap value greater than 3.1 eV cannot absorb visible light. Therefore, for materials to absorb a part of the visible spectrum and exhibit a colored appearance, they must have bandgap values between 1.8 and 3.1 eV [30].

The bandgap for nanofibers synthesized by electrospinning is presented in Table 3. The values confirm its photochromic and photocatalytic application, as in both processes, it is necessary to have photon absorption with energy greater than the

Table 3 Bandgap energy of TiO_2 and TiO_2/WO_3 nanofibers synthesized by electrospinning

Nanofibers	Bandgap (eV)
TiO_2—650 °C	3.04
TiO_2	2.93
TiO_2	2.85
TiO_2	2.82
TiO_2/WO_3—650 °C	2.58
TiO_2/WO_3—700 °C	2.57
TiO_2/WO_3—750 °C	2.56
TiO_2/WO_3—800 °C	2.54

bandgap. They are also important to differentiate semiconductor oxides from insulators, as this is done based on the occupation of the energy bands. Note that the reduction in the nanofiber bandgap occurs as the heat treatment temperature increases. This increase in temperature favors the optical properties of the material and the surface effects (O_2 vacancies) on the distribution of electronic levels, it also allows the TiO_2/WO_3 nanofibers to have an inhibition of the recombination of the charges of the electron/hole pair allowing the transfer of charges between the two oxides (TiO_2 and WO_3), increasing the light absorption capacity [28, 30].

6.2 Photochromism

This effect causes reversible changes in materials, and becomes visible when an object is subjected to some type of electromagnetic radiation, which can be UV, visible light or infrared [31]. It is observed through colorimetric tests associated with a color system, usually the CIELab. The equipment used to measure photochromism are colorimeters and spectrophotometers. The mechanism used to describe this effect is based on the formation of color centers, through the generation of O_2 vacancies. Because, in almost all oxygen ion conductors, propagation occurs through consecutive jumps of oxygen ions in vacant positions of the crystal structure. Which makes this a very important parameter to obtain high conductivity. The concentration of O_2 vacancies, which can be native (intrinsic conductors) or inserted through partial substitutions (extrinsic conductors), determine the atomic lattice positions [28]. The generation of O_2 vacancies plays an influential role in determining absorbance, reflectance, transmittance and photocatalytic properties.

Photochromism in TiO_2 and TiO_2/WO_3 nanofibers is observed through the software that comes with the spectrophotometer. The measuring range covers the entire visible spectrum (400–700 nm). The software records the colorimetric coordinates for each sample through the CIE-Lab system, where according to the negative or positive values of the coordinates a* (variation between green and red) and b* (variation between yellow and blue) the different colors in the nanofibers are expressed.

In this system, luminescence values (%L) are also registered, that is, the amount of light that is seen in a certain color, and ΔL*. Luminescence (%L) close to 0%, characterizes the absence of reflected light (black), and if it is close to 100%, it characterizes the total reflection of light (white). The values of ΔL* inform us about the differences existing between the shades in lighter or darker. Positive (+) values of ΔL* indicate the lightest color and negative (−) values of ΔL* indicate the darkest color [31].

All nanofibers exhibited photochromism, as they reversibly changed color when subjected to colorimetric tests. They preferentially absorbed the blue color of the electromagnetic spectrum, returning to the initial white color after the end of the analysis.

6.3 Absorbance

All nanofibers synthesized by electrospinning are white before and after colorimetric tests. During the colorimetric test, the TiO_2 nanofibers had maximum absorbance in the dark-blue region, influenced by positive values of a* (red color) and negative values of b* (blue color). Negative values of ΔL* define the dark hue of TiO_2 nanofibers. TiO_2/WO_3 nanofibers had maximum absorbance in the light blue color region, influenced by negative values of a* (green color) and negative values of b* (blue color). Positive L* values determine the light hue of TiO_2/WO_3 nanofibers. The maximum absorbance of TiO_2 and TiO_2/WO_3 nanofibers occurs in the blue color region. Predictably, because both precursor solutions have a yellow coloration, differing only by their hue. In colorimetric analyses, the maximum absorbance is contacted in the complementary staining region. And in the case of both nanofibers, the complementary color to yellow is blue. The TiO_2 and TiO_2/WO_3 nanofibers had a good amount of light perceived, according to the luminescence values (%L) shown in Table 4.

Table 4 Results of absorbance tests performed on nanofibers synthesized by electrospinning

Nanofibers (°C)	a*	b*	Hue difference (clear/dark) ΔL*	Absorbed color	%L
TiO_2 650	+1.47	−12.51	−35.99	Dark-blue	83.33
TiO_2 700	+3.29	−2.68	−57.43	Dark-blue	61.42
TiO_2 750	+7.16	−10.44	−24.32	Dark-blue	92.14
TiO_2 800	+4.14	−8.21	−42.86	Dark-blue	86.76
TiO_2/WO_3 650	−3.13	−1.45	+66.91	Clear-blue	59.73
TiO_2/WO_3 700	−4.42	−10.37	+58.91	Clear-blue	96.26
TiO_2/WO_3 750	−3.48	−11.46	+75.41	Clear-blue	84.69
TiO_2/WO_3 800	−5.18	−5.99	+56.68	Clear-blue	85.47

6.4 Transmittance

The color of a solution is defined by the color of transmitted light. In other words, both precursor solutions for the synthesis of nanofibers by electrospinning are yellow because they transmit yellow light, differing only in hue. A solution is white when it transmits light of all colors and black when it absorbs light of all colors. The vividness of the color of a solution is strongly related to the concentration of molecules capable of absorbing light. The light-absorbing capacity will be greater the more concentrated the solution [32].

6.5 Reflectance

TiO_2 and TiO_2/WO_3 nanofibers absorbed blue light from the electromagnetic spectrum. The absorption/reflection process occurred when the light was focused on the white nanofibers. During the colorimetric test, when light is irradiated, the color reflected by the nanofibers reflect the complementary color region to the light absorbed (yellow to blue) in both types of nanofibers. Much of the light absorbed on the surface of the samples is re-emitted in the form of visible light, as a reflected light [30].

The reflectance of the nanofibers was observed in a range that comprised the entire visible spectrum, between 400 and 700 nm. Before and after the colorimetric test, all nanofibers were white, that is, they reflected all colors. During the colorimetric test they have shown a light reflectance between 65.3 and 79.9% for TiO_2 nanofibers, and between 82.73 and 99.99% for TiO_2/WO_3 nanofibers. TiO_2 nanofibers were compared with standard TiO_2-P25 Evonik, in order to compare the light reflection capacity of the synthesized TiO_2 nanofibers. The nanofibers showed a high reflectance difference. Initially, at 400 nm TiO_2-P25 and TiO_2 and TiO_2/WO_3 nanofibers reflected 57.73%, 65.32%, and 82.73% of the incident light, respectively. And at 700 nm TiO_2-P25 and TiO_2 and TiO_2/WO_3 nanofibers reached the maximum incident light reflection of 57.73%, 79.90%, and 99.9% respectively.

Table 5 shows that the nanofiber reflectance values are influenced by the different heat treatment temperatures to which the samples are subjected.

7 Photocatalytic Application of TiO_2 and TiO_2/WO_3 Nanofibers

Photolysis of water was first introduced in 1969. The system used TiO_2 as a photocatalyst under irradiation (500 W xenon lamps). From this moment on, photoelectrochemical processes have been extensively studied and gained prominence in the 70's with Fujishima and Honda; in 1980 with the photocatalytic production of H_2;

Table 5 Reflectance values obtained by TiO_2-P25 and by nanofibers synthesized at different temperatures

Nanofiber	% Reflectance
TiO_2-P25	57.73
TiO_2 650 °C	65.32
TiO_2 700 °C	68.19
TiO_2 750 °C	75.89
TiO_2 800 °C	79.90
TiO_2/WO_3 650 °C	82.73
TiO_2/WO_3 700 °C	90.89
TiO_2/WO_3 750 °C	93.19
TiO_2/WO_3 800 °C	99.99

in 1990 with photocatalysis and hydrophilicity in TiO_2 films and, nanoengineering, nanotechnology, and TiO_2 catalysis in the year 2000 [8, 33]. Figure 7 shows the mechanism involved in the photocatalytic degradation processes.

Figure 8a, b shows the effectiveness of TiO_2-P25, TiO_2 and TiO_2/WO_3 nanofibers in the degradation of 125 mL of a 20 ppm solution of methyl orange dye during 120 min of exposure to UVA light ($\lambda = 365$ nm).

All synthesized nanofibers were effective to decompose the methyl orange dye under UVA irradiation. For TiO_2 nanofibers, the most photoactive were those that received heat treatment at 650 °C, degrading around 40% of the dye in 120 min. Nanofibers treated at 700 °C and the commercial TiO_2-P25 degraded around 30% of the dye in this same period of time. The nanofibers treated at 750 and 800 °C degraded around 20% and 10%, respectively, of the dye In these same conditions. When heat treated above 700 °C, a decline in degradation capacity is observed.

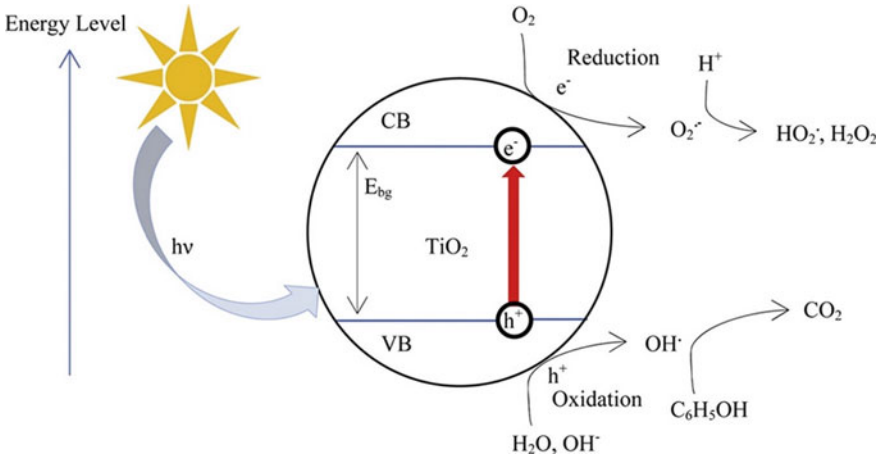

Fig. 7 A schematic diagram showing the mechanism of photocatalytic degradation processes. Reproduced with permission from Ling, et al. [34]

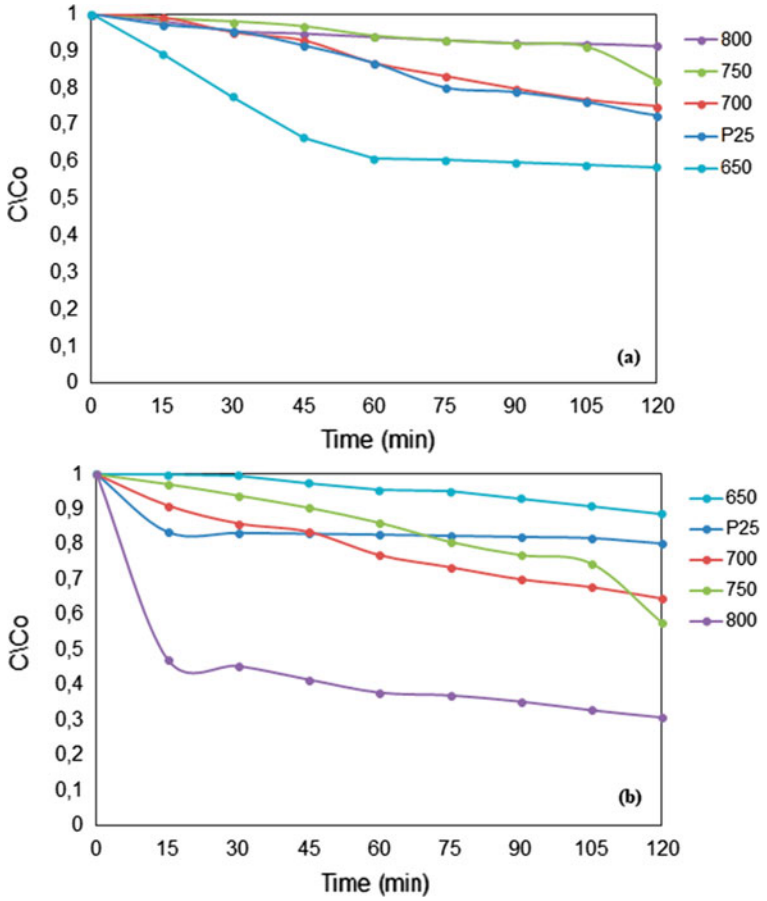

Fig. 8 Photocatalytic performance of TiO_2-P25 and synthesized nanofibers in degradation tests

Probably because the formation of the rutile phase, which among the polymorphic phases of TiO_2 is the one with the lowest photoactivity [31].

The addition of tungsten to the TiO_2/WO_3 samples increased the degradation capacity of treated nanofibers at temperatures of 700 °C, 750 °C and 800 °C, to approximately 36%, 50% and 90%, respectively. Some factors like the reduction of the bandgap from 3.04 to 2.89 eV, the inhibition of the recombination of the electron/hole pair [$(e^-)/(h^+)$], which allowed the transfer of charges between TiO_2 and WO_3, and the formation of point defects (O_2 vacancies), contributed to this observation. With the increase in the heat treatment temperature, the O_2 vacancies are able to move quickly, causing a disorganization in the network, thus improving the photoactivity and process efficiency [31].

8 Existing Synergism Between Photochromism and Heterogeneous Photocatalysis

Based on the results obtained, it is believed that there is a synchrony between the photochromic and photocatalytic processes, due to phenomena that occur at the same time and that are necessary to achieve success in both:

(a) Existence of a specific wavelength, which must be equal to or less than that determined by the Planck equation, which will provide the energy that will excite the electrons of material in the case of photocatalysis and reflect a certain color in the case of photochromism [35];
(b) Migration of electrons from the valence band to the conduction band, generating positive electron holes in the valence band, when irradiated with light at an energy level higher than the band gap of the samples, which will degrade the dye and reflect/absorb light and, change the color of the material [35]. In photochromism, electrons from the valence band, occupied only by the 2p orbitals of the O, are promoted to the conduction band, occupied by the 5d orbitals of the W, forming electron/hole pairs (e/h^+). The W^{6+} sites capture electrons that are promoted to the conduction band, causing the reduction of ions. The holes, on the other hand, are capable of dissociating H_2O molecules or organic molecules [5]. The reflection/absorption of light modifies the material's color, generating positively charged O_2 holes, which capture the photoexcited electrons [4, 5].
(c) Generation of O_2 vacancies. In almost all oxygen ion conductors, conduction occurs through consecutive jumps of these ions. The presence of the tungsten, and the reduction in the bandgap, increased the number of O_2 vacancies in the TiO_2 crystal structure. With the increase in temperature, the O_2 vacancies managed to move disorganizedly, giving the TiO_2 stability of the structural phase, responsible for the increase in conductivity [28].

9 Conclusions

The use of nanofibers synthesized by electrospinning as semiconductors in heterogeneous photocatalysis was a promising alternative for the most diverse applications. The TiO_2/WO_3 nanofibers treated at 800 °C showed the best results in the degradation of the methyl orange dye (90%), due to the presence of WO_3, which prevented the recombination of the electron/hole pair [$(e-)/(h^+)$], providing the transfer of charges between the two oxides (TiO_2 and WO_3), with a smaller bandgap and the formation of a greater number of O_2 vacancies. The latter is also responsible for the highest reflectance values (99.99%) for this sample. The observed results point to the existence of synergism between photochromism and photocatalysis, as they simultaneously modify the color of the sample, generate extra electronic holes in the band structure, besides degradete the dye.

References

1. Kulkarni, S.: Nanotechnology Principles and practices. Springer, New York Dordrecht London (2015)
2. Galvão, J., et al.: Fotocromismo em filmes finos de óxidos de tungstênio de diferentes composições. Quím Nova **26**, 488–492 (2003). https://doi.org/10.1590/S0100-40422003000400008
3. Chiang, Y., et al.: Physical Ceramics Principles for Ceramics Science and Engineering. Wiley, New York (1997)
4. Gonçalves, A.: Desenvolvimento de Tintas Fotocrómicas para Aplicação em Embalagens Inteligentes. Dissertação de Mestrado (Faculdade de Ciências e Tecnologia), Universidade Nova de Lisboa (2013)
5. Sobrinho, J.: Fotocromismo e Luminescência de Compostos a Base de Tungstênio e Íons Terras Raras Trivalentes Via Síntese Hidrotérmica. Dissertação de Mestrado (Programa de Pós-Graduação em Química), Universidade Estadual Paulista, Araraquara (2015)
6. Bertolini, C.: Sistema para medição de cores utilizando espectrofotômetro. Trabalho de Conclusão de Curso (Centro de Ciências Exatas e Naturais Curso de Ciência da Computação, Bacharelado), Universidade Regional de Blumenau, Blumenau (2010)
7. Andrade, Q.: Correlação entre as técnicas de espectrofotometria de reflectância e colorimetria da blenda poli (metacrilato de metila)/poli (tereftalato de etileno) reciclado (pmma/pet_{rec}) no estudo da opacidade. In: 20 º Congresso Brasileiro de Engenharia e Ciência dos Materiais, CBECIMAT, Joinville, SC, Brasil (2012)
8. Rahimi, N., et al.: Review of functional titanium oxides. I: TiO_2 and its modifications. Prog. Solid State Chem. **44**, 86–105 (2016). https://doi.org/10.1016/j.progsolidstchem.2016.07.002
9. Gupta, S., et al.: A review of TiO_2 nanoparticles. Chin. Sci. Bull. **56**, 1639–1657 (2011). https://doi.org/10.1007/s11434-011-4476-1
10. Mingzheng, G., et al.: A review of TiO_2 nanostructured catalysts for sustainable H_2 generation. Int. J. Hydrogen Energ. **42**, 8418–8449 (2017). https://doi.org/10.1016/j.ijhydene.2016.12.052
11. Pasini, S., et al.: An overview on nanostructured TiO_2–containing fibers for photocatalytic degradation of organic pollutants in wastewater treatment. J. Water Process Eng. **40**, 101–827 (2021). https://doi.org/10.1016/j.jwpe.2020.101827
12. Sharma, S., et al.: Photocatalytic performance of yttrium-doped CNT-ZnO nanoflowers synthesized from hydrothermal method. Mater. Today Chem. **20**, 100452 (2021). https://doi.org/10.1016/j.mtchem.2021.100452
13. Yang, H.: Electrospinning of Polymeric and Ceramic Fibers: Understanding of the Morphological Control and its Application, p. 136. University of Rochester, New York (2013)
14. He, X., et al.: Nanofiber coated hybrid yarn fabricated by novel electrospinning-airflow twisting method. Surf. Coat. Technol. **258**, 398–404 (2014). https://doi.org/10.1016/j.surfcoat.2014.08.062
15. Wannapop, S., et al.: Characterization of $SrWO_4$–PVA and $SrWO_4$ spiders' webs synthesized by electrospinning. Ceram. Int. **37**, 3499–3507 (2011). https://doi.org/10.1016/j.ceramint.2011.06.005
16. Çinar, B., et al.: Hydrothermal/electrospinning synthesis of CuO plate-like particles/TiO_2 fibers heterostructures for high-efficiency photocatalytic degradation of organic dyes and phenolic pollutants. Mater. Sci. Semicond. Process. **109**, 104–919 (2020). https://doi.org/10.1016/j.mssp.2020.104919
17. Marques, F., et al.: Estratégias e materiais utilizados em fotocatálise heterogênea para geração de hidrogênio através da fotólise da água. Química Nova **40**, 295–300 (2017). https://doi.org/10.21577/0100-4042.20170685
18. Côrrea, D., et al.: Tungsten oxide thin films grown by thermal evaporation with high resistance to leaching. J. Braz. Chem. Soc. **25**, 822–830 (2014). https://doi.org/10.5935/0103-5053.20140041
19. Adhikari, S., et al.: High efficient electrochromic WO_3 nanofibers. Electrochim. Acta **138**, 115–123 (2014). https://doi.org/10.1016/j.electacta.2014.06.062

20. Sathavisam, S., et al.: Tungsten doped TiO with enhanced photocatalytic and optoelectrical properties via aerosol assisted chemical vapor deposition. Sci. Rep. **5**, 109–152 (2015). https://doi.org/10.1038/srep10952
21. Oliveira, S., et al.: Uma visão das tendências e perspectivas em eletrocromismo: a busca de novos materiais e desenhos mais simples. Quim. Nova **23**, 79–87 (2000). https://doi.org/10.1590/S0100-40422000000100014
22. Pan, L., et al.: Hydrothermal synthesis of WO_3 films on the TiO_2 substrates and their photochromic properties. Mater. Sci. Semicond. Process. **40**, 479–483 (2015). https://doi.org/10.1016/j.mssp.2015.06.041
23. Soares, L., et al.: Analysis of colorimetry using the CIE-L*a*b* system and the photocatalytic activity of photochromic films. Mater. Res. Bull. **105**, 318–321 (2018). https://doi.org/10.1016/j.materresbull.2018.05.012
24. Alves, A., et al.: Photocatalytic activity of titania fibers obtained by electrospinning. Mater. Res. Bull. **44**, 312–317 (2009). https://doi.org/10.1016/j.materresbull.2008.06.001
25. Nguyen, T., et al.: Synthesis of mesoporous tungsten oxide nanofibers using the electrospinning method. Mater. Lett. **65**, 2823–2825 (2011). https://doi.org/10.1016/j.matlet.2011.05.103
26. Sá, M., et al.: Remoção do alaranjado de metila em meio aquoso por microcristais de h-MoO_3 obtidos pelo método micro-ondas hidrotérmico. Cerâmica **66**, 197–207 (2020). https://doi.org/10.1590/0366-69132020663782901
27. Wu, M., et al.: Photocatalytic performance of Cu-doped TiO_2 nanofibers treated by the hydrothermal synthesis and air-thermal treatment. Appl. Surf. Sci. **430**, 390–398 (2018). https://doi.org/10.1016/j.apsusc.2017.09.035
28. Muccillo, E.: Condutores de íons oxigênio - uma breve revisão. Cerâmica **54**, 129–144 (2008). https://doi.org/10.1590/S0366-69132008000200002
29. Bharti, B., et al.: Formation of oxygen vacancies and Ti^{3+} state in TiO_2 thin film and enhanced optical properties by air plasma treatment. Sci. Rep. **6**, 32355 (2016). https://doi.org/10.1038/srep32355
30. Callister, W.: Ciência e Engenharia de Materiais: Uma introdução. Rio de Janeiro (2002)
31. Silva, L., et al.: Luminescência e absorção óptica de nanofibras dos óxidos de titânio e tungstênio na região do uv-visível. Revista Ibero-Americana de Humanidades, Ciências e Educação-REASE **7**, 23–32 (2021). https://doi.org/10.29327/217514.7.1-2
32. Compri, N.: Práticas de Laboratório de Bioquímica e Biofísica, Guanabara Koogan (2009)
33. Fujishima, A., et al.: Electrochemical photolysis of water at a semiconductor electrode. Nature **238**, 37–38 (1972). https://doi.org/10.1038/238037a0
34. Ling, et al.: Photocatalytic degradation of phenol in water on as-prepared and surface modified TiO_2 nanoparticles. Catal. Today **258**, 96–102 (2015). https://doi.org/10.1016/j.cattod.2015.03.048
35. Feltrin, J., et al.: Superfícies fotocatalíticas de titânia em substratos cerâmicos. Parte I: Síntese, estrutura e fotoatividade. Cerâmica **59**, 620–632 (2013). https://doi.org/10.1590/S0366-69132013000400020

Carbon Nanotubes for Gas Sensing

Claudir Gabriel Kaufmann Jr, Rubia Young Sun Zampiva, Marco Rossi, and Annelise Kopp Alves

Abstract Carbon nanotubes (CNTs) are one of the most exciting and challenging research domains in nanotechnology. CNTs present a large surface area, excellent electron transfer, and the ability to be combined with various materials without losing their graphitic structure. Due to these properties, CNTs are considered very promising for application in the gas sensing field. Although the nanotubes can be applied directly as sensors, combining different materials (e.g., metal, oxides, polymers) might improve the sensors' sensitivity and selectivity toward specific gases. This chapter presents an overview of the production and application of gas sensing devices based on CNTs. The use of single-wall CNTs (SWCNTs) and multi-wall CNTs (MWCNTs) over the years to fabricate such devices are described in detail.

Keywords CNTs · Gas sensing · MWCNTs · SWCNTs

Abbreviations

CNTs	Carbon Nanotubes
MWCNTs	Multi-walled Carbon Nanotubes
CVD	Chemical Vapor Deposition
EA	Electric Arc Discharge
SEM	Scanning Electron Microscopy
SWCNTs	Single-walled Carbon Nanotubes
TEM	Transmission Electron Microscopy

C. Gabriel Kaufmann Jr (✉) · R. Y. S. Zampiva · A. K. Alves
Av. Osvaldo Aranha, 99 sala 709, Porto Alegre, RS 90035-190, Brazil

A. K. Alves
e-mail: annelise.alves@ufrgs.br

M. Rossi
Sapienza University of Rome, 00161 Rome, Italy
e-mail: marco.rossi@uniroma1.it

A. Kopp Alves (ed.), *Environmental Applications of Nanomaterials*, Engineering Materials, https://doi.org/10.1007/978-3-030-86822-2_4

1 Introduction

At the beginning of the 1990s, nanoscience emerged as a revolutionary field. In the following decades, with the technological evolution in the area, nanoscience came to be called nanotechnology [1]. Nanotechnology is understood as the manipulation of nanoscale structures in the order of atomic and molecular size. The nanoscale is defined as the billionth part of the meter (10^{-9} m) [1, 2]. The possibility of controlling materials on a nanometric scale has allowed the development of new technologies in various areas of knowledge and their application in the industrial field. Among them; Renewable energy [3–6], biomedicine [7, 8], electronic [9, 10], batteries [11], magnetic storage devices [12], sensors [13], electrochemistry [14, 15], aerospace [16], cosmetics [17] and environmental [18–20].

Carbon nanotubes (CNTs) [21] have a prominent place in the nanotechnological field due to their intrinsical magnetic, optical, mechanical, chemical, and electrical properties [1, 20]. Among them, the electrical properties have been of interest in different areas, such as microelectronics, energy generation and storage, gas sensors, gas adsorbers, supercapacitors, electrochemistry, catalysis, and environmental applications [18, 19]. CNTs present a large surface area, excellent electron transfer, and the ability to be manipulated with other conductive materials and polymers to form chemically active sites [22].

Nowadays, with the advancement and optimization of the techniques to synthesize these nanostructures, elevated quantities of high-quality CNTs can be easily produced [23]. Such improvement has captured the industry's attention, and the use of CNTs to produce different devices has been investigated. Significant growing interest is observed in the gas sensing field, as shown in Fig. 1. More than 2.437 papers were published in 2020 presenting the production/application of CNTs for gas sensing. The CNTs can be used directly or combined with other materials such as metal and oxide nanoparticles, polymers, etc. According to the combined material, the CNTs can become highly sensitive and selective towards specific gas compositions [23]. The "2019 Gas Sensors Market Size, Share, System and Industry Analysis and Market Forecast to 2024 report" published by Markets and Markets™ estimated a projected growth of the gas sensors market size from USD 1.0 billion in 2019 to USD 1.4 billion by 2024 [24].

This chapter presents an overview of the production and application of gas sensing devices based on CNTs. The use of single-wall CNTs (SWCNTs) and multi-wall CNTs (MWCNTs) over the years to produce such devices are described in detail.

2 CNTs

CNTs are structures formed by sheets of graphene rolled into tubes with a nanometer-scale diameter [1]. The carbon sheets are formed by oriented hexagonal crystalline arrays consisting of single and double bonds with sp^2 hybridization. Due to this

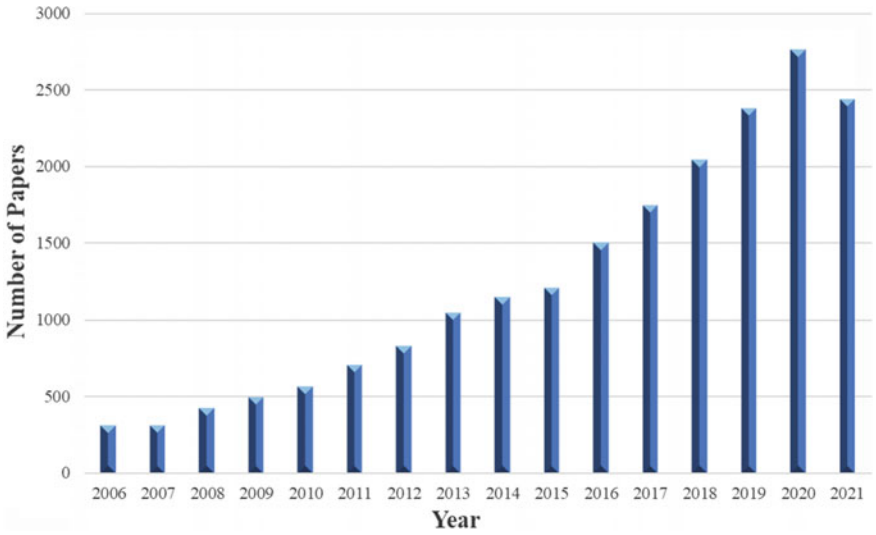

Fig. 1 Number of publications per year presenting the term "Carbon nanotubes for gas sensing" on the Science Direct website (11/06/2021)

conformation, CNTs can be considered crystals rather than molecular species [25], presenting the physical properties of crystalline solids, e.g., high-electrical and thermal conductivity and elevated mechanical resistance [14]. CNTs are usually produced in two distinct structural versions, single-wall CNTs (SWCNTs) and multi-walls (MWCNTs) (Fig. 2). The SWCNT may be understood as a structure formed from a single coiled graphite layer. The ends of which can be closed by halves of fullerenes or opened. MWCNTs, on the other hand, are formed by several SWCNTs

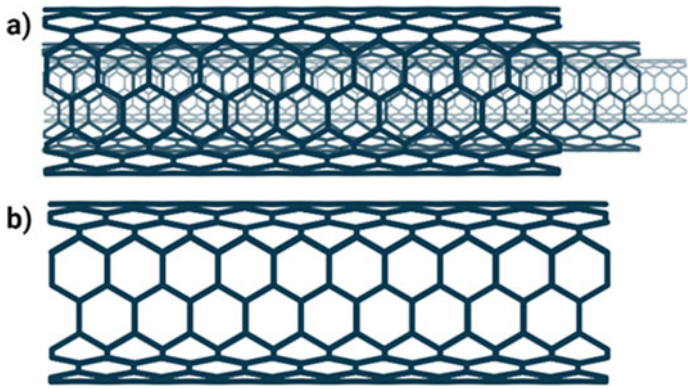

Fig. 2 Representation of MWCNTs **a** and SWCNTs **b**

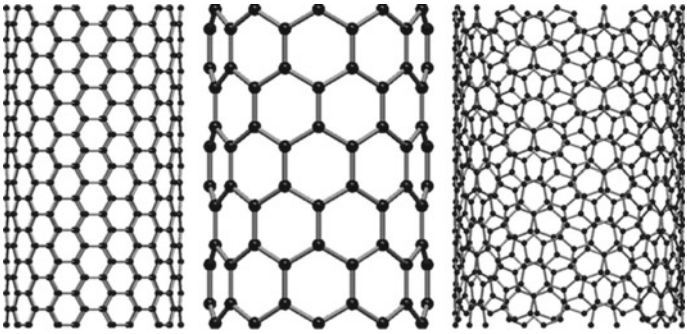

Fig. 3 CNT structures according to chirality. From left to right: Armchair, Zig-zag, and Chiral. Reproduced from Deh and Lee [26] Copyright 2016, with permission from Elsevier

in concentric shapes similar to a coaxial cable [14]. CNTs can present diameters in the range of 1–1000 nm and several micrometers in length.

The structural orientation of the CNTs walls can be controlled. CNTs with zig-zag, armchair, and chiral (Fig. 3) orientations can be produced, adjusting the synthesis parameters of the chosen technique. The CNTs' physicochemical properties are directly influenced by the direction of the wall vectors and the chiral angle. For example, armchair CNTs are metallic, while zig-zag and chiral are semiconductors [14, 25].

3 CNTs Synthesis Routes

The production of CNTs has been extensively investigated for over 3 decades, and even today, there is still room for work aimed at improving the synthesis parameters [15, 19, 20]. However, it is almost a consensus in academia and industry that the best techniques for producing CNTs are chemical vapor deposition (CVD) and electric arc discharge (EA) [19, 20].

3.1 Chemical Vapor Deposition (CVD)

CVD allows the controlled production of a variety of carbon nanostructures. This method produces CNTs by depositing gaseous and volatile carbon sources such as methane, ethylene, and acetylene [14]. The process requires the use of catalysts for the growth of nanotubes. Generally, the catalysts used are transition metals like Fe, Co, and Ni, in the form of nanoparticles [12, 27, 28]. The growth of CNTs in this synthesis route occurs when a precursor gas of carbon atoms (e.g., hexane, acetylene,

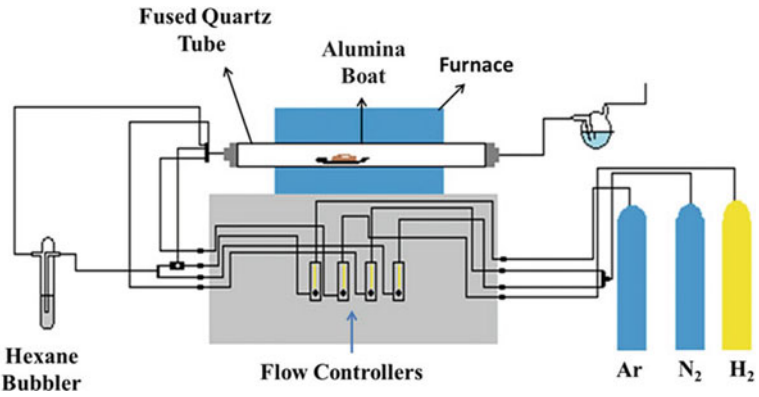

Fig. 4 Schematic drawing of a CVD reactor. Reproduced from Kaufmann [14] Copyright 2019, with permission from Springer

ethylene) is decomposed at temperatures between 750 and 950 °C; the C atoms are deposited on the catalyst particles, starting the in situ nucleation of the CNTs (Fig. 4).

The main advantage of CVD over EA is that CVD allows the variation and meticulous control of various parameters during the synthesis process. Parameters such as gas flow, type of catalyst, temperature, the physical state of precursors, etc. Parameters such as temperature, catalyst composition and crystallinity, gas composition and flow, and substrate composition have a decisive influence on the type of CNTs produced, the quality of the tubes, and their macro-orientation [19].

3.2 Electric Arc Discharge (EA)

EA is extensively used to produce several types of carbon nanostructures such as nano-onions, nano-horns, graphene, and CNTs [15, 20]. For example, commercial SWCNTs are usually synthesized by this technique. The production of CNTs by EA is based on an electric discharge generated by two carbon electrodes in a steel chamber containing an inert gas (usually helium). The precursor, often mineral graphite, is sublimated at the positive electrode (anode), depositing the synthesized nanomaterials at the negative electrode (cathode) and on the chamber walls. The EA in an aqueous medium (Fig. 5) is a more straightforward and low-cost variation of the conventional EA method, with no need for sealed chambers, vacuum, or gas flow [20].

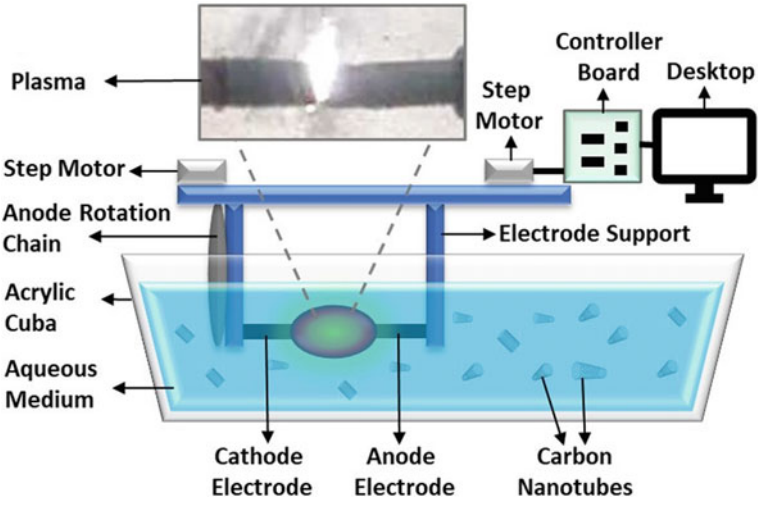

Fig. 5 Schematic drawing of a CVD reactor. Reproduced from Kaufmann [20] Copyright 2020, with permission from Wiley

4 CNTs Structural Characterization Methods

4.1 Raman Spectroscopy

The Raman effect was discovered by Indian physicist Chandrasekhar Raman and is based on the scattering that photons cause when they collide with molecules in a sample. This technique demonstrates the nature of molecular bonds and the degree of disorder of crystal lattices, through which we can define some electronic, optical, and mechanical properties of a variety of materials [19, 25]. Raman spectrometry is considered the main technique for the physical–chemical characterization of CNTs. The Raman spectrum identifies the number of tube layers, defects, chirality, structural crystallinity, and purity degree [19].

Figure 6 presents a classic Raman spectrum for MWCNTs. The D, G, and G' characteristic bands for multi-wall carbon nanotubes (MWCNTs) at 1342, 1572, and 2738 cm^{-1}, respectively. The higher the G' band intensity compared to the D and G bands, the higher the MWCNTs purity, which means less amorphous carbon and defects. The degree of purity of the samples is determined by the intensity ratio of the D and G bands (I_D/I_G) obtained in the Raman spectra. This ratio indicates the degree of carbon graphitization, which is the conversion degree from amorphous, semi-ordered, or free carbon into three-dimensionally ordered graphitic structures. The lower the ratio, the higher the graphitization degree, and the higher the quality of the MWCNTs [19, 20].

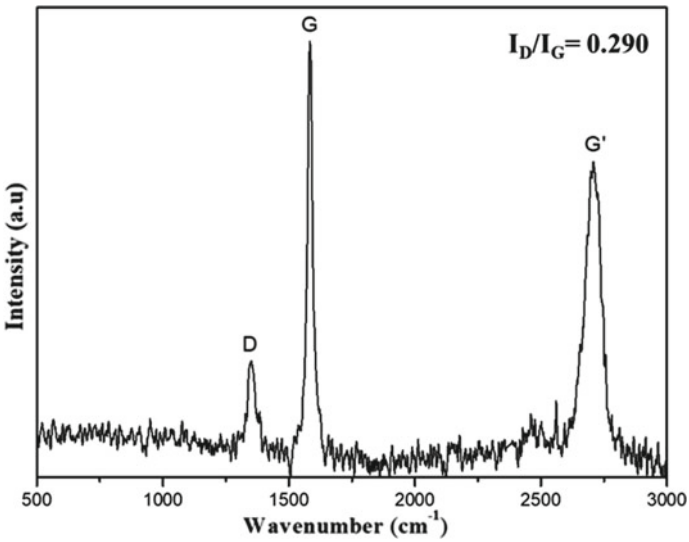

Fig. 6 Raman spectrum for MWCNTs

4.2 Scanning Electron Microscopy (SEM) and Transmission Electron Microscopy (TEM)

Scanning electron microscopy (SEM) and transmission electron microscopy (TEM) are the main techniques used for the morphological characterization of CNTs. SEM works with a beam that sweeps the sample and causes the sample to emit electrons (secondary electrons). The process is carried out by applying a potential difference (in the order of 0.5–30 kV). The beams that hit the sample and return are gathered and analyzed by a receptor, thus assembling an image, as presented in Figs. 7a, b [20]. On the other hand, TEM works with the emission of high kinetic energy electron beams in a vacuum. The beams hit an ultra-thin layer of the sample, producing flat images with a very high magnification capacity, Fig. 7c, d. Through this technique, it is possible to verify the CNTs' external and internal diameter, the number of walls, the presence of structural defects, the distribution of the catalyst in the sample, the purity degree, etc.

5 CNTs for Gas Sensing

The detection and control of gases are crucial in several fields such as environmental monitoring, breath analyzers for medical diagnosis; chemical and polymer manufacturing; and natural and toxic gas detection [24]. In industry, gas sensors are needed to detect harmful and/or toxic gases in real-time. For this application, devices made from

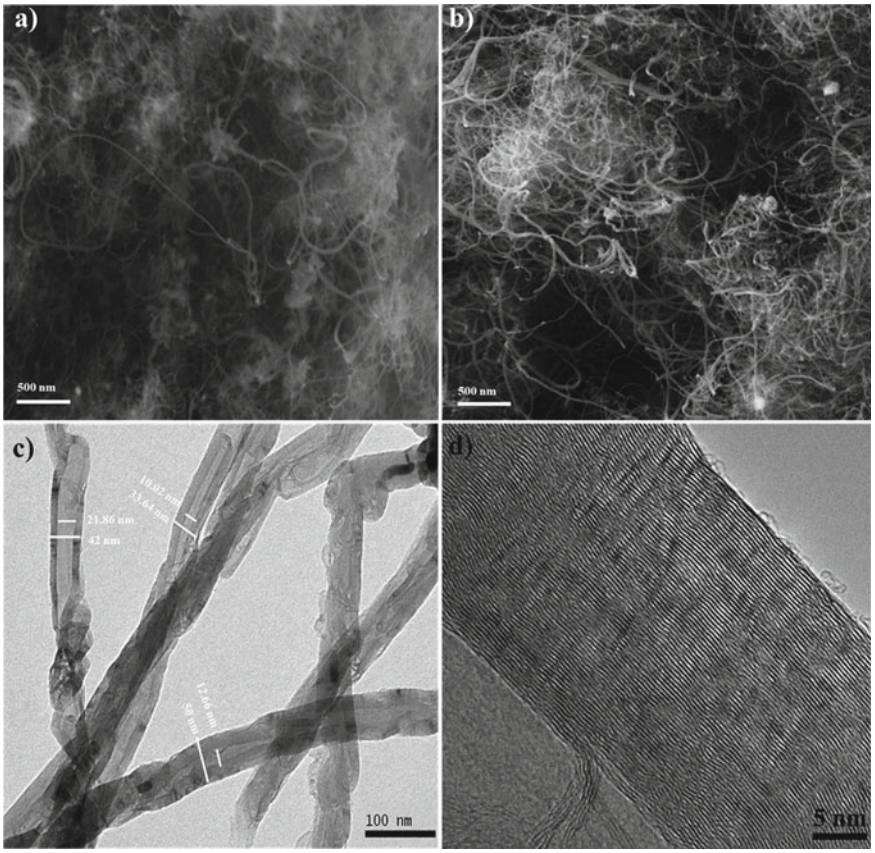

Fig. 7 SEM images showing the tangled MWCNTs in **a** and **b**. TEM images presenting the size and morphology of MWCNTs walls structure **c** and **d**. Reproduced from Kaufmann [20] Copyright 2020, with permission from Wiley

materials with good sensitivity and selectivity to specific gases are required [23, 24]. Nanomaterials are presented as a real revolution for the development of gas detection devices due to their exceedingly high surface-area to mass or volume ratios which might confer elevated sensitivity due to many available molecular binding sites [29]. In addition, nanomaterials can detect minimal gas concentrations (parts per million -ppm or billion -ppb depending on the composition) thanks to the properties listed above.

CNTs present excellent electrical properties at room temperature due to their superconductive nature [22]. Furthermore, this nanomaterial has elevated mechanical properties, with high Young's modulus (E) (0.1–1.7 TPa) [30] and tensile strength (100–200 GPA) [31]. The electrical properties of CNTs are easily influenced by interactions with a variety of atoms and molecules. This characteristic allows their use as gas sensors. The interactions of some gas molecules with the CNTs surface and

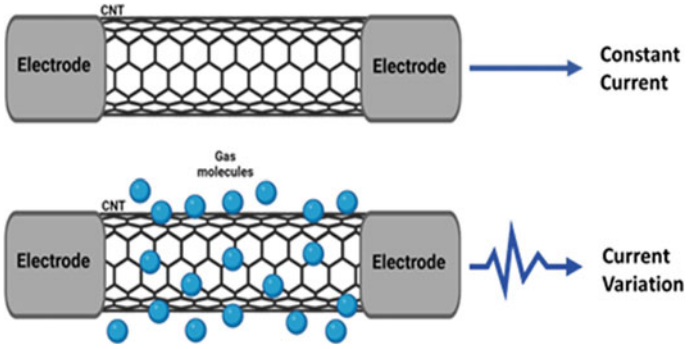

Fig. 8 Schematic representation of the influence of specific gas molecules on the electrical conductivity of CNTs

functionalizations can increase or decrease the electrical conductivity of the tubes. By detecting and measuring these variations, one can determine the presence of a specific gas (Fig. 8). Due to the elevated surface area of the tubes, concentrations of ppm or even ppb can be detected [22, 24].

CNTs can be combined with metal, metal oxides, and polymers to improve the sensibility and the selectivity of the tubes towards specific gases such as NO_x, CO_x, H_2S, NH_3, SO_2, among others [22, 32]. Charge transfer and chemical doping are usually responsible for the high sensitivity of CNTs towards gases. When electron-donating molecules such as NH_3 and electron acceptor molecules such as NO_2 interact with conducting CNTs, the electron concentration of the bulk conductor changes, thereby changing the conductance of the nanotubes [23].

It is possible to find in the literature a variety of publications using SWCNTs as well as MWCNTs for the fabrication of gas sensors. Different types of functionalizations, mixing processes, and decorations were proposed to increase nanotubes' sensibility, selectivity, and catalytic activity toward toxic gasses [22–24]. Some of these publications are presented in detail in the following sections.

5.1 SWCNTs Gas Sensor

SWCNT gas sensors are developed to detect the most different types of gases such as nitrogen dioxide (NO_2), nitrogen monoxide (NO), ammonia (NH_3), hydrogen sulfide (H_2S), hydrogen peroxide (H_2O_2), monoxide of carbon (CO), carbon dioxide (CO_2), chlorine (Cl), trinitrotoluene (TNT) and Hydrogen (H_2), among others. All these gases are harmful to humans in very low concentrations, e.g., H_2S has considerable health effects at concentrations of 10 parts per million (ppm), and it is lethal at 500 ppm [22, 33]. Besides the toxicity, gases such as H_2 and derivates from trinitrotoluene (TNT) commonly found in the industry of fuel and explosives can easily cause accidents involving explosions [22]. In the literature, most of the present studies

referring to SWCNTs sensors are related to detecting NO_x and NH_3 due to their large emission in the environment [22]. Industrial waste products and emissions at various levels are the primary sources of NO_x and NH_3 [34, 35].

In 2013, Li et al. produced a compound (Ni(NiO)/ SWCNTs) to detect NO gas. SWCNTs were synthesized by EA and purified by an acid treatment. The purified SWCNTs were dispersed in a solution containing sodium dodecylbenzene sulfonate (SDBS) and $Ni(NO_3)_2$. A nickel electrode (anode) and an aluminum electrode (cathode) were coated with the produced solution by electrodeposition, forming a thin film. The electrical resistance measurements of the sensor were carried out at room temperature. Different concentrations of NO, NH_3, H_2, and CO were tested, and the system detected only NO. This result indicates a high selectivity of Ni(NiO)/SWCNTs towards NO. The system's conductivity decreased upon exposing the sensor to NO gas since the NO molecules behaved as electron acceptors where the electrons could be transferred from the Ni(NiO)/s-SWCNTs to NO. The best result found for this sensor was a resistivity variation of ~5% with the detection limits of NO at 97 ppb [36].

Woo Choi et al. [37], produced a sensor for NO_2 detection with platinum (Pt)-decorated SWCNTs. The Pt decorated SWCNTs were synthesized using a spray method and sequential thermal treatment. Comparative tests were carried out between pure SWCNTs and the Pt decorated ones. The parameters used were 2 ppm of NO_2 at different temperatures (25–150 °C) during 180 s. At 100 °C, both sensors showed their best sensitivity. SWCNTs decorated with Pt at this presented an improvement of about 63% compared to pure SWCNTs.

Furthermore, the selectivity of the Pt decorated SWCNTs was investigated by measuring the sensing performance toward different gases such as NO, C_6H_6, C_7H_8, C_3H_6O, CO, and NH_3 at room temperature. Pt decorated SWCNTs presented elevated selectivity to NO and NO_2 and an electrical response ~5 times higher than that of pure SWCNTs. Based on these results, the authors concluded that Pt decorated SWCNT is a promising material for high-efficiency NO_2 sensing [37].

In 2014, Asad and Sheikh proposed a surface acoustic wave (SAW) based gas sensor for H_2S detection. SAW sensors operate based on wave modulation due to exposure to changes in physical and chemical phenomena [38]. This type of sensor is applied in various fields; in devices for detecting blood pressure, temperature, atmospheric pressure, gases, among others. For the sensor production, SWCNTs were acid-treated to form carboxylic functionalizations on their surface. Carboxyl functionalized SWCNTs were then mixed with copper sulfate ($CuSO_4$) in water to decorate the tubes with copper. Then, Cu-SWNTs were drop-coated onto a $LiNbO_3$ piezoelectric substrate previously treated with a solution of poly-diallyl dimethylammonium chloride (PDDA). The produced SAW sensor sensitivity and selectivity were evaluated by frequency changes using an HP8751 Network Analyzer. The minimum concentration detected by the Cu-SWNTs system was around 5 ppm. In 2016, the authors published a second paper [35] in which SWCNTs were conjugated to CuO nanoflowers through a hydrothermal route. The synthesized material was inserted in a conventional Radio Frequency Identification (RFID) system to produce a gas sensor with no need for a battery. The method presented highly selectivity towards

H_2S at very low concentrations (100 ppb). SWCNTs conjugated CuO nanoflowers indicated a great potential to be applied in the production of commercial gas sensors for H_2S detection.

Wang et al. [40], showed for the first time the production of SWCNTs functionalized with tetra-α-iso-pentyloxyphthalocyanine copper (CuPcTIP) and tetra- α-(2,2,4-trimethyl-3-pentyloxy) metal phthalocyanines (CuPcTTMP). The CuPc derivates were anchored on the surface of SWCNTs by π−π interactions. SWCNT/CuPcTTMP and SWCNT/CuPcTIP sensors were produced as thin films and were analyzed under a constant flow of 80 ppm of different gases. Both sensors presented selectivity towards NH_3, with a sensitivity around 23.28% to SWCNT/CuPcTTMP and 30.10% to SWCNT/CuPcTIP. As for the other gases tested (CO_2, CH_4, H_2, and CO), the sensitivity was less than 1% at 80 ppm. Furthermore, both sensors demonstrate good repeatability and no visible degradation after consecutive measurements [40].

In 2019, Lone et al. investigated the efficiency of sensors based on pure and ordered (vertically aligned forest-VA) SWCNTs and disordered (random orientation-RO) SWCNTs to detect NH_3. VA-SWCNTs and RO-SWCNTs were produced by plasma-enhanced CVD (PECVD) on a Fe-coated Si substrate. The growth of RO-SWCNTs can be obtained with any selected parameter. In contrast, the growth of VA-SWCNTs requires the proper optimization of the growth parameters like growth, temperature, gas source, among others. For the sensing measurements, Au electrodes were deposited with a simple brush technique having a minimum gap of 2 mm following the heat treatment to convert the electrode solution to metallic form. To evaluate the detection capacity, the two sensors were subjected to a constant flow of NH_3 with 20–40 ppm concentrations at a temperature of 40 °C. The VA-SWCNT sensor presented a lower sensitivity than RO-SWCNTs towards NH_3. Aligned forests have a smaller surface area than disordered CNTs due to their high density, explaining the obtained result. The best results for RO-SWCNTs and VA-SWCNTs towards NH3 detection were 200–250% and 80–100%. A full recovery (90–100%) was observed for RO-SWCNT, while 80–90% recovery was found for VA-SWCNT. Both sensors presented a potential for application in the production of commercial NH_3 gas sensors [41].

Recently, Gupta et al. [35] investigated the selectivity and electric conductivity of SnO_2 decorated SWCNTs towards NH_3 e NO_2. The authors correlated the dependence of the electrical properties on gas concentration, and after analyzing the data using an electrical sensor, they produced a Langmuir model. The Langmuir adsorption isotherm and other adsorption isotherms describe the equilibrium between adsorbate and adsorbent systems for SW and MWCNTs [38]. Pure SWCNTs and SnO_2 decorated SWCNTs were used in this study. SnO_2 nanoparticles were obtained by the reduction of $SnCl_2.2H_2O$ in ammonia solution. The SWCNTs were dispersed in DMF and were decorated with the addition of SnO_2 nanoparticles in the solution. To finalize, the solution was vacuum filtered to separate the solid product. The SnO_2 decorated SWCNTs were annealed at 400 °C in the presence of N_2 for 10 min. The sensor was mounted on a Printed circuit board header with gold electrodes and exposed to NO_2 and NH_3 in a gas cell at 2–20 ppm concentrations. For both gases, the decorated SWCNTs showed greater selectivity than the sensor with pure SWCNTs.

Theoretical studies were carried out to obtain the Langmuir constants kL $(ppm)^{-1}$ and α $(\Omega m)^{-1}$ for the produced sensors. Comparing the obtained results, it was possible to observe an increase in the value of the constants of the decorated nanotubes compared to the pure ones for both NO_2 and NH_3. The SWCNTs surface decoration with SnO_2 nanoparticles improved the SWCNTs adsorption kinetic energy [35].

5.2 MWCNTs Gas Sensor

MWCNT based gas sensors are designed to detect the same types of gases as SWCNTs. MWCNTs sensors are qualified to measure gasses at a very small concentration (e.g., ~0.1 ppm of NO_2). Both MWCTS and SWCNTs present elevated sensitivity at high temperatures (100–250 °C), reaching a resistivity variation, in the presence of NO_2, of 79.8% (150 °C) for SWCNTs and 59.6% (200 °C) for MWCNTs [43]. The main advantage of MWCNTs over SWCNTs is their cost-effective production. Elevated quantities of high-quality MWCNTS can be produced using low-cost processes [19]. This aspect makes MWCNTS very interesting for the development of commercial gas detection devices. The disadvantage of using MWCNTs over SWCNT is that at low temperatures (<100 °C), the sensor can present long recovery times (~2 h). At higher temperatures, between 100 and 200 °C, the recovery time of MWCNTs is similar to SWCNTs [22].

Espinosa et al. [32] described the production of gas sensors based on MWCNTs decorated with Au or Ag nanoclusters. The nanotubes were functionalized in oxygen R.F. plasma and decorated using electron beam evaporation. The decorated nanotubes were deposited over micro-hotplate substrates that included interdigitated electrodes and a micro-heater. The sensitivity of the sensors was evaluated by variating the gases composition and concentration: NO_2 (500 ppb, 1.5 and 6.5 ppm), CO (10 and 50 ppm), CH_3CH_2OH (5, 10 and 50 ppm), and C_2H_4 (5, 10, and 50 ppm). Au-decorated MWCNT could detect NO_2 even at room temperature, with responsiveness up to 6% at 500 ppb. At 6.5 ppm of NO_2, the responsiveness rose to 12%. Although Ag-decorated MWCNT also responded to NO_2, Au-decorated MWCNT sensors showed better results. Both Au and Ag decorated MWCNTs presented very low sensitivity to CO, ethanol, and ethylene, indicating a high selectivity of Au decorated MWCNTs towards NO_2. The produced Au sensor is capable of detecting NO_2 in concentrations of 500 ppb (room temperature). Before this publication, a 500 ppb sensitivity was found only at high temperatures (150 °C) [32].

Yan et al. have recently [44] developed an MWCNTs based sensor by electrophoretically depositing the nanotubes onto porous silicon, forming MWCNTs/porous silicon (PS) composite. Chemiresistive gas sensors were fabricated using the produced composite. For building a gas sensor, two Pt square electrodes were deposited on the top of the MWCNTs/PS sample using a magnetron sputtering system. The sensing activity for the produced gas detector was investigated in the presence of NO_2. The working temperature was optimized by analyzing the dynamic gas-sensing responses of MWCNTs/PS to 1 ppm NO_2 at different

temperatures (25–150 °C). The resistance value of the sensor largely decreases with increasing temperature. The best result was found for CNTs/PS with an electrophoretic deposition time of 5 min, presenting 8.5% (resistivity) and fast response-recovery times (~37 and ~ 34 s) at room temperature (~25 °C) towards 1 ppm NO_2. The MWCNTs/PS composite is an interesting material for application in NO_2 detection at room temperature [44].

In 2021, Bang et al. produced gas sensors based on Cu_2O/CuO decorated MWCNTs. Cu layers with different thicknesses of 3, 6, and 9 nm were coated on MWCNTs using sputtering for different times of 1, 2, and 3 min at 25 °C, respectively, followed by annealing at 500 °C to produce isolated Cu_2O/CuO. The gas selectivity analysis was carried out with concentrations in the range of 1–50 ppm at a temperature of 150 °C. The gases C_3H_6O, NH_3, C_2H_5OH, CO, C_7H_8, C_6H_6, and H_2S were tested. For H_2S, which was the main target of the study, tests were also carried out variating the temperature: 50, 100, 150, and 200 °C. Cu_2O/CuO decorated MWCNTs sensors work as electron receivers in the presence of H_2S, thus increasing their resistivity. The sensing tests indicated 6 nm as the best coating thickness for Cu_2O/CuO. With this parameter defined, tests were performed varying the temperature, and the sensor presented the best results at 150 °C, reaching a variation resistivity of 1613% for 5 ppm of H_2S. The response towards H_2S was much higher than for the other gases, also indicating excellent selectivity. In particular, it showed a gas response of 1244% to 1 ppm H_2S at 150 °C, with a response time of 219 and a recovery time of 77 s. According to the authors, the produced MWCNTs sensor decorated with Cu_2O/CuO (6 nm) is superior to other H_2S sensors found in literature due to the capability of detecting H_2S at low concentrations (1 ppm) and relatively low temperature (150 °C) [45].

Liang et al. [46] fabricated sensors for the detection of NH_3. 2,9,16,23-tetrakis(2,2,3,3-tetrafluoropropoxy) metal (II) phthalocyanine/MWCNT hybrids (TFPMPc/MWCNT, M = Co, Zn, Cu, Pb, Pd, and Ni) were prepared by using a solution self-assembly method based on π–π stacking interactions. To prepare gas sensors composed of TFPMPc/MWCNT hybrids, interdigitated electrodes were fabricated by a standard lithography process on polished ceramic substrates of alumina. Sensors were analyzed for NH_3 at concentrations of 0.1–200 ppm at room temperature. Sensing tests were also performed for NO and NO_2 with concentrations up to 10,000 ppm. The produced sensors presented insignificant responses for NO and NO_2 even in very high concentrations, indicating the elevated selectivity of the produced sensors towards NH_3. The best result was found for the TFPCoPc/MWCNT sensor, which presented a sensitivity of 26% to 50 ppm NH_3 with a limit of detection of 60 ppb. This sensor showed a fast response and recovery time. The sensor's sensitivity decreased according to the metal in the composition: Co > Zn > Cu > Pb > Pd ≅ Ni. The interactions between NH_3 and metallic ions vary depending on the ion composition [46].

Marimuthu et al. have currently [13] presented a study comparing two sensors towards NH_3 detection; Flake-like $NiCo_2O_4$/MWCNTs and $NiCo_2O_4$. $NiCo_2O_4$ nanoparticles were synthesized by the hydrothermal method. $NiCo_2O_4$/MWCNTs

flake-like nanostructured composite was produced by mixing $NiCo_2O_4$ and functionalized MWCNTs. The produced powders were dispersed in deionized water and were dropped onto Fluorine doped Tin Oxide (FTO) substrate with two copper tapes on the extremities. The authors analyzed the frequency difference with the LCR meter device (LCR-SM6023) in the presence of 100 ppm NH_3 at room temperature. Both $NiCo_2O_4$ and $NiCo_2O_4$/MWCNTs sensors demonstrated good sensitivity to NH_3 gas. However, $NiCo_2O_4$/MWCNTs had a better response than $NiCo_2O_4$ concerning sensitivity, but its reproducibility and recovery were much lower. According to the study, $NiCo_2O_4$ and $NiCo_2O_4$/MWCNTs are promising materials for gas monitoring [13].

6 Conclusions

CNTs have been proven effective for the fabrication of gas sensors. The nanotubes can be used directly or combined with other materials such as metal and oxide nanoparticles, polymers, etc. According to the linked material, the CNTs can become highly sensitive and selective towards specific compositions. CNTs based detectors with elevated sensitivity (e.g., ~100 ppb to H_2S) and selectivity (e.g., 1000% to H_2S at 1 ppm) have been produced in the last few years. However, different aspects such as the response-recovery times and the reproducibility of the results should be improved to produce efficient systems for gas detection. Besides, there are a variety of combinations between CNTs and other materials that were not investigated yet. These new combinations can lead to significant advances in the field, enhancing the performance of the current commercial systems for gas sensing.

References

1. Kaufmann, C.G., Zampiva, R.Y.S., Bergmann, C.P., et al.: Production of multi-wall carbon nanotubes starting from a commercial graphite Pencil using an electric arc discharge in aqueous medium. FME Trans. **46**, 151–156 (2018). https://doi.org/10.5937/fmet1802151K
2. Corbett, J., McKeown, P.A., Peggs, G.N., Whatmore, R.: Nanotechnology: international developments and emerging products. CIRP Ann. **49**, 523–545 (2000). https://doi.org/10.1016/S0007-8506(07)63454-4
3. Zampiva, R.Y.S.: Rare-earth doped forsterite: anti-reflection coating with upconversion properties as solar capture solution, pp. 103–130 (2019)
4. Zampiva, R.Y.S., Jr Kaufmann, C.G., Venturini, J., et al.: Energy conversion dynamics of novel lanthanide-doped forsterite photoactive devices. Appl. Surf. Sci. **561**, 150059 (2021). https://doi.org/10.1016/j.apsusc.2021.150059
5. Zampiva, R.Y.S., Kaufmann, C.G., Acauan, L.H., et al.: Luminescent anti-reflection coatings based on Er^{3+} doped forsterite for commercial silicon solar cells applications. Sol. Energ. **170**, 752–761 (2018). https://doi.org/10.1016/j.solener.2018.05.097
6. Zampiva, R.Y.S., Alves, A.K., Bergmann, C.P.: Mg_2SiO_4:Er^{3+} coating for efficiency increase of silicon-based commercial solar cells, pp. 820–828 (2017)

7. Zampiva, R.Y.S., Acauan, L.H., Venturini, J., et al.: Tunable green/red luminescence by infrared upconversion in biocompatible forsterite nanoparticles with high erbium doping uptake. Opt. Mater. (Amst) **76**, 407–415 (2018). https://doi.org/10.1016/j.optmat.2018.01.004
8. Zampiva, R.Y.S., Acauan, L.H., dos Santos, L.M., et al.: Nanoscale synthesis of single-phase forsterite by reverse strike co-precipitation and its high optical and mechanical properties. Ceram. Int. **43**, 16225–16231 (2017). https://doi.org/10.1016/j.ceramint.2017.08.201
9. Zampiva, R.Y.S., Venturini, J., Acauan, L.H., et al.: The impact of the reaction atmosphere on the additive-free growth of Mg_2B2O_5 nanorods. Ceram. Int. **45**, 6228–6235 (2019). https://doi.org/10.1016/j.ceramint.2018.12.101
10. Arcaro, S., Wermuth, T.B., Zampiva, R.Y.S., et al.: Li_2O-ZrO_2-SiO_2/Al_2O_3 nanostructured composites for microelectronics applications. J. Eur. Ceram. Soc. **39**, 491–498 (2019). https://doi.org/10.1016/j.jeurceramsoc.2018.09.033
11. Tao, F., Liu, Y., Ren, X., et al.: Carbon nanotube-based nanomaterials for high-performance sodium-ion batteries: recent advances and perspectives. J. Alloys Compd. **873**, 159742 (2021). https://doi.org/10.1016/j.jallcom.2021.159742
12. Zampiva, R.Y.S., Kaufmann, C.G., Venturini, J., et al.: Role of the fuel stoichiometry and post-treatment temperature on the spinel inversion and magnetic properties of $NiFe_2O_4$ nanoparticles produced by solution combustion synthesis. Mater. Res. Bull. **138**, 111238 (2021). https://doi.org/10.1016/j.materresbull.2021.111238
13. Marimuthu, G., Nguyen, B.-S., Pham, V.-T., et al.: Novel $NiCo_2O_4$/MWCNTs nanocomposite with flake-like architecture as room temperature capacitive-type NH3 gas sensor. Mater. Lett. **283**, 128814 (2021). https://doi.org/10.1016/j.matlet.2020.128814
14. Kaufmann, C.G., Schorne-Pinto, J.: CNT sponges for environmental applications, pp. 1–13 (2019)
15. Kaufmann Junior, C.G., Zampiva, R.Y.S., Anzanello, M.J., et al.: One-step synthesis of carbon nanoflowers by arc discharge in water. Ceram. Int. **46**, 26229–26232 (2020). https://doi.org/10.1016/j.ceramint.2020.07.071
16. Maust, R.L., Li, P., Shao, B., et al.: Controlled polymerization of norbornene cycloparaphenylenes expands carbon nanomaterials design space. ACS Cent. Sci. (2021). https://doi.org/10.1021/acscentsci.1c00345
17. Fytianos, G., Rahdar, A., Kyzas, G.Z.: Nanomaterials in cosmetics: recent updates. Nanomaterials **10**, 979 (2020).https://doi.org/10.3390/nano10050979
18. Zampiva, R.Y.S., Kaufmann Junior, C.G., Pinto, J.S., et al.: 3D CNT macrostructure synthesis catalyzed by $MgFe_2O_4$nanoparticles—a study of surface area and spinel inversion influence. Appl. Surf. Sci. **422**, 321–330 (2017). https://doi.org/10.1016/j.apsusc.2017.06.020
19. Kaufmann Junior, C.G., Zampiva, R.Y.S., Venturini, J., et al.: CNT sponges with outstanding absorption capacity and electrical properties: impact of the CVD parameters on the product structure. Ceram. Int. **45**, 13761–13771 (2019). https://doi.org/10.1016/j.ceramint.2019.04.072
20. Kaufmann, C.G., Zampiva, R.Y.S., Arcaro, S., et al.: Ecofriendly synthesis of MWCNTs by electric arc in aqueous medium: comparative study of 6B pencil and mineral graphite. Int. J. Appl. Ceram. Technol. (2020). https://doi.org/10.1111/ijac.13565
21. Iijima, S.: Helical microtubules of graphitic carbon. Nature **353**, 737–740 (1991)
22. Han, T., Nag, A., Chandra Mukhopadhyay, S., Xu, Y.: Carbon nanotubes and its gas-sensing applications: a review. Sens. Actuators A Phys. **291**, 107–143 (2019). https://doi.org/10.1016/j.sna.2019.03.053
23. Kumar, S., Pavelyev, V., Mishra, P., Tripathi, N.: A review on chemiresistive gas sensors based on carbon nanotubes: device and technology transformation. Sens. Actuators A Phys. **283**, 174–186 (2018). https://doi.org/10.1016/j.sna.2018.09.061
24. Sharafeldin, I., Garcia-Rios, S., Ahmed, N., et al.: Metal-decorated carbon nanotubes-based sensor array for simultaneous detection of toxic gases. J. Environ. Chem. Eng. **9**, 104534 (2021). https://doi.org/10.1016/j.jece.2020.104534
25. Jorio, A., Dresselhaus, G., Dresselhaus, M.S.: Carbon Nanotubes. Springer, Berlin Heidelberg (2008)

26. Doh, J., Lee, J.: Prediction of the mechanical behavior of double walled-CNTs using a molecular mechanics-based finite element method: effects of chirality Prediction of the mechanical behavior of double walled-CNTs using a molecular mechanics-based finite element method. Comput. Struct. **169**, 91–100 (2018). https://doi.org/10.1016/j.compstruc.2016.03.006
27. Zampiva, R.Y.S., Bergmann, C.P., Alves, A.K., Giorgini, L.: Solution combustion synthesis of Mo-Fe/MgO: influence of the fuel composition on the production of doped catalyst nanopowder. IOP Conf. Ser. Mater. Sci. Eng. **659**, 012078 (2019). https://doi.org/10.1088/1757-899X/659/1/012078
28. Kaufmann Junior, C.G., Zampiva, R.Y.S., Alves, A.K., et al.: Synthesis of cobalt ferrite ($CoFe_2O_4$) by combustion with different concentrations of glycine. IOP Conf. Ser. Mater. Sci. Eng. **659**, 012079 (2019). https://doi.org/10.1088/1757-899X/659/1/012079
29. Bogue, R.: Nanomaterials for gas sensing: a review of recent research. Sens. Rev. **34**, 1–8 (2014). https://doi.org/10.1108/SR-03-2013-637
30. Han, Q., Xi, H.: Elastic properties of carbon nanotubes. In: Carbon Nanotubes—Polymer Nanocomposites. InTech (2011)
31. Takakura, A., Beppu, K., Nishihara, T., et al.: Strength of carbon nanotubes depends on their chemical structures. Nat. Commun. **10**, 3040 (2019). https://doi.org/10.1038/s41467-019-10959-7
32. Espinosa, E.H., Ionescu, R., Bittencourt, C., et al.: Metal-decorated multi-wall carbon nanotubes for low temperature gas sensing. Thin. Solid Films **515**, 8322–8327 (2007). https://doi.org/10.1016/j.tsf.2007.03.017
33. Doujaiji, B., Al-Tawfiq, J.A.: Hydrogen sulfide exposure in an adult male. Ann. Saudi Med. **30**, 76–80 (2010). https://doi.org/10.4103/0256-4947.59379
34. Ridhi, R., Neeru, G.S., et al.: Study of the effect of orbital on interaction behaviour of SWCNT-metal phthalocyanines composites with ammonia gas. Sens. Actuators B Chem. **337**, 129767 (2021). https://doi.org/10.1016/j.snb.2021.129767
35. Gupta, S., Anand, A., Neeru, K.R.: Study of adsorption kinetics of pristine and SnO_2 functionalized carbon nanotubes as environment gas sensors for NO_2 and NH_3 gases. Mater. Today Proc. (2021). https://doi.org/10.1016/j.matpr.2021.04.546
36. Li, L., Zhang, G., Chen, L., et al.: Ni(NiO)/single-walled carbon nanotubes composite: synthesis of electro-deposition, gas sensing property for NO gas and density functional theory calculation. Mater. Res. Bull. **48**, 504–511 (2013). https://doi.org/10.1016/j.materresbull.2012.11.005
37. Choi, S.-W., Kim, J., Byun, Y.T.: Highly sensitive and selective NO_2 detection by Pt nanoparticles-decorated single-walled carbon nanotubes and the underlying sensing mechanism. Sens. Actuators B Chem. **238**, 1032–1042 (2017). https://doi.org/10.1016/j.snb.2016.07.153
38. Asad, M., Sheikhi, M.H.: Surface acoustic wave based H_2S gas sensors incorporating sensitive layers of single wall carbon nanotubes decorated with Cu nanoparticles. Sens. Actuators B Chem. **198**, 134–141 (2014). https://doi.org/10.1016/j.snb.2014.03.024
39. Asad, M., Sheikhi, M.H.: Highly sensitive wireless H_2S gas sensors at room temperature based on CuO-SWCNT hybrid nanomaterials. Sens. Actuators B Chem. **231**, 474–483 (2016). https://doi.org/10.1016/j.snb.2016.03.021
40. Wang, B., Wu, Y., Wang, X., et al.: Copper phthalocyanine noncovalent functionalized single-walled carbon nanotube with enhanced NH_3 sensing performance. Sens. Actuators B Chem. **190**, 157–164 (2014). https://doi.org/10.1016/j.snb.2013.08.066
41. Lone, M.Y., Kumar, A., Ansari, N., et al.: Structural effect of SWCNTs grown by PECVD towards NH_3 gas sensing and field emission properties. Mater. Res. Bull. **119**, 110532 (2019). https://doi.org/10.1016/j.materresbull.2019.110532
42. Moradi, O.: Applicability comparison of different models for ammonium ion adsorption by multi-walled carbon nanotube. Arab. J. Chem. **9**, S1170–S1176 (2016). https://doi.org/10.1016/j.arabjc.2011.12.014
43. Naje, A.N., Ibraheem, R.R., Ibrahim, F.T.: Parametric analysis of NO_2 gas sensor based on carbon nanotubes. Photonic Sens. **6**, 153–157 (2016). https://doi.org/10.1007/s13320-016-0304-1

44. Yan, D., Xia, S., Li, S., et al.: Electrophoretic deposition of multiwalled carbon nanotubes onto porous silicon with enhanced NO_2-sensing characteristics. Mater. Res. Bull. **134**, 111109 (2021). https://doi.org/10.1016/j.materresbull.2020.111109
45. Bang, J.H., Mirzaei, A., Choi, M.S., et al.: Decoration of multi-walled carbon nanotubes with CuO/Cu_2O nanoparticles for selective sensing of H_2S gas. Sens. Actuators B Chem. **344**, 130176 (2021). https://doi.org/10.1016/j.snb.2021.130176
46. Liang, X., Chen, Z., Wu, H., et al.: Enhanced NH_3-sensing behavior of 2,9,16,23-tetrakis(2,2,3,3-tetrafluoropropoxy) metal(II) phthalocyanine/multi-walled carbon nanotube hybrids: an investigation of the effects of central metals. Carbon N Y **80**, 268–278 (2014). https://doi.org/10.1016/j.carbon.2014.08.065

Titanium Dioxide Nanomaterials for Renewable Energy Applications

Carol Sippel, Waleska Campos Guaglianoni, and Carlos Pérez Bergmann

Abstract Titanium dioxide has attracted much attention from several researchers due to its excellent physicochemical properties. TiO_2 is an eco-friendly material that has low cost, high chemical stability, and low toxicity. In this chapter, the main properties of TiO_2 and its nanostructures are discussed, as well as the applications of these nanostructures in the generation of renewable energies to replace fossil fuels. We start with an introduction that explains why TiO_2 is suitable for renewable energy technology applications. Next, some renewable energy technologies where TiO_2 has been successfully studied and applied are reviewed. Examples of these technologies include supercapacitors, solar cells, hydrogen production, lithium-ion batteries, and sensors. For each of these applications, we highlight their current challenges and discuss how TiO_2 nanomaterials can improve the performance of the devices.

Keywords Titanium dioxide · Renewable energies · Supercapacitors · Li-ion batteries · Solar cells · Hydrogen production · Sensors

Abbreviations

FESEM	Field Emission Scanning Electron Microscopy
EDS/EDX	Energy-Dispersive X-ray
TEM	Transmission Electron Microscopy
SEM	Scanning Electron Microscopy
XRD	X-ray Diffraction
0D	Zero dimension
1D	One dimension
2D	Two dimensions
3D	Three dimensions
CVD	Chemical Vapour Deposition
CNT	Carbon Nanotubes

C. Sippel (✉) · W. C. Guaglianoni · C. P. Bergmann
Universidade Federal do Rio Grande do Sul, Porto Alegre, Brazil

A. Kopp Alves (ed.), *Environmental Applications of Nanomaterials*, Engineering Materials, https://doi.org/10.1007/978-3-030-86822-2_5

TNT Tunneling Nanotubes
PED Photoelectrochemical

1 Introduction

The global energy demand is increasing every day due to the exponential growth of the population. Currently, fossil fuels are still the primary energy source, causing environmental impacts and climate change [1]. Thus, the development of new renewable and sustainable energy sources becomes necessary.

In this context, it is possible to highlight the energy of hydrogen, capable of producing electricity with pure water as a by-product [2, 3]. The big problem is in the limited availability of hydrogen and high cost [4]. Hydrogen extraction from water molecules is an excellent production method because water is abundant and the process does not produce harmful by-products [5, 6]. However, the division of water molecules requires a high energy (approximately 237.46 kJ/mol of Gibbs energy) [7]. Energy from renewable sources, such as solar energy, can electrolyze these molecules [8].

Solar energy has several advantages over other energy sources, such as: producing lower CO_2 emissions, not producing waste products in the energy generation process, and being an inexhaustible source. Several countries have preferred solar energy as an alternative energy source and many studies have been done to improve the efficiency of solar cells available on the market. Currently, most solar cells are based on silicon; however, their processing requires large amounts of energy and their efficiency decreases at higher temperatures. The presence of these concerns has stimulated researchers to investigate the new materials for photovoltaic applications [9].

The importance of using sensors, especially gases, is also emphasized. There is a growing concern about the safe use, storage and transport of gases since, after certain levels of concentration, some can become flammable and explosive in the air, even though they are colorless and odorless. Gases such as H_2 need real-time monitoring so that there is an early warning in the event of a leak [10].

TiO_2 has been widely used in the areas of solar cells, supercapacitors, lithium-ion batteries, photocatalysis, gas sensor and biosensor (Fig. 1) due to its low cost, high chemical stability, low toxicity and respect for the environment [11]. TiO_2 has a wide bandgap of about 3.2 eV and, therefore, excellent photocatalytic activity under ultraviolet light illumination [12]; however, this value is equivalent to less than 5% of the total sunlight. In addition, photogenerated electron gap pairs can recombine quickly, leading to low quantum efficiency [13]. Some strategies to overcome this problem are discussed throughout this chapter.

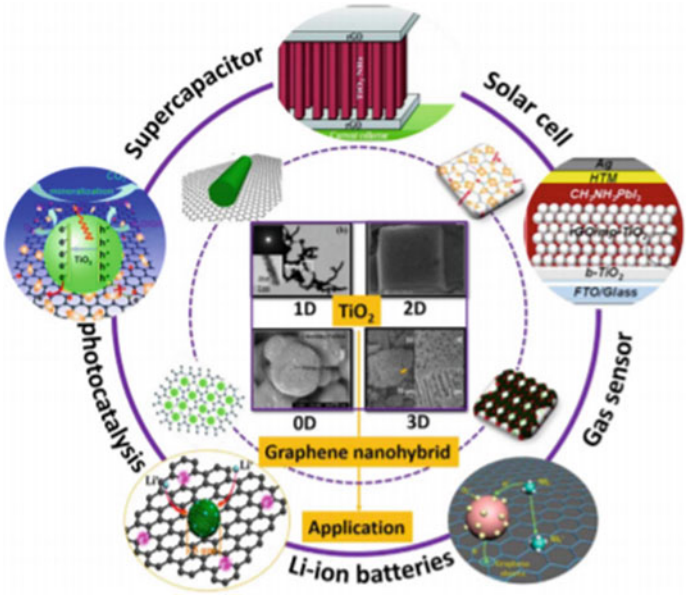

Fig. 1 Scheme of the applications of TiO_2 in different fields. (Reprinted with permission of [14])

2 Titanium Dioxide (TiO_2)

Titanium dioxide has unique properties and characteristics that make it ideal for countless applications. It is widely used as a photocatalyst because of its high oxidability and its activity under the ultraviolet spectrum [15, 16]; in oral consumption products such as food (E171 additive), toothpaste and medicines due to its stability and low toxicity [13]; in the degradation of pollutants and bacteria thanks to its insolubility in aqueous medium [17]; and in the generation of hydrogen gas by water splitting [18]. Titanium dioxide also has attributes such as high electrical resistance (resistivity of $10^{-14}\Omega.cm^{-1}$) [19], high durability and hardness [20], and excellent transmittance in the visible region of the spectrum.

Titanium dioxide (TiO_2) belongs to the transition metal oxide family. It can be found in eight different crystalline forms TiO_2-B, TiO_2-R, TiO_2-H, TiO_2-II, TiO_2-III, rutile, anatase and brookite [22, 23]. Figure 2 presents the most studied crystal structures: (a) rutile, (b) anatase and (c) brookite. The anatase and rutile phases have been extensively researched due to their higher photoactivity. However, they have a band gap energy of 3.2 eV (387 nm) and 3.0 eV (413 nm), respectively, absorbing only UV light (less than 5% of total solar energy). Furthermore, the recombination rate of the e + /h- pairs is fast, which reduces the quantum efficiency [13]. To overcome this problem, it is not uncommon to use techniques to increase photocatalytic activity: (i) TiO_2 nanostructures, (ii) Doping and (iii) Composites with carbonaceous materials.

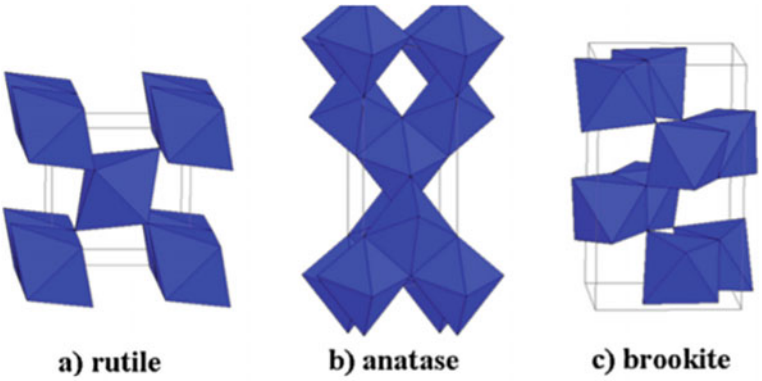

Fig. 2 TiO_2 crystal structures: rutile **a**, anatase **b** and brookite **c**. (Reprinted with permission of [21])

(i) **TiO_2 nanostructures**

Regarding TiO_2 nanostructures, 0D nanoparticles have excellent performance as photocatalysts, adsorbents and sensors due to their large surface area and easy fabrication [24]. However, the inherent disadvantages, such as the fast recombination of electrons and gaps, slow transfer of charge carriers and high recycling cost, limit their photocatalytic efficiency. Recently, one-dimensional (nanotube, nanofibers, nanobands, etc.), two-dimensional (nanofilms) and three-dimensional (nanospheres) structures have shown improvement in electron-gap separation, rapid transfer of charge carriers and increased active surface area compared to TiO_2 nanoparticles, causing an increase in catalytic activity [25]. Figure 3 displays several TiO_2 morphologies reported in the literature.

Comparing the aforementioned structures, there is a special highlight for nanotubes as they present excellent structural parameters such as a large surface area, increasing efficiency in electron transport and, consequently, enhanced catalytic activity [12].

(ii) **Doping**

The doping of TiO_2 nanostructures can occur with non-metallic elements, such as Boron (B), Carbon (C), Nitrogen (N) and Sulfur (S), as well as with transition metals such as Manganese (Mn), Iron (Fe), Cobalt (Co), Nickel (Ni) and Molybdenum (Mo). These materials combine the electrical and optical properties of TiO_2 with magnetic properties. The presence of dopants can also cause the displacement of energy from the TiO_2 band gap to other regions of the electromagnetic spectrum [12].

The doping of TiO_2 nanotubes has recently aroused great interest due to the various possibilities of applications. Some authors, such as Peighambardouts et al. [27], studied the photocatalytic activity of non-doped, N-doped and self-doped (blue) TiO_2 nanotubes. For those doped with N (Fig. 4), it was suggested

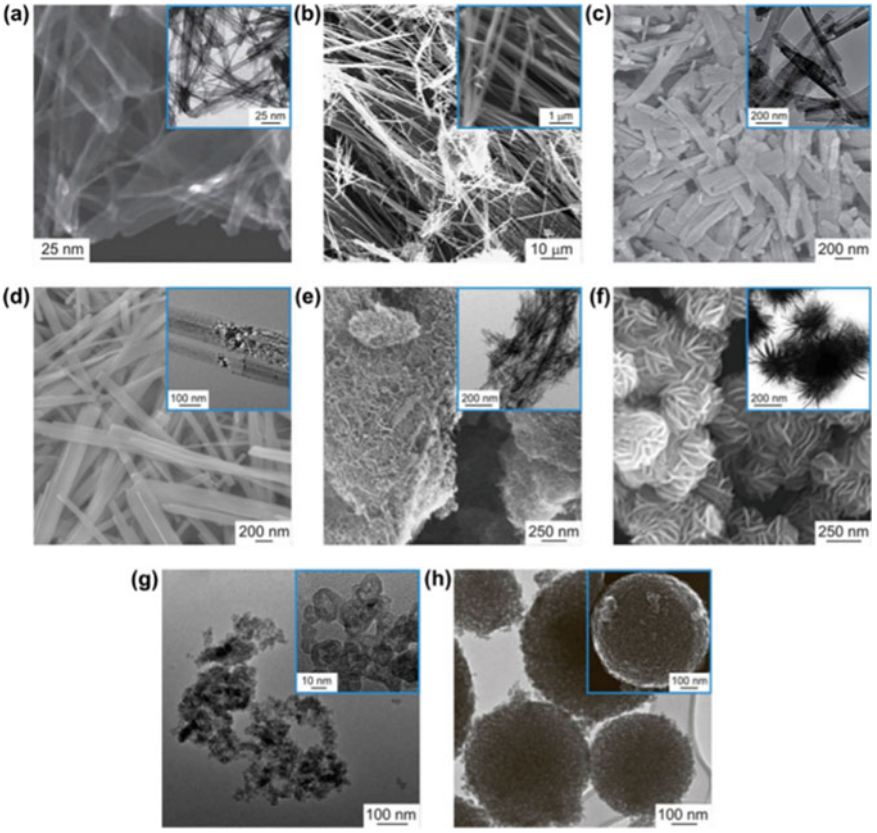

Fig. 3 Different TiO_2 morphologies: **a** nanotubes, **b** nanowires, **c** nanorods, **d** nanoribbons, **e** nanofibers, **f** nanosheets, **g** nanoparticles, and **h** mesoporous microsphere. (Reprinted with permission of [26])

to prepare the TiO_2 nanotubes by anodization (Voltage: 60 V; Time: 4 h; Electrolyte: ethylene glycol/NH_4F/H_2O), and then immerse the samples in a 1 M solution of $NH_3.H_2O$ for 8, 15, 20 and 25 h. In order to manufacture the self-doped TiO_2 nanotubes, the reductive electrochemical doping was performed in a system of three electrodes in the 0.5 M Na_2SO_4 support electrolyte at a potential of −1.4 V for 10 min of polarization. The results showed that the degradation rate is increased by up to 65% through nitrogen doping.

Similarly, Yuan et al. [28] proposed TiO_2 doping in two stages. Initially, TiO_2 nanotubes were prepared by anodization (Voltage: 60 V; Time: 6 h; Electrolyte: ethylene glycol/NH_4F/H_2O) and, sequentially, the nanotubes were immersed in a 1 M NH_4OH solution.

Doping can be performed in a post-treatment after the anodization process, as in the work of Gao et al. [29]. The authors synthesized the TiO_2 nanotubes by

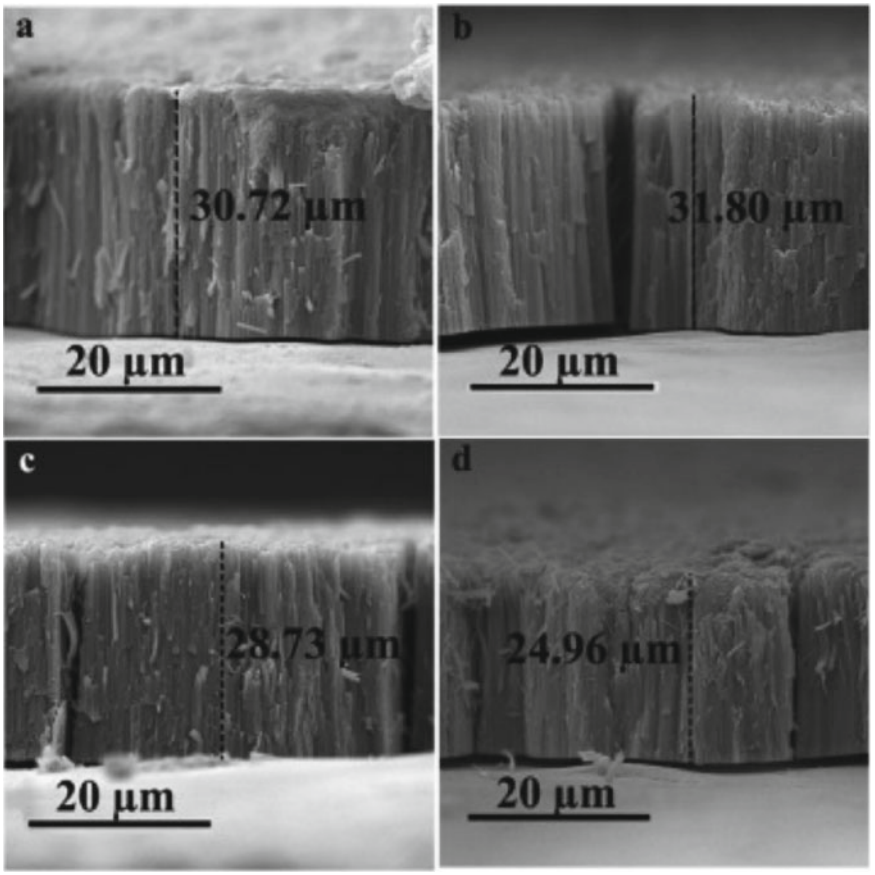

Fig. 4 FESEM images of N-doped TiO_2 nanotubes anodized for 4 h and doped in a NH_3 solution at immersing times of **a** 8, **b** 15, **c** 20, and **d** 25 h. (Reprinted with permission of [27])

anodization (Voltage: 19.9 V; Time: 2 h, magnetic rotation of 700 rpm; Electrolyte: glycerol/H_2O/NH_4F) and subsequently, Boron doped Graphene was deposited on the TiO_2 substrate using Chemical Vapor Deposition (CVD). The development of Boron-Graphene/TiO_2 nanostructures increased the conductivity of TiO_2 nanotubes. Lithium-ion capacitors prepared with these electrodes showed high energy density (221.8 $Wh{\cdot}kg^{-1}$ to 5.98 $kW{\cdot}kg^{-1}$), high power density (35.1 $kW{\cdot}kg^{-1}$ to 102.4 $Wh{\cdot}kg^{-1}$) and excellent cycling stability (91.3% retention after 10,000 cycles). In addition, these structures were produced by anodizing, annealing and CVD processes, each with high operability and good repeatability, allowing industrial production. They can be used for a wide range of other energy and environment-related systems, such as batteries, fuel cells, catalysis and water treatment.

(iii) **Composites with carbonaceous materials**

The development of carbon nanostructure composites is another emerging area. TiO_2 composites based on graphene, fullerene and carbon nanotubes have been shown to improve photocatalytic and photoelectrochemical properties [30–33]. The combination of carbon nanotubes with TiO_2 can promote the separation of electron-gap charges generated in irradiation, and the presence of C-O-Ti bonds reduces the band gap, increasing the absorption wavelength [31].

3 Applications

TiO_2 can be used in numerous applications for energy generation and storage due to its excellent properties that differentiate it from most elements. The following sections will discuss some of the main applications of TiO_2 for energy generation and/or storage.

3.1 Supercapacitors

Supercapacitors are devices capable of managing high energy rates compared to batteries. Although supercapacitors provide hundreds to many thousands of times more power in the same volume due to their fast surface reactions [14], they are not able to store the same amount of charge as batteries, generally being 3−30 times smaller [34, 35]. This makes supercapacitors suitable for applications where energy "explosions" are required, but a high energy storage capacity is not required [36].

Another great advantage of supercapacitors is their life cycle. These devices can withstand millions of cycles thanks to their charge storage mechanism, which does not involve irreversible chemical reactions, storing charges physically on the surface of the electrodes in a double electrical layer. This makes it possible to exceed the life cycle of the batteries, which are, at best, capable of withstanding a few thousand cycles [34]. The main disadvantage related to the charge storage mechanism is the operating voltage of a supercapacitor cell, which must be kept low in order to avoid the chemical decomposition of the electrolytes [34]. There is also a disadvantage in relation to recycling, as it presents problems similar to batteries: difficulty in separating the different materials and high process cost, being, sometimes, more advantageous to create the device from "zero".

A supercapacitor cell comprises two electrodes with a separator between them (Fig. 5). The separator is soaked in an electrolyte and prevents electrical contact between the electrodes. The separating material must be ion-permeable, to allow ionic charge transfer, while having high electrical resistance, high ionic conductance and low thickness to obtain the best performance [37]. The potential for breakage of the electrolyte in one of the electrodes limits the attainable cell voltage, while the

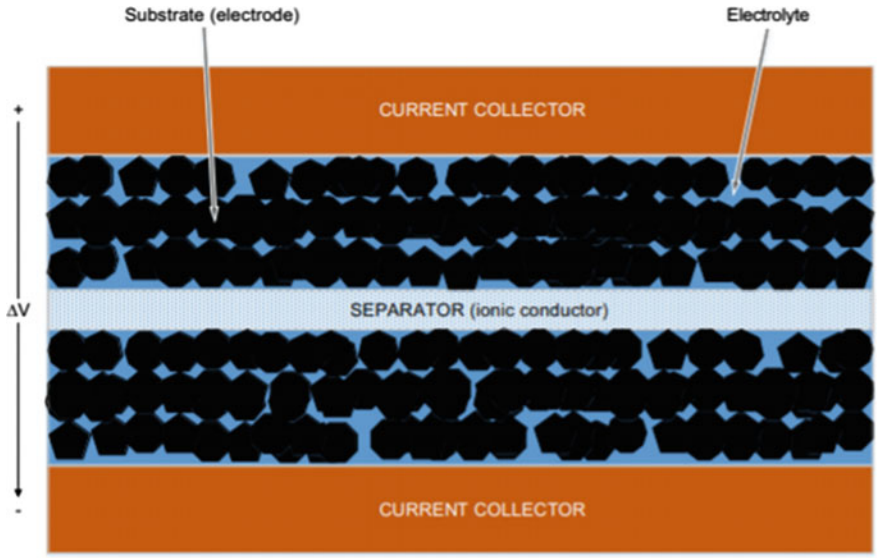

Fig. 5 Symmetric supercapacitor schematic diagram. (Reprinted with permission of [34])

equivalent series resistance (ESR) of the cell will depend heavily on the conductivity of the electrolyte.

In addition to the several advantages of titanium dioxide already presented, nanometric TiO_2 particles can shorten the ion diffusion length, and reduce the ionic resistance to diffusion and resistance to charge transfer of the supercapacitors [14].

Jiang et al. [38] reported a study with N doped TiO_2 microspheres, prepared by a hydrothermal process, for high performance supercapacitors. This structured microsphere can provide a large specific surface area and an appropriate pore size, which leads to electrolyte infiltration. The nitrogen doping improved the intrinsic electrical properties of TiO_2. Su et al. [39] proposed a similar methodology using N-doped TiO_2 nanobands, through a hydrothermal process (Fig. 6). The results showed that the TiO_2 morphology affected the degree of nitrogen doping. The optimized N-TiO_2–3 electrode showed the maximum areal capacitance, which is much higher than that of the seeding sample. This provides a general method to improve the actual capacitance of nanomaterials by adjusting the concentration of seed solution.

Huang et al. found that the characteristics of TiO_2 nanoparticles are further enhanced when doped with Ag for use in supercapacitors [40]. Rajangam et al. showed that the silver ions increased the conductivity, as well as the capacitance of the supercapacitor [41].

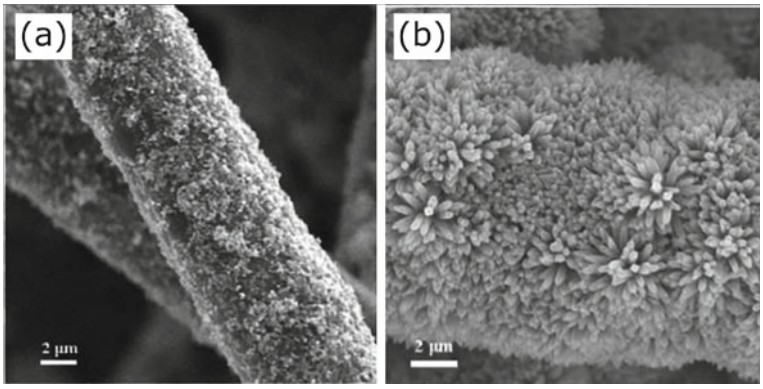

Fig. 6 The morphology of **a** TiO_2-3 and **b** N-TiO_2-3 electrodes. (Reprinted with permission of [39])

3.2 Solar Cells

In 1 h, the earth receives enough energy from the sun to supply its energy needs for almost 1 year, around 5000 times the amount of energy from other energy sources. Among renewable energy resources, solar energy proves to be the source of choice due to its source and energy source [42].

In terms of cost–benefit, excellent efficiency and ease of manufacture, a dye-sensitized solar cell (DSSC), which is a subclass of thin-film solar cells, has proven to be one of the most promising alternatives to silicon solar cells, which are expensive devices due to their complicated production process [43]. A schematic representation of DSSCs is illustrated in Fig. 7.

The system is constituted by four main components [44]:

(i) a photoanode composed of a layer of mesoporous oxide (usually TiO_2) deposited on a transparent conductive glass substrate;
(ii) a dye sensitizer monolayer covalently attached to the surface of the TiO_2 layer to collect light and generate electrons excited by photons;
(iii) an electrolyte containing a redox pair (typically I^-/I_3^-) in an organic solvent to collect electrons in the counter electrode and effect the dye regeneration;
(iv) and a counter electrode made of a platinum-coated conductive glass substrate [45].

One of the main components of solar cells is the photoanode, which greatly affects the total efficiency of light conversion. The matrix of TiO_2 nanotubes, a material with unique properties, has been used in studies with photovoltaic devices for presenting characteristics such as highly ordered nanotube structure, accelerating electron transport, and an ordered surface that increases the absorption of the sensitizer [46, 47].

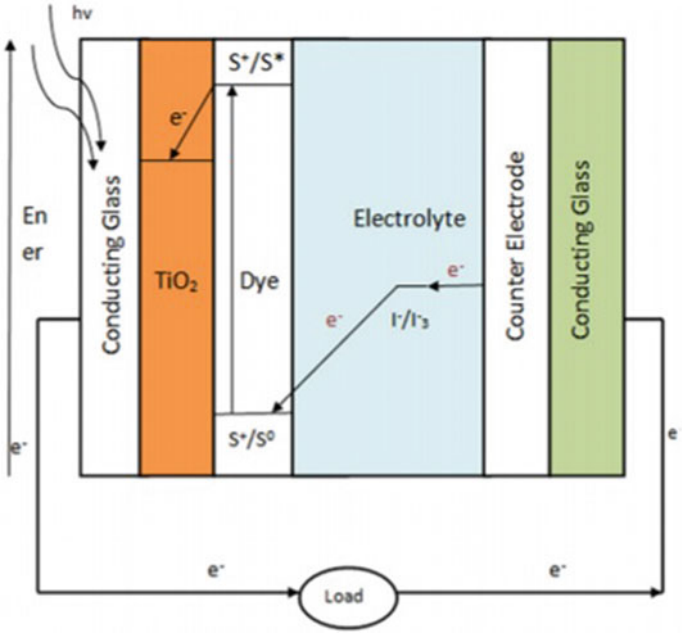

Fig. 7 Arrangement of component and working principle of DSSCs. (Reprinted with permission of [9])

O'Ragan et al. [48] first developed this sensitized solar cell using a TiO_2 particle film as the photoanode. Many efforts have been devoted to improving the light conversion of DSSC cells due to the numerous advantages such as its low cost, easy manufacturing and high efficiency. TiO_2 materials have been shown to be a potential alternative to conventional solid-state solar cells [49].

Madurai Ramakrishnan et al. [50] synthesized TiO_2 nanotubes by the solvothermal method employing nanoparticles as starting material (Fig. 8). They were transformed into nanotubes in the presence of concentrated NaOH. The surface area of the nanotubes was considered to be larger compared to the initial nanoparticles. Dye-sensitized solar cells (DSSC) were prepared using the TiO_2 nanostructures as photoanodes and their conversion efficiencies were analyzed. The maximum efficiency obtained was 7.2%.

Yun et al. [51] studied the effect of light absorption (LS) on dye-sensitized cells (DSSC) using TiO_2 nanotubes with different lengths. The results showed that the TNT matrix, with greater length and larger tube diameter, improved the photoelectrochemical property (PEC) by generating a larger photocurrent and, in addition, provided a larger surface area to yield more dye load. The improved PEC property and the dye loading by the longer nanotube matrix (22 μm) led to a noticeable rate of increase in energy conversion efficiency of 0.7–1.88% (168% increase) after LS treatment 60 min, which was more prominent compared to enhancing DSSCs using mesoporous TiO_2 films. The morphology of TiO_2 nanotubes in photoanodes has

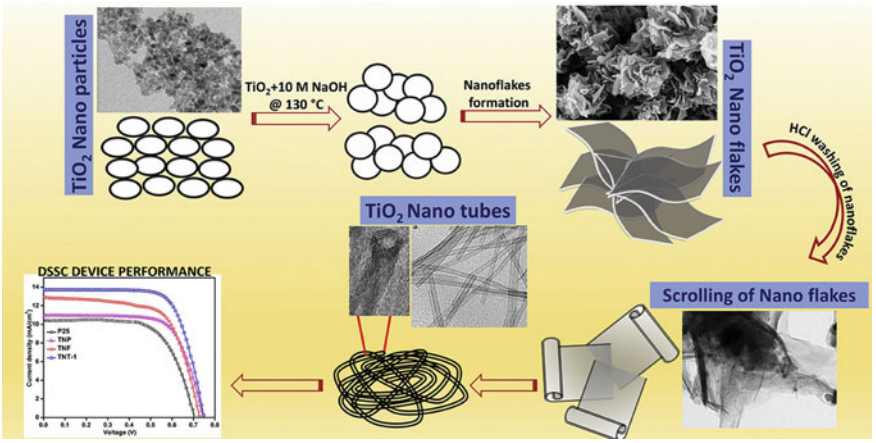

Fig. 8 Schematic diagram of the growth mechanism of TiO_2 nanotubes and DSSC device performance. (Reprinted with permission of [50])

more space, facilitating the cationic exchange in the electrolytic system, favoring the injection of electrons and reducing their recombination.

The doping of semiconductors allows the modification of their properties. In the work presented by Nguyen et al. [52] TiO_2 nanotubes were synthesized by the hydrothermal method assisted by microwave and doped with different concentrations of Chromium (Cr). The results showed that TiO_2 nanotubes doped with Cr had a reduction in the recombination rate of the photogenerated charge carriers, leading to a longer electron life. The DSSC based on Cr-TNT containing an atomic percentage of 7.5% of Cr/Ti demonstrated the best efficiency in converting sunlight among the prepared samples.

Liu et al. [53] synthesized TiO_2 nanotubes by the hydrothermal method and subsequently, the nanotubes were modified by Silver (Ag) nanoparticles by in-situ photodeposition reaction. Results showed that Ag nanoparticles photodeposited on the surface of TiO_2 nanotubes improved the performance of the solar cell, increasing the absorption of light and facilitating the separation and electron-gap transfer. The photoanode of this work showed the best photoelectric conversion efficiency with the fill factor (FF) of 53.63% and the efficiency (η) of 7.2%.

3.3 Hydrogen Production

With the rapid increase in population and industrial activities, renewable energy sources are increasingly being targeted as energy alternatives to reduce CO_2 emissions and climate damage [54]. One of the most investigated renewable energies today is hydrogen energy.

The process of obtaining hydrogen can occur through five different routes: thermal, electrolytic, photolytic, bioprocess and combined. The photoelectrochemical process (photoelectrochemical water splitting) is a combined form of electrochemical and photolytic processes, with low environmental impact [55]. Currently, the most used process is the thermal one. In this case, the steam usually reacts with a hydrocarbon-type fuel, producing hydrogen. The fuels utilized are various, ranging from diesel to natural gas and biogas, for example. In this type of generation, there are carbon emissions. According to the Office of Energy Efficiency and Renewable Energy, 95% of all hydrogen produced comes from natural gas [56].

Hydrogen extraction from water molecules is an excellent production method because water is abundant and the process does not produce harmful by-products [5, 6]. However, the division of water molecules requires a high energy (approximately 237.46 kJ.mol^{-1} of Gibbs energy) [7]. Energy from renewable sources, such as solar energy, can be used to electrolyze these molecules [8].

Several methodologies have been developed for water splitting, such as photoelectrochemical, photocatalytic, radiolysis, photobiological and thermal decomposition. In photoelectrochemical and photocatalytic processes, it is possible to use solar radiation, making them simple, efficient, clean and low-cost methods [57].

The concept of water decomposition using the photoelectrochemical method was first reported by Fujishima and Honda [58]. The photoelectrochemical cell consists of a semiconductor photo-anode, where oxygen is released, and a photo-cathode (platinum), where hydrogen is produced. A voltage is applied in order to direct the photogenerated electrons from the anode to the cathode [57].

Several materials have been used as an anode, such as TiO_2, ZnO, CdSe, CdS, GaP, $SrTiO_3$, Nb_2O_5, WO_3 and Fe_2O_3. Among the materials used, TiO_2 is one of the most studied and was the first material described as a photochemical catalyst for the fission of the water molecule.

The approaches that have been applied to improve the photocatalytic activity of TiO_2 include increasing the active surface area [58], reducing the wide bandgap [59], and improving the processes of charge separation and electron transfer [60]. The active surface area is generally increased by the surface modification of various types of nanostructures, such as nanoparticles (NPs) [61, 62], nanorods (NRs) [63], nanofibers (NFs) [64] and nanotubes (NTs) [65].

Among TiO_2 structures, NTs have the largest surface area, which allows light and reagents to diffuse over the entire tubular depth. Photocatalytic products, that is, electrons, holes and ions, can be transported through the large area of the tube wall [54]. In addition, TiO_2 NTs have a bandgap of approximately 3.00 eV, which is the lowest among the various types of nanostructures [66].

Venturini et al. [67] synthesized TiO_2 nanotubes doped with cobalt (Co-TiO_2) by electrochemical anodization process. A similar approach was adopted by Guaglianoni et al. [68] to obtain iron-doped TiO_2 nanotubes (Fe-TiO_2). The insertion of the metal ions in TiO_2 was carried out directly during the anodizing process, reducing the synthesis steps and consequently the costs involved in producing the material. Figure 9a–b presents the morphology of the synthesized structures. Linear

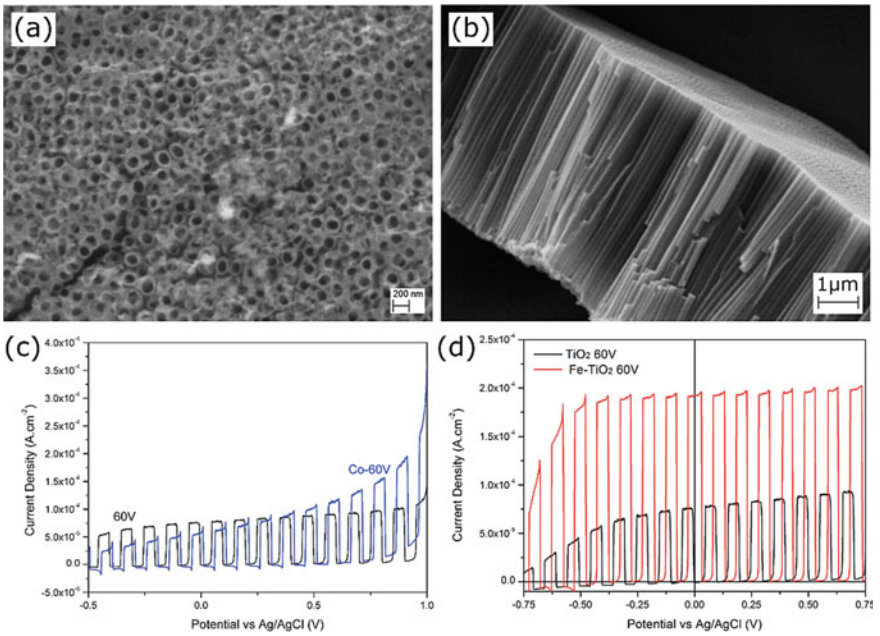

Fig. 9 SEM images of **a** the top view of the Co-TiO_2 nanotubes and **b** the lateral view of the Fe-TiO_2 nanotubes. Current density curves comparing the photoelectrochemical behavior of the TiO_2 pure nanotubes with the doped nanotubes with **c** cobalt (Co-TiO_2) and **d** iron (Fe-TiO_2). (Reprinted with permission of [67, 68])

voltammetry tests evaluated the photoelectrochemical behavior of the produced electrodes. It can be seen in Fig. 9c–d that the doped TiO_2 nanotubes, both with Co and Fe, showed a substantial increase in light conversion efficiency when compared to the pure TiO_2 catalyst. The current density values for the Co-TiO_2 and Fe-TiO_2 nanotubes were 3.6×10^{-4} A.cm^{-2} (at 1.0 V versus Ag/AgCl) and 1.9×10^{-4} A.cm^{-2} (at 0.75 V vs Ag/AgCl), respectively. The doped samples had a generated photocurrent 2.5 times greater than the pure TiO_2. Since the photocurrent is directly related to the evolution of hydrogen gas within the system, the results indicate that these materials are promising candidates for application as photoactive materials for hydrogen production.

TiO_2 nanoparticles treated with different pH solution during hydrothermal synthesis were employed for H_2 production via water splitting [69]. The samples treated at higher pH presented better performance than the commercial TiO_2 (P25). For instance, the nanoparticles obtained with neutral pH (particle size = 11.3 nm; surface area = 144.6 m^2g^{-1}) produced the largest amount of H_2, approximately 110 µmol.g^{-1} h^{-1}. The authors attributed this result to the presence of HO^- groups physisorbed on the catalyst surface, that trapped the holes and transferred the charges between the semiconductor and the electrolyte.

3.4 Lithium-Ion Batteries

Due to better performance and reduced production costs, lithium-ion batteries have been gaining more and more space. Nowadays, they are used in various electronic equipment, such as cell phones, notebooks, pacemakers, digital cameras, electronic toys, among others, dominating the segment of portable rechargeable batteries [70]. In addition to the applications mentioned above, it is projected to be used on a large scale in electric vehicles, which are less aggressive to the environment, and may increase the trade in lithium-ion batteries [70].

The constant exchange of electronic equipment for more modern and convenient ones by consumers has caused an increase in their disposal, increasing the number of batteries in landfills. In developing countries, most batteries are still disposed of in household waste and are subsequently sent to landfills. In 2004, about 45% of the batteries of the EU countries ended up in landfills or were incinerated, while only 17% were sent for treatment. Worldwide, 700 million lithium-ion batteries have been discarded irregularly. In 2006, about 500 tons of these batteries were discarded in Brazil alone [71, 72].

Generally, a lithium-ion battery is formed by a cathode, anode and a separator, immersed in the liquid electrolyte and sealed in stainless steel, aluminum case or plastic bag. The anode contains graphite powder as an active material, which is mixed with a binder, usually PVDF, and coated in a copper foil current collector. On the other hand, the cathode can comprise different types of active materials, including lithium metal oxides or phosphides, such as $LiCoO_2$ (LCO) [73], $LiMn_2O_4$ (LMO) [74] LiNixCoyMnzO_2 (LNCM) [75], LiNixCoyAlzO_2 (LNCA) [76] and $LiFePO_4$ (LFP) [77], which are coated in an Al current collector with carbon black as the conductive agent and PVDF as the binder.

Several studies have been conducted using TiO_2 in lithium-ion batteries due to its various economic and environmental advantages in the preparation of electrodes. It is important to note that TiO_2 is a low voltage and fast insertion host for Li and the TiO_2 structure can remain stable during the extraction/insertion process, making TiO_2 a material with great anode potential in Li-ion batteries of high potency, avoiding the formation of the passivation layer on contact with the electrolyte [78]. However, TiO_2 also has some disadvantages, such as poor performance per cycle because of its low electron transport capacity. Therefore, many efforts are being made to overcome these issues [14]. Guo et al. [79] prepared TiO_2-RuO_2 mesoporous nanocomposites to be used as an anode in Li-ion batteries in order to improve the poor performance of the cycle.

In recent years, several researchers are developing graphene to combine with TiO_2, since together they can improve the structure capacity and cycle performance of TiO_2 in lithium-ion batteries [80]. Huo et al. [81] deposited mesoporous TiO_2 nanoparticles on the surface of a sulfur/nitrogen doped graphene oxide foam (SNG). As an anode material for lithium-ion batteries, SNG/TiO_2 (Fig. 10) exhibited excellent reversible discharge capacity (444 mAh.g^{-1}, 0.1 A.g^{-1}) and good rate capability (217 mAh.g^{-1}, 2.0 A.g^{-1}).

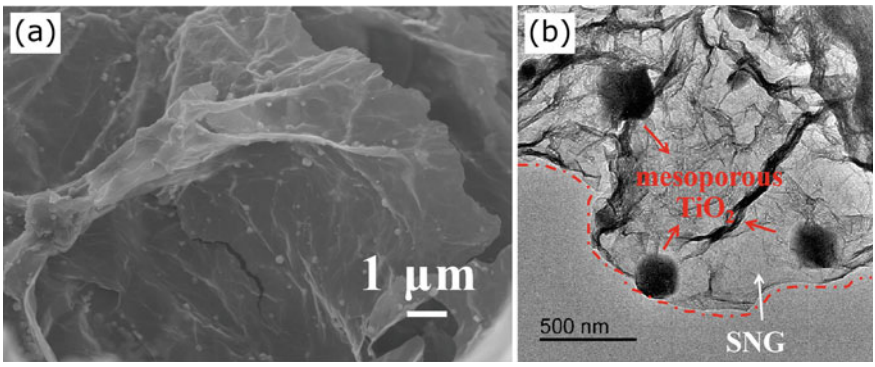

Fig. 10 **a** SEM and **b** TEM images of the SNG/TiO_2 anodes for application in lithium-ion batteries. (Reprinted with permission of [81])

Guo et al. [82] proposed the synthesis of a hybrid mesoporous TiO_2/graphene film using a one-step thermal steam method without the need for an additional annealing process. The resulting material showed a better light harvest and greater charge generation and separation efficiency, showing greater advantages than pure TiO_2 synthesized by a traditional solvothermal method.

One of the big problems with batteries is found in the difficulty of recycling and separation of materials. Currently, the main material recovered from lithium-ion batteries is aluminum. However, this process is much more complex for lithium or graphite. The large consumption of energy makes recycling so expensive that it is generally cheaper to buy raw materials from the mines. In addition, an infrastructure must be created to collect old electric car batteries to reuse them in a regulated recycling process [72].

In this context, studies have also shown that TiO_2 can be used as a facilitator in the recycling process of lithium-ion batteries [83]. Mazurek et al. [84] presented a process for separating lithium and cobalt (II) ions from aqueous solution using hybrid material TiO_2/ZrO_2 enriched with lanthanum. The experimental data collected showed a high selectivity of the synthesized hybrid material in relation to cobalt (II) ions in the presence of lithium ions.

3.5 Sensors

In a world where technological advancement requires accurate information from countless categories, sensors are becoming increasingly important. They have been widely used in industrial, aerospace, marine exploration, environmental protection, resource research, medical diagnostics and bioengineering [85].

The use of sensors, especially gases, is essential because there is a growing concern about safe use, storage and transport since, after certain levels of concentration, some

can become flammable and explosive in the air, even if they lack color and odor. Gases such as H_2, previously mentioned in the hydrogen production section, need real-time monitoring to detect early warning in case of leakage [10].

Nanostructured materials can detect and monitor gases at high temperatures. Semiconductor materials based on titanium dioxide have been gaining ground due to their excellent properties [86]. The literature presents multiple sensors based on TiO_2 nanoparticles to detect different gases: CO [87, 88], ethanol [89], toluene [90], NO_2 [91], O_2 [88], CO_2 [92], SO_2 [93], NH_3 [94], H_2S [95], among others.

Hsu et al. [87] developed a CO sensor using $TiO_2/La_{0.8}Sr_{0.2}Co_{0.5}Ni_{0.5}O_3$ (LSCNO) perovskite. The experimental results showed that the TiO_2/LSCNO heterojunction structure had a PN junction rectifier and is a better CO sensor at 200 °C for a CO concentration of 400 ppm. The response of the CO sensors was 38.41%, with good recovery and reproducibility.

The detection properties of TiO_2 films were examined at different concentrations of ethanol in the liquid phase by a simple procedure developed by Singh et al. [89]. The sensitivity of the sensor found was 0.052 $mA.M^{-1}.cm^{-2}$ for ethanol. Thus, the degradation rate and the subsequent chemical detection properties of the TiO_2 nanoarchitecture are of immense importance for the functions of the TiO_2 structure as a photocatalyst and chemical sensor.

Seekaew et al. [90] presented a highly sensitive gas sensor to detect toluene at room temperature based on 3D nanotubes of titanium dioxide, graphene and carbon nanotubes (3D TiO_2/G-CNT). The structure was manufactured by chemical vapor deposition and sparking methods. The mechanisms of toluene detection of the 3D TiO_2/G-CNT structure were proposed based on the formation of metal–semiconductor Schottky junctions between metal structures of 3D graphene-CNT and n-type semiconductor TiO_2 nanoparticles due to the adsorption of toluene molecules via low-temperature reduction reactions or direct charge transfer process.

Ramgir et al. [91] developed a highly selective NO_2 sensor based on TiO_2/ZnO heterostructure nanowires (NWs) (Fig. 11). The sensor film is made by modifying the surface of ZnO NWs with Ti (~30 nm) and subsequent annealing at 350 °C. XPS studies indicated that Ti is present in the form of TiO_2 on the surface. In addition, the

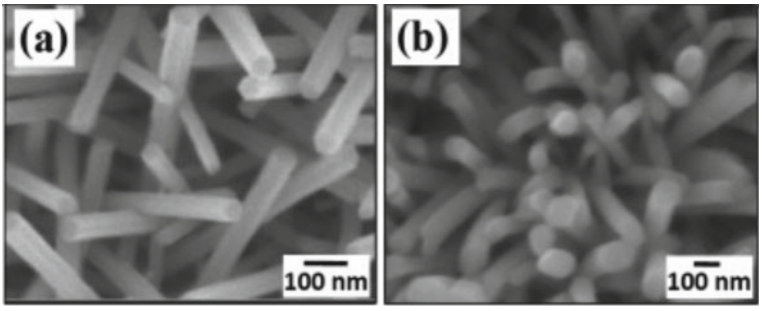

Fig. 11 **a–b** SEM images of the NO_2 sensor based on TiO_2/ZnO nanowires . (Reprinted with permission of [91])

detection of NO_2 was achieved with a faster response kinetics, in which the response and recovery times of 65 and 98 s, respectively, were obtained. Interestingly, the response parameters were considered independent of the NO_2 concentration; that is, no significant variation in the response/recovery times was observed for different gas concentrations. The results indicated that the TiO_2/ZnO NW heterostructure film is highly sensitive and selective for NO_2.

In the study developed by Frank et al. [88] TiO_2/La_2O_3 and TiO_2/CuO-La_2O_3 sensors were fabricated. The concept of sensor orthogonality was developed, which is a quantitative measure of how well the set of sensors can discriminate between the two gases of interest. This model was then used to extract the concentrations of CO and O_2 in a mixture of gases in the ranges of 2–10% O_2 and 250–1000 ppm of CO. The prediction capacity was considered reasonable in certain concentration ranges and was determined by the orthogonality of the sensor responses.

The monitoring of the CO_2 level, especially in closed spaces, is increasingly necessary in technological applications or human activities. Most data in the literature reveal CO_2 detection materials with high sensitivity above 300 °C, but Mardare et al. [92] investigated the CO_2 gas detection abilities close to room temperature and atmospheric pressure, using thin TiO_2 films doped with Cr. The increase in the percentage of Cr^{3+} increased the power of interaction with the adsorbed species (O_2 and/or CO_2).

Thangamani et al. [93]. recently reported the preparation of polyvinyl formal (PVF)/titanium dioxide (TiO_2) nanocomposite films. The results obtained in different analyzes confirmed that the TiO_2 NPs were finely dispersed in the PVF matrix and that there is good compatibility between the polymeric matrix and the nanocarrier. The chemo resistive sensor made from pure TiO_2 NPs exhibits a maximum sensitivity of 50.25% at 370 °C, while the PVF/TiO_2 nanocomposite sensor showed improved sensitivity: 83.75% at a relatively low operating temperature of 150 °C towards 600 ppm sulfur dioxide (SO_2). The PVF/TiO_2 nanocomposite film sensors manufactured on the work have the advantages of low energy consumption, cost-effectiveness and differentiated detection skills for SO_2 detection that enables potential applications. Thus, the experimental results showed excellent behavior in relation to the detection of SO_2 gas to control industrial processes and environmental monitoring applications.

Pan et al. [94] synthesized Pd-TiO_2 films by the technique of flame stabilization on rotating surface (FSRS) with different proportions of Pd doping. It was found that the TiO_2 particles prepared by the FSRS technique have diameters ranging from 9 to 17 nm and are of the anatase type. TiO_2 films doped with Pd remained porous anatase and the Pd element was well dispersed in the TiO_2 film. The detection test results demonstrated that the TiO_2 film nanosensors responded quickly to the change in the concentration of CO, while slightly slowly to the change in the concentration of NH_3. Pd doping remarkably improved the response sensitivity of the TiO_2 sensor for CO detection, and to some extent for NH_3.

Tong et al. [95] obtained a film of autonomous arrangement of TiO_2 nanotubes (TiNT) by a one-step anodizing method. The results of the characterization with SEM, TEM, XRD and EDX indicated that the main compound in the TiNT matrix

film was titania with anatase phase, and the average inner diameter of the nanotube was about 110 nm with a wall thickness of 16 nm and a layer thickness of 3.8 μm. Subsequently, the detection properties for H_2S of the TiNT-based gas sensor were investigated. The results showed that operating at 300 °C, the gas sensor had not only excellent reversibility, selectivity and stability, but also good linearity between the sensor response and the H_2S concentration. The excellent gas detection properties and the easy fabrication of the TiNT-based gas sensor have presented potential industrial applications in the future.

4 Conclusion

Due to the rapid technological development and the significant population expansion, there is an increasing search for alternative energy sources that can meet the energy demand and reduce the environmental problems caused by the use of non-renewable energy. Titanium dioxide has been widely used in the fields of solar cell, photocatalysis, gas sensor and batteries due to its low cost, high chemical stability and respect for the environment. In particular, TiO_2 nanostructures have gained much attention among researchers, as these nanomaterials improve the separation of charge carriers, increasing quantum efficiency, and, in addition, they can be explored in various morphologies, such as nanorods, nanotubes, nanofibers, nanowires, among others. TiO_2 nanostructures can also be combined with several other components and materials, such as graphene, making their applications in energy generation and storage promising.

Acknowledgements The authors would like to thank the Human Resources Program of the National Agency of Petroleum, Natural Gas and Biofuels (PRH-ANP 13.1; grant number 042319) for the financial support.

References

1. Acar, C., Dincer, I.: The potential role of hydrogen as a sustainable transportation fuel to combat global warming. Int. J. Hydrogen Energy (2018). https://doi.org/10.1016/j.ijhydene.2018.10.149
2. Staffell, I., Scamman, D., Velazquez Abad, A., Balcombe, P., Dodds, P.E., Ekins, P., Ward, K.R.: The role of hydrogen and fuel cells in the global energy system. Energy Environ. Sci. (2019). https://doi.org/10.1039/c8ee01157e
3. Brandon, N.P., Kurban, Z.: Clean energy and the hydrogen economy. Philosophical Trans. Royal Soc. A: Mathem. Phys. Eng. Sci. **375**(2098), 20160400 (2017). https://doi.org/10.1098/rsta.2016.0400
4. Nazir, S.M., Cloete, J.H., Cloete, S., Amini, S.: Pathways to low-cost clean hydrogen production with gas switching reforming. Int. J. Hydrogen Energy (2020). https://doi.org/10.1016/j.ijhydene.2020.01.234

5. Han, Z., Eisenberg, R.: Fuel from water: the photochemical generation of hydrogen from water. Acc. Chem. Res. **47**(8), 2537–2544 (2014). https://doi.org/10.1021/ar5001605
6. Jacoby, M.: Hydrogen from sun and water. Chem. Eng. News Archive **87**, 7 (2009). https://doi.org/10.1021/cen-v087n032.p007
7. Lousada, C.M., Johansson, A.J., Korzhavyi, P.A.: Thermodynamics of H_2O splitting and H_2 formation at the Cu(110)–water interface. J. Phys. Chem. C **119**(25), 14102–14113 (2015). https://doi.org/10.1021/acs.jpcc.5b01154
8. Hisatomi, T., Domen, K.: Reaction systems for solar hydrogen production via water splitting with particulate semiconductor photocatalysts. Nat. Catal. (2019). https://doi.org/10.1038/s41929-019-0242-6
9. Aslam, A., Mehmood, U., Arshad, M.H., Ishfaq, A., Zaheer, J., Ul Haq Khan, A., Sufyan, M.: Dye-sensitized solar cells (DSSCs) as a potential photovoltaic technology for the self-powered internet of things (IoTs) applications. Solar Energy **207**, 874–892 (2020). https://doi.org/10.1016/j.solener.2020.07.029
10. Li, Z., Yao, Z., Haidry, A.A., Plecenik, T., Xie, L., Sun, L., Fatima, Q.: Resistive-type hydrogen gas sensor based on TiO_2: a review. Int. J. Hydrogen Energy (2018). https://doi.org/10.1016/j.ijhydene.2018.09.051
11. Yu, X., Han, X., Zhao, Z., Zhang, J., Guo, W., Pan, C., Lin Wang, Z.: Hierarchical TiO_2 nanowire/graphite fiber photoelectrocatalysis setup powered by a wind-driven nanogenerator: a highly efficient photoelectrocatalytic device entirely based on renewable energy. Nano Energy **11**, 19–27 (2015). https://doi.org/10.1016/j.nanoen.2014.09.024
12. Nah, Y.-C., Paramasivam, I., Schmuki, P.: Doped TiO_2 and TiO_2 nanotubes: synthesis and applications. ChemPhysChem **11**(13), 2698–2713 (2010). https://doi.org/10.1002/cphc.201000276
13. Chen, Z., Han, S., Zhou, S., Feng, H., Liu, Y., Jia, G.: Review of health safety aspects of titanium dioxide nanoparticles in food application. NanoImpact 100224 (2020). https://doi.org/10.1016/j.impact.2020.100224
14. Yu, X., Lin, D., Li, P., Su, Z.: Recent advances in the synthesis and energy applications of TiO_2—graphene nanohybrids. Sol. Energy Mater. Sol. Cells **172**, 252–269 (2017). https://doi.org/10.1016/j.solmat.2017.07.045
15. Haider, A.J., Jameel, Z.N., Al-Hussaini, I.H.M.: Review on: titanium dioxide applications. Energy Procedia **157**, 17–29 (2019). https://doi.org/10.1016/j.egypro.2018.11.159
16. Gopinath, K.P., Madhav, N.V., Krishnan, A., Malolan, R., Rangarajan, G.: Present applications of titanium dioxide for the photocatalytic removal of pollutants from water: a review. J. Environ. Managem. **270**, 110906 (2020). https://doi.org/10.1016/j.jenvman.2020.110906
17. He, T., Zhao, H., Liu, Y., Zhao, C., Wang, L., Wang, H., … Wang, H.: Facile fabrication of superhydrophobic titanium dioxide-composited cotton fabrics to realize oil-water separation with efficiently photocatalytic degradation for water-soluble pollutants. Colloids Surf. A: Physicochem. Eng. Aspects 124080 (2019). https://doi.org/10.1016/j.colsurfa.2019.124080
18. Fiorenza, R., Sciré, S., D'Urso, L., Compagnini, G., Bellardita, M., Palmisano, L.: Efficient H_2 production by photocatalytic water splitting under UV or solar light over variously modified TiO_2-based catalysts, Int. J. Hydrog. Energy (2019). https://doi.org/10.1016/j.ijhydene.2019.04.035
19. Clark, R.J.H.: The chemistry of titanium and vanadium. In: An Introduction to the Chemistry of the Early Transition Elements. Amsterdam. New York Elsevier Pub. Co (1968)
20. Brown, W.D., Grannemann, W.W.: C-V characteristics of metal-titanium dioxide-silicon capacitors. Solid-State Electron. **21**(6), 837–846 (1978). https://doi.org/10.1016/0038-1101(78)90308-8
21. Regonini, D., Bowen, C.R., Jaroenworaluck, A., Stevens, R.: A review of growth mechanism, structure and crystallinity of anodized TiO_2 nanotubes. Mater. Sci. Eng. R. Rep. **74**(12), 377–406 (2013). https://doi.org/10.1016/j.mser.2013.10.001
22. Callister Jr, W.D.: Ciência e engenharia de materiais: uma introdução. Livros Técnicos e Científicos Editora LTC, 8°. ed., pp. 588–589. (2008)

23. Silva, F.L.R.: Síntese e Caracterização de Nanoestruturas à Base de Dióxido de Titânio. 2012. 102 f. Dissertação (Mestrado em Física)—Universidade Federal de Minas Gerais, Belo Horizonte (2012)
24. Zeng, L., Lu, Z., Li, M., Yang, J., Song, W., Zeng, D., Xie, C.: A modular calcination method to prepare modified N-doped TiO_2 nanoparticle with high photocatalytic activity. Appl. Catal. B **183**, 308–316 (2016). https://doi.org/10.1016/j.apcatb.2015.10.048
25. Ge, M., Cai, J., Iocozzia, J., Cao, C., Huang, J., Zhang, X., Lin, Z.: A review of TiO_2 nanostructured catalysts for sustainable H_2 generation. Int. J. Hydrogen Energy **42**(12), 8418–8449 (2017). https://doi.org/10.1016/j.ijhydene.2016.12.052
26. Opra, D.P., Gnedenkov, S.V., Sinebryukhov, S.L.: Recent efforts in design of TiO_2(B) anodes for high-rate lithium-ion batteries: a review. J. Power Sources **442**, 227225 (2019). https://doi.org/10.1016/j.jpowsour.2019.227225
27. Peighambardoust, N.S., Khameneh Asl, S., Maghsoudi, M.: The effect of doping concentration of TiO_2 nanotubes on energy levels and its direct correlation with photocatalytic activity. Thin Solid Films **690**, 137558 (2019). https://doi.org/10.1016/j.tsf.2019.137558
28. Yuan, B., Wang, Y., Bian, H., Shen, T., Wu, Y., Chen, Z.: Nitrogen doped TiO_2 nanotube arrays with high photoelectrochemical activity for photocatalytic applications. Appl. Surf. Sci. **280**, 523–529 (2013). https://doi.org/10.1016/j.apsusc.2013.05.021
29. Gao, J., Qiu, G., Li, H., Li, M., Li, C., Qian, L., Yang, B.: Boron-doped graphene/TiO_2 nanotube-based aqueous lithium-ion capacitors with high energy density. Electrochimica Acta, 135175(2019). https://doi.org/10.1016/j.electacta.2019.135175
30. Tang, Z.-R., Li, F., Zhang, Y., Fu, X., Xu, Y.-J.: Composites of titanate nanotube and carbon nanotube as photocatalyst with high mineralization ratio for gas-phase degradation of volatile aromatic pollutant. J. Phys. Chem. C **115**(16), 7880–7886 (2011). https://doi.org/10.1021/jp1115838
31. Awfa, D., Ateia, M., Fujii, M., Yoshimura, C. (2019). Novel magnetic carbon nanotube-tio_2 composites for solar light photocatalytic degradation of pharmaceuticals in the presence of natural organic matter. J. Water Process Eng. **31**, 100836 (2019). https://doi.org/10.1016/j.jwpe.2019.100836
32. Low, F.W., Lai, C.W.: Recent developments of graphene-TiO_2 composite nanomaterials as efficient photoelectrodes in dye-sensitized solar cells: a review. Renew. Sustain. Energy Rev. **82**, 103–125 (2018). https://doi.org/10.1016/j.rser.2017.09.024
33. Cho, E.-C., Ciou, J.-H., Zheng, J.-H., Pan, J., Hsiao, Y.-S., Lee, K.-C., Huang, J.-H.: Fullerene C_{70} decorated TiO_2 nanowires for visible-light-responsive photocatalyst. Appl. Surf. Sci. **355**, 536–546 (2015). https://doi.org/10.1016/j.apsusc.2015.07.062
34. González, A., Goikolea, E., Barrena, J.A., Mysyk, R.: Review on supercapacitors: technologies and materials. Renew. Sustain. Energy Rev. **58**, 1189–1206 (2016). https://doi.org/10.1016/j.rser.2015.12.249
35. Panda, P.K., Grigoriev, A., Mishra, Y.K., Ahuja, R.: Progress in supercapacitors: roles of two dimensional nanotubular materials. Nanoscale Adv. (2019). https://doi.org/10.1039/c9na00307j
36. Mensah-Darkwa, K., Zequine, C., Kahol, P., Gupta, R.: Supercapacitor energy storage device using biowastes: a sustainable approach to green energy. Sustainability **11**(2), 414 (2019). https://doi.org/10.3390/su11020414
37. Sharma, P., Bhatti, T.S.: A review on electrochemical double-layer capacitors. Energy Convers. Manage. **51**(12), 2901–2912 (2010). https://doi.org/10.1016/j.enconman.2010.06.031
38. Jiang, L., Tian, H., Shen, W., Wang, Y., Ma, Y., Hou, P., Wu, Y., Xiang, P., Xiao, T., Tan, X.: N-doped TiO_2 hierarchical microspheres as electrode for high-performance supercapacitors. Mater. Lett. 295 (2021). https://doi.org/10.1016/j.matlet.2021.129840
39. Su, X., He, Q., Yang, Y., Cheng, G., Dang, D., Yu, L.: Free-standing nitrogen-doped TiO_2 nanorod arrays with enhanced capacitive capability for supercapacitors. Diamond Related Mater. 114 (2021). https://doi.org/10.1016/j.diamond.2020.108168
40. Huang, Q., Li, J., Wei, W., Wu, Y., Li, T.: Synthesis, characterization and application of TiO_2/Ag recyclable SERS substrates. RSC Adv. **7**(43), 26704–26709 (2017). https://doi.org/10.1039/c7ra03112b

41. Rajangam, K., Amuthameena, S., Thangavel, S., Sanjanadevi, V.S., Balraj, B.: Synthesis and characterisation of Ag incorporated TiO_2 nanomaterials for supercapacitor applications. J. Molecular Struct. 128661 (2020). https://doi.org/10.1016/j.molstruc.2020.128661
42. Faninger, G.: The Potential of Solar Heat in the Future Energy System. IFF-University of Klagenfurt, Austria, Faculty for Interdisciplinary Research and Continuing Education (2010)
43. Shakeel Ahmad, M., Pandey, A.K., Abd Rahim, N.: Advancements in the development of TiO_2 photoanodes and its fabrication methods for dye sensitized solar cell (DSSC) applications. a review. Renew. Sustain. Energy Rev. **77**, 89–108 (2017). https://doi.org/10.1016/j.rser.2017.03.129
44. Gong, J., Liang, J., Sumathy, K.: Review on dye-sensitized solar cells (DSSCs): fundamental concepts and novel materials. Renew. Sustain. Energy Rev. **16**(8), 5848–5860 (2012). https://doi.org/10.1016/j.rser.2012.04.044
45. Gong, J., Sumathy, K., Qiao, Q., Zhou, Z.: Review on dye-sensitized solar cells (DSSCs): Advanced techniques and research trends. Renew. Sustain. Energy Rev. **68**, 234–246 (2017). https://doi.org/10.1016/j.rser.2016.09.097
46. Şenol, D., Kaya, İ: Synthesis and characterizations of poly(phenoxy-imine)s via catalyzed oxidative polymerization by polymer-metal complex. Arab. J. Sci. Eng. **42**(6), 2381–2396 (2017). https://doi.org/10.1007/s13369-016-2390-1
47. Kim, H.-S., Chun, M.-H., Suh, J., Jun, B.-H., Rho, W.-Y.: Dual functionalized freestanding TiO_2 nanotube arrays coated with Ag nanoparticles and carbon materials for dye-sensitized solar cells. Appl. Sci. **7**(6), 576 (2017). https://doi.org/10.3390/app7060576
48. O'Regan, B., Grätzel, M.: A low-cost, high-efficiency solar cell based on dye-sensitized colloidal TiO_2 films. Nature **353**(6346), 737–740 (1991). https://doi.org/10.1038/353737a0
49. Dewalque, J., Cloots, R., Mathis, F., Dubreuil, O., Krins, N., Henrist, C.: TiO_2 multilayer thick films (up to 4 μm) with ordered mesoporosity: influence of template on the film mesostructure and use as high efficiency photoelectrode in DSSCs. J. Mater. Chem. **21**(20), 7356 (2011). https://doi.org/10.1039/c1jm10288e
50. Madurai Ramakrishnan, V., N., M., P., B., Pitchaiya, S., Velauthapillai, D., Pugazhendhi, A.: Transformation of TiO_2 nanoparticles to nanotubes by simple solvothermal route and its performance as dye-sensitized solar cell (DSSC) photoanode. Int. J. Hydrog. Energy (2020). https://doi.org/10.1016/j.ijhydene.2020.04.021
51. Yun, J.-H., Mozer, A.J., Wagner, P., Offier, D.L., Amal, R., Ng, Y.H.: Light soaking effect driven in porphyrin dye-sensitized solar cells using 1D TiO_2 nanotube photoanodes. Sustain. Mater. Technol. e00165 (2020). https://doi.org/10.1016/j.susmat.2020.e00165
52. Nguyen, H.H., Gyawali, G., Martinez-Oviedo, A., Kshetri, Y.K., Lee, S.W.: Physicochemical properties of Cr-doped TiO_2 nanotubes and their application in dye-sensitized solar cells. J. Photochem. Photobiol. A: Chem. 112514 (2020). https://doi.org/10.1016/j.jphotochem.2020.112514
53. Liu, C., Li, T., Zhang, Y., Kong, T., Zhuang, T., Cui, Y., Li, C.: Silver nanoparticle modified TiO_2 nanotubes with enhanced the efficiency of dye-sensitized solar cells. Microporous Mesoporous Mater. **287**, 228–233 (2019). https://doi.org/10.1016/j.micromeso.2019.06.011
54. Arifin, K., Yunus, R.M., Minggu, L.J., Kassim, M.B.: Improvement of TiO_2 nanotubes for photoelectrochemical water splitting: review. Int. J. Hydrog. Energy (2020). https://doi.org/10.1016/j.ijhydene.2020.11.063
55. Oliveira, S.M.: Produção fotocatalítica de hidrogênio utilizando catalisadores baseados no dióxido de titânio. 2015. 93 f. Dissertação (Mestrado em Ciências Exatas e da Terra)—Universidade Federal de Uberlândia, Uberlândia (2015)
56. Hydrogen Fuel Basics (2021). https://www.energy.gov/eere/fuelcells/hydrogen-fuel-basics. Online may 2021
57. Guaglianoni, W.C.: Nanoarquiteturas de nanotubos de carbono e nanotubos de tio_2 dopados com cobalto: síntese, caracterização microestrutural e de propriedades fotoeletroquímicas para aplicação na produção de H_2 por water splitting. 2019. 83 f. Tese (Doutorado em Ciência e Tecnologia dos Materiais)—Faculdade de Engenharia. Universidade Federal do Rio Grande do Sul, Porto Alegre (2019)

58. Fujishima, A., Honda, K.: Electrochemical photolysis of water at a semiconductor electrode. Nature **238**(5358), 37–38 (1972). https://doi.org/10.1038/238037a0
59. Shankar, K., Mor, G.K., Prakasam, H.E., Yoriya, S., Paulose, M., Varghese, O.K., Grimes, C.A.: Highly-ordered TiO_2 nanotube arrays up to 220 μm in length: use in water photoelectrolysis and dye-sensitized solar cells. Nanotechnology **18**(6), 065707 (2007). https://doi.org/10.1088/0957-4484/18/6/065707
60. Ismael, M.: A review and recent advances in solar-to-hydrogen energy conversion based on photocatalytic water splitting over doped-TiO_2 nanoparticles. Sol. Energy **211**, 522–546 (2020). https://doi.org/10.1016/j.solener.2020.09.073
61. Shwetha, R.R., Mohan, S., Fernando, C.A.N., Binas, V., Balakrishna, G.R.: Recent advances and strategies applied to tailor energy levels, active sites and electron mobility in titania and its doped/composite analogues for hydrogen evolution in sunlight. Catal. Sci. Technol. (2018). https://doi.org/10.1039/c8cy01395k
62. Sánchez-Tovar, R., Blasco-Tamarit, E., Fernández-Domene, R.M., Villanueva-Pascual, M., García-Antón, J.: Electrochemical formation of novel TiO_2-ZnO hybrid nanostructures for photoelectrochemical water splitting applications. Surf. Coatings Technol. 125605 (2020).https://doi.org/10.1016/j.surfcoat.2020.125605
63. Shen, S., Chen, J., Wang, M., Sheng, X., Chen, X., Feng, X., Mao, S.S.: Titanium dioxide nanostructures for photoelectrochemical applications. Prog. Mater Sci. **98**, 299–385 (2018). https://doi.org/10.1016/j.pmatsci.2018.07.006
64. Bashiri, R., Irfan, M.S., Mohamed, N.M., Sufian, S., Ling, L.Y., Suhaimi, N.A., Samsudin, M.F.R.: Hierarchically $SrTiO_3$@TiO_2@Fe_2O_3 nanorod heterostructures for enhanced photoelectrochemical water splitting. Int. J. Hydrog. Energy (2020). https://doi.org/10.1016/j.ijhydene.2020.02.106
65. Barakat, N.A.M., Erfan, N.A., Mohammed, A.A., Mohamed, S.E.I.: Ag-decorated TiO_2 nanofibers as Arrhenius equation-incompatible and effective photocatalyst for water splitting under visible light irradiation. Colloids Surf. A: Physicochem. Eng. Aspects 125307 (2020).https://doi.org/10.1016/j.colsurfa.2020.125307
66. Camposeco, R., Castillo, S., Navarrete, J., Gomez, R.: Synthesis, characterization and photocatalytic activity of TiO_2 nanostructures: nanotubes, nanofibers, nanowires and nanoparticles. Catal. Today **266**, 90–101 (2016). https://doi.org/10.1016/j.cattod.2015.09.018
67. Venturini, J., Bonatto, F., Guaglianoni, W.C., Lemes, T., Arcaro, S., Kopp Alves, A., Bergmann, C. P.: Cobalt-doped titanium oxide nanotubes grown via one-step anodization for water splitting applications. Appl. Surf. Sci. (2018). https://doi.org/10.1016/j.apsusc.2018.09.093
68. Guaglianoni, W C., Ruwer, T.L., Caldeira, L.E.N., Wermuth, T.B., Venturini, J., Bergmann, C.P.: Single-step synthesis of Fe-TiO_2 nanotube arrays with improved light harvesting properties for application as photoactive electrodes. Mater. Sci. Eng.: B **263**, 114896 (2021). https://doi.org/10.1016/j.mseb.2020.114896
69. Garcia, A.P., Guaglianoni, W.C., Garcia, D.R., Soares, L.G., de Oliveira Vaz, M., Teixeira, S.R., Bergmann, C.P.: Facile synthesis by peroxide method and microwave-assisted hydrothermal treatment of TiO_2 with high photocatalytic efficiency for dye degradation and hydrogen production. ChemistrySelect **3**(41), 11454–11459 (2018). https://doi.org/10.1002/slct.201802188
70. Costa, R.C.: Reciclagem de baterias de íons de lítio por processamento mecânico. Dissertação (Mestrado em Engenharia)—Programa de pós graduação em Engenharia de Minas, Metalúrgica e Materiais PPGE3M, Universidade Federal do Rio Grande do Sul (2010)
71. Paulino, J.F., Busnardo, N.G., Afonso, J.C.: Processamento de pilhas Li/MnO_2 usadas. Quim. Nova **30**(3), 718–722 (2007). https://doi.org/10.1590/s0100-40422007000300036
72. O Desafio de reciclar baterias de veículos elétricos (2021). https://www.dw.com/pt-br/o-desafio-de-reciclar-baterias-de-ve%C3%ADculos-el%C3%A9tricos/a-52178600. Online may 2021
73. Papp, J.K., Li, N., Kaufman, L.A., Naylor, A.J., Younesi, R., Tong, W., McCloskey, B.D.: A comparison of high voltage outgassing of $LiCoO_2$, $LiNiO_2$, and Li_2MnO_3 layered li-ion cathode materials. Electrochimica Acta 137505 (2020).https://doi.org/10.1016/j.electacta.2020.137505

74. Luo, F., Wei, C., Zhang, C., Gao, H., Niu, J., Ma, W., Zhang, Z.: Operando X-ray diffraction analysis of the degradation mechanisms of a spinel $LiMn_2O_4$ cathode in different voltage windows. J. Energy Chem. (2019).https://doi.org/10.1016/j.jechem.2019.09.011
75. Chemere, E.B., Wang, F.-M., Chien, W.-C.: Improvement in the electrochemical stability of $Li[Ni_{0.5}Co_{0.2}Mn_{0.3}]O_2$ as a lithium-ion battery cathode electrode with the surface coating of branched oligomer. Surf. Coatings Technol. 126121 (2020). https://doi.org/10.1016/j.surfcoat.2020.126121
76. Zheng, J., Yang, Z., He, Z., Tong, H., Yu, W., Zhang, J.: In situ formed $LiNi_{0.8}Co_{0.15}Al_{0.05}O_2@Li_4SiO_4$ composite cathode material with high rate capability and long cycling stability for lithium-ion batteries. Nano Energy (2018). https://doi.org/10.1016/j.nanoen.2018.09.014
77. Ayuso, P., Beltran, H., Segarra-Tamarit, J., Pérez, E.: Optimized profitability of LFP and NMC Li-ion batteries in residential PV applications. Math. Comput. Simul. (2020). https://doi.org/10.1016/j.matcom.2020.02.011
78. Curcio, M., De Bonis, A., Brutti, S., Santagata, A.: Pulsed laser deposition of thin films of TiO_2 for Li-ion batteries. Appl. Surf. Sci. Adv. **4**(2021). https://doi.org/10.1016/j.apsadv.2021.100090
79. Guo, Y.-G., Hu, Y.-S., Sigle, W., Maier, J.: Superior electrode performance of nanostructured mesoporous TiO_2 (Anatase) through efficient hierarchical mixed conducting networks. Adv. Mater. **19**(16), 2087–2091 (2007). https://doi.org/10.1002/adma.200602828
80. Li, W., Wang, F., Liu, Y., Wang, J., Yang, J., Zhang, L., Zhao, D.: General strategy to synthesize uniform mesoporous TiO_2/Graphene/Mesoporous TiO_2 Sandwich-Like Nanosheets for highly reversible lithium storage. Nano Lett. **15**(3), 2186–2193 (2015). https://doi.org/10.1021/acs.nanolett.5b00291
81. Hou, J., Ren, Y., Xue, Y., Liu, Y., Guo, S.: Sulfur/nitrogen dual-doped three-dimensional reduced graphene oxide modified with mesoporous TiO_2 nanoparticles for promising lithium-ion battery anodes. J. Alloys Compounds **868**(2021). https://doi.org/10.1016/j.jallcom.2021.159183
82. Guo, J., Li, Y., Li, S., Cui, X., Liu, Y., Huang, W., Zhang, X.: One-step fabrication of TiO_2/graphene hybrid mesoporous film with enhanced photocatalytic activity and photovoltaic performance. Chin. J. Catal. **41**(8), 1208–1216 (2020). https://doi.org/10.1016/s1872-2067(19)63511-4
83. Wang, Y., An, N., Wen, L., Wang, L., Jiang, X., Hou, F., Liang, J.: Recent progress on the recycling technology of Li-ion batteries. J. Energy Chem. (2020). https://doi.org/10.1016/j.jechem.2020.05.008
84. Mazurek, K., Weidner, E., Drużyński, S., Ciesielczyk, F., Kiełkowska, U., Wróbel-Kaszanek, A., Jesionowski, T.: Lanthanum enriched TiO_2–ZrO_2 hybrid material with tailored physicochemical properties dedicated to separation of lithium and cobalt (II) raising from the hydrometallurgical stage of the recycling process of lithium-ion batteries. Hydrometallurgy 105448 (2020). https://doi.org/10.1016/j.hydromet.2020.105448
85. Bai, J., Zhou, B.: Titanium dioxide nanomaterials for sensor applications. Chem. Rev. **114**(19), 10131–10176 (2014). https://doi.org/10.1021/cr400625j
86. Simonetti, E., Oliveira, T., Machado, A., Silva, A., Santos, A.: TiO_2 as a gas sensor: the novel carbon structures and noble metals as new elements for enhancing sensitivity—a review. Ceramics Int (2021). https://doi.org/10.1016/j.ceramint.2021.03.189
87. Hsu, K.-C., Fang, T.-H., Hsiao, Y.-J., Wu, P.-C.: Response and characteristics of TiO_2/perovskite heterojunctions for CO gas sensors. J. Alloys Compounds (2019). https://doi.org/10.1016/j.jallcom.2019.04.238
88. Frank, M.L., Fulkerson, M.D., Patton, B.R., Dutta, P.K.: TiO_2 based sensor arrays modeled with nonlinear regression analysis for simultaneously determining CO and O_2 concentrations at high temperatures. Sensors and Actuators: B Chemical, **87**(3), 471–479 (2002). https://doi.org/10.1016/s0925-4005(02)00296-4
89. Singh, P., MAbdullah, M., Sagadevan, S., Kaur, C., Ikram, S.: Highly sensitive ethanol sensor based on TiO_2 nanoparticles and its photocatalyst activity. Optik (2019). https://doi.org/10.1016/j.ijleo.2019.01.077

90. Seekaew, Y., Wisitsoraat, A., Phokharatkul, D., Wongchoosuk, C.: Room temperature toluene gas sensor based on TiO_2 nanoparticles decorated 3D graphene-carbon nanotube nanostructures. Sens. Actuators, B Chem. **279**, 69–78 (2019). https://doi.org/10.1016/j.snb.2018.09.095
91. Ramgir, N., Bhusari, R., Rawat, N.S., Patil, S.J., Debnath, A.K., Gadkari, S.C., Muthe, K.P.: TiO_2/ZnO heterostructure nanowire based NO_2 sensor. Mater. Sci. Semiconduct. Process. **106**(2020). https://doi.org/10.1016/j.mssp.2019.104770
92. Mardare, D., Cornei, N., Mita, C., Florea, D., Stancu, A., Tiron, V., Adomnitei, C.: Low temperature TiO_2 based gas sensors for CO_2. Ceram. Int. **42**(6), 7353–7359 (2016). https://doi.org/10.1016/j.ceramint.2016.01.137
93. Thangamani, G.J., Pasha, S.K.K.: Titanium dioxide (TiO_2) nanoparticles reinforced polyvinyl formal (PVF) nanocomposites as chemiresistive gas sensor for sulfur dioxide (SO_2) monitoring. Chemosphere. **275** (2021). https://doi.org/10.1016/j.chemosphere.2021.129960
94. Pan, F., Lin, H., Zhai, H., Miao, Z., Zhang, Y., Xu, K., Zhang, H.: Pd-doped TiO_2 film sensors prepared by premixed stagnation flames for CO and NH_3 gas sensing. Sens. Actuators, B Chem. **261**, 451–459 (2018). https://doi.org/10.1016/j.snb.2018.01.173
95. Tong, X., Shen, W., Chen, X., Corriou, J.-P.: A fast response and recovery H_2S gas sensor based on free-standing TiO_2 nanotube array films prepared by one-step anodization method. Ceram. Int. **43**(16), 14200–14209 (2017). https://doi.org/10.1016/j.ceramint.2017.07.165

Nanostructured Catalysts for Biomass Gasification

Márcia Cristina dos Santos, Tania Maria Basegio, Luís António da Cruz Tarelho, and Carlos Pérez Bergmann

Abstract This chapter presents studies on nanostructured catalysts used in biomass gasification processes. Initially, an overview of gasification is presented, as well as the characteristics of the process and equipment. Some studies from the literature are discussed, with examples of nanocatalysts used to remove tar in gasification. The synthesis processes, characterizations, and efficiencies of these catalysts are shown.

Keywords Nanocatalysts · Catalysts nanostructured · Biomass · Gasification · Tar removal

Abbreviations

PAH	Polycyclic aromatic hydrocarbon
SCWG	Supercritical water gasification

1 Introduction

Gasification is a process that consists of the thermochemical conversion of biomass into a combustible gaseous product through the supply of a gasification agent. This gasification agent is a gaseous compound, which can be atmospheric air, oxygen, water vapor, and mixtures of the above. Gasification is recognized as a process with numerous environmental and social advantages since it is an alternative for the valorization of waste (biomass), obtaining a renewable fuel that can be used to replace fossil fuels in selected applications [1].

M. C. dos Santos (✉) · T. M. Basegio · C. P. Bergmann
Universidade Federal do Rio Grande do Sul, Porto Alegre, Brazil

L. A. da Cruz Tarelho
Universidade de Aveiro, Aveiro, Portugal

A. Kopp Alves (ed.), *Environmental Applications of Nanomaterials*, Engineering Materials, https://doi.org/10.1007/978-3-030-86822-2_6

The gaseous compounds generated by the gasification process depend on several factors, such as characteristics of the biomass used and operational conditions of the process (temperature, equivalence ratio, type of reactor). From this process, a mixture of gases is obtained, which include carbon dioxide, water, carbon monoxide, hydrogen, light hydrocarbons, as well as ash and slag. The feedstock and gasification agent together with the process conditions that minimize the formation of tar need to be optimized in order to generate a gas rich in hydrogen and carbon monoxide, and with good calorific value.

Tar consists of a mixture of heavy hydrocarbons generated in the process. In addition, to reduce the calorific value of the gas obtained, the tar can also cause problems of clogging, fouling and pollutant emissions during the use of the gas in combustion systems [2].

Tar is among the most relevant drawbacks found during biomass gasification. The elimination of this technological barrier is the focus of many studies, which comprise primary or secondary measures (see Fig. 1). Primary measures consist of processes carried out inside the gasification reactor (alteration of operating parameters, use of catalysts, changes in the reactor design), while secondary measures are performed downstream the gasification reactor, and can include gas scrubbing or catalytic processes. In general, studies with catalysts are focused on obtaining suitable materials capable of destroying the tar, and for which can be minimized the deactivated by carbon deposition, contamination and microstructural changes, in addition to problems related to erosion [1].

For a catalyst to have good potential for tar destruction, a relevant property is a high specific surface area, to provide a large contact surface for the reaction of transforming the tar into light hydrocarbons, H_2 and CO. In addition, it must have low cost, low-pressure drop, ease of obtaining and operation, and resistance to the temperatures of the process, which, in general, are around 800–1200 °C [4].

The gasification process can be developed in distinct types of reactors, and the most common include the fixed bed (e.g., downdraft, updraft, cross-draft), fluidized beds (e.g., bubbling fluidized bed and circulating fluidized bed) and entrained flow reactor [5].

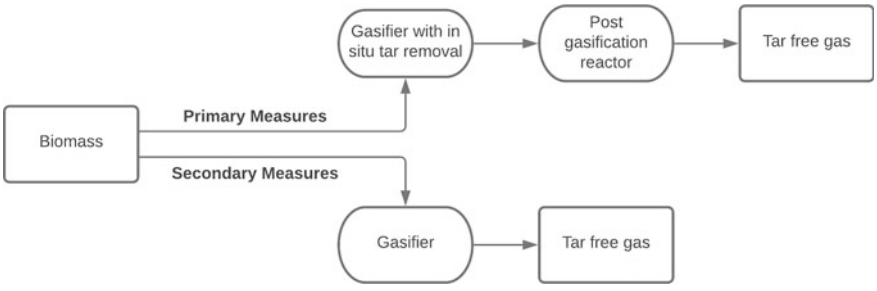

Fig. 1 Scheme of primary and secondary measures for tar reduction and removal (Reprinted adapted with permission [3])

The gasifier capacity range and the amount of tar produced vary by each type of gasifier configuration. In general, downdraft fixed bed gasifiers are used in smaller scale applications, and produce a good syngas quality with low tar content (around 0.1 $g \cdot m^3$). In contrast, updraft fixed bed gasifiers are not attractive due to the high tar levels generated (10 to 100 $g \cdot m^3$). Fluidized bed gasifiers can be used in large installations and for processes with high daily quantities, generating an intermediate amount of tar (from 1 to 10 $g \cdot m^3$) [4].

2 Tar Compounds in Biomass Gasification

As seen previously, the formation of tar is a limiting factor for the gasification process, which makes the study of its removal or reduction so important. Tar is a black, sticky, and viscous liquid, formed by a complex mixture of aromatic hydrocarbons that condense in the cooler areas of the gasifier [3].

The formation of tar as a byproduct of the gasification process decreases the efficiency of the process and limits the subsequent applications of the obtained products [6], in addition to causing clogging and incrustations in the gasifier.

The formed tar can be classified as primary, secondary, and tertiary, depending on the process conditions in which it is formed. Primary tar is produced at lower temperatures, from 200 to 500 °C, and contains significant amounts of oxygen. At temperatures above 500 °C, the components start to become heavier molecules called secondary and tertiary tar, which are formed by the recombination of fragments of the primary tar, with the removal of oxygen [2, 3].

The composition of the tar depends on several factors, as mentioned before. Figure 2 shows an example of a typical composition of biomass tar.

There are several factors that can reduce the formation of tar. According to a study by Rabou et al. [2], a higher moisture content of the feedstock, an increase in the gas residence time in hot areas of the gasifier, a higher temperature and the addition of olivine or dolomite to the reactor bed are factors that decrease the amount of tar produced during the gasification process.

Once formed, the tar can be removed in post gasification, either by physical removal or by cracking. Physical removal consists of using filters, cyclones, electrostatic precipitators, particulate scrubbers or alkaline salts, and is similar to removing dust particles from a flue gas. The choice of the physical method to be used will depend on the concentration and size distribution of the incoming particles (which is difficult to measure), in addition to the tolerance of residual particles for the subsequent application of the gas [3].

Cracking removal can be thermal or catalytic, and consists, respectively, of heating the tar to high temperatures (around 1200 °C) or exposing it to catalysts at lower temperatures (approximately 800 °C). Rabou et al. [2] tested the thermal cracking of tar on laboratory scale and analyzed the effect of different temperatures and different residence times of the gas in the reactor, observing a high reduction in the concentration of tar for higher temperatures and residence times (Fig. 3).

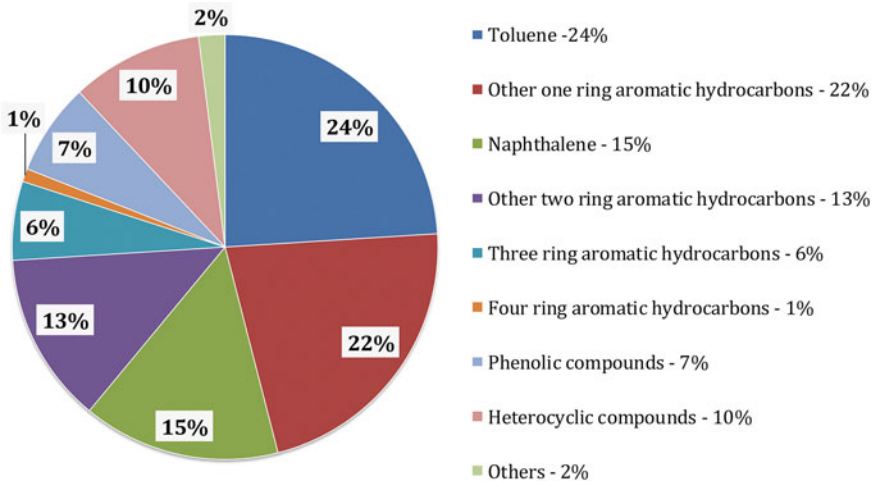

Fig. 2 Typical tar composition (Reprinted with permission [7])

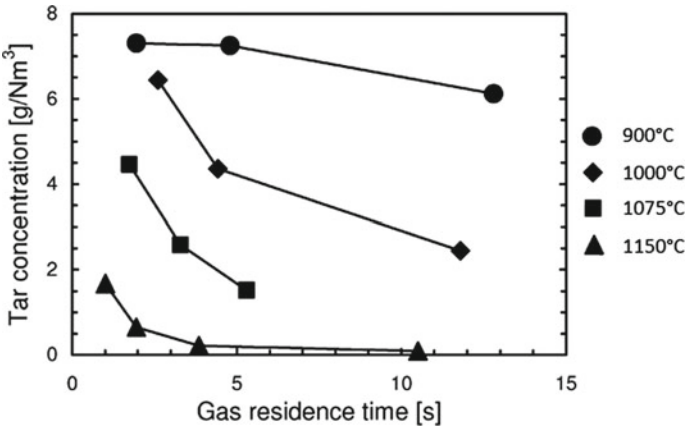

Fig. 3 Effect of temperature and residence time on the tar removal by thermal cracking (Reprinted adapted with permission [2])

3 Catalysts for Tar Destruction in Biomass Gasification

The catalytic processes for removing tar occur by the addition of a catalyst to break the bonds of the tar macromolecules. When compared to thermal cracking, this process has the advantage of causing reactions to occur at lower temperatures [6].

The development of catalysts that have ideal characteristics for the process has been carried out, and this includes materials that are stable at high temperatures, do not undergo deactivation by coke and H_2S poisoning, have adequate resistance to

Table 1 Examples of materials used as catalysts in gasification processes

Material	References
Dolomite ($CaMg(CO_3)_2$)	[8]
Olivine ($(Mg, Fe)_2SiO_4$)	[8]
Bed bottom particles resulting from the combustion of forest biomass	[1]
Char particles derived from the wood pellets gasification process	[1]
Synthetic fayalite (Fe_2SiO_4)	[1]
Alkali-feldspar ore (general formula (K, Na) $AlSi_3O_8$)	[9]
Natural ilmenite ($FeTiO_3$)	[10]
Concrete	[11]
Iron and nickel-based catalysts	[12]
Calcium oxide-based catalysts	[13]

friction, are easily regenerated, have good activity and high efficiency in tar cracking, are not environmentally toxic, in addition to commercially available and at low cost [7].

Some examples of materials used as catalysts in gasification processes that were already described in the literature are displayed in Table 1.

Other type of catalyst with improved functionalities include the nanomaterials, and this subject will be analyzed in the following sections.

3.1 Modified Char-Supported Ni–Fe Catalyst

Lin et al. [6] studied the synthesis of a modified char-supported Ni–Fe catalyst, and obtained a high reduction in the amount of PAH in the tar, due to the good activity of this metallic alloy in the cleavage of the macromolecules present.

The synthesis of this catalyst was carried out via hydrothermal carbonization. $FeCl_3$ and $NiCl_2$ solutions were mixed in different proportions, stirred with sawdust and taken to a hydrothermal autoclave reactor for hydrothermal carbonization (reaction temperature of 200 °C and time of 4 h). The resulting product was cooled, filtered, dried, and calcined in a tubular oven at 700 °C for 1 h in an N_2 atmosphere, thus obtaining the catalyst.

The presence of metal chlorides in the char during the thermal treatment carried out, caused the formation of a porous carbon structure in the nucleus, and a dense layer of carbon nanofibers of different morphologies. In addition, it was observed that the Ni–Fe alloy was well dispersed in the carbon matrix. It was possible to notice that the Ni/Fe molar ratio directly influenced the length and diameter of the carbon nanofibers formed, and the increase in this ratio made the fibers longer, sparser and with a smaller diameter.

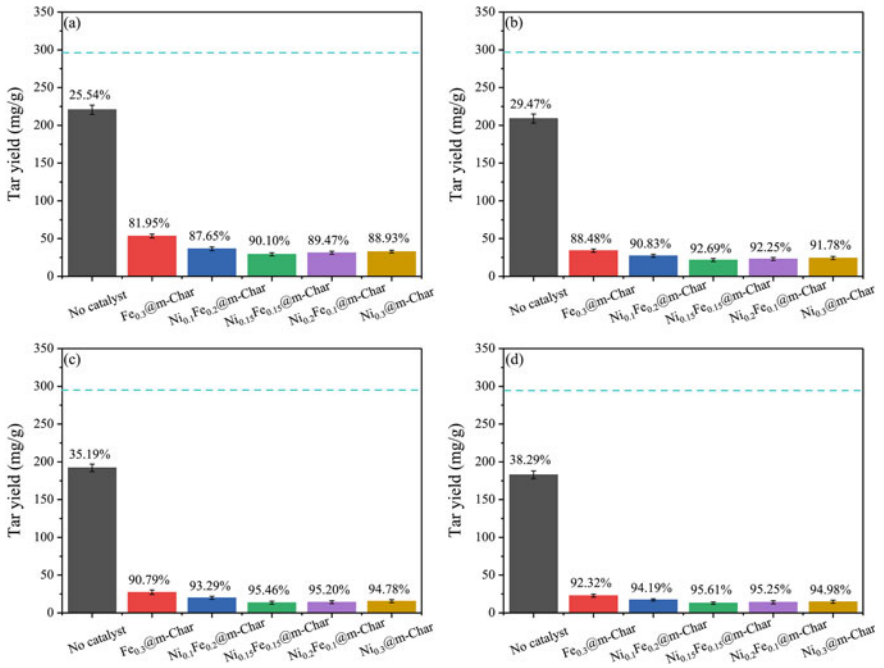

Fig. 4 Tar yield ($mg \cdot g^{-1}$ biomass) and tar conversion efficiency, with the names of the catalysts referring to the concentration of Ni^{2+} and Fe^{3+} (in $mol \cdot L^{-1}$) used in the preparation of the material, at different catalytic cracking temperatures **a** 600 °C, **b** 650 °C, **c** 700 °C and **d** 750 °C (Reprinted with permission [6])

The efficiency of catalytic cracking with modified char-supported Ni–Fe catalyst is shown in Fig. 4, with tests at different temperatures. An increase in temperature, even without using a catalyst, leads to a decrease in the amount of tar, which can be explained by the cleavage of macromolecule bonds due to thermal cracking. With the presence of catalysts, the best conversion efficiency of 95.46% was obtained, at a temperature of 700 °C, with a catalyst prepared with a solution of char and a concentration of 0.15 $mol \cdot L^{-1}$ of Ni^{2+} and 0.15 $mol \cdot L^{-1}$ of Fe^{3+}. The best performance of this catalyst is due to the hierarchical pore structures with a larger surface area (460.61 $m^2 \cdot g^{-1}$), when compared to others with different Ni–Fe molar ratios.

3.2 Graphene-Supported Metal Nanoparticles Catalysts

Samiee-Zafarghandi et al. [14] studied the use of various graphene-supported metal nanoparticles as catalysts in supercritical water gasification (SCWG) processes. This process consists of a technology that uses wet biomass to produce gases with good calorific value (H_2 and CH_4). The supercritical conditions of the water reduce the

dielectric constant, increase the dissolution capacity of organic compounds and generate an adequate medium for the occurrence of free radical reactions, which is still maximized with the use of catalysts and with the increase of the temperature.

Powdered graphite oxide obtained by the Hummers method [15], was subjected to ultrasound and the resulting dispersion was kept under agitation. Separately, solutions of metals (Cu, Ni, Co, Cr and Mn) were prepared from metallic nitrates (20% by weight), and added slowly to the dispersion of graphene. Afterward, urea was added as a precipitant, and the system was heated to 80 °C and stirred for 2 h. Then, cooling, washing with water and ethanol, centrifugation and finally vacuum drying at 300 °C for 2 h to dry the catalyst and to reduce the graphite oxide. The average sizes of metallic particles deposited on the graphite oxide surface obtained were 38.4, 37.4, 27.7, 25.0, and 21.8 nm for Cu, Cr, Mn, Co, and Ni, respectively.

The effects of the obtained catalysts, their quantities and the process temperature were tested in the SCWG process of *chlorella sp.* Microalgae, and the results are shown in Fig. 5.

The best results obtained were for the graphene-supported nickel nanoparticles catalyst, which decreased the formation of tar and solid phase, in addition to increasing the production of H_2. The Mn catalyst, on the other hand, demonstrated to have weak activity for the SCWG process. The increase in the amount of Ni catalyst increased the production of H_2 and the conversion of biomass, generating a fewer number of byproducts. Regarding the temperature, with its increase, the amount of tar produced is reduced.

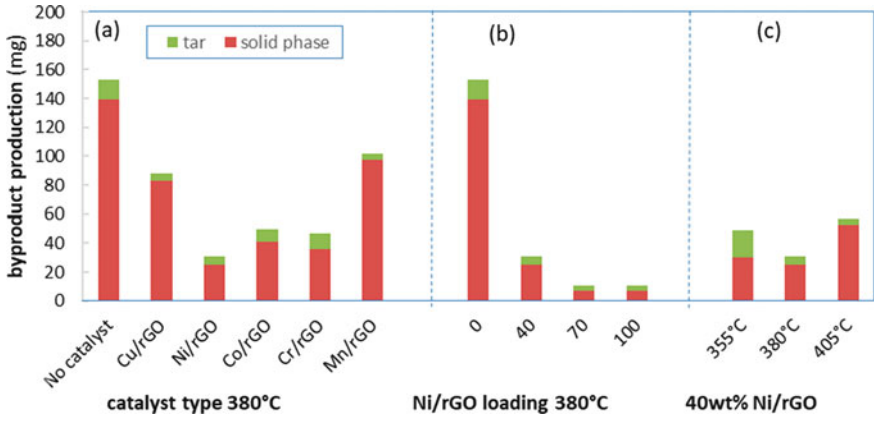

Fig. 5 Byproducts quantification obtained in the SCWG process under different conditions **a** effect of catalyst type, **b** effect of catalyst loading and **c** effect of temperature (Reprinted with permission [14])

3.3 Nanostructured Ni-Co/Si-P Catalyst

Kannaiyan et al. [16] investigated the synthesis and performance of a low-cost and environmentally friendly bimetallic nanocatalyst based on Ni-Co/Si-P for applying in gasification processes to mitigate the production of tar.

Nickel-based catalysts are widely used in tar cracking, as they have a strong ability to break the C–C bond of tar compounds, while cobalt carries electrons of the unpaired "f" sublevel, through which it chemically adsorbs oxygen, and can be used for oxidation. These two metals were supported on a silicophosphate base.

The studied catalyst was synthesized using the deposition–precipitation method, described by Kannaiyan [16], from $Ni(NO_3)_2.6H_2O$ and $Co(NO_3)_3.6H_2O$ with a molar ratio of 0.15 and 0.05, respectively. After the process of precipitation of metal ions as hydroxides in the particles of silicophosphates, the sample was filtered, dried in a hot air oven at 120 °C for 2 h and underwent a heat treatment of calcination in a muffle for 6 h, with a rate of heating of 20 °C·min^{-1}. The resulting sample was pulverized and pelletized. According to catalyst characterization, it was observed that the material had an average particle size of 10 nm and a specific surface area of 128 m^2·g^{-1}.

After experiments using this catalyst in the gasification process, an increase in the calorific value of the gas produced was obtained, in addition to a 99% tar removal efficiency, at a temperature of 800 °C. The temperature influence was tested, with 800 °C showing the best result in tar cracking, when compared to the other temperatures tested (700, 750, 775, 800 and 825 °C). The use of the catalyst also resulted in an increase in the composition of H_2 and CO, and a decrease in the composition of CO_2 and CH_4.

3.4 Nanoarchitectured Ni_5TiO_7 Catalyst

Nickel-based catalysts have high initial activity for tar removal, as shown in the previous examples. However, they have the disadvantage of being deactivated quickly by depositing coke [17]. Alkali metal catalysts are easily deactivated by sintering. When using more noble metal catalysts, such as Rh, more promising results of activity and stability are obtained, but they have a higher cost.

Jiang et al. [17] proposed synthesizing and using a nanoarchitectured Ni_5TiO_7 catalyst for tar removal in gasification processes. A titanium supporting material was plasma electrolytically oxidized, forming a porous TiO_2 layer on the surface. Afterward, NiO and CuO_X crystals were formed by impregnation in a solution of nickel and copper salts and a heating step at 500 °C in air. Then, the Ni_5TiO_7 needles were growing by in situ annealing in atmosphere of air and temperatures between 650 and 950 °C. It is believed that the CuO_X crystals limited the connection area between NiO and TiO_2, controlling the diameter of the microcrystals formed later. After analysis, it was noticed a strongly reduced portion of CuO_X, attributed to thermal

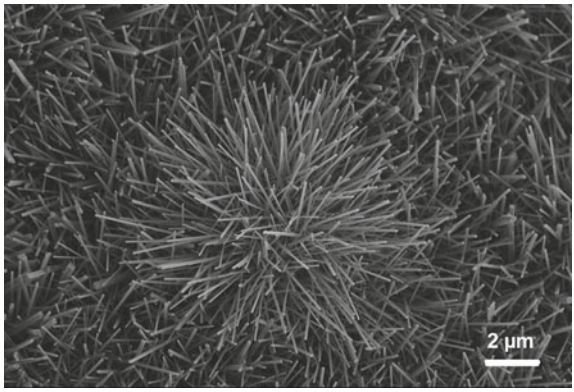

Fig. 6 SEM image of synthesized crystals (Reprinted with permission [17])

diffusion. The material obtained showed needle-shaped nanocrystals (Fig. 6), with a length of approximately 10 µm and diameters varying between tens of nanometers and 200 nm. The growth of these nanocrystals started at temperatures around 650 °C and had a higher growth rate between 750 and 800 °C.

Regarding the tar destruction, the catalyst's efficiency in cracking naphthalene ($C_{10}H_8$) was tested and compared to that of a commercial Ni-based catalyst G117 (Sudchemie AG, Munich, Germany). At a temperature of 650 °C, there was a naphthalene conversion of 60%, at 700 °C it was 90% (approximately three times higher than that of the commercial catalyst), and at 750 °C an almost complete conversion of naphthalene was achieved. In addition, the tested material showed high long-term stability, high efficiency and characteristics suitable for operations at high temperatures in biomass gasification processes.

4 Conclusion

Gasification as an energy generation process is a promising and eco-friendly alternative. One of the main drawbacks of this process is the formation of tar, which limits the use of the produced gas in several applications. In this context, the development of catalysts to promote tar destruction has been of major relevance. From the analysis made on the subject, it can be concluded that the specific surface area is among the most relevant properties of the catalyst, by strongly influencing the efficiency of a catalyst, which ends up favoring the use of nanostructured compounds for this application. Studies demonstrated that nickel-based catalysts have a high activity for this purpose, are easily available and low cost, when compared to noble metal catalysts. However, they can be quickly deactivated by coke deposition. Therefore, the search for a cheap and efficient catalyst for removing tar still presents many challenges and further needs of research and development, to make gasification an energy conversion process even more commercially feasible.

References

1. Pio, D.T., Tarelho, L.A.C., Pinto, R.G., Matos, M.A.A., Frade, J.R., Yaremchenko, A., Mishra, G.S., Pinto, P.C.R.: Low-cost catalysts for in-situ improvement of producer gas quality during direct gasification of biomass. Energy **165**, 442–454 (2018). https://doi.org/10.1016/j.energy.2018.09.119
2. Rabou, L.P.L.M., Zwart, R.W.R., Vreugdenhil, B.J., Bos, L.: Tar in biomass producer gas, the energy research centre of the netherlands (ECN) experience: an enduring challenge. Energy Fuels **23**, 6189–6198 (2009). https://doi.org/10.1021/ef9007032
3. Basu P.: Chapter 6—tar production and destruction. In: Biomass Gasification, Pyrolysis and Torrefaction, 3rd edn. pp. 189–210. (2018). https://doi.org/10.1016/B978-0-12-812992-0.00006-6
4. Claude, V., Courson, C., Köhler, M., Lambert, S.D.: Overview and essentials of biomass gasification technologies and their catalytic cleaning methods. Energy Fuels **30**, 8791–8814 (2016). https://doi.org/10.1021/acs.energyfuels.6b01642
5. Fletcher, T.H.: 6—Gasification fundamentals. Integra. Gasification Combined Cycle (IGCC) Technolog. 223–256 (2017). https://doi.org/10.1016/B978-0-08-100167-7.00006-8
6. Qunqing, L., Shuping, Z., Jiaxing, W., Haoxin, Y.: Synthesis of modified char-supported Ni-Fe catalyst with hierarchical structure for catalytic cracking of biomass tar. Renew. Energy **174**,188–198 (2021). https://doi.org/10.1016/j.renene.2021.04.084
7. Valderrama, R.M.L., Martínez, G.A., Silva, L.E.E., Olmo, D., Almazán del Olmo, O.A.: Reduction of tar generated during biomass gasification: a review. Biomass Bioenergy **108**, 345–370 (2018). https://doi.org/10.1016/j.biombioe.2017.12.002
8. Ma, X., Zhao, X., Gu, J., Shi, J.: Co-gasification of coal and biomass blends using dolomite and olivine as catalysts. Renew. Energy **132**, 509–514 (2019). https://doi.org/10.1016/j.renene.2018.07.077
9. Nicolas B., Jelena, M., Teresa Berdugo, V., Henrik, T.: Use of alkali-feldspar as bed material for upgrading a biomass-derived producer gas from a gasifier. Chem. Eng. J. **295**, 80–91 (2016).https://doi.org/10.1016/j.cej.2016.02.060
10. Pio, D.T., Gomes, H.G.M.F., Tarelho, L.A.C., Ruivo, L.C.M., Matos, M.A.A., Pinto, R.G., Frade, J.R., Lemos, F.M.S.: Energy Rep. **6**, 325–330 (2020). https://doi.org/10.1016/j.egyr.2019.08.063
11. Pio, D.T., Gomes, H.G.M.F., Ruivo, L.C.M., Matos, M.A.A., Monteiro, J.F., Frade, J.R., Tarelho, L.A.C.: Concrete as low-cost catalyst to improve gas quality during biomass gasification in a pilot-scale gasifier. Energy (2021). https://doi.org/10.1016/j.energy.2021.120931
12. Ruivo, L.C.M., Pio, D.T., Yaremchenko, A.A., Tarelho, L.A.C., Frade, J.R., Kantarelis, E., Engvall, K.: Iron-based catalyst (Fe_2-xNixTiO_5) for tar decomposition in biomass gasification. Fuel 300 (2021). https://doi.org/10.1016/j.fuel.2021.120859
13. Hui, L., Yangyang, W., Nan, Z., Leilei, D., Wenyi, D., Chenhui, L., Yanling C., Yuhuan, L., Kirk, C., Paul, C., Roger R.: Applications of calcium oxide–based catalysts in biomass pyrolysis/gasification—a review. J. Cleaner Prod. **291**(2021). https://doi.org/10.1016/j.jclepro.2021.125826
14. Samiee-Zafarghandi, R., Hadi, A., Karimi-Sabet, J.: Graphene-supported metal nanoparticles as novel catalysts for syngas production using supercritical water gasification of microalgae. Biomass Bioenerg. **121**, 13–21 (2019). https://doi.org/10.1016/j.biombioe.2018.11.035
15. Marcano, D.C., Kosynkin, D.V., Berlin, J.M., Sinitskii, A., Sun, Z., Slesarev, A., Alemany, L.B., Lu, W., Tour, J.M.: Improved synthesis of graphene oxide. ACS Nano **4**, 4806–4814 (2010). https://doi.org/10.1021/nn1006368
16. Shanmuganandam K., Venkata Ramanan M., Saravanan R., Anichai J.: An experimental analysis on tar cracking using nano structured Ni-Co/Si-P catalyst in a biomass gasifier-based power generating system. Appl. Therm. Eng. **97**, 13–21 (2016). https://doi.org/10.1016/j.applthermaleng.2015.10.150

17. Jiang, X., Zhang, L., Wybornov, S., Staedler, T., Hein, D., Wiedenmann, F., Krumm, W., Rudnev, V., Lukiyanchuk, I.: Highly efficient nanoarchitectured Ni_5TiO_7 catalyst for biomass gasification. ACS Appl. Mater. Interfaces. **4**, 4062–4066 (2012). https://doi.org/10.1021/am3008449

Nanomaterials to Improve Bio-Oil from Biomass Pyrolysis: State-Of-Art and Challenges

Tailane Hauschild, Luís António da Cruz Tarelho, Carlos Pérez Bergmann, and Tania Maria Basegio

Abstract Catalytic pyrolysis is a thermochemical conversion process that has emerged as a suitable technology for converting biomass into energy vectors. Among the energy vectors, the production of bio-oil stands out, which can represent an intermediate product of great value for industry, in particular for biorefineries, where it can be integrated in co-processing for the synthesis of liquid fuels, or in the synthesis of others chemical products of commercial interest. However, the feasibility of biomass pyrolysis is conditioned by the limited efficiency and quality of the bio-oils obtained, especially by the formation of corrosive oxygen compounds and the high water content. Therefore, it is essential to explore pyrolysis technologies and catalytic pyrolysis concepts, with low cost catalysts, in order to increase oil yield and suppress the formation of undesirable compounds. Thus, the development and application of different catalytic materials have been explored with the objective of promoting the improvement of yield and quality of bio-oil. Among the methods applied, the catalytic cracking of biomass pyrolysis vapors stands out. The influence of catalysts on the composition and yield of pyrolysis products, particularly bio-oil, is directly related to the characteristics of the catalytic materials. For example, specific surface area, number of active sites, pore size, particle size are among the characteristics that most influence the performance of the material catalytic activity. Therefore, particular attention is focused on materials with improved properties, such as nanomaterials. In this context, this chapter presents a review on the development and application of several classes of materials in catalytic pyrolysis processes and technology, their properties and its influence on the bio-oil production and characteristics, with particular emphasis on nanomaterials. Relevant aspects on challenges and future perspectives in the development and application of nanomaterials as catalysts in pyrolysis processes are also addressed.

T. Hauschild (✉) · C. P. Bergmann · T. M. Basegio
Graduate Program in Mining, Metallurgical and Materials Engineering (PPGE3M), Ceramic Materials Laboratory (LACER), Federal University of Rio Grande do Sul (UFRGS), Rio Grande do Sul Porto Alegre, Brasil

L. A. da Cruz Tarelho
Department of Environment and Planning, Centre for Environmental and Marine Studies (CESAM), University of Aveiro, Aveiro, Portugal

A. Kopp Alves (ed.), *Environmental Applications of Nanomaterials*, Engineering Materials, https://doi.org/10.1007/978-3-030-86822-2_7

Keywords Nanomaterials · Bio-oil · Biomass · Pyrolysis · Catalysts

Abbreviations

ACBS	Aesculus chinesis Bunge Seed
BBNs	Biochar-based nanocatalysts
BTX	Benzene, tuluene, xylene
CFB	Circulating fluidized bed
DSC	Diferential Scanning Calometry
ENSYN	Ensyn Technologies, Inc.
FeHC@hydrochar	Ferro rice husk hydrochar
FeHC+WI@hydrochar	Ferro rice husk hydrochar wet impregnation
FeWI@biochar	Ferro wet impregnation biochar
FP	Fast pyrolysis
GC–MS	Gas chromatography–mass spectrometry
HTC	Hydrothermal carbonization
HDO	Hydrodeoxygenation
IP	Intermediate pyrolysis
Nm	Nanometer
NREL	National Renewable Energy Laboratory
SP	Slow pyrolysis
TEM	Transmission electron microscopy
TG-FTIR	Fourier transform infrared spectroscopy
XRD	X-ray diffraction
wt	Weight

1 Introduction

Pyrolysis is a thermochemical conversion process that has emerged as suitable for converting biomass into energy vectors (e.g. biochar and bio-oil) or organic products (e.g., biochar for adsorbents, bio-oil for chemical bio-based products) [1–5]. Its properties depend on operating conditions [6], feedstock and technology used [2, 7].

In the pyrolysis process, the main components of lignocellulosic biomass (lignin, hemicellulose and cellulose) are thermally decomposed [1]. The decomposition of hemicellulose and cellulose occurs at temperatures between 220 and 400 °C, while lignin is more difficult to decompose, occurring in a wide temperature range from 160 to 900 °C. Therefore, pyrolysis of biomass with high lignin content can lead to a high fraction of solids (biochar) in the products [8].

The pyrolysis process can be divided into three major classes, following the operating conditions, namely, the heating rate: slow pyrolysis (SP), intermediate pyrolysis

(IP) and fast pyrolysis (FP) [1, 2, 9, 10]. The SP is used to produce biochar or charcoal using low heating rates (0.1–0.8 °C/s) [1] and long residence times of gases (5–30 min) in a temperature range within 300–550 °C [11]. Otherwise, in FP the main product is oil, and the process is characterised by the use of high heating rates (10^3–10^5 °C/s), moderate temperatures (500–650 °C), and small fuel particles sizes (recommended in range 1–2 mm) in order to increase the rate of heat transfer and to minimise the occurrence of secondary reactions [12], and also short gas residence time to (below 2 s) to minimise secondary reactions [12].

Regarding pyrolysis technologies, the semi-continuous and continuous reactors are the most suitable when the objective is to produce bio-oils. The main technologies available and their respective liquid yields are: bubbling fluidized bed reactors (BFB) with liquids yields in range 60–70%wt, circulating fluidized bed (CFB) with liquids yields in range 70–75%wt, auger reactor with liquids yields in range 30–9%wt [2]. The complex design of the BFB and CFB, the high demand for gas fluidization and the complex operation have restricted these technologies to be used in large-scale bio-oil production, and makes these processes expensive [13].

On the other hand, in general, the auger reactor is a compact system that presents excellent reproducibility and stability of operation. The disadvantage is that the auger reactor also requires a continuous flow of inert gas, and the process temperature remains around 400 °C. Because most moving parts are in the hot zone, large-scale heat transfer is not suitable, so auger reactors are best suited for distributed or decentralized processing schemes [2, 14].

Bio-oil generated from different pyrolysis technologies represents an important intermediate product that can have a high added-value, e.g., to be integrated as a raw material in conventional refineries for the synthesis of liquid fuels (e.g., gasoline, diesel) [3, 9, 15].

However, the direct use of bio-oil is challenging because of its low quality as fuel coupled with its undesirable attributes such as high water and oxygen content, acidity and chemical instability during storage and transport [15, 16]. In addition, bio-oils are more viscous and have a lower calorific value compared to crude oil [17].

When comparing the characteristics between bio-oil and crude oil, the most marked difference between the two oils is the elemental composition, with bio-oil containing between 28 and 40%wt of oxygen, while petroleum has less of 1%wt of oxygen [18, 19]. This high oxygen concentration influences also other characteristics such as the oil's homogeneity, polarity, calorific value, viscosity, and acidity. For example, the high concentration of oxygen in bio-oil causes a reduction in energy density by up to 50%, and limits its mixing with hydrocarbon fuels [20].

Furthermore, the complex composition of bio-oil, characterized by compounds of very different molar mass, e.g., ranging from 18 to 5000 g/mol or more [21], implies bio-oils having a wide range of boiling point. Consequently, the slow heating rate during distillation can promote polymerization of some reactive components, causing the boiling of the bio-oil to start from below 100 °C and to remain at around 250–280 °C, leaving between 35 and 40%wt of a solid residue. This wide range of boiling points also hinders the use of bio-oils in conditions for which complete evaporation occurs before combustion [19].

Regarding the high water concentration (15–30%wt) present in bio-oils, this characteristic reduces the calorific value and combustion temperature of bio-oils. The water in bio-oil comes from the moisture in the biomass or it can be the product of dehydration during the pyrolysis reactions and even during storage. Shihadeh and Hochgreb [22] compared bio-oils produced by NREL (National Renewable Energy Laboratory, US) with bio-oils produced by ENSYN (Ensyn Technologies, Inc., CA) and concluded that additional thermal cracking contributed to improve chemical and vaporization characteristics of biooils. The NREL bio-oil showed better performance and better ignition due to the lower water fraction and lower molecular weight compounds on its composition.

From literature data, it is evident that the quality of bio-oils is lower than that of petroleum-based fuels. Therefore, some techniques for refining bio-oil have been developed to promote its improvement as an energy vector.

2 Techniques to Improve the Quality of Bio-Oil

Among the different bio-oil upgrading techniques available are included: (i) pyrolysis under a reactive atmosphere (using several main components of the pyrolysis gas, namelly, CO_2, CO, CH_4 e H_2 [23], (ii) addition of solvents (e.g., methanol, ethanol, isopropanol) added directly to the liquid product of pyrolysis [24], conversion of acidic bio-oil compounds into esters over acid catalysts [25], hydrodeoxygenation (HDO) [26], catalytic fast pyrolysis [27], co-pyrolysis of biomass and plastic solid wastes [28], biomass liquefaction, catalytic hydrogenation and catalytic cracking [29, 30].

Among the upgrading methods, major efforts have been employed in the catalytic cracking of pyrolysis vapours [19], where acidic or basic solid catalysts are used at moderate temperatures and atmospheric pressure [20], making this method more economical, e.g., in relation to HDO, which is a catalytic hydrotreatment with hydrogen under high pressure (in the range of 30–140 bar) or in the presence of hydrogen donor solvents [31].

In the scope of catalytic pyrolysis, the catalytic cracking of pyrolysis vapours occurs by directly deoxygenated when passing through a catalytic bed under atmospheric pressure and in a temperature range between 350 and 650 °C [20]. With catalytic cracking of uncondensed vapours using suitable catalysts, catalytic fast pyrolysis can convert low quality pyrolysis vapours into high quality bio-oils. Catalytic pyrolysis has the advantage of being a simplified process and avoids the condensation and re-evaporation of the pyrolysis oil [32]. Thus, some studies have been developed to promote deoxygenation reactions during fast pyrolysis to produce a bio-oil with low oxygen concentration [33, 34].

Cracking of the pyrolysis gases can be carried out in in-situ or ex-situ configurations (see Fig. 1). In the in-situ process, the catalyst is placed inside the reactor, together with the biomass, most often forming a layer over the biomass. In the ex-situ

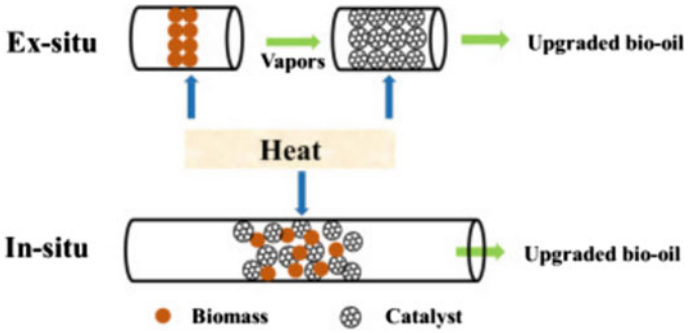

Fig. 1 Configuration of ex-situ and in situ catalysts fast pyrolysis. Reprinted with permission from Chen et al. [27]

process, the catalyst is used in a secondary reactor or even within the biomass pyrolysis reactor itself, however, the biomass and the catalyst are physically separated [35, 36].

Hu e Gholizadeh [9] observed favourable catalytic cracking conditions of the pyrolysis volatiles during the ex-situ process. The results indicated that compared to the in-situ process, the ex-situ configuration removes the producing of a bio-oil with lower oxygen content. Furthermore, the in-situ cracking process has disadvantages such as difficulty in recovering the catalyst after use; deposition of impurities and inorganic compounds, and deposition of carbonaceous material on the catalyst surface [36].

Furthermore, during catalytic fast pyrolysis, the process has lower energy consumption and shorter reaction time than the thermal fast pyrolysis process [37]. However, even though efforts to ensure higher energy efficiency of the pyrolysis process have positive results, one of the major challenges of catalytic fast pyrolysis has been to improve the quality of bio-oil, particularly in terms of calorific value. One of the main methods to increase the calorific value of bio-oil is to reduce its content in oxygenated compounds. In this context, different catalytic materials have been used to obtaining a low concentration of oxygen in the bio-oil. The development and application of catalysts in the pyrolysis process to improve bio-oil characteristics is discussed in the following sections.

3 Materials Used in Catalytic Pyrolysis

The introduction of catalysts in the biomass pyrolysis process seems to improve the performance of the process from the perspective of producing bio-oils with better quality. Different catalysts have been used in the cracking of pyrolysis vapours in order to promote dehydration, decarbonylation and cracking of organic molecules,

reduce the oxygen content of the bio-oil, convert large organic molecules into smaller molecules, and improve the quality of the bio- oil in terms of calorific value [41, 48].

Among the catalysts that have been applied, there are materials based on zeolites [41, 81, 82], functionalized zeolites [82, 83], metal oxides such as alumina (Al_2O_3) and silica-alumina (SiO_2-Al_2O_3) [81], and molecular sieves [84].

Zeolite-based catalysts are extensively applied, particularly for their high selectivity in the cracking of high molecular weight hydrocarbons (C_{14}-C_{17}) and dehydration reactions. Zeolites are a class of aluminosilicate (Al_2O_3/SiO_2) with homogeneous pores, which are presented in different three-dimensional structures. Zeolite structures are classified into three main categories according to their pore size [7], comprising catalysts based on microporous zeolites (e.g., ZK-5 and SAPO-34), the zeolites with medium pore size (e.g., Ferrierite, ZSM-23, MCM-22, SSZ-20, ZSM-11, ZSM-5, IM-5, TNU-9), and zeolites with large pore size (p.e, SSZ-55, Beta zeolite, Y zeolite) [38].

The complex structure and pore size of zeolites allows catalysts to perform as molecular sieves and to have specific selectivity for each molecule size. In addition to the pore size, the acidic sites of the zeolite-based catalysts influence the chemical composition of the bio-oil produced by catalytic pyrolysis of biomass. For example, the concentration of acidic sites promotes the formation of aromatic compounds in the bio-oil, and this has been explained as resulting from the Brønsted acidic sites, on the other hand the Lewis acidic sites produce alkanes [39].

The acid sites are controlled by the Al/Si ratio as it increases, but the surface protons of the Brønsted acidic site will complete the Al octet, making these acidic Brønsted sites weaker. Zheng et al. [40] observed that ZSM-5 (Si/Al = 25) with average crystal size (200 nm) showed an optimal proportion of Brønsted acidic sites compared to Lewis acidic sites and therefore exhibited better performance in aromatics production (24.5 mol%-carbon) during in-situ fast catalytic pyrolysis of pine wood.

The pore dimensions of solid catalysts have direct influence on the diffusion properties of the reactive gas species resulting from the biomass pyrolysis process. For example, due to the limited pore size of ZSM-5 (5,5–5,6 Å), this zeolite has a specific selectivity for monoaromatics, especially for benzene, toluene and xylene (BTX) [41]. As a result of their average pore sizes and internal pore space, only small molecule compounds are able to diffuse into the pores resulting in products with half of the size of trimethylbenzene [42]. Resulting from this catalytic performance, closely linked to its crystallographic structure, ZSM-5 is considered the most effective catalyst for the production of hydrocarbons during biomass pyrolysis [38].

However, the limiting of larger molecules, such as levoglucosan, into narrow pore openings can lead to polymerization on the outer surface. Therefore, this polymerization can also limit the diffusion of the formed monoaromatics, leading to reactions in the pores to form polyaromatics and even lead to coking, consequently reducing the formation of the target products [41]. For example, for catalytic pyrolysis of cellulose, Wang, Kim and Brown [43] refer an efficiency of only 28.8% in converting the carbon from cellulose in aromatic structures, and an efficiency of up to 30.6%

in converting the cellulose carbon into coke, although an efficiency of 66.7% was theoretically expected for the conversion of cellulose carbon into aromatic structures.

In addition to the coking problem, most of the zeolite materials employed are sensitive to water at elevated temperatures and the resulting dealumination causes irreversible deactivation [41]. Thus, many efforts have been made to improve the structure of the ZSM-5 zeolite, considered the most efficient among all zeolites [7]. The influence of pore size and active sites, including modifications of the structures of the ZSM-5 zeolites, in catalyst performance has been addressed in several studies, some of them shown in Table 1.

Due to their redox properties and/or acid–base properties, metal oxides have been widely used in catalytic fast pyrolysis of biomass. Several metal oxides, including acidic metal oxides (e.g., SiO_2 and Al_2O_3), base metal oxides (e.g., MgO and CaO), transition metal oxides (e.g., ZnO, CuO, Fe_2O_3, TiO_2, ZrO_2, MnO_2 and CeO_2), complex metal oxides (e.g., Fe/CaO and Cu/Al_2O_3) were investigated as catalysts or catalysts supports for improving bio-oil quality [48].

In general, Al_2O_3 is the most investigated acid metal oxide for catalytic fast pyrolysis of biomass, it promotes dehydration reactions and therefore leads to an increase in water content [85]. For example, Stefanidis et al. [86] found that the addition of Al_2O_3 with a surface area of 93 m^2/g significantly reduced the oxygen content of the bio-oil from 41.68 to 24.00%wt., promoting an increase in the yield of water from 21.38 to 29.08%wt.

Due to the low costs and results that indicate an improvement in the quality of bio-oil, basic metal oxides have been also widely studied [27]. Results from a study using Fourier transform infrared spectroscopy (TG-FTIR) to investigate the influence of CaO on corncob pyrolysis showed that CaO promoted the formation of hydrocarbons through catalytic reactions [48].

The effect of CaO on biomass pyrolysis can be a particularly complex process. Chen et al. [49] evaluated the addition of different proportions of CaO/biomass (cotton stem) in a fixed bed reactor and found that CaO could act as a reactant, an absorbent and a catalyst at CaO/biomass mass ratios of <0.2, >0.2 and >0.4, respectively. When acting as a catalyst, the best performance was at temperatures above 600 °C, promoting an increase in the concentration of furan and hydrocarbon, and a decrease in the concentration of esters and anhydrosugars in the bio-oil. In another example of CaO acting as a catalyst, where the CaO/biomass mass ratio of 5 was applied in a fluidized bed reactor, the oxygen content in the bio-oil was reduced from 39%wt. to 31%wt. at expenses of a slight decrease (5.3%wt) on the bio-oil production [50].

Analogous to CaO, the MgO improves the quality of the bio-oil in terms of removal of oxygenated groups, hydrocarbon compounds distribution and increase in calorific value, although a slight decrease on bio-oil production can be observed. Pütün [51] reported a decrease from 9.56 to 4.90%wt. in the concentration of oxygen in the bio-oil, and an increase from 1.83 to 2.39 in the molar ratio H/C, during catalytic pyrolysis of cottonseed at 550 °C and applying MgO as catalyst.

On the other hand, modified metal oxides are effective catalysts for deoxygenation. For example, doping CaO with Fe(III) increases the catalytic effects, reducing

Table 1 Selected works on catalytic pyrolysis

Catalyst type	Feedstock	Reactor type reaction temperature	Ex-situ In-situ	In results	References
HZSM-5 and its variations dopped with Cu, Zn, Ga, Co, Mg or Ni	Yunnan pine particles	Fixed-bed 500 °C	Ex-situ	All metal-modified HZSM-5 catalysts proved effective in reducing oxygenated compounds Ni/HZSM-5 catalyst improved C_{10+} hydrocarbons (31.36 wt. %) The Zn-Co/HZSM-5 were more selective for light (C_6-C_8) and heavy hydrocarbons (C_{10+})	[1]
HZSM-5 (Z5) and its dopped variations with 0.5 to 2% Fluor and with 0.5 to 5% Ni	Cellulose	Drop tube quartz reactor 500 °C	In-situ	Excellent yields of light aromatics (LAs) obtained with Z5 were attributed to an increase in small mesopores and a decrease in Brønsted acid sites Adjusting acid sites with Ni loading further improved catalytic performance. 1Ni-FZ5 showed higher yield (31.3%) of BTEXN (B: benzene, T: toluene, E: ethylbenzene, X: xylene, N: naphthalenes)	[2]

(continued)

Table 1 (continued)

Catalyst type	Feedstock	Reactor type reaction temperature	Ex-situ In-situ	In results	References
ZSM-5 e Fe/ZSM-5	Wood sawdust	CDS Pyroprobe 5200HP 500 – 800 °C	Ex-situ	Both catalysts ZSM-5 and Fe/ZSM-5 influenced the increase in the production of aromatic hydrocarbons The catalyst Fe/ZSM-5 was more active to produce monocyclic aromatic hydrocarbons (MAHs) and to decrease the production of polycyclic aromatic hydrocarbons (PAHs) The production of hydrocarbons increased with the increase in the temperature from 500 to 600 °C, and decreased with further increasing temperature from 600 to 800 °C	[44]
ZSM-5, MCM-41, Distinct metal oxides (MgO, Al_2O_3, CuO, Fe_2O_3, MgO, NiO, ZnO, ZrO_2, TiO2)	Cotton stalk	Fixed-bed reactor 450 °C	In-situ	Metal oxides exhibited better performance in deoxygenation than zeolites: CaO removed more oxygen in the form of CO_2, while the other catalysts promoted deoxygenation through dehydration (with formation of H_2O) CaO, Al_2O_3 and NiO exhibited better deoxygenation effect	[3]

(continued)

Table 1 (continued)

Catalyst type	Feedstock	Reactor type reaction temperature	Ex-situ In-situ	In results	References
HZSM-5 with varying Si/Al ratios (22, 30, 70, 100, 300)	Teak wood chips	Fluidized-bed 450 °C	In-situ	There was a decrease in the desired products such as light phenols and in the production of hydrocarbons with an increase in the ratios of Si/Al, which has been attributed to the reduction of Brønsted acid sites	[45]
HZSM-5 (Si/Al ratio = 38)	Pine sawdust	Fluidized-bed/fixed-bed combination 550 °C	In-situ ex-situ	Fast catalytic pyrolysis with ex-situ catalyst produced aromatics in an amount similar (~20%) to the in-situ fast catalytic pyrolysis, but produced approximately twice as many olefins (10.3%) and less char (42.7%) in comparison to in-situ fast catalytic pyrolysis (5.8% and 48.4%, respectively)	[46]
MgO *vs* ZSM-5	beech wood sawdust	bench-scale fixed bed tubular reactor 500	Ex-situ	Basic MgO catalysts showed better catalytic effects on bio-oil production in terms of organic fraction yield and lower oxygen concentration: (thermal pyrolysis: 38.9 wt.% biooil yield with 38.7 wt.% oxygen; catalytic pyrolysis with ZSM-5 based catalyst: 20.7 wt.% biooil yield with 30.9 wt.% oxygen; natural MgO catalyst: 25.7 wt.% biooil yield with 31.0 wt.% oxygen)	[47]

oxygenated compounds (acids, aldehydes and ketones) while increasing the production of furans and hydrocarbons [52, 53]. The Fe (III)/CaO catalytic activities are attributed to the synergistic effect between the CaO support and the Fe, and the $Ca_2Fe_2O_5$ phase formed in the catalysts can protect the CaO support and inhibit the sintering of Fe during the catalytic reaction [48].

The Al_2O_3 modified with Cu (5%wt. Cu/Al_2O_3) by means of the co-precipitation method and applied in the catalytic fast pyrolysis of biomass (tomato waste) resulted in a relatively higher bio-oil yield (30.31%wt) and in a lower oxygen concentration (16.74%wt.) in the bio-oil, when compared to the 35.33%wt oxygen concentration in the bio-oil produced by thermal pyrolysis [54].

Transition metal oxides such as ZnO, CuO, Fe_2O_3, TiO_2 and ZrO_2 have also been extensively tested in catalytic fast pyrolysis of biomass [27]. Torri et al. [55] investigated different types of catalysts in pine sawdust pyrolysis at 500 °C and concluded that ZnO, CuO, Fe_2O_3 catalysts were effective in reducing the concentration of heavy compounds, although with a slight reduction in bio-oil yield. The reduction in the concentration of heavy compounds is a positive aspect because their presence in bio-oil results in higher viscosity and slower combustion [56].

In this sense, catalysts of transition metals, including Ga, Cu, Fe, Ni and Zn, etc., were considered effective to promote the production or selectivity of aromatics in the catalytic pyrolysis of biomass [41, 57]. In the field of Fe-based catalysts, several works, including laboratorial-scale studies on catalytic fast pyrolysis [58], catalytic cracking of pyrolysis vapours [59, 60], indicate these low cost materials as a good alternative for deoxygenation/conversion of oxygenated compounds at intermediate temperatures.

Moud et al. [58] applied an unsupported Fe-based catalyst for cracking the pyrolysis gas produced from pyrolysis of biomass from chipped tree tops and branches at 450 °C. Their results showed that there was significant cracking of oxygenated compounds/vapor reforming of the pyrolysis gas, with 70–80%wt reduction of acetic acid, methoxyphenols and a 55–65%wt reduction of non-aromatic ketones, benzene, toluene, xylene and heterocyclic compounds [58]; all the other compounds yield was also influenced by the use of Fe as a catalyst.

The different properties of catalysts, such as particle size, pore size, acidity and mesoporosity, have been reported in the literature as factors that influence significantly the reaction pathways, yields and selectivities of pyrolysis products [20]. For example, reducing the particle size of a catalyst to nanoscale (size 1–100 nm in at least one dimension) can result in the generation of new catalytic materials enriched with specific active sites on the surface and improved reducing properties that can be substantially different from their source particles [61, 62]. The specific surface area of nanometer catalysts can also be significantly improved due to the higher surface to volume ratio, allowing pyrolysis gases to better access to surface active sites [63]. In this context, the following section will address the development and characteristics of nanomaterials used as catalysts in biomass pyrolysis to improved bio-oil production.

4 Nanomaterials Used in Catalytic Pyrolysis

In recent years, nanocatalysts have attracted major interest in result of their unique properties (e.g. catalytic, electronic and magnetic) and potential application in several fields compared to conventional catalysts [64]. The excellent properties of electrocatalysis and magnetic catalysis exhibited by nanocatalysts have been exploited in several industrial sectors, including the oil, chemical and energy [65, 66].

Fine-tuning of the morphology of catalyst particles, especially metals or metal oxides, optimizes the electronic and geometric properties of the catalyst surface. Nanostructured metal oxides may preferentially expose large amounts of active crystal faces. As a result of the high specific surface area, interactions between active sites and reactive species can be increased, which is a key driving force for obtaining high catalytic reaction rates, for example, useful in the processes of energy conversion of biomass [67].

In this sense, according to the study carried out by Gokdai et al. [68] about the catalytic effect of SnO_2 nanoparticles, the smaller particle size and the larger specific surface area of the catalyst favour secondary reactions of pyrolysis vapours in the reactor and also the secondary decomposition of charcoal at higher temperatures. The authors compared the influence of SnO_2 nanoparticles with the influence of Bulk SnO_2, red mud, HZSM-5 and K_2CO_3 catalysts on the distribution of products from pyrolysis of hazelnut shell. The nano-SnO_2 catalyst synthesized by hydrothermal route, which presented agglomerated particles with an average diameter of 3 to 4 nm (Fig. 2), favoured the increase in gas production and the decrease in oil production, which was explained as a result of cracking of tar in gaseous products at higher temperatures (700 °C). GC–MS analysis of pyrolytic oils obtained from pyrolysis of hazelnut shell showed that fatty acids (e.g., oleic, stearic, and palmitic acids) were found in the presence of nano-SnO_2, however, the percentage of oleic acid was more significant in the presence of HZSM-5; this result can be attributed to the high

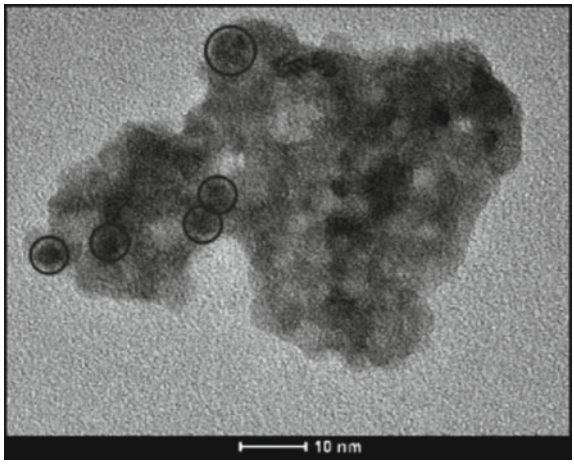

Fig. 2 TEM image of hydrothermally synthesized SnO_2 nano particles. Reprinted with permission from Gokdai et al. [68]

efficiency of HZSM-5 in converting unsaturated fatty acids into branched chain fatty acids. On the other hand, the addition of nano-SnO_2 led to the formation of etheric structures in the bio-oil [69].

When comparing the catalytic activity of nanoparticles from a metal oxide with those of the same metal oxide in a micro-scale, a lower value of activation energy is observed with nanoparticles, thus, indicating that catalytic pyrolysis with nanoparticles can be more attractive considering energy and economic parameters.

For example, NiO particles in nanoscale (nano-NiO) and micro-scale (micro-NiO) were used by Li et al. [70] as catalysts in pyrolysis of cellulose by thermogravimetry. The nano-NiO particles were synthesized by the homogeneous precipitation method and showed high purity and a fine crystal phase of cubic syngony with an average size between 7 and 9 nm and specific surface area of 187.98 m^2/g. The catalytic activity of nano-NiO particles in cellulose pyrolysis (10 °C/min to 900 °C) was compared with the catalytic activity of micro-NiO particles (specific surface area 28.58 m^2/g, 325 mesh (approximately 44 mm)). The results show that in comparison to thermal pyrolysis, the catalytic pyrolysis of cellulose in presence of micro-NiO particles (3%wt.) reduced in 6% (12.24 kJ/mol) the activation energy of the process in, and in the presence of the nano-NiO particles (3%wt.) the activation energy was further reduced in 11% (22.42 kJ/mol). Therefore, the nano-NiO particles demonstrated a more effective catalytic effect on cellulose pyrolysis compared to micro-NiO particles.

The influence of nanoparticles on the decomposition reactions of biomass molecules has been also analysed by the absorption of heat during catalytic pyrolysis of biomass in a thermobalance. In this context, Li et al. [64] applied different proportions of nano-catalysts of NiO, Fe_2O_3 and NiO/Fe_2O_3 in the production of bio-oil by catalytic fast pyrolysis of Aesculus chinesis Bunge Seed (ACBS) and also ACBS pre-processed with a solution of $NaHCO_3$. The treatment of ACBS samples with $NaHCO_3$ had a particular influence on the composition of the products of pyrolysis, and the nano-Fe_2O_3 catalyst accelerated the ACBS decomposition reaction. Both nano-NiO and nano-Fe_2O_3 influenced the composition of acids, aromatics and alkanes and inhibited the production of alkenes and amines. However, the nano-Fe_2O_3 showed higher catalytic effects, and this higher efficiency on the decomposition of biomass was reflected by a lower heat absorption as revealed by Differential Scanning Calorimetry (DSC). It is of note the positive effects of the $NaHCO_3$, such as the neutralization of acidic pesticides present in the biomass, and its potential interference in the pyrolysis process, and particularly the further influence of the $NaHCO_3$ in promoting lower particle sizes of the iron oxide catalyst and an higher aggregation time of the nanocrystals [71].

In addition to particle size and specific surface area, the presence of oxygen vacancy-type defects in the metal oxide structure can influence its activity and catalytic selectivity. One benefit of oxygen vacancies is their moderate acid strength, which can influence a specific reaction pathway for the formation of desirable bio-based chemicals [72]. For example, Rogers and Zheng [73] compared the influence of oxygen vacancy sites (acid sites) of MoO_3 in the hydrogenation route and in the direct deoxygenation of compounds resulting from pyrolysis of lignin. The results

showed that MoO_3 with oxygen vacancies favoured the deoxygenation route more than the hydrogenation route. Oxygen vacancy defects can be generated during the synthesis process, catalytic reaction or by post-synthesis treatment with hydrogen [72].

In the context of the influence of the acid sites of the nanocatalysts on the pyrolysis products, one can mention a positive effect on the selectivity to the formation of valuable chemical compounds present in some bio-oils, such as furfural [74]. Most of the solid acid catalysts contain Bronsted acid sites and Lewis acid sites, which influence the dehydration of cellulose, favouring the increase in the selectivity towards furfural formation [75]. However, some catalytic materials can experiment agglomeration of particles during synthesis, as it is the case of materials with high iron content. For example, Mian et al. [76] observed the agglomeration of particles in the synthesis of the nanocatalyst TiO_2/Fe/Fe_3C-biochar. In this context, the doping of iron-based materials with other chemical elements, e.g., Li^+, Na^+, K^+, can influence the nucleation and growth of nanoparticles in order to reduce agglomeration [77]. An example of such an iron-based nanocatalyst doped with another chemical element, for the production of furfural, is the nano Na/Fe-solid acid produced by Bai et al. [78]. This catalyst was synthesized by precipitation process and subsequent co-precipitation, using different mass ratios of Na/Fe_x ($x = 0.36, 0.69, 1.42, 2.17$), promoting the formation of different surface morphologies. The results in Fig. 3 show that the morphologies of the particles changed as the Na/Fe_x mass ratios were increased, at first, they changed from a long clariform crystal to a crystal with a prismatic angle, and for higher mass ratios it was noticed the disappearance of the prismatic angle and the formation of spherical particles. The Na/Fe mass ratio of 1.42 was appropriate to inhibit agglomeration and form the uniform catalyst with spherical particles (50–100 nm). The catalyst Na/Fe (1.42) solid acid with spherical morphology also had a high specific surface area (201.5 m^2/g) and more sites acid. This catalyst Na/Fe (1.42) solid acid promoted the higher selectivity (61.4%) for furfural formation during ex-situ cracking of vapours from pyrolysis of cellulose at 550 °C, when compared to Na/Fe (0.36) and Na/Fe (0.69) for which the selectivity was 15.65% and 15.33%, respectively. According to the authors, the acidic activity of the nanocatalyst promoted the conversion of glucose monomers into dehydrated sugars and these sugars underwent secondary cracking to form furfural [78].

The performance of nanoscale catalysts can be significantly influenced by the support material in terms of surface area, pore size, functional groups and mechanical strength [79]. Several types of support materials such as Al_2O_3, SiO_2, zeolites, have been investigated for the synthesis of nanoscale metal catalysts. Metal oxides can play the role of both active phase and catalyst support, which is why they are considered essential components for the development of various industrial heterogeneous catalysts, particularly in the petrochemical industry [80]. Recently, carbonaceous materials (e.g., activated carbon, biochar, hydrochar) have been explored as supports for the synthesis of nanoscale catalysts based on their porous structure, which generally has high specific surface area, excellent pore size distribution to stabilize metallic nanoparticles and a surface enriched with relevant functional groups [81].

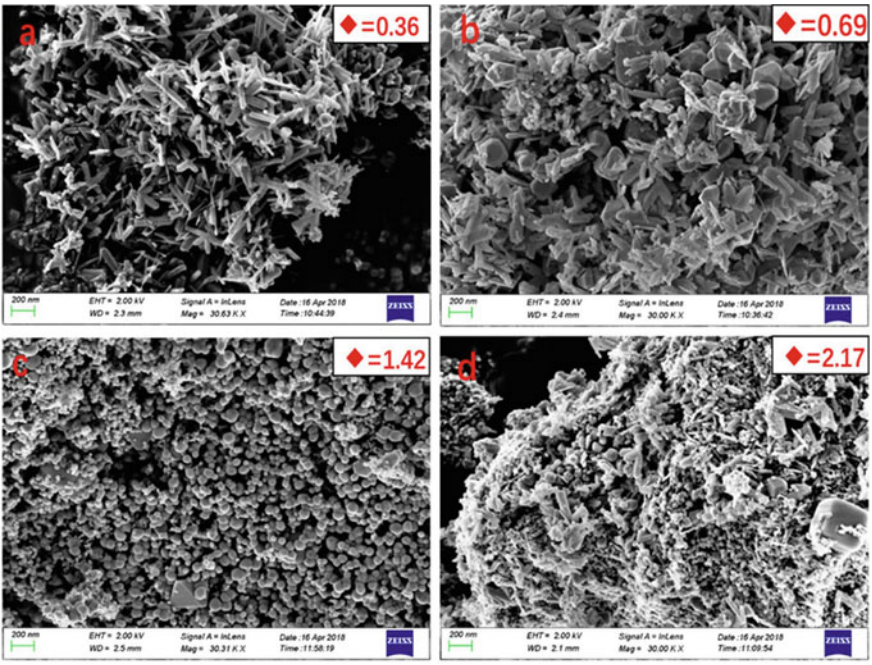

Fig. 3 SEM images of Na/Fe nano catalysts. **a** Na/Fe ratio = 0.36, **b** Na/Fe ratio = 0.69, **c** Na/Fe ratio = 1.42, **d** = Na/Fe ratio = 2.17. Reprinted with permission from Bai et al. [78]

Regarding zeolite structures as support for nanomaterials, an attractive alternative is the incorporation of low-cost materials. Non-noble Ni-based nanomaterials, e.g., supported on zeolite structures, may have selectivity for aromatics and hydrocarbons (formed by deoxygenation) similar to the noble metals supported on the same structure. For example, Murata et al. [82] considered catalysts supported on zeolite, NiMo(O)/ZSM, NiMo(O)/Y, NiMo(O)/Beta and Ni_2P/Beta effective and with similar results to PtPd/ZSM during fast pyrolysis (500–600 °C) of Jatropha waste to produce bio-oil. The size of nanoparticles in the porous supports were between 20.9 to 62.2 nm for NiMo(O)/Y and between 36.5 to 49.0 nm for Ni_2P. The specific surface area, pore volume, and pore diameter of these catalysts were 176.0 to 464.5 m^2g^{-1}, 0.098 to 0.286 cm^3g^{-1} and 1.50 to 11.5 nm, respectively. The pore diameter of ZSM was 2.58 nm. The largest liquid yield (49.9%wt., including 21.3%wt. of organic liquid) was obtained with NiMo(O)/Y at 500 °C. The acid values of the organic liquids obtained at 500 ºC were expressed in terms of the amount of KOH at equivalent point and was only 1.99 mg-KOH kg^{-1} for the catalytic material NiMo(O)/Y, that was significantly lower than the result (38.7 mg-KOH kg^{-1}) obtained by the same authors in a previous study [83] using as catalyst the PtPd/ZSM. Under these pyrolysis conditions, Ni-based nanomaterials showed to be a more economical alternative and with similar, or even better, catalytic activity than noble metals, e.g., when compared to the PtPd system.

In addition to incorporating low-cost nanoparticles without compromising the effectiveness in catalytic cracking of pyrolysis vapours, low-cost supports with high catalytic activity and high resistance to coke formation are one of the main research topics in the context of obtaining high quality bio- oil. In this sense, among the different materials for supports, the carbonaceous ones have been emerging of particular interest, e.g., the biochar [81]. Furthermore, the incorporation of metals can also improve the catalytic performance of biochars and, thus, the so-called bifunctional catalysts are produced [81]. In this context, regarding low-cost nanoparticles, Fe-based catalysts are reported as materials with excellent catalytic activity for the production of high quality syngas and bio-oil [78, 84].

The application of Fe nanoparticles supported on biochar is an example of a bifunctional catalyst. Dong et al. [81] used rice husk as a precursor to produce a Fe nanocatalyst supported in biochar. The raw rice husk was impregnated with Fe $(NO_3)_3 \cdot 9H_2O$ and was heated in a horizontal oven (electric heating) at 800 °C for 1 h under a N_2 atmosphere, and the resulting material was named RHC/Fe. The catalyst was characterized for mineralogy by X-ray diffraction (XRD) and morphology by scanning electron microscopy (SEM). The three peaks shown in Fig. 4b ($2\theta = 44.6°$, 65°, 82.3°) characterize the existence of Fe^0 which was formed during biomass pyrolysis due to the reduction of the Fe precursor impregnated by carbon and reducing gas (H_2, CO). The diffraction peaks corresponding to the existence of Fe_3O_4 ($2\theta = 30.1°$, 35.4°, 43.1°, 53.4°, 57°, 62.6°), show that a fraction of Fe^0 is not stable in contact with air and may be oxidized during storage. In addition, the three-dimensional porous structures of RHC and RHC/Fe shown in Fig. 4c–d, are a result of the thermal decomposition of organic compounds and the release of volatile substances during the pyrolysis of rice husk. Although they have a similar structure, the surface conditioning of RHC/Fe has been improved due to the addition of Fe $(NO_3)_3 \cdot 9H_2O$ during catalyst preparation, leading to a more porous structure. The catalyst RHC/Fe was tested during pyrolysis of *Sargassum*, and it was observed that

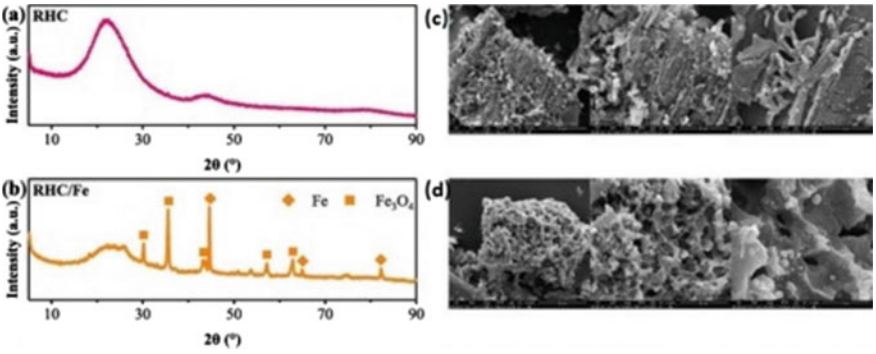

Fig. 4 Characterization of the catalysts: **a** XRD analysis of RHC, **b** XRD analysis of RHC/Fe, **c** SEM images of RHC, **d** SEM images of RHC/Fe. Edited and reprinted with permission from Chen et al. [81]

esterification reactions and secondary reactions were promoted, with formation of a bio-oil enriched in esters.

The use of Fe nanoparticles supported on rice husk hydrochar in the ex-situ catalytic cracking of pyrolysis vapours carried out in a microwave oven, has shown that it is possible to double the yield of high purity phenolic compounds in the bio-oil produced from pyrolysis of corn cobs [85]. To produce the catalyst, the iron nanoparticles were inserted into the hydrochar matrix via hydrothermal carbonization (HTC), using a solution of Fe $(NO_3)_3$ at 200 °C followed by pyrolysis at 800 °C under N_2 atmosphere. This catalytic material was named FeHC@hydrochar, and the uniform distribution of Fe nanoparticles was mainly attributed to the strong interaction between Fe and several oxygenated functional groups of the hydrochar during HTC. Besides, the FeHC@hydrochar presented the smallest particle size (7.27 nm) in relation to the other catalysts synthesized using wet impregnation, namely FeHC + WI@hydrochar with particle size of 12.49 nm, and FeWI@biochar with particle size 13.50 nm; WI means wet impregnation. The smaller-sized nanoparticles have a larger specific surface area of contact with the functional groups of carbonaceous supports and, thus, promote a better distribution of Fe on the surface of the support. However, as a result of the increased incorporation of nano-Fe species, the BET surface area of FeHC@hydrochar (206.62 m^2/g) was the smallest compared to FeWI@biochar (244.56 m^2/g) and FeHC + WI@hydrochar (248.64 m^2/g). Nevertheless, the reduction in surface area does not seems to have influenced the phenol selectivity in the catalytic cracking of pyrolysis vapours. The selectivity of phenol compounds showed an increasing trend with FeHC@hidrochar when the catalyst to raw material ratio was increased from 1:10 to 7:10 during the pyrolysis process. Finally, the objective of producing a bio-oil with a high concentration of phenolic compounds was at the expense of a reduction (from 23.2 to 20.8%wt) in the production of bio-oil [85].

It has been observed a significant progress in the development of nanomaterials to be used as catalysts in pyrolysis process for different purposes. However, several drawbacks in the development of these materials have been noticed that need further research and development. In this sense, some emerging perspectives and challenges in this field need to be addressed, and those are briefly analysed in the following section.

5 Perspectives and Challenges in Development of Nanomaterials as Catalysts

There is an increasing demand to develop nanomaterials for use as catalysts in pyrolysis technologies with different objectives. For example, the development of biochar-based nanocatalysts (BBNs) for cracking of pyrolysis vapours during biomass pyrolysis for production of high quality bio-oil. In general, BBNs have great potential as a new type of catalyst due to their high catalytic activity and a homogeneous distribution of metal nanoparticles on the surface of the supporting biochar [86]. However,

some efforts must be continued in order to obtain an advance in synthesis methods and commercial applications.

Among the challenges to be overcome are included: the precise control of particle size, homogeneity and incorporation of nanoparticles in the biochar matrix, thus ensuring the greatest possible chemical interaction between the biochar surface and the nanoparticles. Improved interaction between biochar and nanoparticles can prevent nanoparticles from detaching from biochar under conditions of high temperatures and complex reactions involving carbon deposition during catalytic cracking of pyrolysis vapours [79]. Therefore, exploring new synthesis methods and new metals are important to seek greater stability and performance of BBNs.

The regeneration capacity of a catalyst is also a determining aspect in choosing the material to be applied in a catalytic pyrolysis process. For example, under the pyrolysis conditions of the research carried out by Murata et al. [82], the catalysts based on Ni nanoparticles, particularly NiMo(O)/Y(14), have shown to be materials with better catalytic activity and cheaper than the PtPd systems. However, the specific surface area of NiMo(O)/Y(14) has decreased significantly (from 464 to 255 m^2g^{-1}) after the regeneration process. Although the authors claim that changing these physical structures would not have a critical impact on catalyst performance and that all catalysts tested were regenerated, the number of cycles that this material can undergo regeneration and maintaining the catalytic activity must be investigated, to determine the economic viability of this material.

In the context of the relationship between the catalytic activity of a catalyst and its specific surface area, the results of several research studies analysed in this chapter indicate that a high specific surface area has a positive influence on the catalytic performance of nanoparticles. However, during the synthesis of nanomaterials, agglomeration of nanoparticles can occur, particularly when the materials have high Fe content [76], thus, reducing the specific surface area, and the potential decrease in the catalytic activity of these materials [87]. In addition, restricting particle agglomeration can guarantee an higher quantity of acidic sites, favouring selectivity for the production of desirable compounds [78]. Therefore, some techniques such as the incorporation of chemical elements capable of restricting the agglomeration of nanoparticles by controlling the growth and nucleation of particles during synthesis is a potential alternative to be better investigated [77].

Regarding the application of nanocatalyts at industrial scale, some challenges still need to be overcome. A technical barrier is the deactivation of nanocatalysts by carbon deposition and H_2S poisoning, as is the case with Ni-based nanomaterials [70]. Carbon deposition also causes obstruction of the pores of the supports consisting of different materials, such as carbonaceous (e.g., biochar [86], hidrochar [85]) and zeolite structures [88]. Obstruction of pores by coking leads to catalyst deactivation due to blocking access to active sites (e.g., acidic sites) by the molecules to be broken down. In this sense, in addition to improving the characteristics of catalysts and their supports, advanced catalysis techniques are needed to improve the performance of these materials. An example of a technique that has emerged for application in fast catalytic pyrolysis of biomass is the dual-catalyst method. This method combines the advantages of different catalysts, where pyrolysis vapours are cracked by mesoporous

catalysts (e.g., CaO and Al_2O_3) arranged in sequence or physically mixed with microporous catalysts (e.g., ZSM-5). Mesoporous catalysts convert large molecules into smaller molecules with a low content of oxygen, that undergo further conversion into aromatics by microporous structures [89, 90]. Therefore, the use of the dual-catalyst method with the application of porous materials impregnated with nanoparticles, presents itself as a potential alternative to improve the catalytic performance of these bifunctional catalysts.

Besides the relevance and performance of nanomaterials as catalysts in the pyrolysis process, an import subject to be addressed is that related to potential environmental impacts of nanomaterials. Those impacts can emerge either during the pyrolysis process itself or during the further use of the biooil in downstream applications, e.g., as fuel. In fact, during the pyrolysis process the nanoparticles can detach from the catalyst support and become mixed with the products flows, e.g., the bio-oil. Thereafter, because of their nano-size these particles can represent an environment problem during the use of the bio-oil. In order to minimize those risks, a subject that must deserve most attention is the recovering of the nanocatalyts particles during the pyrolysis process and from the products of the process. This recovering of the nanocatalyst represents also an economic issue. In this sense, an alternative that has been emerging to ensure the recovery of these nanoscale materials is the use of ferromagnetic nanoparticles. Fe-based materials is an example of a ferromagnetic material that has been used as catalyst in distinct applications [91–93], which has efficient catalytic properties and can be easily recovered by magnetic processes, and, in addition, it is a low-cost material.

As concluding remark, the development of materials with catalytic properties to improve the quality of bio-oil and at the same time ensure a minimization of environmental impacts, as well as guarantee the economic viability of the process, is a subject that requires further research.

Acknowledgements The authors would like to thank the Human Resources Program of the National Agency of Petroleum, Natural Gas and Biofuels (PRH-ANP 13.1; grant number 042319) and the Coordination for Improvement in Higher Education Personnel (CAPES) for the financial support. Thanks are due to the Portuguese Foundation for Science and Technology (FCT)/Ministry of Science, Technology and Higher Education (MCTES) for the financial support to CESAM (UIDP/50017/2020+UIDB/50017/2020), through national funds.

References

1. Roy, P., Dias, G.: Prospects for pyrolysis technologies in the bioenergy sector: a review. Renew. Sustain. Energy Rev. **77**, 59–69 (2017). https://doi.org/10.1016/j.rser.2017.03.136
2. Qureshi, K.M., Kay Lup, A.N., Khan, S., Abnisa, F., Wan Daud, W.M.A.: A technical review on semi-continuous and continuous pyrolysis process of biomass to bio-oil. J. Anal. Appl. Pyrol. **131**, 52–75 (2018) https://doi.org/10.1016/j.jaap.2018.02.010
3. Meier, D., van de Beld, B., Bridgwater, A.V., Elliott, D.C., Oasmaa, A., Preto, F.: State-of-the-art of fast pyrolysis in IEA bioenergy member countries. Renew. Sustain. Energy Rev. **20**, 619–641 (2013). https://doi.org/10.1016/j.rser.2012.11.061.

4. Dhyani, V., Bhaskar, T.: A comprehensive review on the pyrolysis of lignocellulosic biomass. Renew. Energy **129**, 695–716 (2018). https://doi.org/10.1016/j.renene.2017.04.035
5. Mattos, C., Veloso, M.C.C., Romeiro, G.A., Folly, E.: Biocidal applications trends of bio-oils from pyrolysis: characterization of several conditions and biomass, a review. J. Analyt. Appl. Pyrol. **139**, 1–12 (2019). https://doi.org/10.1016/j.jaap.2018.12.029s
6. Cantrell, K.B., Hunt, P.G., Uchimiya, M., Novak, J.M., Ro, K.S.: Impact of pyrolysis temperature and manure source on physicochemical characteristics of biochar. Bioresour. Technol. **107**, 419–428 (2012). https://doi.org/10.1016/j.biortech.2011.11.084
7. Bhoi, P.R., Ouedraogo, A.S., Soloiu, V., Quirino, R.: Recent advances on catalysts for improving hydrocarbon compounds in bio-oil of biomass catalytic pyrolysis. Renew. Sustain. Energy Rev. **121**, 109676 (2020). https://doi.org/10.1016/j.rser.2019.109676
8. Yang, H., Yan, R., Chen, H., Lee, D.H., Zheng, C.: Characteristics of hemicellulose, cellulose and lignin pyrolysis. Fuel **86**(12), 1781–1788 (2007). https://doi.org/10.1016/j.fuel.2006.12.013
9. Hu, X., Gholizadeh, M.: Biomass pyrolysis: a review of the process development and challenges from initial researches up to the commercialisation stage. J. Energy Chem. **39**, 109–143 (2019). https://doi.org/10.1016/j.jechem.2019.01.024.
10. Garcia-Nunez, J.A.: Historical developments of pyrolysis reactors: a review. Energy Fuels **31**(6), 5751–5775 (2017). https://doi.org/10.1021/acs.energyfuels.7b00641.
11. Homagain, K., Shahi, C., Luckai, N., Sharma, M.: Biochar-based bioenergy and its environmental impact in Northwestern Ontario Canada: a review. J. For. Res. **25**(4), 737–748 (2014). https://doi.org/10.1007/s11676-014-0522-6
12. Kan, T., Strezov, V., Evans, T.J.: Lignocellulosic biomass pyrolysis: a review of product properties and effects of pyrolysis parameters. Renew. Sustain. Energy Rev. **57**, 1126–1140 (2016). https://doi.org/10.1016/j.rser.2015.12.185.
13. Bridgwater, A.V.: Renewable fuels and chemicals by thermal processing of biomass. Chem. Eng. J. **91**(2), 87–102 (2003). https://doi.org/10.1016/S1385-8947(02)00142-0.
14. Isahak, W.N.R.W., Hisham, M.W.M., Yarmo, M.A., Yun Hin, T.-Y.: A review on bio-oil production from biomass by using pyrolysis method. Renew. Sustain. Energy Rev. **16**(8), 5910–5923 (2012). https://doi.org/10.1016/j.rser.2012.05.039.
15. No, S.-Y.: Application of bio-oils from lignocellulosic biomass to transportation, heat and power generation—a review. Renew. Sustain. Energy Rev. **40**, 1108–1125 (2014). https://doi.org/10.1016/j.rser.2014.07.127
16. Yang, Z., Kumar, A., Huhnke, R.L.: Review of recent developments to improve storage and transportation stability of bio-oil. Renew. Sustain. Energy Rev. **50**, 859–870 (2015). https://doi.org/10.1016/j.rser.2015.05.025.
17. Mortensen, P.M., Grunwaldt, J.-D., Jensen, P.A., Knudsen, K.G., Jensen, A.D.: A review of catalytic upgrading of bio-oil to engine fuels. Appl. Catal. A General **407**(1), 1–19 (2011). https://doi.org/10.1016/j.apcata.2011.08.046.
18. Scholze, B., Meier, D.: Characterization of the water-insoluble fraction from pyrolysis oil (pyrolytic lignin). Part I. PY–GC/MS, FTIR, and functional groups. J. Analyt. Appl. Pyrol. **60**(1), 41–54 (2001). https://doi.org/10.1016/S0165-2370(00)00110-8
19. Zhang, Q., Chang, J., Wang, T., Xu, Y.: Review of biomass pyrolysis oil properties and upgrading research. Energy Conv. Manage. **48**(1), 87–92 (2007). https://doi.org/10.1016/j.enconman.2006.05.010
20. Rezaei, P.S., Shafaghat, H., Daud, W.M.A.W.: Production of green aromatics and olefins by catalytic cracking of oxygenate compounds derived from biomass pyrolysis: a review. Appl. Catal. A General **469**, 490–511 (2014). https://doi.org/10.1016/j.apcata.2013.09.036
21. Lu, Q., Li, W.-Z., Zhu, X.-F.: Overview of fuel properties of biomass fast pyrolysis oils. Energy Conv. Manage. **50**(5), 1376–1383 (2009). https://doi.org/10.1016/j.enconman.2009.01.001
22. Shihadeh, A., Hochgreb, S.: Impact of biomass pyrolysis oil process conditions on ignition delay in compression ignition engines. Energy Fuels **16**(3), 552–561 (2002). https://doi.org/10.1021/ef010094d

23. Zhang, H., et al.: Biomass fast pyrolysis in a fluidized bed reactor under N_2, CO_2, CO, CH_4 and H_2 atmospheres. Biores. Technol. **102**(5), 4258–4264 (2011). https://doi.org/10.1016/j.biortech.2010.12.075
24. Oasmaa, A., Kuoppala, E.: Fast pyrolysis of forestry residue. 3. Storage stability of liquid fuel. Energy Fuels **17**(4), 1075–1084 (2003). https://doi.org/10.1021/ef030011o
25. Wang, J.-J., Chang, J., Fan, J.: Upgrading of bio-oil by catalytic esterification and determination of acid number for evaluating esterification degree. Energy Fuels **24**(5), 3251–3255 (2010). https://doi.org/10.1021/ef1000634.
26. Mendes, M.J., Santos, O.A.A., Jordão, E., Silva, A.M.: Hydrogenation of oleic acid over ruthenium catalysts. Appl. Catal. A General **217**(1), 253–262 (2001). https://doi.org/10.1016/S0926-860X(01)00613-5
27. Chen, X., et al.: Recent developments in lignocellulosic biomass catalytic fast pyrolysis: strategies for the optimization of bio-oil quality and yield. Fuel Process. Technol. **196**, 106180 (2019). https://doi.org/10.1016/j.fuproc.2019.106180.
28. Özsin, G.: Pütün, A.E.: A comparative study on co-pyrolysis of lignocellulosic biomass with polyethylene terephthalate, polystyrene, and polyvinyl chloride: Synergistic effects and product characteristics. J. Cleaner Prod. **205**, 1127–1138 (2018). https://doi.org/10.1016/j.jclepro.2018.09.134
29. Jamil, F., Ahmad, M.M., Yusup, S., Abdullah, B.: Upgrading of bio-oil from palm kernel shell by catalytic cracking in the presence of HZSM-5. Int. J. Green Energy **13**(4), 424–429 (2016). https://doi.org/10.1080/15435075.2014.966370
30. Stefanidis, S.D., Kalogiannis, K.G., Lappas, A.A.: Co-processing bio-oil in the refinery for drop-in biofuels via fluid catalytic cracking. WIREs Energy and Environ. **7**(3), e281 (2018). https://doi.org/10.1002/wene.281
31. Furimsky, E.: Catalytic hydrodeoxygenation. Appl. Catal. A General **199**(2), 147–190 (2000). https://doi.org/10.1016/S0926-860X(99)00555-4
32. Cheng, Y.-T., Wang, Z., Gilbert, C.J., Fan, W., Huber, G.W.: Production of p-Xylene from biomass by catalytic fast pyrolysis using ZSM-5 catalysts with reduced pore openings. Angew. Chem. Int. Ed. **51**(44), 11097–11100 (2012). https://doi.org/10.1002/anie.201205230
33. Bridgwater, A.V.: Review of fast pyrolysis of biomass and product upgrading. Biomass Bioenergy **38**, 68–94 (2012). https://doi.org/10.1016/j.biombioe.2011.01.048
34. Wang, K., Dayton, D.C., Peters, J.E., Mante, O.D.: Reactive catalytic fast pyrolysis of biomass to produce high-quality bio-crude. Green Chem **19**(14), 3243–3251 (2017). https://doi.org/10.1039/C7GC01088E
35. Artetxe, M., Lopez, G., Amutio, M., Elordi, G., Bilbao, J., Olazar, M.: Light olefins from HDPE cracking in a two-step thermal and catalytic process. Chem. Eng. J. **207–208**, 27–34 (2012). https://doi.org/10.1016/j.cej.2012.06.105
36. Aguado, J., Serrano, D.P., San Miguel, G., Castro, M.C., Madrid, S.: Feedstock recycling of polyethylene in a two-step thermo-catalytic reaction system. J.Analyt. Appl. Pyroly. **79**(1), 415–423 (2007). https://doi.org/10.1016/j.jaap.2006.11.008
37. Bezerra, F.A., Figueiredo, A.L., de Araujo, A.S., de Guedes, A.P.M.A.: Pirólise catalítica do PEBD usando como catalisador a vermiculita modificada TT—Catalytic pyrolysis of LDPE using modified vermiculite as a catalyst. Polímeros **26**(spe), 55–59, 2016. https://doi.org/10.1590/0104-1428.1761
38. Jae, J., et al.: Investigation into the shape selectivity of zeolite catalysts for biomass conversion. J. Catal. **279**(2), 257–268 (2011). https://doi.org/10.1016/j.jcat.2011.01.019
39. Tan, S., Zhang, Z., Sun, J., Wang, Q.: Recent progress of catalytic pyrolysis of biomass by HZSM-5. Chinese J. Catal. **34**(4), 641–650 (2013). https://doi.org/10.1016/S1872-2067(12)60531-2
40. Zheng, A., et al.: Effect of crystal size of ZSM-5 on the aromatic yield and selectivity from catalytic fast pyrolysis of biomass. J. Mol. Catal. A Chem. **383–384**, 23–30 (2014). https://doi.org/10.1016/j.molcata.2013.11.005
41. Dai, G., Wang, S., Zou, Q., Huang, S.: Improvement of aromatics production from catalytic pyrolysis of cellulose over metal-modified hierarchical HZSM-5. Fuel Process. Technol. **179**, 319–323 (2018). https://doi.org/10.1016/j.fuproc.2018.07.023

42. Liu, C., Wang, H., Karim, A.M., Sun, J., Wang, Y.: Catalytic fast pyrolysis of lignocellulosic biomass. Chem. Soc. Rev. **43**(22), 7594–7623 (2014). https://doi.org/10.1039/C3CS60414D
43. Wang, K., Ho Kim, K., Brown, R.C.: Catalytic pyrolysis of individual components of lignocellulosic biomass. Green Chem. **16**(2), 727–735 (2014). https://doi.org/10.1039/C3GC41288A
44. Sun, L., Zhang, X., Chen, L., Zhao, B., Yang, S., Xie, X.: Comparision of catalytic fast pyrolysis of biomass to aromatic hydrocarbons over ZSM-5 and Fe/ZSM-5 catalysts. J. Analyt. Appl. Pyrol. **121**, 342–346 (2016). https://doi.org/10.1016/j.jaap.2016.08.015
45. Zhang, Y., Chen, P., Lou, H.: In situ catalytic conversion of biomass fast pyrolysis vapors on HZSM-5. J. Energy Chem. **25**(3), 427–433 (2016). https://doi.org/10.1016/j.jechem.2016.03.014
46. Hu, C., Xiao, R., Zhang, H.: Ex-situ catalytic fast pyrolysis of biomass over HZSM-5 in a two-stage fluidized-bed/fixed-bed combination reactor. Biores. Technol. **243**, 1133–1140 (2017). https://doi.org/10.1016/j.biortech.2017.07.011
47. Stefanidis, S.D., et al.: Natural magnesium oxide (MgO) catalysts: A cost-effective sustainable alternative to acid zeolites for the in situ upgrading of biomass fast pyrolysis oil. Appl. Catal. B Environ. **196**, 155–173 (2016). https://doi.org/10.1016/j.apcatb.2016.05.031
48. Wang, D., Xiao, R., Zhang, H., He, G.: Comparison of catalytic pyrolysis of biomass with MCM-41 and CaO catalysts by using TGA–FTIR analysis. J. Analyt. Appl. Pyrol. **89**(2), 171–177 (2010). https://doi.org/10.1016/j.jaap.2010.07.008
49. Chen, X., Chen, Y., Yang, H., Chen, W., Wang, X., Chen, H.: Fast pyrolysis of cotton stalk biomass using calcium oxide. Biores. Technol. **233**, 15–20 (2017). https://doi.org/10.1016/j.biortech.2017.02.070
50. Deoxygenation of bio-oil during pyrolysis of biomass in the presence of CaO in a fluidized-bed reactor | energy & fuels. https://pubs.acs.org/doi/10.1021/ef1009605. Acessado 21 Mar 2021
51. Pütün, E.: Catalytic pyrolysis of biomass: effects of pyrolysis temperature, sweeping gas flow rate and MgO catalyst. Energy **35**(7), 2761–2766 (2010). https://doi.org/10.1016/j.energy.2010.02.024
52. Sun, L., Zhang, X., Chen, L., Zhao, B., Yang, S., Xie, X.: Effects of Fe contents on fast pyrolysis of biomass with Fe/CaO catalysts. J. Analyt. Appl. Pyrol. **119**, 133–138 (2016). https://doi.org/10.1016/j.jaap.2016.03.008
53. Zhang, X., et al.: Comparison of catalytic upgrading of biomass fast pyrolysis vapors over CaO and Fe(III)/CaO catalysts. J. Analyt. Appl. Pyrol. **108**, 35–40 (2014). https://doi.org/10.1016/j.jaap.2014.05.020
54. Ozbay, N., Yargic, A.S., Yarbay Sahin, R.Z.: Tailoring Cu/Al2O3 catalysts for the catalytic pyrolysis of tomato waste. J. Energy Inst. **91**(3), 424–433 (2018). https://doi.org/10.1016/j.joei.2017.01.010
55. Torri, C., Reinikainen, M., Lindfors, C., Fabbri, D., Oasmaa, A., Kuoppala, E.: Investigation on catalytic pyrolysis of pine sawdust: catalyst screening by Py-GC-MIP-AED. J. Analyt. Appl. Pyrol. **88**(1), 7–13 (2010). https://doi.org/10.1016/j.jaap.2010.02.005
56. Oasmaa, A., Czernik, S.: Fuel oil quality of biomass pyrolysis oilsstate of the art for the end users. Energy Fuels **13**(4), 914–921 (1999). https://doi.org/10.1021/ef980272b
57. Persson, H., Duman, I., Wang, S., Pettersson, L.J., Yang, W.: Catalytic pyrolysis over transition metal-modified zeolites: a comparative study between catalyst activity and deactivation. J. Analyt. Appl. Pyrol. **138**, 54–61 (2019). https://doi.org/10.1016/j.jaap.2018.12.005
58. Moud, P.H., Kantarelis, E., Andersson, K.J., Engvall, K.: Biomass pyrolysis gas conditioning over an iron-based catalyst for mild deoxygenation and hydrogen production. Fuel **211**, 149–158 (2018). https://doi.org/10.1016/j.fuel.2017.09.062
59. Olcese, R.N., Francois, J., Bettahar, M.M., Petitjean, D., Dufour, A.: Hydrodeoxygenation of guaiacol, a surrogate of lignin pyrolysis vapors, over iron based catalysts: kinetics and modeling of the lignin to aromatics integrated process. Energy Fuels **27**(2), 975–984 (2013). https://doi.org/10.1021/ef301971a
60. Sonoyama, N., et al.: Production of chemicals by cracking pyrolytic tar from Loy Yang coal over iron oxide catalysts in a steam atmosphere. Fuel Process. Technol. **92**(4), 771–775 (2011). https://doi.org/10.1016/j.fuproc.2010.09.036

61. Campelo, J.M., Luna, D., Luque, R., Marinas, J.M., Romero, A.A.: Sustainable preparation of supported metal nanoparticles and their applications in catalysis. ChemSusChem **2**(1), 18–45 (2009). https://doi.org/10.1002/cssc.200800227
62. Wang, Y., De, S., Yan, N.: Rational control of nano-scale metal-catalysts for biomass conversion. Chem. Commun. **52**(37), 6210–6224 (2016). https://doi.org/10.1039/C6CC00336B
63. Mintova, S., Jaber, M., Valtchev, V.: Nanosized microporous crystals: emerging applications. Chem. Soc. Rev. **44**, 2015. https://doi.org/10.1039/c5cs00210a
64. Li, Y., et al.: Pyrolysis of Aesculus chinensis Bunge Seed with Fe_2O_3/NiO as nanocatalysts for the production of bio-oil material. J. Hazard. Mater. 126012 (2021). https://doi.org/10.1016/j.jhazmat.2021.126012
65. Balasubramanian, S., Wang, P., Schaller, R.D., Rajh, T., Rozhkova, E.A.: High-Performance bioassisted nanophotocatalyst for hydrogen production. Nano Lett. **13**(7), 3365–3371 (2013). https://doi.org/10.1021/nl4016655
66. Carenco, S., et al.: Nickel phosphide nanocatalysts for the chemoselective hydrogenation of alkynes. Nano Today **7**(1), 21–28 (2012). https://doi.org/10.1016/j.nantod.2011.12.003
67. Sudarsanam, P., Peeters, E., Makshina, E.V., Parvulescu, V.I., Sels, B.F.: Advances in porous and nanoscale catalysts for viable biomass conversion. Chem. Soc. Rev. **48**(8), 2366–2421 (2019). https://doi.org/10.1039/C8CS00452H
68. Gökdai, Z., Sınağ, A., Yumak, T.: Comparison of the catalytic efficiency of synthesized nano tin oxide particles and various catalysts for the pyrolysis of hazelnut shell. Biomass Bioenergy **34**(3), 402–410 (2010). https://doi.org/10.1016/j.biombioe.2009.12.003
69. Ngo, H.L., Nuñez, A., Lin, W., Foglia, T.A.: Zeolite-catalyzed isomerization of oleic acid to branched-chain isomers. Eur. J. Lipid Sci. Technol. **109**(3), 214–224 (2007). https://doi.org/10.1002/ejlt.200600246
70. Li, J., Xiao, B., Du, L., Yan, R., Liang, T.D.: Preparation of nano-NiO particles and evaluation of their catalytic activity in pyrolyzing cellulose. J. Fuel Chem. Technol. **36**(1), 42–47 (2008). https://doi.org/10.1016/S1872-5813(08)60010-9
71. Wang, D., Yang, P., Ma, Q., Cao, Y., Zhang, A., Huang, B.: Micro- and nano-structures of iron oxide with tunable morphologies fabricated via solvothermal process. CrystEngComm **15**(44), 8959–8965 (2013). https://doi.org/10.1039/C3CE41085D
72. Tosoni, S., Chen, H.-Y. T., Ruiz Puigdollers, A., Pacchioni, G.: TiO_2 and ZrO_2 in biomass conversion: why catalyst reduction helps. Philos. Trans. Royal Soc. A Math. Phys. Eng. Sci. **376**(2110), 20170056 (2018). https://doi.org/10.1098/rsta.2017.0056
73. Rogers, K.A., Zheng, Y.: Selective Deoxygenation of Biomass-derived bio-oils within hydrogen-modest environments: a review and new insights. ChemSusChem **9**(14), 1750–1772 (2016). https://doi.org/10.1002/cssc.201600144
74. Decostanzi, M., Auvergne, R., Boutevin, B., Caillol, S.: Biobased phenol and furan derivative coupling for the synthesis of functional monomers. Green Chem. **21**(4),724–747 (2019). https://doi.org/10.1039/C8GC03541E
75. Lu, Q., Dong, C., Zhang, X., Tian, H., Yang, Y., Zhu, X.: Selective fast pyrolysis of biomass impregnated with ZnCl2 to produce furfural: analytical Py-GC/MS study. J. Analyt. Appl. Pyrol. **90**(2), 204–212 (2011). https://doi.org/10.1016/j.jaap.2010.12.007
76. Mian, M.M., Liu, G.: Sewage sludge-derived TiO_2/Fe/Fe_3C-biochar composite as an efficient heterogeneous catalyst for degradation of methylene blue. Chemosphere **215**, 101–114 (2019). https://doi.org/10.1016/j.chemosphere.2018.10.027.
77. Wang, F., et al.: Simultaneous phase and size control of upconversion nanocrystals through lanthanide doping. Nature **463**(7284), 1061–1065 (2010). https://doi.org/10.1038/nature08777
78. Bai, X., et al.: Preparation of furfural by catalytic pyrolysis of cellulose based on nano Na/Fe-solid acid. Fuel **258**, 116089 (2019). https://doi.org/10.1016/j.fuel.2019.116089
79. Guo, F., Jia, X., Liang, S., Zhou, N., Chen, P., Ruan, R.: Development of biochar-based nanocatalysts for tar cracking/reforming during biomass pyrolysis and gasification. Biores. Technol. **298**, 122263 (2020). https://doi.org/10.1016/j.biortech.2019.122263

80. Védrine, J.C.: Heterogeneous catalysis on metal oxides. Catalysts **7**(11), (2017). https://doi.org/10.3390/catal7110341
81. Dong, Y. et al.: Application of low-cost Fe-based catalysts in the microwave-assisted pyrolysis of macroalgae and lignocellulosic biomass for the upgradation of bio-oil. Fuel **300**, 120944 (2021). https://doi.org/10.1016/j.fuel.2021.120944
82. Murata, K., Kreethawate, L., Larpkiattaworn, S., Inaba, M.: Evaluation of Ni-based catalysts for the catalytic fast pyrolysis of jatropha residues. J. Analyt. Appl. Pyrol. **118**, 308–316 (2016). https://doi.org/10.1016/j.jaap.2016.02.014.
83. Murata, K., Khongwong, W., Larpkattaworn, S., Liu, Y., Inaba, M., Takahara, I.: Evaluation of PtPd-modified zeolite catalysts (ZSM-5, beta, USY) for pyrolysis of Jatropha Waste. J. Jpn. Pet. Inst. **57**(3), 133–145 (2014). https://doi.org/10.1627/jpi.57.133
84. Lu, Q. et al.: Experimental study on catalytic pyrolysis of biomass over a Ni/Ca-promoted Fe catalyst. Fuel **263**, 116690 (2020). https://doi.org/10.1016/j.fuel.2019.116690
85. Dai, L. et al.: Synthesis of iron nanoparticles-based hydrochar catalyst for ex-situ catalytic microwave-assisted pyrolysis of lignocellulosic biomass to renewable phenols. Fuel **279**, 118532 (2020). https://doi.org/10.1016/j.fuel.2020.118532
86. Guo, F., Peng, K., Liang, S., Jia, X., Jiang, X., Qian, L.: One-step synthesis of biomass activated char supported copper nanoparticles for catalytic cracking of biomass primary tar. Energy **180**, 584–593 (2019). https://doi.org/10.1016/j.energy.2019.05.115
87. Donar, Y.O., Sınağ, A.: Catalytic effect of tin oxide nanoparticles on cellulose pyrolysis. J. Analyt. Appl. Pyrol. **119**, 69–74 (2016). https://doi.org/10.1016/j.jaap.2016.03.016
88. Atanda, L., et al.: Hybridization of ZSM-5 with spinel oxides for biomass vapour upgrading. ChemCatChem **12**(5), 1403–1412 (2020). https://doi.org/10.1002/cctc.201902023
89. Zhang, H., Xiao, R., Jin, B., Xiao, G., Chen, R.: Biomass catalytic pyrolysis to produce olefins and aromatics with a physically mixed catalyst. Bioresour. Technol. **140**, 256–262. (2013). https://doi.org/10.1016/j.biortech.2013.04.094
90. Che, Q. et al.: Aromatics production with metal oxides and ZSM-5 as catalysts in catalytic pyrolysis of wood sawdust. Fuel Process. Technol. **188**, p. 146–152, jun. 2019, doi: https://doi.org/10.1016/j.fuproc.2019.02.016.
91. Abu-Dief, A.M., Abdel-Fatah, S.M.: Development and functionalization of magnetic nanoparticles as powerful and green catalysts for organic synthesis. Beni-Suef Univ. J. Basic Appl. Sci. **7**(1), 55–67 (2018). https://doi.org/10.1016/j.bjbas.2017.05.008
92. Zhang, Z., Li, K., Ma, S., Cui, M., Lu, Q., Yang, Y.: Fast pyrolysis of biomass catalyzed by magnetic solid base catalyst in a hydrogen atmosphere for selective production of phenol. Ind. Crops Prod. **137**, 495–500 (2019). https://doi.org/10.1016/j.indcrop.2019.05.066
93. Tripathy, A., Nine, M.J., Silva, F.S.: Biosensing platform on ferrite magnetic nanoparticles: synthesis, functionalization, mechanism and applications. Adv. Colloid Interface Sci. **290**, 102380 (2021). https://doi.org/10.1016/j.cis.2021.102380.

Iron-Based Nanomaterials for Fenton Reaction

Thays de Oliveira Guidolin, Maria Alice Prado Cechinel, and Sabrina Arcaro

Abstract Fenton process is widely recognized as an efficient technique for degrading complex organic pollutants. The method is based on the hydrogen peroxide decomposition by an iron catalyst, forming highly reactive hydroxyl radicals. It can be used together with other techniques coupled to the system that improves the degradation mechanism, such as electrodes, ultrasound, irradiation, or solid catalysts. In addition, several materials can be used as heterogeneous Fenton catalysts for oxygen-active species formation. With the advancement of nanotechnology, the development and application of iron-based nanomaterials for contaminated water treatment have increased. This chapter brings a discussion about Fenton processes for degrading organic compounds present in water and recent advances related to the use of nanomaterials in this process, especially those derived from iron oxides.

Keywords Fenton Oxidation · Iron-Based Nanomaterials · Iron Oxides

1 Introduction

Currently, researchers around the world are looking for water treatment processes that remove pollutants more effectively. These processes can be simple methods or a combination of methods that complement each other [1]. For example, many personal, pharmaceuticals, and industrial chemical products are found in aquatic environments, in addition to urban and agricultural wastewater that carries many organic chemicals [2]. Unfortunately, these pollutants are often recalcitrant and

T. de Oliveira Guidolin (✉) · M. A. P. Cechinel · S. Arcaro
Grupo de Biomateriais e Materiais Nanoestruturados, Programa de Pós-Graduação em Ciência e Engenharia de Materiais, Universidade do Extremo Sul Catarinense, Av. Universitária 1105, P.O. Box 3167, Criciúma 88806-000, Brazil

M. A. P. Cechinel
e-mail: maria.cechinel@unesc.net

S. Arcaro
e-mail: sarcaro@unesc.net

A. Kopp Alves (ed.), *Environmental Applications of Nanomaterials*, Engineering Materials, https://doi.org/10.1007/978-3-030-86822-2_8

emerge as a challenge to conventional water treatment plants due to their high toxicity [3].

As a solution to these issues, Advanced Oxidative Processes (AOPs) have been widely used to treat organic contaminants due to their high oxidation capacity. The applications of these processes are vast, with emphasis on the remediation of agrochemical industrial effluents, pulp and paper, textiles, oil fields and metallization residues; treatment of hospital waste, slaughterhouses, pathogens and pharmaceutical waste, as well as heavy metals such as arsenic and chromium [1]. Among the existing AOP's, Fenton's oxidation, photochemistry, electrochemistry, ozonization, gamma-ray, persulfate-based, humid air, and ultrasound stand out [4].

The Fenton process is the most used among these oxidizing mechanisms due to its efficiency in degrading overly complex organic pollutants, such as polycyclic aromatic hydrocarbons (PAHs). This method consists of decomposing hydrogen peroxide by the catalytic action of iron, forming hydroxyl radicals, which are highly oxidizing [5]. Furthermore, Fenton reactions can be used together with other techniques to improve this mechanism. Figure 1 shows this derived Fenton process from the addition of different techniques to the system. When using ultrasound, these methods are usually sono-Fenton, electro-Fenton, when using electrodes, and photo-Fenton, when using irradiation.

The system using light irradiation in the Fenton system (photo-Fenton) is most commonly reported in the literature as the degradation of organic pollutants can be accelerated by the ability of light to reduce Fe^{3+} to Fe^{2+} ions [6]. Another combination that similarly contributes to the Fenton oxidation is the use of high-frequency acoustic cavitation. This mechanism, called sono-Fenton, uses ultrasound waves to generate cavitation bubbles that break the bonds of water molecules forming •OH [7]. Another widely used technique is electro-Fenton, whose pollutant degradation occurs from the oxidizing agent generation (•OH) *in-situ*, which moves from the electrode surface and reacts in the solution. The electrode is immersed in a mixture of H_2O_2 and ferrous

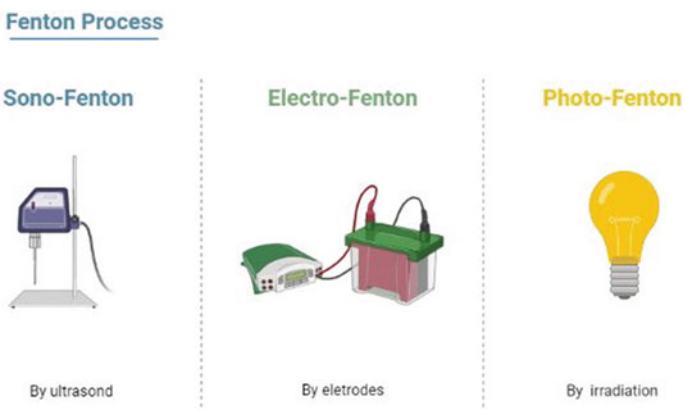

Fig. 1 Derived fenton process and its techniques

ions [8]. The oxidation mechanisms of the Fenton Process and its conjugates will be discussed more fully in Sect. 8 of this chapter.

2 Fenton Process

The Fenton process consists of reactions where hydrogen peroxide is catalyzed by iron ions, generating oxygen-active species that oxidize organic and inorganic compounds. Henry J. Fenton described the Fenton reaction in 1894, showing that hydrogen peroxide (H_2O_2) could be activated by ferrous salts (Fe^{2+}), oxidizing tartaric acid [9]. In 1934, Haber et al. [10] described that hydroxyl radicals (•OH) are the components present in Fenton reactions. According to Zhang et al. [11], the oxidation mechanism for the Fenton process has been studied for almost 90 years. Research shows that Fenton's oxidation process includes more than twenty chemical reactions, highlighting Eqs. 1–10:

$$Fe^{2+} + H_2O_2 \rightarrow Fe^{3+} + OH^- + \bullet OH \quad (1)$$

$$Fe^{3+} + H_2O_2 \rightarrow Fe^{2+} + H^+ + \bullet O_2H \quad (2)$$

$$Fe^{2+} + \bullet OH \rightarrow Fe^{3+} + OH^- \quad (3)$$

$$Fe^{2+} + \bullet O_2H \rightarrow Fe^{3+} + HO_2^- \quad (4)$$

$$Fe^{3+} + \bullet O_2H \rightarrow Fe^{2+} + H^+ + O_2 \quad (5)$$

$$\bullet OH + \bullet OH \rightarrow H_2O_2 \quad (6)$$

$$\bullet OH + H_2O_2 \rightarrow \bullet O_2H + H_2O \quad (7)$$

$$\bullet O_2H + \bullet O_2H \rightarrow H_2O_2 + O_2 \quad (8)$$

$$\bullet OH + \bullet O_2H \rightarrow H_2O + O_2 \quad (9)$$

$$2\,H_2O_2 \rightarrow O_2 + 2H_2O \quad (10)$$

In the primary reaction (Eq. 1), known as the Fenton Reaction, hydrogen peroxide is activated by ferrous ions (Fe^{2+}), generating ferric ions (Fe^{3+}) and hydroxyl radicals. Ferric ions can be reduced by reacting with excess hydrogen peroxide to form ferrous

ions again and more radicals (Eq. 2). Hydroperoxyl radicals ($\bullet O_2H$) are produced, which can oxidize organic components less effectively [9].

Equations 3, 4, and 5 are reactions present in the Fenton oxidation process and represent, together with Eq. 2, the limiting steps of the Fenton reaction, as there is the consumption of oxygen-active species. The produced radicals can be eliminated by the action of ferrous ions (Eq. 3), by reaction with peroxide (Eq. 7), by hydroperoxyl radicals (Eq. 9), and even be eliminated by itself (Eqs. 6 and 8) [9]. The decomposition of hydrogen peroxide into molecular oxygen and water takes place according to Eq. (10).

The equations presented prove the complex mechanism associated with Fenton reactions. In the same way that hydrogen peroxide acts as a radical generator, as illustrated in Eq. 1, it can also act as a scavenger of these radicals. The hydroxyl radicals generated are compounds with high redox potential, as shown in Table 1, which compares the redox potentials values of some species.

Note that the redox potential of the hydroxyl radical (2.8 V) is only lower than that of fluorine (3.03 V), proving its high performance. Another radical present in Fenton's equations, the hydroperoxyl radical ($\bullet O_2H$), has a low redox potential, confirming its lower capacity to oxidize organic species.

The traditional Fenton reaction, also known as homogeneous Fenton, has some operational disadvantages that make it difficult to operate on a large scale or in some specific treatment processes. Among the disadvantages, we can list the high consumption of hydrogen peroxide, the restricted pH range for effective operation (pH~3), and the excessive generation of ferric hydroxide and consequent sludge formation. Therefore, researchers have begun to investigate Fenton's heterogeneous catalysis [13–15]. In this process, iron is stable in a solid structure, decomposing the H_2O_2 into $\bullet OH$ without leaching iron ions into the solution, preventing its precipitation. The more stable condition of the catalysts used in the heterogeneous Fenton reaction also guarantees a wide range of working pH values and allows for easy recovery and reuse of the material [14].

Table 1 Redox potentials of some compounds [1, 12]

Species	Redox potencial (V)
Fluorine	3.03
Hydroxyl radical	2.8
Atomic oxygen	2.42
Ozone	2.07
Hydrogen peroxide	1.78
Hydroperoxyl radical	1.70
Permanganate	1.68
Chlorine dioxide	1.57
Chlorine	1.36
Iodine	0.54

The heterogeneous catalysts used in the Fenton oxidation process can be materials of different types, such as zero-valent iron, some types of soils rich in iron, iron oxides, and residual materials with iron in their composition. Among the iron oxides, it can be mentioned ferrihydrite ($Fe_5HO_8.\ 4H_2O$) [16], hematite (α-Fe_2O_3) [17], goethite (α-FeOOH) [18], lepidocrocite (γ-FeOOH) [19], maghemite (γ-Fe_2O_3) [20] and pyrite (FeS_2). Among the soils are hydroxides (LDHs) [21] and pillared clays [22]. Among the residues used as catalysts can be cited fly ash, pyrite ash, and blast furnace dust [23]. These catalysts are often supported by other materials to maintain iron immobilization. The most common supports are clay, activated carbon, alumina, silica, zeolites, fibers in general, biosorbents, and hydrogels [23].

The use of iron-based nanomaterials as catalysts brings new application perspectives for Fenton reactions. Nanomaterials have a better catalytic performance when compared to the same materials on the micro-scale. This fact is mainly due to the large surface area that gives greater chemical reactivity [24]. According to Zeidman et al. [25], the use of immobilized nanomaterials in AOPs has been reported to be highly efficient in the degradation of emerging organic compounds such as antibiotics. Some iron-based nanomaterials most used in Fenton oxidation processes will be discussed in Sect. 4 of this chapter.

2.1 Photo-Fenton

As previously presented, the photo-Fenton process is a branch of the homogeneous Fenton process where there is a combination of hydrogen peroxide with Fe^{2+} ions and irradiation. Overall, the photo-Fenton system produces more hydroxyl radicals than the Fenton process alone, increasing the rate of organic pollutants degradation [26]. The radiation effect in the system is attributed to the photo-reduction of Fe^{3+} to Fe^{2+} in parallel with the photolysis of H_2O_2 (UV/H_2O_2). Thus, different reactions occur in the system and are represented in Eqs. 11 and 12.

$$Fe^{3+} + H_2O_2 + hv \rightarrow Fe^{2+} + \bullet OH \tag{11}$$

$$H_2O_2 + hv \rightarrow \bullet OH + \bullet OH \tag{12}$$

The regeneration of Fe^{2+} by photo-reduction of Fe^{3+} is accelerated in this process (Eq. 11), providing an increase in the formation of hydroxyl radicals. Furthermore, the photolysis reaction of H_2O_2 (Eq. 12) also produces •OH, contributing to the oxidation efficiency. Figure 2 shows a representative scheme of the photo-Fenton reaction.

In the photo-Fenton system, the type of light source interferes with the pollutants degradation performance. In the case of lamps, commonly used in this process, the model and its power can interfere with its efficiency. Commonly used artificial lamps emit UVA with $\lambda = 315–400$ nm, UVB with $\lambda = 280–315$ nm, or UVC with $\lambda =$

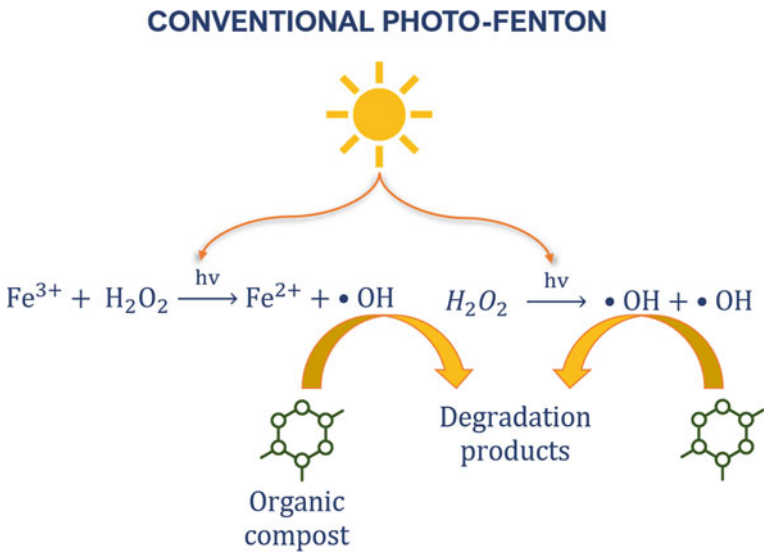

Fig. 2 Conventional photo-Fenton reaction

100–280 nm [27]. Studies show that the shorter the wavelength, the greater the efficiency of photoreduction. In this case, ultraviolet radiation (with $\lambda < 400$ nm) is highlighted in the application for photo-Fenton reactions. However, at wavelengths above 320 nm, photolysis of H_2O_2 does not occur. Thus, UVA radiation does not activate the decomposition of H_2O_2, only participates in the iron photo-reduction.

The increase in radiation energy positively influences the catalytic activity of the system. When changing an 8 W for a 16 W lamp, for example, there is an increase in the rate of iron photo-reduction and a more significant formation of hydroxyl radicals, enhancing photo-Fenton degradation [11]. Wavelength radiation in visible and near-ultraviolet range (between 400 and 700 nm, approximately) also showed efficiency in the degradation of some organic pollutants, including 4-chlorophenol, nitrobenzene, anisole, herbicides, and ethylene glycol [26].

In general, the photo-Fenton process takes place at a pH close to 3, with a molar ratio of H_2O_2/Fe between 2 and 150 and a molar ratio of H_2O_2/DQO between 1 and 3.5. A disadvantage of this process is the low pH, which makes large-scale application difficult. For the photo-Fenton reaction to occur at pH close to neutral (6.5–7.5), it would be necessary to add chelating agents to the system, forming organic complexes of dissolved iron. An advantage of this process is the use of a low iron concentration for the reaction. As photons quickly regenerate iron, it is not necessary to use it in high amounts. Furthermore, removing iron from the solution after the oxidation process may be unnecessary if the concentration is below the limit imposed for disposal [28].

2.2 *Sono-Fenton*

The sonochemical degradation process emerged in the 1990s and is characterized using ultrasound waves that propagate with compression and rarefaction cycles, generating the phenomenon of acoustic cavitation. Cavitation generates numerous bubbles in the system, called microreactors, and at its center, chemical reactions occur [29]. The cavitation bubbles violently collapse and produce localized shock waves, with a temperature around 5000 °C and pressure close to 500 atm for a few microseconds. This extreme condition called a "hot spot," allows the pyrolytic cleavage of water molecules into a hydrogen atom and a hydroxyl radical [30]. Equations 13–15 present the generation process of oxygen-active species, while Eqs. 16 and 17 show how pollutants are degraded using ultrasound. The symbol ")))" indicates the presence of ultrasound.

$$H_2O+))) \rightarrow \bullet OH + \bullet H \tag{13}$$

$$O_2+))) \rightarrow \bullet O + \bullet O \tag{14}$$

$$H_2O + \bullet O \rightarrow \bullet OH + \bullet OH \tag{15}$$

$$\text{Pollutants} +))) \rightarrow \text{degradation products} \tag{16}$$

$$\text{Pollutants} + \bullet OH \rightarrow \text{degradation products} \tag{17}$$

Ultrasound can be used for the degradation of the pollutant without the addition of chemical substances, through high temperature (Eq. 16) or by the oxidative attack of hydroxyl radicals (Eq. 17) [31]. A wide variety of organic pollutants can be degraded using sonochemical degradation without chemicals, making this technique environmentally safe. However, its application is limited. The main disadvantage is the excessive use of energy to carry out the process. Therefore, combining this method with the Fenton reaction becomes interesting, aiming at high process efficiency and low operating cost. The method is called sono-Fenton, where sonication improves mass transfer, increasing •OH formation and decreasing chemical consumption.

On the other hand, it is ideal for adding the right amount of Fe^{2+} to react with the H_2O_2 and amplify the •OH production. Figure 3 illustrates the mechanism of the sono-Fenton process reaction for the degradation of antibiotics, presented by Liu et al. (2021) [29]. As shown, iron corrosion at the solid–liquid interface, oxygen activation, and Fenton reactions are the primary oxidation pathways in the sono-Fenton processes, during which sonication performs mechanical and chemical functions [29]. In addition to pharmaceutical compounds, the sono-Fenton process is efficient in degrading dyes and pesticides [32].

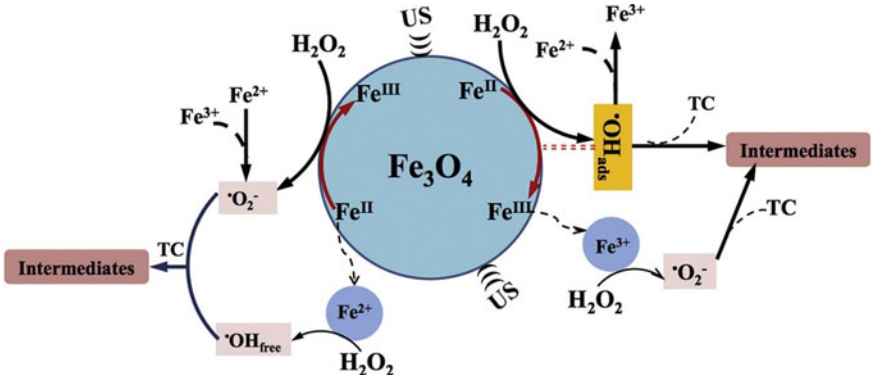

Fig. 3 Mechanism schematic of sono/Fenton-like processes. Reprinted from ref. [29] Copyright (2021), with permission from Elsevier

2.3 Electro-Fenton

The mechanism of the electro-Fenton process is composed of a few steps:

1. H_2O_2 electrogeneration in situ from the O_2 cathodic reduction, step dependent on the intensity of the applied current and the dissolved O_2;
2. •OH formation through the Fenton reaction between ferrous ions and the electrogenerated H_2O_2;
3. •OH formation on the electrode surface, which occurs when materials such as diamond are doped with boron (BDD) and are used as anodes; and
4. regeneration of Fe^{3+} to Fe^{2+} by direct cathode reduction.

Equations 18–20 show the reactions of oxygen-active species formation and Fe regeneration [8, 33]:

$$O_2 + 2\,H^+ + 2e^- \rightarrow\ H_2O_2 \tag{18}$$

$$Fe^{2+} + H_2O_2 \rightarrow Fe^{3+} + OH^- + \bullet OH \tag{19}$$

$$Fe^{3+} + e^- \rightarrow Fe^{2+} \tag{20}$$

The electro-Fenton is characterized as an advanced and sustainable electrochemical oxidation technique. Figure 4 illustrates the mechanism of the electro-Fenton process, presented by Nidheesh [34].

The most exciting feature of this process is the continuous electrogenerated of H_2O_2, making the transport and storage of this chemical indispensable [35]. Another attractive advantage is the constant regeneration of Fe^{2+} at the cathode (Eq. 20), causing a high mineralization rate and avoiding the Fe^{3+} accumulation in the solution and possible sludge formation. Electro-Fenton becomes much more effective

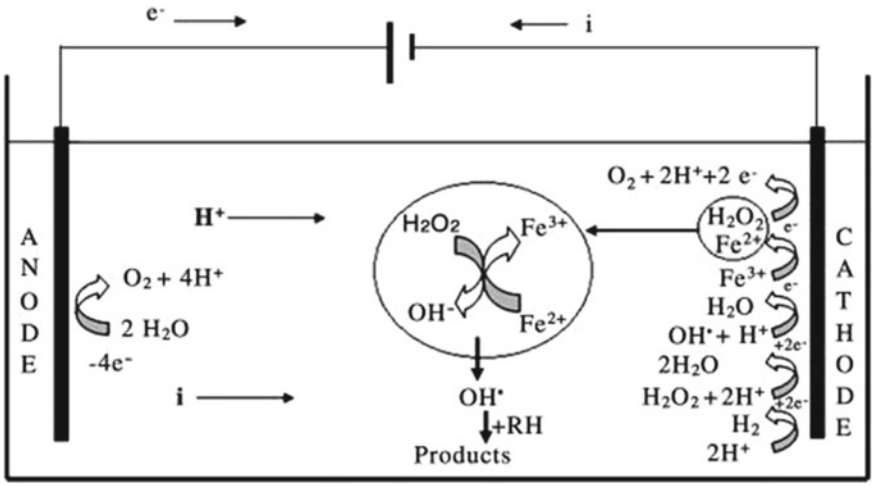

Fig. 4 Reaction mechanism of Electro-Fenton process. Reprinted from ref. [34] Copyright (2021), with permission from Elsevier

compared to electrochemical oxidation and the Fenton reaction [36]. On the other hand, the most significant disadvantage is the high energy consumption to reach complete mineralization, generating a high cost for the process. A combination of biological treatments could be used to solve this problem, for example, making the process successful [37].

2.4 Operating Parameters

The main operating parameters that have a significant effect on the effectiveness of the Fenton reaction are pH, catalyst concentration, H_2O_2 concentration, and the concentration of the pollutant in the solution. Therefore, these parameters need to be studied and optimized to obtain the best process efficiency with the lowest operating cost [11].

Solution pH is considered one of the main factors that affect the Fenton process performance, as it influences the oxidizing activity of the system [38]. At lower pH ranges (up to pH~2), the hydroxyl radical reacts with the H^+ ions in the solution instead of oxidizing the organic pollutants. Thus, there is a reduction in the oxidation capacity of the Fenton process. At higher pH values, there is hydrolysis and precipitation of Fe^{3+} present in the solution and, therefore, there is a decrease in the catalytic capacity to form •OH [11]. The pH also changes the stability of H_2O_2: at very acidic pH, H_2O_2 becomes stable, creating $H_3O_2^+$, decreasing the rate of •OH formation [39]; the alkaline pH ranges promote the decomposition of H_2O_2 and also reduce the generation of hydroxyl radicals and the oxidizing activity of the system [40]. When

it comes to homogeneous Fenton Reactions, the oxidation of the pollutants occurs more satisfactorily in pH between 2 and 4 [38].

The concentration of H_2O_2 in the Fenton process is another critical parameter, as both excess and lack of this reagent can cause •OH extinction. When adding a low amount of H_2O_2, there may be insufficient hydroxyl radicals in the system, and the oxidation will take place inefficiently. On the other hand, the excess of reagent, in addition to producing hydroxyl radicals, will produce other substances, such as the hydroperoxyl radical ($•O_2H$), which decreases the contaminant oxidation rate [38]. Some studies indicate efficient oxidation results using low H_2O_2concentrations due to the use of modified heterogeneous catalysts. For example, Dantas et al. (2006) [41] used a heterogeneous catalyst to treat textile industry wastewater by a heterogeneous Fenton process. As a result, it was necessary to consume less hydrogen peroxide than in the homogeneous Fenton process and apply the process at a pH above 3.0.

The concentration of the pollutant in the wastewater influences the degree of oxidation. In general, high pollutants concentrations lead to low degradation efficiency. In addition to the difficulty of oxidizing the contaminants, the reaction time becomes more prolonged, and the expenses with Fenton's reagents also increase. In many studies where there is a high concentration of organic compounds, the Fenton reaction does not reach the complete mineralization of the system due to the total consumption of the oxidizing agent and catalyst [11]. Thus, there may be a more significant amount of intermediate products formed [39]. However, there are cases where the increase in the pollutant concentration causes more significant degradation in the system. This happens due to the limitation of mass transfer between •OH radicals and pollutant molecules. A higher concentration of contaminant increases the number of collisions with the •OH molecules, optimizing the oxidation of the compound [40].

Finally, iron is the commonly used material regarding the catalyst used in Fenton reactions because it is more economical, safer, and ecologically correct. However, other transition metals can be used for the same function, such as copper, ruthenium, cerium, and manganese. The requirement is that the metal has at least two oxidation states. However, Fe^{2+} has higher performance compared to other catalysts [42]. The catalyst concentration used in the process is linked to the efficiency of organic pollutants degradation. According to Zhang et al. [11], the degradation of pollutants intensifies with the increase in the Fe^{2+} concentration; however, the unrestricted addition can harm the process since the excess of Fe^{2+} causes the scavenging of hydroxyl radicals. Furthermore, when it comes to a homogeneous Fenton reaction, the accumulation of Fe^{2+} in solution causes sludge formation and an increase in total dissolved solids and the conductivity in the generated effluent [38].

As described in Sect. 2 of this chapter, many iron-based materials are used as catalysts in oxidative processes. In recent years, with the advancement of the nanotechnology area, there has been a growing interest in developing and applying new nanomaterials in the environmental area to treat contaminated water. Recent applications of iron oxide nanomaterials in Fenton processes will be discussed in Sect. 3 of this chapter.

3 Nanomaterials

Nanomaterials have morphological characteristics that facilitate their application in catalytic and adsorptive processes, such as a significant relationship between surface and volume and high surface charges [43]. Furthermore, the activity and selectivity of nanoparticles depend on their size, shape, surface structure, and bulk composition, which can be appropriately adjusted during their synthesis.

The morphology and reactivity of the exposed faces of nanometric materials directly influence the activation of H_2O_2 through the absorption of Fe^{2+} and other reactive species on its surface [14, 44–46]. The importance of nanoparticle morphology is evidenced by studies carried out in recent years, especially with hematite, to obtain catalysts with specific faces used in environmental remediation processes [45, 47–49]. Huang et al. [48] report that ferrous ions confined to specific faces of the hematite crystal can significantly promote the decomposition of H_2O_2 to produce •OH than unconfined counterparts. Hematite nanorods with {001} and {110} exposed faces exhibit a better confinement effect than nanoplates with {001} exposed faces. Zhong et al. [50] identified that the catalytic activity of Fe_3O_4 in different morphologies, under UVA irradiation, followed the order: nanospheres > nanoplates > nanooctahedra ≈ nanocubes > nanorods. The greater catalytic performance of Fe_3O_4 nanospheres was attributed to their smaller particle size but above all to the larger specific surface area and greater exposure of {111} reactive faces. Huang et al. [49] reported that hematite nanocubes with {002} exposed faces in the presence of ascorbate exhibited lower Fenton catalytic performance when compared to hematite nanoplates with {001} exposed faces.

The surface area of iron base nanomaterials is also an essential factor influencing the degradation of organic pollutants by the Fenton reaction. Kwan and Voelker [51] described a method to determine the rate of hydroxyl radicals formation in iron oxide/hydrogen peroxide systems. In this method, the amount of •OH generated is proportional to the surface area concentrations of iron oxide and hydrogen peroxide, with a different proportionality coefficient for each iron oxide. Wan et al. [52] evaluated the performance of Fe_3O_4 nanoparticles with mean diameters between 30 and 600 nm. The result obtained proved that the surface area was more remarkable for the smaller particles and that the catalytic activity increased with the reduction in the size of the nanoparticles, as there is a greater specific surface area to interact with the substrate [53].

Another attractive property of iron-based nanomaterials is that the magnetic properties are related to the composition of the nanomaterials and the size of the particles [54]. For example, Fe_3O_4 is ferrimagnetic at room temperature, while Fe_3O_4 with a size below 6–8 nm is superparamagnetic [55]. This magnetic characteristic is attractive because it favors an easy, fast and economic separation by applying a magnetic field, simplifying the recovery and reuse of the catalyst, which are critical points for large-scale application [56]. However, it has been stated that the magnetism of ferromagnetic nanoparticles favors the aggregation of nanoparticles, thus reducing

their dispersibility and activity [57]. Furthermore, the immobilization of ferromagnetic nanoparticles on high surface supports has been reported as an ecologically friendly solution that maintains the unique properties of these materials [58–60]. Recent literature brings two trends in the nanomaterials preparation: the synthesis of composites where iron is part of the structure and the impregnation of ferromagnetic nanoparticles on porous supports [56].

Among the various nanoparticles used in catalytic processes, magnetic iron oxide nanoparticles are promising to treat different wastewater using heterogeneous Fenton [41, 61, 62]. The ferromagnetic nanoparticles of zero-valent iron and the ferrimagnetic or superparamagnetic nanoparticles of magnetite (Fe_3O_4) and maghemite (γ-Fe_2O_3) are widely reported for wastewater or underground environments treatment in recent decades. Iron oxides have been preferred in use for conversion to nanostructured magnetic materials [1, 63]. According to Munoz et al. [56], since 2008, magnetic nanoparticles have been applied in Fenton oxidation and represent a new generation of catalysts for this technology. The nanomaterials mentioned here and their perspectives for use in Fenton processes will be presented below.

3.1 Hematite

Hematite (α-Fe_2O_3) is one of the main iron ores used as heterogeneous catalysts. Its use is associated with the fact that it is an abundant and low-cost material, with a large surface area, large surface-to-volume ratio, and interesting topology and morphology. Another essential feature is that even after losing its reactivity, it can be used as a raw material to produce pig iron, avoiding inappropriate disposal and without causing an environmental impact.

The use of hematite has been reported in remediation processes for various organic and inorganic contaminants through adsorption processes and Fenton oxidation [64, 65], and nanoscale material [66]. Doping hematite with heavy metals and non-metallic ions also improves its performance to degrade pollutants [23]. Synthesized hematite nanoparticles with sodium pyrophosphate as a chelating agent were used by Jorfi et al. [67] to pre-treatment soil contaminated with pyrene, obtaining a pyrene removal rate of 96%. Photocatalytic degradation of Rhodamine B using visible light and structurally well-defined hematite nanoparticles reached 70% efficiency [68]. Hematite nanoparticles (α-Fe_2O_3) were synthesized using ferrous sulfate residues ($FeSO_4 \cdot 7H_2O$) and pyrite (FeS_2) as raw materials and used for methyl orange decolorization by the photo-Fenton system, obtaining a decolorization efficiency of 99.55% in 4 min [69]. A disadvantage of this ore is its paramagnetic behavior, which means it is slightly attracted to magnetic fields. Although this characteristic does not affect the Fenton oxidation efficiency, the application of hematite nanoparticles on a large scale is complex since the separation by magnetic field will not be effective [24].

3.2 Magnetite

Magnetite is an iron oxide that has a mixed-valence and belongs to the spinel group, having unique redox properties. Among the ores found in nature, magnetite is the most magnetic and is widely used in the Fenton process because of its structural ferrous ions. Due to its magnetic properties, that is, its ferrimagnetic behavior, Fe_3O_4 can be easily separated in wastewater purification processes, such as functioning continuously as a heterogeneous catalyst, without considerable loss and mass.

The literature presents efficient results using magnetite as a catalyst for the heterogeneous Fenton reaction in the degradation of organic pollutants. The degradation of carbamazepineand ibuprofen was investigated using nano-magnetite as a catalyst for the heterogeneous Fenton reaction, obtaining degradation percentages more significant than 80% [70]. Magnetite nanoparticles, synthesized by the sol-gel citrate-nitrate method, were applied as precursors for methylene blue degradation obtained a color removal of 93.4% [71]. Amoxicillin degradation reached the maximum removal efficiency of 98.2% using heterogeneous electro-Fenton without external aeration with nano-Fe_3O_4 synthesized by chemical co-precipitation method [72]. Microwave irradiation was used in the heterogeneous activation of nano-Fe_3O_4 to obtain •OH radicals from the decomposition of H_2O_2. In addition to the remarkable reuse in up to seven cycles, being completely removed by applying a simple magnetic field, the degradation of the dye Rhodamine B reached 97.55% [73].

3.3 Maghemite

Maghemite has properties similar to those of magnetites, such as spinel structure and ferrimagnetic behavior. However, γ-Fe_2O_3 can be more stable and resistant to acidic environments than magnetite and can be used in applications with adverse conditions. Maghemite has a lower magnetization value than magnetite (~80 emu/g), and for this reason, it ends up being less used [24].

Maghemite nanoparticles (γ-Fe_2O_3) and maghemite/silica nanocomposite microspheres (γ-Fe_2O_3/SiO_2) were evaluated as heterogeneous Fenton magnetic catalysts in the degradation of different organic compounds (methyl orange, methylene blue, and paranitrophenol), obtaining mineralization rates between 50 and 99% [74]. The decolorization of the triphenylmethane dye using a sliding arc plasma discharge in humid air and maghemite nanoparticles (γ-Fe_2O_3) obtained a discoloration rate of 55.6% [75]. Maghemite differs from magnetite since all iron species are in the form of Fe^{3+} and Fe^{2+} ions are absent. This characteristic decreases the effectiveness of the catalytic activity of this material compared to magnetite [76].

3.4 Other Ferrites

Ferrites are iron oxides with one or more transition metals in their composition. They have a general structure given by MFe_3O_4, where M represents the divalent transition metal ions present in the material, for example, Cu, Zn, Ni, Co, Mn, and Fe. Ferrites are up-and-coming materials as heterogeneous catalysts for photo-Fenton reactions due to their narrow bandgap and high stability. Furthermore, they generally have good magnetic properties and are easily separated from solutions. Among the possible formed ferrites, ferrites have remarkable properties for the degradation of organic compounds. Some metals, such as Co, Mn, and Cu (M^{n+}, with n = 1.2), can react with H_2O_2 to generate $\bullet O_2H$ and $\bullet OH$ through a Haber–Weiss type mechanism during the Fenton reaction (Eqs. 21 and 22). The metals mentioned can also participate in the redox cycling of Fe^{3+}/Fe^{2+}, as shown in Eqs. 23–25 [14, 77]. The symbol ≡ represents the metals bonded to the nanomaterial surface.

$$M^{n+} + H_2O_2 \rightarrow M^{(n+1)+} + OH^- + \bullet OH \tag{21}$$

$$M^{(n+1)+} + H_2O_2 \rightarrow M^{n+} + H^+ + \bullet O_2H \tag{22}$$

$$Fe^{2+} + Co^{3+} \rightarrow Fe^{3+} + Co^{2+} \tag{23}$$

$$Fe^{2+} + Mn^{3+} \rightarrow Fe^{3+} + Mn^{2+} \tag{24}$$

$$\equiv Fe(III) + \equiv Cu(I) \rightarrow \equiv Fe(II) + \equiv Cu(II) \tag{25}$$

Cobalt nanoferrites ($CoFe_2O_4$) were used as photocatalysts for methylene blue dye degradation under visible light irradiation, reaching a degradation efficiency of 80% after 140 min [78]. Nanostructured catalysts $Co_{1-x}Zn_xFe_2O_4$ ($0 \leq x \leq 0{,}5$) synthesized by the microwave combustion method were used in the photocatalytic degradation of Rhodamine B under visible light. Among all samples, $Co_{0,6}Zn_{0,4}Fe_2O_4$ exhibited a degradation efficiency of 99.9% in the visible light exposure time of 210 min [79]. Cobalt Ferrite Nanoparticles ($CoFe_2O_4$) were used for the sonocatalytic removal of various organic dyes (AO7, AR17, BR46, and BY28). The maximum removal efficiency of 90.5% was reached, and nanocomposites' reuse suffered a 22% drop in efficiency after 5 cycles [80]. The photocatalytic activity of different ferrites ($NiFe_2O_4$, $CuFe_2O_4$, $MnFe_2O_4$, and $SrFe_2O_4$) was investigated for methylene blue dye degradation, obtaining efficiencies above 98% for all studied materials [81]. Finally, the incorporation of Co and Mn in the magnetite structure, studied by Costa et al. [77], significantly increased the Fenton reactivity of the magnetite due to the increased H_2O_2 decomposition.

4 Final Considerations and Future Directions

The versatility of Fenton's oxidation process is unquestionable. The method, which can be improved with the addition of light, ultrasound, electricity, and/or solid iron source particles, can remediate contaminated water from different sources. The use of iron-based nanomaterials represents a promising alternative for heterogeneous Fenton oxidation and a potential field of studies related to the application of nanocatalysts. Nanoparticles are also considered promising and efficient catalysts due to their high surface area and low resistance to diffusion. Nanomaterials from iron oxides are highlighted in recent literature since magnetic natural minerals have high availability and low cost. However, its immobilization on support proves to be a field of study yet to be explored. The ease of applying the Fenton process and advances in the materials area suggest that the method will still be widely investigated in the coming decades, especially regarding underexplored contaminants, such as emerging pollutants.

References

1. Kurian, M.: Advanced oxidation processes and nanomaterials -a review. Clean. Eng. Technol. **2**, 100090 (2021). https://doi.org/10.1016/j.clet.2021.100090
2. Miklos, D.B., Remy, C., Jekel, M., et al.: Evaluation of advanced oxidation processes for water and wastewater treatment—a critical review. Water Res. **139**, 118–131 (2018)
3. Mohammed, M., Aziz, A., Raman, A., Asghar, A.: A review on approaches for addressing the limitations of Fenton oxidation for recalcitrant wastewater treatment. Process. Saf. Environ. Prot. **126**, 119–140 (2019). https://doi.org/10.1016/j.psep.2019.03.028
4. Wang, J., Wang, S.: Reactive species in advanced oxidation processes: formation, identification and reaction mechanism. Chem. Eng. J. **401**. https://doi.org/10.1016/j.cej.2020.126158
5. Usman, M., Hanna, K., Haderlein, S.: Fenton oxidation to remediate PAHs in contaminated soils: A critical review of major limitations and counter-strategies. Sci. Total Environ. **569–570**, 179–190 (2016). https://doi.org/10.1016/j.scitotenv.2016.06.135
6. Saleh, R., Taufik, A.: Degradation of methylene blue and congo-red dyes using Fenton, photo-Fenton, sono-Fenton, and sonophoto-Fenton methods in the presence of iron(II, III) oxide/zinc oxide/graphene (Fe3O4/ZnO/graphene) composites. Sep. Purif Technol. **210**, 563–573 (2019). https://doi.org/10.1016/j.seppur.2018.08.030
7. Ma, Y.S.: Short review: current trends and future challenges in the application of sono-Fenton oxidation for wastewater treatment. Sustain. Environ. Res. **22**, 271–278 (2012)
8. Poza-Nogueiras, V., Rosales, E., Pazos, M., Sanromán, M.Á.: Current advances and trends in electro-Fenton process using heterogeneous catalysts—a review. Chemosphere **201**, 399–416 (2018). https://doi.org/10.1016/j.chemosphere.2018.03.002
9. Babuponnusami, A., Muthukumar, K.: A review on Fenton and improvements to the Fenton process for wastewater treatment. J. Environ. Chem. Eng. **2**, 557–572 (2014). https://doi.org/10.1016/j.jece.2013.10.011
10. Haber, F., Weiss, J., Seph, J.O., Eiss, W.: The catalytic decomposition of hydrogen peroxide by iron salts. Proc. R. Soc. London Ser. A. Math. Phys. Sci. **147**, 332–351 (1934). https://doi.org/10.1098/rspa.1934.0221
11. Zhang M hui, Dong H, Zhao L, et al (2019) A review on Fenton process for organic wastewater treatment based on optimization perspective. Elsevier B.V.

12. Armstronga, D.A., Huie, R.E., Lymar, S., et al.: Standard electrode potentials involving radicals in aqueous solution: Inorganic radicals. Bioinorg React Mech **9**, 59–61 (2013). https://doi.org/10.1515/irm-2013-0005
13. Lu, S., Liu, L., Demissie, H., et al.: Design and application of metal-organic frameworks and derivatives as heterogeneous Fenton-like catalysts for organic wastewater treatment: a review. Environ. Int. **146**, 106273 (2021). https://doi.org/10.1016/j.envint.2020.106273
14. Zhu Y, Zhu R, Xi Y, et al (2019) Strategies for enhancing the heterogeneous fenton catalytic reactivity: A review. Appl. Catal. B Environ.
15. Farhadian, N., Liu, S., Asadi, A., et al.: Enhanced heterogeneous Fenton oxidation of organic pollutant via Fe-containing mesoporous silica composites: a review. J. Mol. Liq. **321**, 114896 (2021). https://doi.org/10.1016/j.molliq.2020.114896
16. Zhu, Y., Zhu, R., Xi, Y., et al.: Heterogeneous photo-Fenton degradation of bisphenol A over Ag/AgCl/ferrihydrite catalysts under visible light. Chem. Eng. J. **346**, 567–577 (2018). https://doi.org/10.1016/j.cej.2018.04.073
17. Pradhan, G.K., Sahu, N., Parida, K.M.: Fabrication of S, N co-doped α-Fe2O3 nanostructures: Effect of doping, OH radical formation, surface area, [110] plane and particle size on the photocatalytic activity. RSC Adv. **3**, 7912–7920 (2013). https://doi.org/10.1039/c3ra23088k
18. Xu, J., Li, Y., Yuan, B., et al.: Large scale preparation of Cu-doped α-FeOOH nanoflowers and their photo-Fenton-like catalytic degradation of diclofenac sodium. Chem. Eng. J. **291**, 174–183 (2016). https://doi.org/10.1016/j.cej.2016.01.059
19. He, D., Chen, Y., Situ, Y., et al.: Synthesis of ternary g-C 3 N 4 /Ag/γ-FeOOH photocatalyst: an integrated heterogeneous Fenton-like system for effectively degradation of azo dye methyl orange under visible light. Appl. Surf. Sci. **425**, 862–872 (2017). https://doi.org/10.1016/j.apsusc.2017.06.124
20. Ma, Y., Wang, B., Wang, Q., Xing, S.: Facile synthesis of A-FeOOH/Γ-Fe_2O_3 by a pH gradient method and the role of Γ-Fe_2O_3 in H_2O_2 activation under visible light irradiation. Chem. Eng. J. **354**, 75–84 (2018). https://doi.org/10.1016/j.cej.2018.08.011
21. Bai, J., Liu, Y., Yin, X., et al.: Efficient removal of nitrobenzene by Fenton-like process with Co-Fe layered double hydroxide. Appl. Surf Sci. **416**, 45–50 (2017). https://doi.org/10.1016/j.apsusc.2017.04.117
22. Xu, T., Zhu, R., Zhu, J., et al.: BiVO4/Fe/Mt composite for visible-light-driven degradation of acid red 18. Appl. Clay. Sci. **129**, 27–34 (2016). https://doi.org/10.1016/j.clay.2016.04.018
23. Nidheesh, P.V.: Heterogeneous Fenton catalysts for the abatement of organic pollutants from aqueous solution: a review. RSC Adv. **5**, 40552–40577 (2015). https://doi.org/10.1039/c5ra02023a
24. Leonel, A.G., Mansur, A.A.P., Mansur, H.S.: Advanced Functional Nanostructures based on Magnetic Iron Oxide Nanomaterials for Water Remediation: A Review. Water Res. **190**, 116693 (2021)
25. Zeidman, A.B., Rodriguez-Narvaez, O.M., Moon, J., Bandala, E.R.: Removal of antibiotics in aqueous phase using silica-based immobilized nanomaterials: a review. Environ. Technol. Innov. **20**, 101030 (2020)
26. Aramyan, S.M.: Advances in fenton and fenton based oxidation processes for industrial effluent contaminants control—A review. Int. J. Environ. Sci. Nat. Resour. **2**, (2017). https://doi.org/10.19080/ijesnr.2017.02.555594
27. Brillas, E.: A review on the photoelectro-Fenton process as efficient electrochemical advanced oxidation for wastewater remediation. Treatment with UV light, sunlight, and coupling with conventional and other photo-assisted advanced technologies. Chemosphere **250**, 126198 (2020). https://doi.org/10.1016/j.chemosphere.2020.126198
28. Rueda-Márquez, J.J., Levchuk, I., Manzano, M., Sillanpää, M.: Toxicity reduction of industrial and municipal wastewater by advanced oxidation processes (Photo-fenton, UVC/H_2O_2, electro-fenton and galvanic fenton): a review. Catalysts **10**(2020). https://doi.org/10.3390/catal10060612
29. Liu, P., Wu, Z., Abramova, A.V., Cravotto, G.: Sonochemical processes for the degradation of antibiotics in aqueous solutions: a review. Ultrason. Sonochem. **74**, 105566 (2021)

30. Moradi, M., Elahinia, A., Vasseghian, Y., et al.: A review on pollutants removal by Sono-photo -Fenton processes. J. Environ. Chem. Eng. **8**,104330 (2020). https://doi.org/10.1016/j.jece.2020.104330
31. Adityosulindro, S., Barthe, L., González-Labrada, K., et al.: Sonolysis and sono-Fenton oxidation for removal of ibuprofen in (waste)water. Ultrason Sonochem **39**, 889–896 (2017). https://doi.org/10.1016/j.ultsonch.2017.06.008
32. Gholami, P., Khataee, A., Bhatnagar, A.: Environmentally superior cleaning of diatom frustules using sono-Fenton process: Facile fabrication of nanoporous silica with homogeneous morphology and controlled size. Ultrason Sonochem **64**, 105044 (2020).https://doi.org/10.1016/j.ultsonch.2020.105044
33. Ismail, S.A., Ang, W.L., Mohammad, A.W.: Electro-Fenton technology for wastewater treatment: a bibliometric analysis of current research trends, future perspectives and energy consumption analysis. J. Water Process. Eng. **40**, 101952 (2021). https://doi.org/10.1016/j.jwpe.2021.101952
34. Nidheesh, P.V., Gandhimathi, R.: Trends in electro-Fenton process for water and wastewater treatment: an overview. Desalination **299**, 1–15 (2012). https://doi.org/10.1016/j.desal.2012.05.011
35. Brillas, E., Garcia-Segura, S.: Benchmarking recent advances and innovative technology approaches of Fenton, photo-Fenton, electro-Fenton, and related processes: a review on the relevance of phenol as model molecule. Sep. Purif. Technol. **237**, 116337 (2020).
36. Casado, J.: Towards industrial implementation of Electro-Fenton and derived technologies for wastewater treatment: a review. J. Environ. Chem. Eng. **7** (2019)
37. Monteil, H., Péchaud, Y., Oturan, N., Oturan, M.A.: A review on efficiency and cost effectiveness of electro- and bio-electro-Fenton processes: application to the treatment of pharmaceutical pollutants in water. Chem. Eng. J. **376** (2019).https://doi.org/10.1016/j.cej.2018.07.179
38. Wu, C., Chen, W., Gu, Z., Li, Q.: A review of the characteristics of Fenton and ozonation systems in landfill leachate treatment. Sci. Total Environ. **762**, 143131 (2021)
39. Herney-Ramirez, J., Vicente, M.A., Madeira, L.M.: Heterogeneous photo-Fenton oxidation with pillared clay-based catalysts for wastewater treatment: a review. Appl. Catal. B Environ. **98**, 10–26 (2010)
40. Liu, Y., Zhao, Y., Wang, J.: Fenton/Fenton-like processes with in-situ production of hydrogen peroxide/hydroxyl radical for degradation of emerging contaminants: advances and prospects. J. Hazard. Mater. **404**, 124191 (2021)
41. Dantas, T.L.P., Mendonça, V.P., José. H.J., et al.: Treatment of textile wastewater by heterogeneous Fenton process using a new composite Fe_2O_3/carbon. Chem. Eng. J. **118**, 77–82 (2006). https://doi.org/10.1016/j.cej.2006.01.016
42. Diya'uddeen, B.H., Abdul Aziz, A.R., Daud, W.M.A.W.: On the limitation of Fenton oxidation operational parameters: a review. Int. J. Chem. React. Eng. **10** (2012)
43. Li, J., Zhang, X., Wang, T., et al.: Construction of layered hollow Fe_3O_4/Fe1−xS @MoS2 composite with enhanced photo-Fenton and adsorption performance. J. Environ. Chem. Eng. **8**, 103762 (2020).https://doi.org/10.1016/j.jece.2020.103762
44. Dai, C., Tian, X., Nie, Y., et al.: Surface Facet of $CuFeO_2$ Nanocatalyst: a key parameter for H_2O_2 activation in Fenton-Like reaction and organic pollutant degradation. Environ. Sci. Technol. **52**, 6518–6525 (2018). https://doi.org/10.1021/acs.est.8b01448
45. Huang, X., Hou, X., Song, F., et al.: Ascorbate induced facet dependent reductive dissolution of hematite nanocrystals. J. Phys. Chem. C. **121**, 1113–1121 (2017). https://doi.org/10.1021/acs.jpcc.6b09281
46. Patra, A.K., Kundu, S.K., Bhaumik, A., Kim, D.: Morphology evolution of single-crystalline hematite nanocrystals: magnetically recoverable nanocatalysts for enhanced facet-driven photoredox activity. Nanoscale **8**, 365–377 (2016). https://doi.org/10.1039/C5NR06509G
47. Li, H., Shang, J., Yang, Z., et al.: Oxygen vacancy associated surface fenton chemistry: surface structure dependent hydroxyl radicals generation and substrate dependent reactivity. Environ. Sci. Technol. **51**, 5685–5694 (2017). https://doi.org/10.1021/acs.est.7b00040

48. Huang, X., Hou, X., Zhao, J., Zhang, L.: Hematite facet confined ferrous ions as high efficient Fenton catalysts to degrade organic contaminants by lowering H_2O_2 decomposition energetic span. Appl. Catal. B. Environ. **181**, 127–137 (2016). https://doi.org/10.1016/j.apcatb.2015.06.061
49. Huang, X., Hou, X., Jia, F., et al.: Ascorbate-Promoted surface iron cycle for efficient heterogeneous fenton alachlor degradation with hematite nanocrystals. ACS Appl. Mater. Interfaces **9**, 8751–8758 (2017). https://doi.org/10.1021/acsami.6b16600
50. Zhong, Y., Yu, L., Chen, Z.-F., et al.: Microwave-Assisted Synthesis of Fe_3O_4 Nanocrystals with predominantly exposed facets and their heterogeneous UVA/Fenton catalytic activity. ACS Appl. Mater. Interfaces **9**, 29203–29212 (2017). https://doi.org/10.1021/acsami.7b06925
51. Kwan, W.P., Voelker, B.M.: Influence of electrostatics on the oxidation rates of organic compounds in heterogeneous fenton systems. Environ. Sci. Technol. **38**, 3425–3431 (2004). https://doi.org/10.1021/es034676g
52. Wan, D., Li, W., Wang, G., Wei, X.: Size-controllable synthesis of Fe_3O_4 nanoparticles through oxidation–precipitation method as heterogeneous Fenton catalyst. J. Mater. Res. **31**, 2608–2616 (2016). https://doi.org/10.1557/jmr.2016.285
53. Gao, L., Fan, K., Yan, X.: Iron Oxide nanozyme: a multifunctional enzyme mimetic for biomedical applications. Theranostics **7**, 3207–3227 (2017). https://doi.org/10.7150/thno.19738
54. Wallyn, J., Anton, N., Vandamme, T.F.: Synthesis, principles, and properties of magnetite nanoparticles for in vivo imaging applications—a review. Pharm. **11** (2019)
55. Ghosh, A., Srinivas, V., Sundara, R.: Comprehensive structural and magnetic properties of iron oxide nanoparticles synthesized through chemical routes. J. Alloys Compd. **818**, 152931 (2020). https://doi.org/10.1016/j.jallcom.2019.152931
56. Munoz, M., de Pedro, Z.M., Casas, J.A., Rodriguez, J.J.: Preparation of magnetite-based catalysts and their application in heterogeneous Fenton oxidation—a review. Appl. Catal. B. Environ. **176–177**, 249–265 (2015). https://doi.org/10.1016/j.apcatb.2015.04.003
57. Zubir, N.A., Yacou, C., Motuzas, J., et al.: Structural and functional investigation of graphene oxide–Fe_3O_4 nanocomposites for the heterogeneous Fenton-like reaction. Sci. Rep. **4**, 4594 (2014). https://doi.org/10.1038/srep04594
58. Hou, L., Zhang, Q., Jérôme, F., et al.: Shape-controlled nanostructured magnetite-type materials as highly efficient Fenton catalysts. Appl. Catal. B. Environ. **144**, 739–749 (2014). https://doi.org/10.1016/j.apcatb.2013.07.072
59. Wang, W., Liu, Y., Li, T., Zhou, M.: Heterogeneous Fenton catalytic degradation of phenol based on controlled release of magnetic nanoparticles. Chem. Eng. J. **242**, 1–9 (2014). https://doi.org/10.1016/j.cej.2013.12.080
60. Cleveland, V., Bingham, J.-P., Kan, E.: Heterogeneous Fenton degradation of bisphenol a by carbon nanotube-supported Fe_3O_4. Sep. Purif. Technol. **133**, 388–395 (2014). https://doi.org/10.1016/j.seppur.2014.06.061
61. Li, X., Kong, Y., Zhou, S., Wang, B.: In situ incorporation of well-dispersed Cu–Fe oxides in the mesochannels of AMS and their utilization as catalysts towards the Fenton-like degradation of methylene blue. J. Mater. Sci. **52**, 1432–1445 (2017). https://doi.org/10.1007/s10853-016-0436-0
62. Vu, A.T., Xuan, T.N., Lee, C.H.: Preparation of mesoporous Fe2O3·SiO2 composite from rice husk as an efficient heterogeneous Fenton-like catalyst for degradation of organic dyes. J. Water. Process. Eng. **28**, 169–180 (2019). https://doi.org/10.1016/j.jwpe.2019.01.019
63. Thomas, N., Dionysiou, D.D., Pillai, S.C.: Heterogeneous Fenton catalysts: a review of recent advances. J. Hazard. Mater. **404**, 124082 (2021)
64. Dai, M., Xia, L., Song, S., et al.: Adsorption of As(V) inside the pores of porous hematite in water. J. Hazard Mater. **307**, 312–317 (2016). https://doi.org/10.1016/j.jhazmat.2016.01.008
65. Chen, X., Chen, F., Liu, F., et al.: Ag nanoparticles/hematite mesocrystals superstructure composite: A facile synthesis and enhanced heterogeneous photo-Fenton activity. Catal Sci. Technol. **6**, 4184–4191 (2016). https://doi.org/10.1039/c6cy00080k

66. Zheng, C., Cheng, X., Yang, C., et al.: Hydrophilic modification of ordered mesoporous carbon supported Fe nanoparticles with enhanced adsorption and heterogeneous Fenton-like oxidation performance. RSC Adv. **5**, 98842–98852 (2015). https://doi.org/10.1039/c5ra15156b
67. Jorfi, S., Samaei, M.R., Darvishi Cheshmeh Soltani, R., et al.: Enhancement of the bioremediation of pyrene-contaminated soils using a hematite nanoparticle-based modified fenton oxidation in a sequenced approach. Soil Sediment Contam An Int. J. **26**, 141–156 (2017). https://doi.org/10.1080/15320383.2017.1255875
68. Huang, X., Chen, Y., Walter, E., et al.: Facet-Specific photocatalytic degradation of organics by heterogeneous fenton chemistry on hematite nanoparticles. Environ. Sci. Technol. **53**, 10197–10207 (2019). https://doi.org/10.1021/acs.est.9b02946
69. Xiang, H., Ren, G., Yang, X., et al.: A low-cost solvent-free method to synthesize α-Fe_2O_3 nanoparticles with applications to degrade methyl orange in photo-fenton system. Ecotoxicol Environ. Saf. **200**, 110744 (2020). https://doi.org/10.1016/j.ecoenv.2020.110744
70. Sun, S.-P., Zeng, X., Lemley, A.T.: Nano-magnetite catalyzed heterogeneous Fenton-like degradation of emerging contaminants carbamazepine and ibuprofen in aqueous suspensions and montmorillonite clay slurries at neutral pH. J. Mol. Catal. A Chem. **371**, 94–103 (2013). https://doi.org/10.1016/j.molcata.2013.01.027
71. de Oliveira Guidolin, T., Possolli, N.M., Polla, M.B., Wermuth, T.B., de Oliveira, T.F., Eller, S., et al.: Photocatalytic pathway on the degradation of methylene blue from aqueous solutions using magnetite nanoparticles. J. Clean. Prod. **318**, 128556 (2021). https://doi.org/10.1016/j.jclepro.2021.128556
72. Kalantary, R.R., Farzadkia, M., Kermani, M., Rahmatinia, M.: Heterogeneous electro-Fenton process by Nano-Fe_3O_4 for catalytic degradation of amoxicillin: process optimization using response surface methodology. J. Environ. Chem. Eng. **6**, 4644–4652 (2018). https://doi.org/10.1016/j.jece.2018.06.043
73. Vieira, Y., Silvestri, S., Leichtweis, J., et al.: New insights into the mechanism of heterogeneous activation of nano-magnetite by microwave irradiation for use as Fenton catalyst. J. Environ. Chem. Eng. **8**, 103787 (2020).https://doi.org/10.1016/j.jece.2020.103787
74. Ferroudj, N., Nzimoto, J., Davidson, A., et al.: Maghemite nanoparticles and maghemite/silica nanocomposite microspheres as magnetic Fenton catalysts for the removal of water pollutants. Appl. Catal B Environ. **136–137**, 9–18 (2013). https://doi.org/10.1016/j.apcatb.2013.01.046
75. Tiya-Djowe, A., Acayanka, E., Lontio-Nkouongfo, G., et al.: Enhanced discolouration of methyl violet 10B in a gliding arc plasma reactor by the maghemite nanoparticles used as heterogeneous catalyst. J. Environ. Chem. Eng. **3**, 953–960 (2015). https://doi.org/10.1016/j.jece.2014.11.016
76. Pereira, M.C., Oliveira, L.C.A., Murad, E.: Iron oxide catalysts: Fenton and Fentonlike reactions—a review. Clay Miner **47**, 285–302 (2012). https://doi.org/10.1180/claymin.2012.047.3.01
77. Costa, R.C.C., Lelis, M.F.F., Oliveira, L.C.A., et al.: Novel active heterogeneous Fenton system based on Fe_3-xMxO_4 (Fe, Co, Mn, Ni): the role of M^{2+} species on the reactivity towards H_2O_2 reactions. J. Hazard Mater. **129**, 171–178 (2006). https://doi.org/10.1016/j.jhazmat.2005.08.028
78. Kalam, A., Al-Sehemi, A.G., Assiri, M., et al.: Modified solvothermal synthesis of cobalt ferrite ($CoFe_2O_4$) magnetic nanoparticles photocatalysts for degradation of methylene blue with H2O2/visible light. Results Phys. **8**, 1046–1053 (2018). https://doi.org/10.1016/j.rinp.2018.01.045
79. Sundararajan, M., Sailaja, V., John Kennedy, L., Judith Vijaya, J.: Photocatalytic degradation of rhodamine B under visible light using nanostructured zinc doped cobalt ferrite: Kinetics and mechanism. Ceram Int. **43**, 540–548 (2017). https://doi.org/10.1016/j.ceramint.2016.09.191
80. Hassani, A., Çelikdağ, G., Eghbali, P., et al.: Heterogeneous sono-Fenton-like process using magnetic cobalt ferrite-reduced graphene oxide ($CoFe_2O_4$-rGO) nanocomposite for the removal of organic dyes from aqueous solution. Ultrason Sonochem **40**, 841–852 (2018). https://doi.org/10.1016/j.ultsonch.2017.08.026

81. Vinosha, P.A., Xavier, B., Anceila, D., Das, S.J.: Nanocrystalline ferrite (MFe2O4, M=Ni, Cu, Mn and Sr) photocatalysts synthesized by homogeneous Co-precipitation technique. Optik (Stuttg) **157**, 441–448 (2018). https://doi.org/10.1016/j.ijleo.2017.11.016

Nanomaterials for Fuel Production

João Víctor Pereira Abdalla, Adriane de Assis Lawisch Rodríguez, and Annelise Kopp Alves

Abstract Fuel production is an essential part of modern society. The use of fossil fuels increases every day, generating more greenhouse gases. Processes are developed to reduce global warming, aiming to convert these gases into hydrocarbons, which will be used as fuel. The main problem consists of the energy needed to allow the process to happen. The use of solar energy becomes more likely to succeed every day. This chapter will discuss current fuel production methods and alternatives to convert greenhouse gases into usable products.

Keywords Nanomaterials · Solar fuels · Nanocatalysts · Dry reforming

Abbreviations

PC	Photochemical
PEC	Photoeletrochemical
MOF	Metal-Organic Framework

1 Introduction

Over the years, energy demand has been increasing due to industrialization and significant population growth. As a result, it causes an increase in fossil fuel combustion, substantially increasing greenhouse gas emissions [1, 2].

Nowadays, global warming hits values of about 2ºC, compared with temperatures pre-industrialization [3]. Thus, to Karmaker et al. [1], thermoelectric power plants' energy production is responsible for a significant part of greenhouse gas emissions.

J. V. P. Abdalla (✉) · A. de Assis Lawisch Rodríguez · A. K. Alves
Universidade Federal do Rio Grande do Sul, Porto Alegre, Brazil

A. Kopp Alves (ed.), *Environmental Applications of Nanomaterials*, Engineering Materials, https://doi.org/10.1007/978-3-030-86822-2_9

Projections show that the human race's energy consumption will be doubled until 2050 and triplicated until 2100 [4]. Given this problem, the search for alternative energy sources increases, making new technologies emerge every day.

In 2015, the UN established the Paris Agreement, which recognizes the climate change caused by industrialization and establishes goals to reduce greenhouse gas emissions until 2030.

In this agreement, countries like Brazil committed to reducing greenhouse gas emissions by 37% until 2025 and 43% until 2030, compared with the emission level observed in 2005.

In this context, the USA created "The United States Biofuel Mandate," which aims to reduce the consumption of fossil fuels, increasing the use of biofuels, reducing the impact of greenhouse gas emissions.

Against this problem, new technologies are developed to recycle greenhouse gas emissions generated in industrial processes (mainly CO_2), converting them, again, into hydrocarbons [5]. In addition, those technologies can also produce hydrogen from water splitting, making it a usable fuel that will not emit new greenhouse gases.

Among those technologies, Advanced Oxidation Processes highlights the importance of nanocatalysts in this context. When applied in heterogeneous photocatalysis, those materials are revolutionizing the industry, allowing the use of light as an energy source for fuel synthesis [6].

2 Nanocatalysts

Among the nanomaterials, nanocatalysts' class involves semiconductors and metal oxides, which, due to their reduced size and shape, have their properties modified, increasing superficial area for reactions and changing their applications [7, 8]. They are divided into three different groups [9], as seen in Table 1. Also, mixed non-noble metal oxide consists of merging two non-noble metal oxides to obtain various properties. Also, those materials can be classified as perovskites.

The perovskites consist of materials composed of semiconductors and oxygen. Usually, niobium-based perovskites are excellent materials to work with, allowing the catalyst to be shaped into different forms. In those systems, metal–organic frameworks have the function mainly to improve the catalytic activity of the materials, avoiding recombination and stabilizing materials. In this class, the niobium

Table 1 Nanocatalysts groups

Noble metal	Non-noble metal oxide
High activity	Lower activity compared to noble metal
High stability	Easier size manipulation
Easier to deactivate	Resistant to deactivation
High cost	Low cost

compounds also demonstrate to be a good candidate for fuel production. Furthermore, the association of niobium and other metals creates catalysts that can be used for this purpose and improved with research.

In recent years, the nanostructure engineering of catalysts creates a new way to produce valuable fuels, the structure for this purpose divides into nanosheets, nanowire, nanotube, nanorod, and quantum dots [10]. To be activated, the photon energy focused on the material must be higher than its bandgap, allowing the creation of an electron–hole pair [11].

2.1 Metal–Organic Frameworks

Metal–organic frameworks (MOFs) are characterized as coordinated metal ions linked by an organic compound [12]. Compared to ceramics, MOFs show a similar pore structure with the advantage that they can be shaped into different designs. Also, it's characterized as a flexible nanoporous material with low structure density. Furthermore, creating catalytic interfaces makes them a good choice for catalytic purposes [13–17]. Again, as a high coordination environment, the MOFs can stabilize single atoms catalysts, nanomaterials, and quantum dots [16, 18]. Figure 1 illustrates MOFs applications in catalytic reactions while Fig. 2 demonstrates the utilization of MOFs in different applications. The upper applications demonstrate an encapsulation of the original material, allowing photocatalytic systems improvements, avoiding nanoparticle agglomeration.

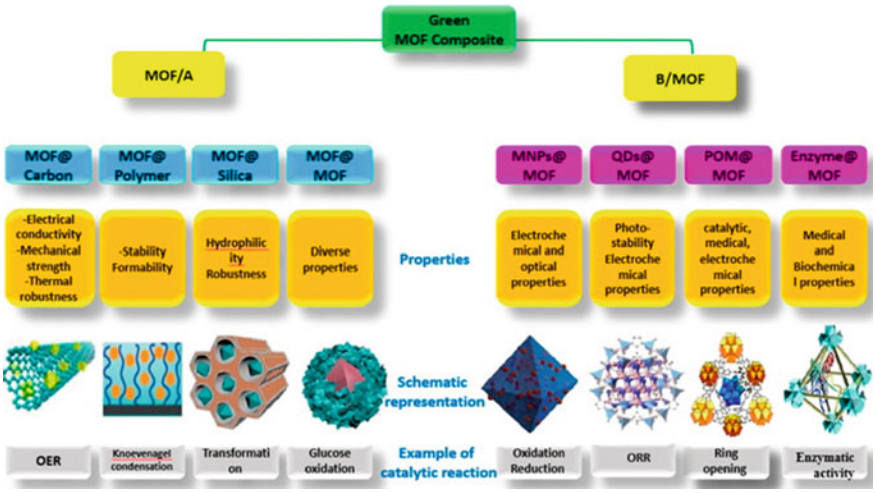

Fig. 1 MOFs applications. Reprinted with permission from Liu et al. [14]

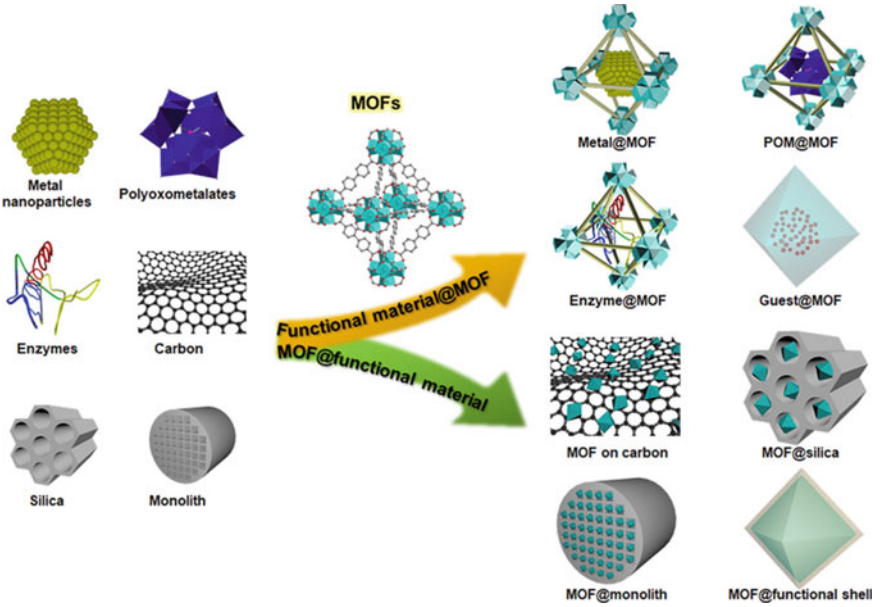

Fig. 2 MOFs integration. Reprinted with permission from Chen et al. [16]

2.2 Niobium

Since it's an accessible material to tune optical and electrical properties, niobium-based nanocatalysts are being studied to develop a new photocatalytic way to produce fuels [19]. For example, processes like electrocatalytic water splitting can benefit from these properties, as tuning the bandgap and potentials can increase the selectivity towards H_2 formation [20].

The bulk niobium pentoxide doesn't achieve good photocatalytic performance when utilized since its charge recombination rate is very high. However, the niobium compounds have the facility easier to shape, allowing modifications that turn them into excellent material for fuel production [21].

2.3 Perovskites

Perovskites are materials that associate two or more elements in the structure, providing a highly tunable band structure. This material demonstrates to be efficient in solar energy production and photocatalysis [22, 23]. Furthermore, these materials seem to fulfill the requirements for fuel production since it's possible to develop a high-efficiency charge separation material [17, 24, 25].

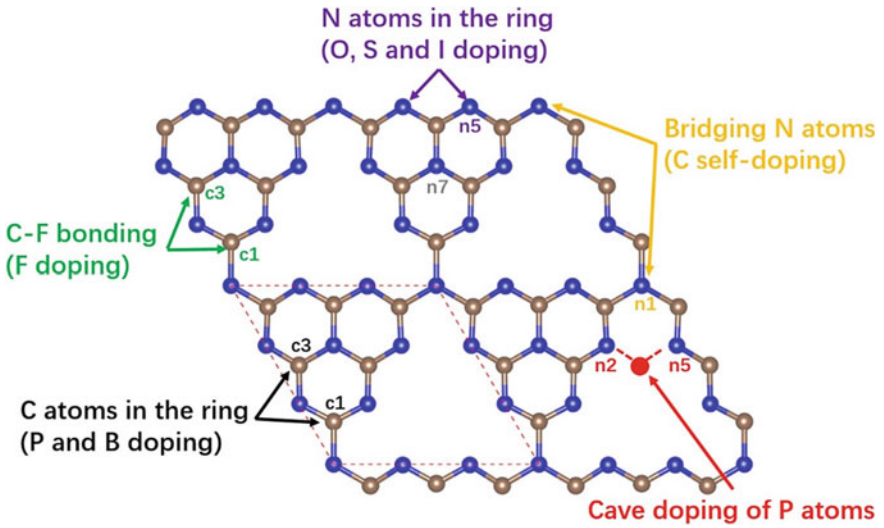

Fig. 3 Structural doping. Reprinted with permission from Zhu et al. [28]

2.4 Graphitic Carbon Nitride (g-C_3N_4)

Graphitic carbon nitride is a two-dimensional network (nanosheet) with bandgaps around 2.67 eV, close to the visible light region. Since it haves a high surface area and increased stability, this material is ideal for catalyst [26, 27]. However, like other materials, it has a high recombination rate and low carrier mobility. These problems can be fixed by doping the g-C_3N_4 structure [28]. When doped with heteroatoms, their recombination rates are reduced, and their potentials can be tuned to produce hydrocarbons [28].

Figure 3 demonstrates the possibilities for heteroatom doping in the g-C_3N_4 structure, while Fig. 4 shows the band gaps and potentials for each doping system.

As seen above, this material shows a lot of advantages. The figures demonstrate the capacity for the material to be shaped and manipulated into the process's needs.

3 Alternative Fuel Production Methods

As alternatives for the traditional process, nanomaterials can be used as catalysts, making the process cleaner, recycling greenhouse gases into hydrocarbons, and splitting water into hydrogen (Hydrogen Evolution). Table 2 demonstrates processes used to produce different fuels. The photocatalytic systems can be used with solar energy originating the solar fuel production method.

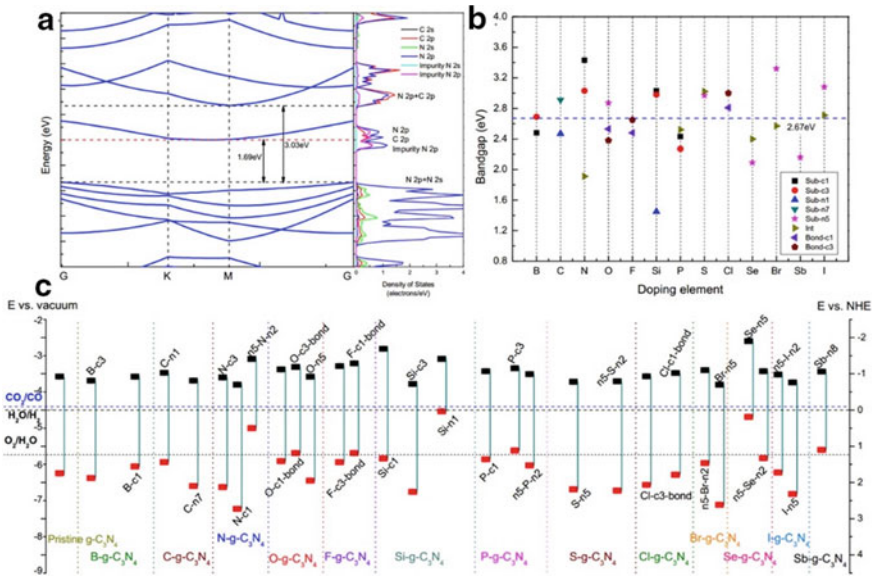

Fig. 4 g-C_3N_4 potentials. Reprinted with permission from Zhu et al. [28]

Table 2 Most common gases, processes, and fuel products

Gases	Process	Product	Reference
CH_4	Thermocatalysis	CH_3OH, HCOOH, CO_2, CH_3OOH	[29–31]
CH_4, CO_2	Electrocatalysis	CH_3OH, HCOOH, CO_2, CH_3OOH, HCHO	[29, 30, 32]
CH_4	Photocatalysis	CH_3OH, HCHO, HCOOH, H_2	[29, 30, 33]
CH_4, CO_2	Dry reforming	H_2, CO	[33–39]
CO_2, H_2O	Photocatalysis	HCOOH, CH_3OH, C_2H_5OH, CO, CH_4	[30, 40–43]
CO_2, H_2O	Photocatalysis	CH_3OH, H_2O	[44]

4 Hydrogen Evolution

Being an environmentally friendly fuel, hydrogen gas (H_2) is a promising form of energy transportation [45, 46]. However, the high infrastructure costs create a barrier between humanity and a hydrogen economy [47].

Hydrogen can be produced mainly by two different processes, water splitting and Steam Reforming of Methane [48]. In both cases, specific catalysts are used to improve the process.

Mainly, the reaction for hydrogen production from water splitting is described as below:

$$2H_2O + 4e^- \rightarrow 2H_2 + O_2$$

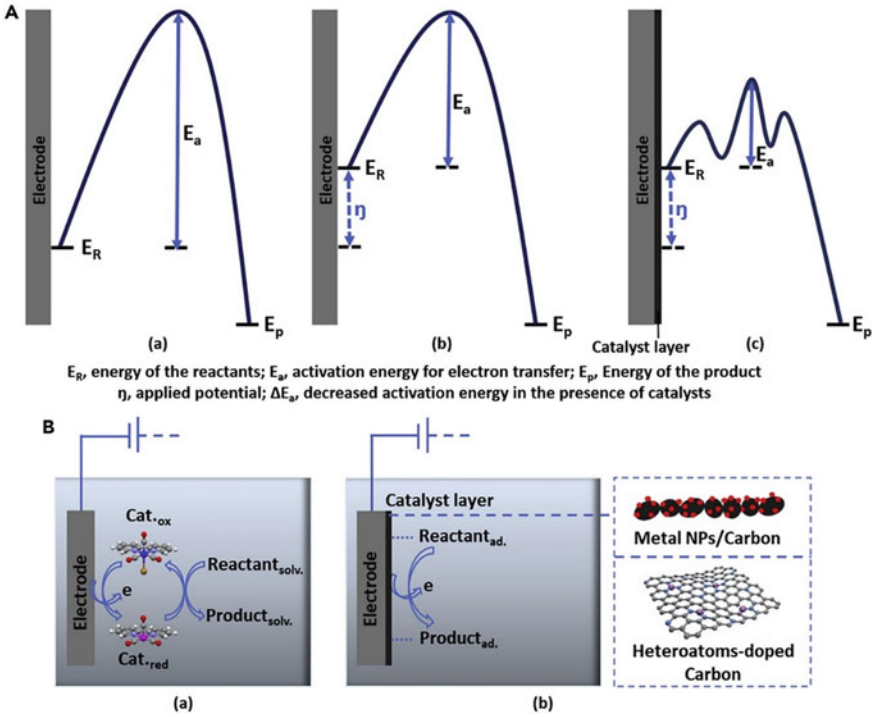

Fig. 5 Activation energy reduction. (Reprinted with permission from Lin et al. [48])

The electrons described in the equation can be obtained by electro or photochemical methods [49, 50], including a catalyst's association. In this case, the electron will be obtained from the material after activation.

Figure 5 shows the activation energy with and without a catalyst, demonstrating its reduction in the nanomaterial presence.

The photocatalytic process associates a catalyst with a light source, creating electron–hole pairs to react and form the required products. Heterojunction systems associate two catalysts as ZnO/ZnS and MoS_2/CdS, aiming to improve the catalytic efficiency of both [46, 51]. However, one of the process problems is catalyst aggregation, which needs to be corrected to maintain the high surface area. As mentioned before, this problem can be fixed by associating the catalyst with a MOF. Recent research demonstrates that the material can be related to nanodiamonds, avoiding the aggregation problem [45].

Nanotubes are also used as catalysts for water splitting systems with TiO_2 [52] and CeO_2 [53]. However, their efficiency can be improved by adding doping elements in the structure, like Nitrogen [52], or sensitizing the material.

Table 3 indicates some of the current catalysts researches for hydrogen production from water splitting, indicating the energy source, the amount of H_2 produced, and characteristics of the respective catalyst.

Table 3 Research on hydrogen production from water splitting, indicating the energy source, the amount of H_2 produced, and characteristics of the respectively used catalysts

Catalyst	Method	Energy source	Production	Characteristics	Authors
ZnS-ZnO	PC	UVC light	1600 $\mu molh^{-1} g^{-1}$	Heterojunction improves the electron–hole pair generation; an ideal sulfur content	[51]
Photocatalyst/ nanodiamond	PEC	–	–	Small particle size and low density, aggregates that reduce the surface energy and spread into the air; stability, high catalytic activity	[45]
MoS_2/CdS	PC	Visible Light	27,72 $mmolh^{-1} g^{-1}$	MoS_2 reduced charge recombination; higher MoS_2 ranges reduced H_2 production (covering CdS active sites)	[46]
N-doped TiO_2 nanotubes	PC	Solar Light	19,848 $\mu molh^{-1} g^{-1}$	After optimal concentration, the catalytic activity decreases due to the formation of recombination centers	[52]
CeO_2/SnO_2 Aerogel	PC	300 W 380 nm Xenon lamp	21,937 $\mu molh^{-1} g^{-1}$	The electrons of CeO_2 are transferred to the defect energy level of SnO_2, while SnO_2 holes are transferred to CeO_2, improving the electron–hole pair generation	[53]

5 Dry Reforming

This process consists of breaking carbon dioxide and methane into syngas (hydrogen and carbon monoxide) [54, 55]. Usually, the process depends on high temperatures due to the high activation energy in CO_2 and CH_4 [56].

The syngas obtained in the process can produce different hydrocarbons with the Fischer–Tropsch process [57, 58]. Those can be used as fuel. Besides that, hydrogen itself can perform as fuel, generating water as the combustion product.

Due to methane decomposition to hydrogen and carbon monoxide, the catalyst can be deactivated from coke deposition at high temperatures [57, 59, 60]. Using systems like Metal–organic frameworks could avoid this problem due to the encapsulation of the catalyst by the organic framework [61].

In dry reforming, noble metals have shown higher activity and better resistance for coke deposition, but their high cost restrains industry applications [58]. So, alternative metals are used as substitutes, such as cobalt and nickel. Table 4 demonstrates the most common catalysts being researched and their respective characteristics.

6 Solar Fuel Production

The solar fuel production method consists of synthesizing fuels using the sun as the energy source for the reaction. Similar to others processes, the solar method associates electro and photochemical procedures. Some systems unite both ways and create a photoelectrochemical process that mainly improves fuel production.

As seen before, CO_2 demands very high energy to break its bonds, since, in the other process, the energy source is thermal, the synthesis needs a fuel consumption to happen. Therefore, aiming for valuable fuel synthesis, solar light can remove the overconsumption of non-renewable fuels [69].

This system differs from dry reforming, as dry reforming mainly focuses on product syngas, and solar production methods aim to convert carbon dioxide and hydrogen into usable fuels [70].

Sunlight can be divided into three wavelengths: Ultraviolet (approximately 4% of the energy, 3.2 eV), Visible (43% of the energy, 1.6 eV), and infrared (53% of the energy) [71]. Nowadays, most of the catalysts are activated by UV light, this being a minor part of the sunlight. For the process to be improved, the catalysts will need to be activated in visible light, while the energy potentials maintain values adequates for the synthesis.

Figure 6 demonstrates the needed energy potentials to synthesize different hydrocarbons. As observed, the potentials are very close, so studies are necessary to develop a catalyst that shows a higher selectivity to the desired product.

Figure 7 represents the photoelectrochemical system, associating a photocatalyst with an electrochemical technique for fuel production. The generated electrical current split the water into hydrogen and oxygen, allowing fuel synthesis to occur.

As seen in Fig. 8, this process could be associated with the industry, capturing the generated CO_2 to turn into a helpful hydrocarbon again, obtaining hydrogen from water splitting and activation energy from solar light. Inside the solar photoreactor, the catalyst will directly influence the process efficiency. Therefore, catalyst selection, being the central part of the process, requires deep analysis.

Table 4 Most common catalysts used for dry reforming

Catalyst	Energy source	CH_4 conversion (%)	CO_2 conversion (%)	Characteristics	Authors
Ni/SiO_2 core, ZrO_2 Shell	Thermal (900 °C)	98,80%	95%	ZrO_2 shell avoid coke deposition	[57]
Pd core, SiO_2 Shell	Thermal (750 °C)	85%	85%	SiO_2 shell increases stability. Stable for at least 10 h	[59]
Ni/Al_2O_3	Thermal	75	80	25wt % Ni has optimum performance. Additional Ni decrease dispersion, lowering the catalytic activity	[58, 62]
Ni/Al_2O_3—eO_2	Thermal (850 °C)	–	–		[55, 63, 64]
NiCo-$NiAl_2O_4$	Thermal (750 °C)	–	–	Potassium decreases the catalytic activity, but increases material stability	[60]
Co/Al_2O_3	Thermal (800 °C)	76,2	81,6	10 wt% Co exhibits excellent performance with high stability	[65]
Ni/$MeAl_2O_4$ Me = Fe, Co, Ni, Cu, Zn, Mg	Thermal (700 °C)	Ni 73	Ni 68	Ni support demonstrates higher production: higher surface area reduced coke deposition	[66]
		Mg 70	Mg 65		
		Co 68	Co 60		
		Zn 60	Zn 50		
		Fe 48	Fe 30		
		Cu 37	Cu 10		
Pd/CeO_2	Thermal	–	–	The catalyst remains stable after 9 h. Stability was affected by sintering and reoxidation	[67]

(continued)

Table 4 (continued)

Catalyst	Energy source	CH_4 conversion (%)	CO_2 conversion (%)	Characteristics	Authors
Pt-Ni	Thermal (700 ºC)	–	–	Improved selectivity towards H_2. Also, reduce the carbon deposition in the catalyst, enhancing its stability	[68]

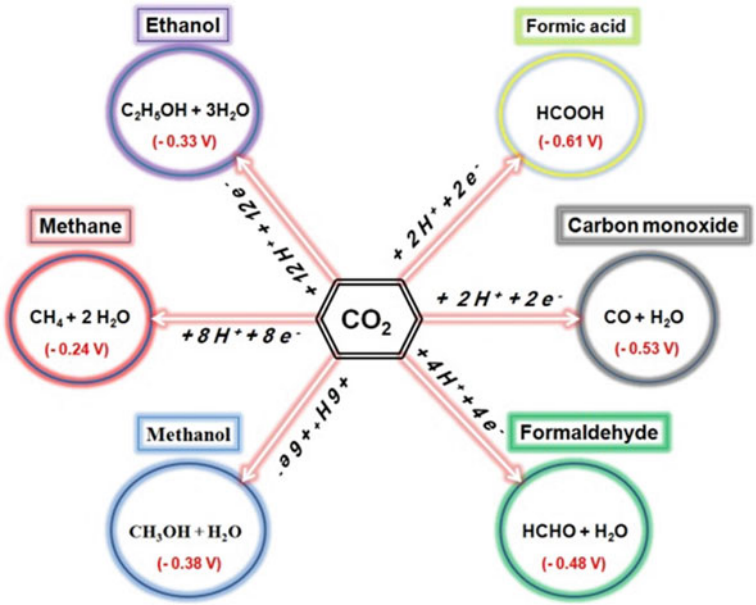

Fig. 6 Energy potentials. (Reprinted with permission from Ikreedeegh and Tahir [72])

As mentioned before, MOFs demonstrates to be a strong candidate for this process due to their structure, high potential for CO_2 adsorption, and maximized surface efficiency, isolating active sites and avoiding recombinations [73].

Nowadays, the photo-assisted Fischer–Tropsch process can convert syngas into valuable hydrocarbons. Still, due to the high recombination rate and low efficiency in synthesizing the products, the process needs improvements.

In this case, materials like graphitic carbon nitride (g-C_3N_4) have shown interesting properties, especially when doped with heteroatoms that tune their bandgap into visible light and their potentials to produce hydrocarbons [28].

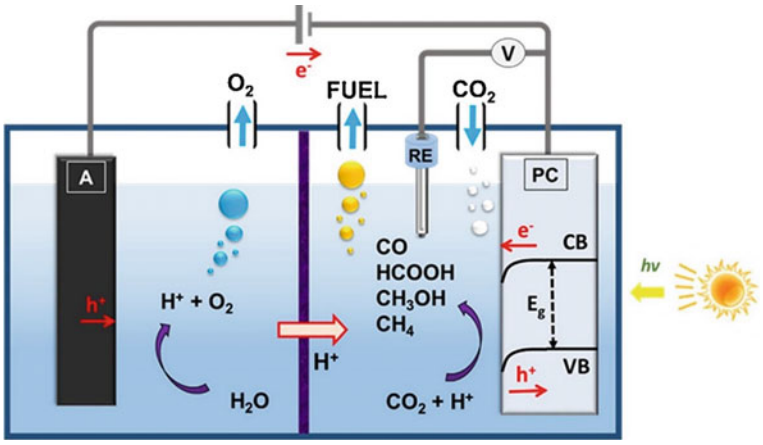

Fig. 7 Photoelectrochemical process. (Reprinted with permission from Kalamaras [40])

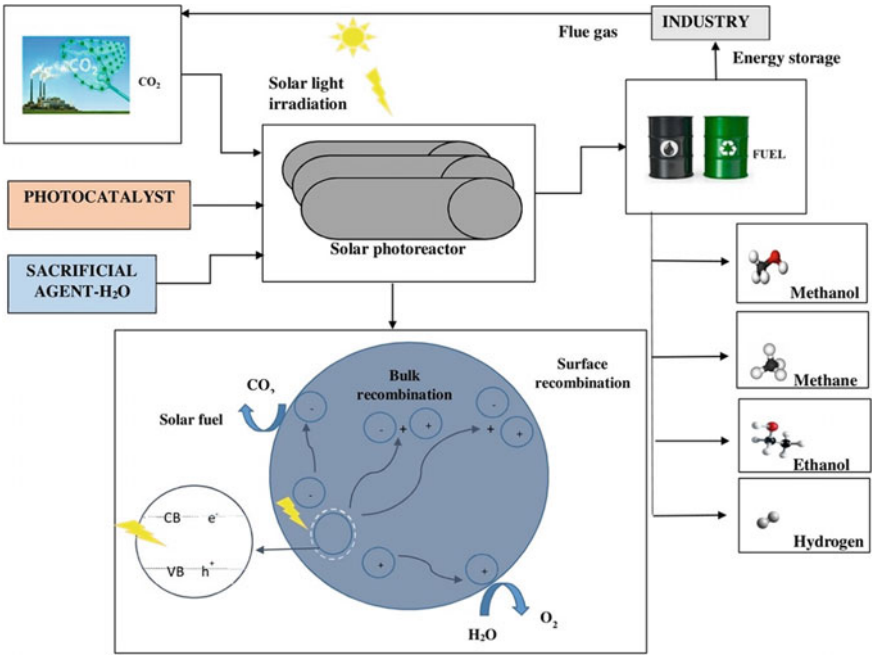

Fig. 8 Solar production process. (Reprinted with permission from Francis et al. [70])

Table 5 Developed catalysts for solar fuel production

Catalyst	Light Source	Products	Production	Reference
$ZnS_{1-x}Se_x$ nanobelts	300 W Xe lamp	CO, H_2	–	[74]
$Zn_{0.5}Cd_{0.5}S$/Au@g-C_3N_4	300 W Xe lamp/ UV- cutoff filter	CH_3OH	1.31 $\mu molg^{-1} h^{-1}$	[75]
Dolomite supported Cu_2O	LED visible 20 W	CH_3OH and HCOH	38 $\mu molg^{-1} h^{-1}$	[76]
Ni/CeO_2	THERMAL (350 °C)	CH_4	–	[77]
Ni/In_2O_3	300 W Xe lamp/ UV- cutoff filter	CH_4	55 $\mu molg^{-1} h^{-1}$	[78]
$CsPbBr_3/MoS_2$	300 W Xe lamp/ UV- cutoff filter	CH_4	125 $\mu molg^{-1} h^{-1}$	[24]
$CsPbBr_3$/UiO-66(NH_2)	300 W Xe lamp/UV- cutoff filter	CO, CH_4	10 $\mu molg^{-1} h^{-1}$	[17]

Table 5 demonstrates the catalysts being developed for the solar fuel production method. Most of the tests utilize a simulated solar light, using a UV cutoff filter to reduce the ultraviolet contribution in the synthesis.

Metal–Organic Frameworks produced a higher value of methane. Mainly, this material has the advantage of prevents recombinations and material aggregation, maintaining the catalyst stable for an extended period.

7 Future Perspectives

As they are today, alternative fuel production methods have low synthesis efficiency, converting a minimal amount of CO_2 in each process. Therefore, for these processes to be used as alternatives to conventional fuels, further research will be needed to improve them.

As the day passes, new materials emerge as strong candidates for solar fuel production. However, for those systems to be capable of an environmentally friendly synthesis, the new materials need to be activated under visible light irradiation, allowing better use of sunlight.

The fuel production by photo and electrocatalysis can mainly benefit industries since the photocatalyst can help decrease the electrical energy used to synthesize the products.

Thermochemical methods, such as dry reforming and the Fischer–Tropsch process, need to be evaluated since they need to achieve high temperatures. In those cases, the catalysts can help to reduce those temperatures. Besides, catalysts with coke deposition resistance can make the process more efficient since they will be active for a longer time.

Nowadays, sunlight can be associated with the Fischer–Tropsch synthesis, originating the photo-assisted Fischer–Tropsch process. This process can convert syngas into valuable hydrocarbons. Still, due to the high recombination rate and low efficiency in synthesizing the products, the process needs improvements.

The hydrogen production processes can achieve a great potential, mainly in the automobile industry, since it solves the hydrogen transportation problem, allowing vehicles to carry only water that can be split into hydrogen, used, and then produce water again.

References

1. Karmaker, A.K., Rahman, M.M., Hossain, M.A., Ahmed, M.R.: Exploration and corrective measures of greenhouse gas emission from fossil fuel power stations for Bangladesh. J. Cleaner Prod. **244**, 118645 (2020)
2. Wenchao, L., Yihui, Y., Lixin, T.: Spatial spillover effects of industrial carbon emissions in China. In: Energy Procedia, vol. 152, pp. 679–684. Elsevier Ltd. (2018)
3. Zheng, X., et al.: A review of greenhouse gas emission profiles, dynamics, and climate change mitigation efforts across the key climate change players. J. Clean. Prod. **234**, 1113–1133 (2019)
4. Gonçalves, J.M., Matias, T.A., Toledo, K.C.F., Araki, K.: Electrocatalytic materials design for oxygen evolution reaction. In: Advances in Inorganic Chemistry, vol. 74, pp. 241–303. Academic Press Inc. (2019)
5. Miller, B.: Greenhouse gas—carbon dioxide emissions reduction technologies. In: Fossil Fuel Emissions Control Technologies, pp. 367–438. Elsevier (2015). https://doi.org/10.1016/b978-0-12-801566-7.00008-7
6. Augugliaro, V., et al.: Heterogeneous photocatalysis and catalysis: An overview of their distinctive features. In: Heterogeneous Photocatalysis: Relationships with Heterogeneous Catalysis and Perspectives, pp. 1–24. Elsevier (2019). https://doi.org/10.1016/B978-0-444-64015-4.00001-8
7. Vaiano, V., Sannino, D., Sacco, O.: The use of nanocatalysts (and nanoparticles) for water and wastewater treatment by means of advanced oxidation processes. In: Nanotechnology in the Beverage Industry, pp. 241–264. Elsevier (2020). https://doi.org/10.1016/b978-0-12-819941-1.00009-2
8. Nayana, K., Sunitha, A.P.: Probing nanostructure MoS_2 as catalyst in light activated and electro activated hydrogen evolution reaction. Mater. Today: Proc. (2021). https://doi.org/10.1016/j.matpr.2021.01.115
9. Tai, X.H., Lai, C.W., Juan, J.C., Lee, K.M.: Nanocatalyst-based catalytic oxidation processes. In: Nanomaterials for Air Remediation, pp. 133–150. Elsevier (2020). https://doi.org/10.1016/B978-0-12-818821-7.00007-5
10. Zhang, H., et al.: Hybrid niobium and titanium nitride nanotube arrays implanted with nanosized amorphous rhenium–nickel: An advanced catalyst electrode for hydrogen evolution reactions. Int. J. Hydrogen Energy **45**, 6461–6475 (2020)
11. Ayyub, M.M., Rao, C.N.R.: Design of efficient photocatalysts through band gap engineering. In Nanostructured Photocatalysts, pp. 1–18. Elsevier (2020). https://doi.org/10.1016/b978-0-12-817836-2.00001-6
12. Ghosh, S.K., Kitagawa, S.: 1—Introduction. In: Metal-Organic Frameworks (MOFs) for Environmental Applications, pp. 1–4 (2019). https://doi.org/10.1016/B978-0-12-814633-0.00001-6
13. Kumari, A., et al.: Bimetallic metal organic frameworks heterogeneous catalysts: Design, construction, and applications. Mater. Today Energy **20**, 100667 (2021)

14. Liu, K. G., et al.: Metal-organic framework composites as green/sustainable catalysts. Coord. Chem. Rev. **436**, 213827 (2021)
15. Xu, W. et al.: Metal/metal-organic framework interfacial ensemble-induced dual site catalysis towards hydrogen generation. Appl. Catal. B: Environ. **286**, 119946 (2021)
16. Chen, L., Xu, Q.: Metal-organic framework composites for catalysis. Matter **1**, 57–89 (2019)
17. Wan, S., et al.: Perovskite-type CsPbBr3 quantum dots/UiO-66(N_H2) nanojunction as efficient visible-light-driven photocatalyst for C_O2 reduction. Chem. Eng. J. **358**, 1287–1295 (2019)
18. Hu, L., et al.: Turning metal-organic frameworks into efficient single-atom catalysts via Pyrolysis with a focus on oxygen reduction reaction catalysts. Energy Chem 100056 (2021). https://doi.org/10.1016/j.enchem.2021.100056
19. Zhou, C., et al.: Recent advances in niobium-based semiconductors for solar hydrogen production. Coord. Chem. Rev. **419**, 213399 (2020)
20. Franceschini, E.A., et al.: Niobium-based semiconductor electrodes for hydrogen evolution reaction. Int. J. Hydrogen Energy **44**, 31940–31948 (2019)
21. Nunes, B.N., et al.: Recent advances in niobium-based materials for photocatalytic solar fuel production. Catalysts **10**, 126 (2020)
22. Wang, Y., et al.: High efficiency reduction of CO_2 to CO and CH4 via photothermal synergistic catalysis of lead-free perovskite Cs3Sb2I9. Appl. Catal. B: Environ. **294**, 120236 (2021)
23. Tasleem, S., Tahir, M.: Current trends in strategies to improve photocatalytic performance of perovskites materials for solar to hydrogen production. Renew. Sustain. Energy Rev. **132** 110073 (2020)
24. Wang, X. et al.: CsPbBr3 perovskite nanocrystals anchoring on monolayer MoS2 nanosheets for efficient photocatalytic CO_2 reduction. Chem. Eng. J. **416**, 128077 (2020)
25. Dandia, A., et al.: Visible light-driven perovskite-based photocatalysts: A new candidate for green organic synthesis by photochemical protocol. Current Res. Green Sustain. Chem. **3**, 100031 (2020)
26. Zhang, J., et al.: Ni$(OH)_2$/Ni/g-C_3N_4 composite: An efficient electrocatalyst for hydrogen evolution. J. Fuel Chem. Technol. **49**, 198–204 (2021)
27. Yu, H. et al.: Novel application of a Z-scheme photocatalyst of Ag_3PO_4@g-C_3N_4 for photocatalytic fuel cells. J. Environ. Manage. **254** (2020)
28. Zhu, Y. et al.: Catalytic origin and universal descriptors of heteroatom-doped photocatalysts for solar fuel production. Nano Energy **63**, 103819 (2019)
29. Meng, X., et al.: Direct methane conversion under mild condition by thermo-, electro-, or photocatalysis. Chem **5**, 2296–2325 (2019)
30. Tjandra, A.D., Huang, J.: Photocatalytic carbon dioxide reduction by photocatalyst innovation. Chin. Chem. Lett. **29**, 734–746 (2018)
31. Shan, J., Li, M., Allard, L.F., Lee, S., Flytzani-Stephanopoulos, M.: Mild oxidation of methane to methanol or acetic acid on supported isolated rhodium catalysts. Nature **551**, 605–608 (2017)
32. Zhang, W. et al.: Progress and perspective of electrocatalytic CO_2 reduction for renewable carbonaceous fuels and chemicals. Adv. Sci. 5 (2018)
33. Liu, W.C., et al.: The methanol economy: methane and carbon dioxide conversion. Top. Catal. **61**, 530–541 (2018)
34. Chung, W.C., et al.: Syngas production via plasma photocatalytic reforming of methane with carbon dioxide. Int. J. Hydrogen Energy **44**, 19153–19161 (2019)
35. Akhter, P., et al.: Novel nanostructured-TiO_2 materials for the photocatalytic reduction of CO_2 greenhouse gas to hydrocarbons and syngas. Fuel **149**, 55–65 (2015)
36. Pan, F. et al.: Integrating photocatalysis and thermocatalysis to enable efficient CO_2 reforming of methane on Pt supported CeO_2 with Zn doping and atomic layer deposited MgO overcoating. Appl. Catal. B: Environ. **260**, 118189 (2020)
37. Jang, W.J., et al.: A review on dry reforming of methane in aspect of catalytic properties. Catal. Today **324**, 15–26 (2019)
38. Rego de Vasconcelos, B. et al.: Upgrading greenhouse gases (methane and carbon dioxide) into syngas using nickel-based catalysts. Fuel **226**, 195–203 (2018)

39. Osazuwa, O.U., Cheng, C.K.: Catalytic conversion of methane and carbon dioxide (greenhouse gases) into syngas over samarium-cobalt-trioxides perovskite catalyst. J. Clean. Prod. **148**, 202–211 (2017)
40. Kalamaras, E., et al.: Solar carbon fuel via photoelectrochemistry. Catal. Today **317**, 56–75 (2018)
41. Karamian, E., Sharifnia, S.: On the general mechanism of photocatalytic reduction of CO_2. J. CO_2 Utilization **16**, 194–203 (2016)
42. Steinlechner, C., Junge, H.: Renewable methane generation from carbon dioxide and sunlight. Angew. Chem. Int. Ed. **57**, 44–45 (2018)
43. Ulmer, U., et al.: Fundamentals and applications of photocatalytic CO_2 methanation. Nat. Commun. **10**, 1–12 (2019)
44. Hussain, M., Akhter, P., Russo, N., Saracco, G.: New optimized mesoporous silica incorporated isolated Ti materials towards improved photocatalytic reduction of carbon dioxide to renewable fuels. Chem. Eng. J. **278**, 279–292 (2015)
45. Bagheri, S., Muhd Julkapli, N.: Nano-diamond based photocatalysis for solar hydrogen production. Int. J. Hydrogen Energy **45**, 31538–31554 (2020)
46. Bo, T. et al.: Photocatalytic H_2 evolution on CdS modified with partially crystallized MoS_2 under visible light irradiation. Chem. Phys. Letters **746**, 137305 (2020)
47. Kim, J.W., Boo, K.J., Cho, J.H., Moon, I.: Key challenges in the development of an infrastructure for hydrogen production, delivery, storage and use. In: Advances in Hydrogen Production, Storage and Distribution, pp. 3–31 Elsevier (2014). https://doi.org/10.1533/9780857097736.1.3
48. Lin, H., Wei, K., Yin, Z., Sun, S.: Nanocatalysts in electrosynthesis. iScience **24**, 102172 (2021)
49. Chiarello, G.L., Selli, E.: Photocatalytic production of hydro-gen. In: Advances in Hydrogen Production, Storage and Distribution, pp. 216–247. Elsevier (2014). https://doi.org/10.1533/9780857097736.2.216
50. Kelly, N.A.: Hydrogen production by water electrolysis. In: Advances in Hydrogen Production, Storage and Distribution, pp. 159–185. Elsevier (2014). https://doi.org/10.1533/9780857097736.2.159
51. Gil, J.J., et al.: Efficient ZnS–ZnO/ZnAl-LDH composite for H_2 production by photocatalysis. Renew. Energy **145**, 124–132 (2020)
52. Divyasri, Y.V. et al.: Optimization of N doping in TiO_2 nanotubes for the enhanced solar light mediated photocatalytic H_2 production and dye degradation. Environ. Pollut. **269**, 116170 (2021)
53. Fu, W. et al.: CeO_2 sensitized nanotubes embed ordered porous SnO_2 aerogel and its photocatalytic water splitting for H_2 production characteristics. J. Solid State Chem. **297**, 122098 (2021)
54. Franz, R., Tichelaar, F.D., Uslamin, E.A., Pidko, E.A.: Dry reforming of methane to test passivation stability of Ni/Al_2O_3 catalysts. Appl. Catal. A: General **612** (2021)
55. Aghamohammadi, S., Haghighi, M., Maleki, M., Rahemi, N.: Sequential impregnation vs. sol-gel synthesized Ni/Al_2O_3-CeO_2 nanocatalyst for dry reforming of methane: Effect of synthesis method and sup-port promotion. Mol. Catal. **431**, 39–48 (2017)
56. Wang, C. et al.: Recent advances in nanostructured catalysts for photo-assisted dry reforming of methane. Mater. Today Nano **14** (2021)
57. Dou, J., et al.: Sandwiched SiO_2@Ni@ZrO_2 as a coke resistant nanocatalyst for dry reforming of methane. Appl. Catal. B **254**, 612–623 (2019)
58. Rahbar Shamskar, F., Rezaei, M., Meshkani, F.: The influence of Ni loading on the activity and coke formation of ultrasound-assisted co-precipitated Ni–Al_2O_3 nanocatalyst in dry reforming of methane. Int. J. Hydrogen Energy **42**, 4155–4164 (2017)
59. Yue, L., et al.: Thermal-stable Pd@mesoporous silica core-shell nanocatalysts for dry reforming of methane with good coke-resistant performance. Fuel **218**, 335–341 (2018)
60. Sajjadi, S.M., Haghighi, M., Eshghi, J.: Synergic influence of potassium loading and plasma-treatment on anti-coke property of K-Promoted bimetallic NiCo NiAl2O4 nanocatalyst applied in O_2-Enhanced dry reforming of CH4. Int. J. Hydrogen Energy **44**, 13397–13414 (2019)

61. Otun, K.O., Liu, X., Hildebrandt, D.: Metal-organic framework (MOF)-derived catalysts for Fischer-Tropsch synthesis: Recent progress and future perspectives. J. Energy Chem. **51**, 230–245 (2020)
62. Medeiros, R.L.B.A. et al.: One-pot microwave-assisted combustion synthesis of Ni-Al_2O_3 nanocatalysts for hydrogen production via dry reforming of methane. Fuel **287**, 119511 (2021)
63. Hassani Rad, S.J., Haghighi, M., Alizadeh Eslami, A., Rahmani, F., Rahemi, N.: Sol-gel vs. impregnation preparation of MgO and CeO_2 doped Ni/Al_2O_3 nanocatalysts used in dry reforming of methane: Effect of process conditions, synthesis method and support composition. Int. J. Hydrogen Energy **41**, 5335–5350 (2016)
64. Khajeh Talkhoncheh, S., Haghighi, M.: Syngas production via dry reforming of methane over Ni-based nanocatalyst over various sup-ports of clinoptilolite, ceria and alumina. J. Nat. Gas Sci. Eng. **23**, 16–25 (2015)
65. Tran, N.T., et al.: Improvements in hydrogen production from methane dry reforming on filament-shaped mesoporous alumina-supported cobalt nanocatalyst. Int. J. Hydrogen Energy (2020). https://doi.org/10.1016/j.ijhydene.2020.06.142
66. Jalali, R., Rezaei, M., Nematollahi, B., Baghalha, M.: Preparation of Ni/MeAl2O4-MgAl2O4 (Me=Fe Co, Ni, Cu, Zn, Mg) nanocatalysts for the syngas production via combined dry reforming and partial oxidation of methane. Renew. Energy **149**, 1053–1067 (2020)
67. Singha, R.K., Yadav, A., Shukla, A., Kumar, M., Bal, R.: Low-temperature dry reforming of methane over Pd-CeO_2 nanocatalyst. Catal. Commun. **92**, 19–22 (2017)
68. García-Diéguez, M., Pieta, I.S., Herrera, M.C., Larrubia, M.A., Alemany, L.J.: Improved Pt-Ni nanocatalysts for dry reforming of methane. Appl. Catal. A **377**, 191–199 (2010)
69. Patial, S. et al.: Boosting light-driven CO_2 reduction into solar fuels: Mainstream avenues for engineering ZnO-based photocatalysts. Environ. Res. **197**, 111134 (2021)
70. Francis, A., Shanmuga Priya, S., Harish Kumar, S., Sudhakar, K., Tahir, M.: A review on recent developments in solar photoreactors for carbon dioxide conversion to fuels. J. CO_2 Utilization **47**, 101515 (2021)
71. Guo, X. et al.: Bandgap engineering of metal-organic frameworks for solar fuel productions. Coord. Chem. Rev. **435**, 213785 (2021)
72. Ikreedeegh, R.R., Tahir, M.: A critical review in recent developments of metal-organic-frameworks (MOFs) with band engineering alteration for photocatalytic CO_2 reduction to solar fuels. J. CO_2 Utilization **43**, 101381 (2021)
73. Mazari, S.A., et al.: An overview of catalytic conversion of CO_2 into fuels and chemicals using metal organic frameworks. Process Saf. Environ. Prot. **149**, 67–92 (2021)
74. Li, P., Hussain, S., Li, L., Guo, L., He, T.: Composition-tunable ZnS1–Se nanobelt solid solutions for efficient solar-fuel production. Chin. J. Catal. **41**, 1663–1673 (2020)
75. Madhusudan, P. et al.: Construction of highly efficient Z-scheme $_{ZnxCd1-x}$S/Au@g-C_3N_4 ternary heterojunction composite for visible-light-driven photocatalytic reduction of CO_2 to solar fuel. Appl. Catal. B: Environ. **282**, 119600 (2021)
76. Luévano-Hipólito, E., Torres-Martínez, L.M.: Dolomite-supported Cu_2O as heterogeneous photocatalysts for solar fuels produc-tion. Mater. Sci. Semicond. Process. **116**, 105119 (2020)
77. Feng, X., et al.: Metal organic framework derived Ni/CeO_2 catalyst with highly dispersed ultra-fine Ni nanoparticles: Impregnation syn-thesis and the application in CO_2 methanation. Ceram. Int. **47**, 12366–12374 (2021)
78. Wan, Z., Wang, J., Wang, K., Hu, M., Wang, X.: Photocatalytic reduction of CO_2 with H_2O vapor into solar fuels over Ni modified porous In_2O_3 nanosheets. Catal. Today (2020). https://doi.org/10.1016/j.cattod.2020.10.008

Photoelectrochemical Performance of Doped and Undoped TiO_2 Nanotubes for Light-Harvesting and Water Splitting Techniques: Systematic Review and Meta-Analysis

Maria Luisa Puga, Carla Schwengber ten Caten, and Carlos Pérez Bergmann

Abstract Strategies for optimizing the performance of titanium dioxide (TiO_2) nanotubes on photoelectrochemical applications include morphological adjustments via doping or deposition techniques. This systematic review and meta-analysis summarize published articles from 2015 to date on pure and modified TiO_2 nanotubes (TNTs) anodized in organic electrolytes and evaluate potential relationships between anodization parameters, tube morphology, and water splitting applicability. Studies were searched on Science Direct online database, screened according to predefined criteria, and evaluated for their eligibility. Fourteen studies composed the meta-analysis, 11 of them on pure and six on doped TNTs. Multiple linear regression was performed to test if percentages of water (H_2O) and ammonium fluoride (NH_4F) in the electrolyte, anodizing time, applied voltage, and the presence of a doping agent significantly predicted the developed photocurrent density. The overall regression was statistically significant ($R^2 = 0.893$, F (10, 20) = 3.90, $p = 0.0000$). The main effects predicting photocurrent density were H_2O ($p = 0.014$), NH_4F ($p = 0.001$), anodizing time ($p = 0.012$), and type of nanotube modification ($p = 0.005$). Doped nanotubes yielded a mean photocurrent density value 65% higher than pure TiO_2 nanotubes (1.082 and 0.656 $mA.cm^{-2}$, respectively).

Keywords TiO_2 nanotubes · Doping · Water splitting · Anodization · Systematic review · Meta-analysis

1 Introduction

The ever-increasing global concern about sustainability has shifted efforts to developing innovative environmentally friendly energy resources [1]. Among the prospective alternatives, hydrogen fuel has been described as an ideal solution to counter the negative impacts of fossil fuel exploration, primarily because its generation occurs

M. L. Puga (✉) · C. S. ten Caten · C. P. Bergmann
Universidade Federal do Rio Grande do Sul, Porto Alegre, Brazil
e-mail: maria.puga@ufrgs.br

A. Kopp Alves (ed.), *Environmental Applications of Nanomaterials*, Engineering Materials, https://doi.org/10.1007/978-3-030-86822-2_10

through the electrolysis of water under sunlight irradiation, two naturally abundant and renewable resources [1–5]. Electrochemical systems for hydrogen generation via water splitting using the semiconductor TiO_2 as photoelectrode were first reported in 1972 [6]. The technique is also carbon–neutral [7], which holds a fundamental asset to the worldwide decarbonization goals ratified by the 2016 Paris Agreement.

The working principle of the technique is based on the generation and transferring of electron–hole pairs under direct solar illumination. As illustrated in Fig. 1, light absorption induces the generation of excited electrons (e^-) and holes (h^+) in the conduction and valence bands of the semiconductor, respectively [3, 8]. Charge carriers then migrate to the TiO_2-electrolyte interface, where the photo-generated holes promote water oxidation into oxygen (H_2O to O_2), while electrons reduce the hydrogen ions to form molecular hydrogen (H^+ to H_2) [6, 9, 10].

Even though TiO_2 is an outstanding, cost-effective photocatalyst semiconductor [11], its wide band gap (3.0–3.2 eV) restricts the effective range of the incoming solar energy spectrum utilized in water splitting processes to the UV radiation [12]. Moreover, TiO_2 nanoparticles are prone to a fast recombination rate of the photo-induced charge carriers, which further restricts photocatalytic activity [13, 14]. Given these aspects, morphological alterations are required to maximize the light-harvesting efficiency of TiO_2 as a photoanode [9, 10].

A chief modification of the pure TiO_2 structure is to shift from randomly oriented nanoparticles to well-defined nanotube arrays (TNTs). The TNT structure is also defined by a large surface area, which provides additional active sites for photochemical reactions while reducing charge carrier recombination rates [15, 16]. Regarding TiO_2 nanotube synthesis, electrochemical anodization has taken up the spotlight since their first reports in 1999 [17, 18]. The technique is a straightforward, versatile, and scalable way to fabricate highly-ordered, self-assembled nanotube arrays from metallic titanium substrates [10, 19].

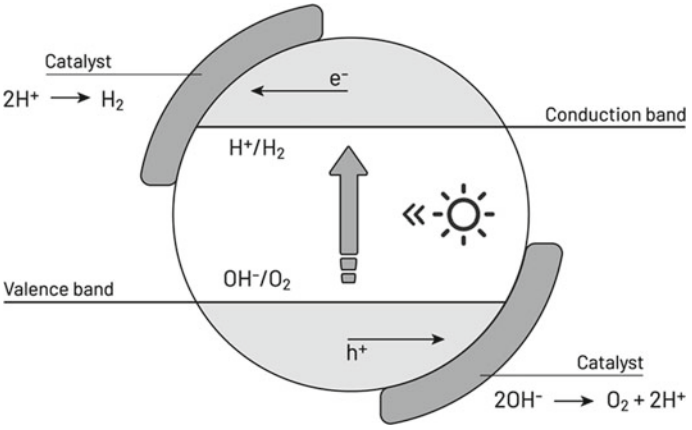

Fig. 1 Schematic principle of photocatalytic water splitting. Adapted and reprinted with permission from [3]

It is important to note that accurate control over anodizing parameters and electrolyte composition is pivotal in fine-tuning TNT morphology [20]. To date, employing organic-based electrolytes with the addition of specific amounts of water and ammonium fluoride (NH_4F) is shown to set up the most beneficial environment for optimized tube growth [21, 22].

The optimization of electronic properties on TNTs is mainly achieved by introducing a comprehensive variety of materials into the TiO_2 lattice [23], such as noble and transition metals, rare-earths, non-metal ions, and other semiconductors [9, 14]. The doping method aims to decrease band gap energy levels and broaden the effective absorption range to the visible light spectrum [15]. Dopants also support higher separation rates of electron–hole pairs through oxygen vacancies and electron trapping mechanisms [24, 25].

Given its fitting to long-term sustainability goals, hydrogen production is expected to hold up to 22% of the global energy consumption in 2050 [7, 26]. So, it is fundamental to outline the effects of anodization parameters on TiO_2 photoelectrochemical output to maximize TNT suitability in hydrogen fuel generation production.

2 Methods

This study was conducted following the Preferred Reporting Items for Systematic Reviews and Meta-Analyses (PRISMA) Statement [27]. Research papers published between 2015 and 2021 were selected from the online database Science Direct in April 2021, using the key term "TiO_2 nanotubes anodization water splitting". Searching results were limited to subscription journals.

2.1 Eligibility Criteria and Study Selection

The online database search yielded 707 results, which were manually selected by the authors. Studies meeting the following criteria were eligible for meta-analysis: (i) nanotubes fabricated via electrochemical anodization; (ii) anodizing electrolyte prepared with ethylene glycol, H_2O, and NH_4F; (iii) samples consisting of either pure OR doped TiO_2 nanotubes; (iv) substrate made of Ti foils, plates or sheets; linear voltammetry conducted in (v) Ag/AgCl electrode and (vi) 1 M KOH electrolyte.

Screened papers were saved to the Mendeley database for further evaluation. Studies were excluded if (i) they had insufficient data on electrolyte composition, band gap analysis, or photoelectrochemical performance; or (ii) the photoelectrochemical performance was conducted in any other electrolyte or set-up condition than the one stated above. The study flow diagram is presented in Fig. 2.

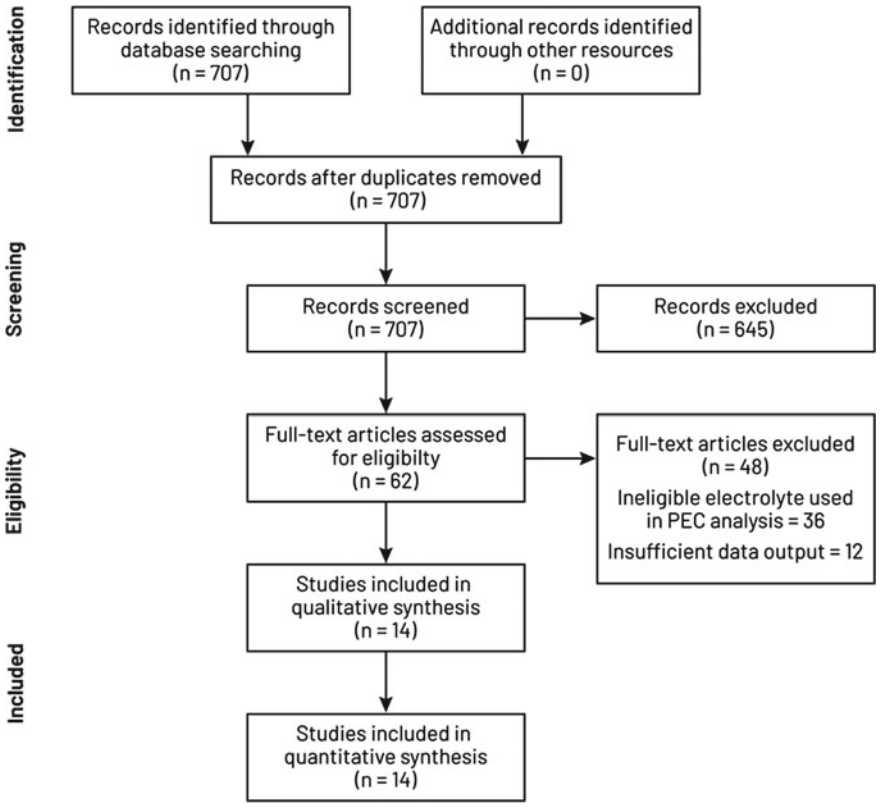

Fig. 2 PRISMA study flow diagram

2.2 Analytic Approach

The meta-analysis was conducted through a multiple linear regression model for 14 eligible studies, detailed in Table 1. Continuous predictors selected were (i) applied potential (V); (ii) anodizing time (h); (iii) H_2O content (vol.%); and (iv) NH_4F content (wt.%); and the categorical predictor was (v) type of TNT, i.e., doped or pure. The response was defined as (vi) photocurrent (PC) density developed at 0 V ($mA.cm^{-2}$).

Table 1 Summary of the 14 studies included in the meta-analysis

Modification on TNTs	Electrolyte composition	Anodizing condition	Photocurrent density at 0 V	References
Pure	EG + 0.67% NH_4F + 3% H_2O	50 V—1 h	0.06 mA cm^{-2}	[28]
Pure	EG + 0.5% NH_4F + 3% H_2O	40 V—0.3 h	0.42 mA cm^{-2}	[29]
Pure	EG + 0.5% NH_4F + 3% H_2O	60 V—0.28 h	0.16 mA cm^{-2}	[30]
Pure	EG + 0.3% NH_4F + 2% H_2O	60 V—1 h	0.47 mA cm^{-2}	[31]
Pure	EG + 0.8% NH_4F + 8% H_2O	60 V – 6 h	1.42 mA cm^{-2}	[25]
Pure	EG + 0.5% NH_4F + 5% H_2O	60 V—0.5 h	0.45 mA cm^{-2}	[25]
Pure	EG + 0.3% NH_4F + 5% H_2O	60 V—0.5 h	0.02 mA cm^{-2}	[32]
Pure	EG + 0.3% NH_4F + 2% H_2O	20 V—1 h	0.54 mA cm^{-2}	[33]
Pure	EG + 0.3% NH_4F + 2% H_2O	20 V—2 h	0.57 mA cm^{-2}	[33]
Pure	EG + 0.3% NH_4F + 2% H_2O	20 V—3 h	0.18 mA cm^{-2}	[33]
Pure	EG + 0.3% NH_4F + 2% H_2O	20 V—6 h	0.48 mA cm^{-2}	[33]
Pure	EG + 0.3% NH_4F + 2% H_2O	40 V—1 h	0.78 mA cm^{-2}	[33]
Pure	EG + 0.3% NH_4F + 2% H_2O	40 V—3 h	0.12 mA cm^{-2}	[33]
Pure	EG + 0.3% NH_4F + 2% H_2O	40 V—6 h	0.24 mA cm^{-2}	[33]
Pure	EG + 0.3% NH_4F + 2% H_2O	60 V—6 h	0.49 mA cm^{-2}	[33]
Pure	EG + 0.5% NH_4F + 2% H_2O	60 V—1 h	0.08 mA cm^{-2}	[34]
Pure	EG + 0.35% NH_4F + 2% H_2O	30 V—0.3 h	0.8 mA cm^{-2}	[35]
Pure	EG + 0.4% NH_4F + 12% H_2O	30 V—0.3 h	0.97 mA cm^{-2}	[35]
Pure	EG + 0.4% NH_4F + 12% H_2O	30 V – 1 h	1.12 mA cm^{-2}	[36]
Pure	EG + 0.5% NH_4F + 2% H_2O	55 V – 0.5 h	0.013 mA cm^{-2}	[37]

(continued)

Table 1 (continued)

Modification on TNTs	Electrolyte composition	Anodizing condition	Photocurrent density at 0 V	References
Doping (Na_2Co_3)	EG + 0.67% NH_4F + 3% H_2O + 0,03 M Na_2CO_3	50 V—1 h	0.28 mA cm^{-2}	[28]
Doping (Ti-5%Si alloy)	EG + 0.5% NH_4F + 3% H_2O	40 V—0.3 h	0.75 mA cm^{-2}	[29]
Doping (T-1%Ni alloy)	EG + 0.5% NH_4F + 3% H_2O	40 V—0.3 h	0.84 mA cm^{-2}	[38]
Doping (Ti-10%Ni alloy)	EG + 0.5% NH_4F + 3% H_2O	40 V—0.3 h	0.60 mA cm^{-2}	[38]
Doping (Al_2O_3)	EG + 0.5% NH_4F + 2% H_2O + 6.35 mM $Al(NO_3)_3$	60 V—1 h	0.2 mA cm^{-2}	[34]
Doping (Ti-1%Nb alloy)	EG + 0.35% NH_4F + 3.8% H_2O	30 V—0.3 h	1.14 mA cm^{-2}	[39]
Doping (Ti-1%Nb alloy)	EG + 0.35% NH_4F + 3.8% H_2O	30 V—1 h	1.2 mA cm^{-2}	[39]
Doping (Ti-1%Nb alloy)	EG + 0.35% NH_4F + 3.8% H_2O	45 V—0.3 h	0.86 mA cm^{-2}	[39]
Doping (Ti-1%Nb alloy)	EG + 0.35% NH_4F + 3.8% H_2O	45 V—1 h	0.88 mA cm^{-2}	[39]
Doping (Ti-1%Nb alloy)	EG + 0.35% NH_4F + 3.8% H_2O	60 V—0.3 h	0.92 mA cm^{-2}	[39]
Doping (Ti-1%Nb alloy)	EG + 0.35% NH_4F + 3.8% H_2O	60 V—1 h	1.10 mA cm^{-2}	[39]
Doping (H^+)	EG + 0.5% NH_4F + 2% H_2O	55 V—0.5 h	0.028 mA cm^{-2}	[37]

3 Findings

The regression model for developed photocurrent density in doped and pure TiO_2 nanotubes is statistically significant ($p = 0.000$), with a coefficient of determination (R^2) of 0.893 and an adjusted R^2 of 0.84. Table 2 details the contribution and p-values for the statistically significant predictors. The main effects included in the model are H_2O and NH_4F content in the anodic electrolyte, duration of nanotube synthesis via electrochemical anodization, and type of TNT evaluated. Noteworthy contributions were calculated for H_2O percentage and tube modification, namely 21.5% and 19.4%. A quadratic effect of NH_4F was also found to be responsible for 15.2% of the observed responses on PC density at 0 V.

Results highlight the importance of a deliberate electrolyte preparation, as the effective growth of TiO_2 nanotubes is entirely dependent on a well-balanced rate between chemical dissolution and electrochemical formation of the oxide layer. In

Table 2 Analysis of variance for PC density developed at 0 V

Source	Contribution (%)	F-Value	*P*-Value
Regression	89.32	16.73	0.000
H_2O (vol.% in electrolyte)	21.50	7.31	0.014
NH_4F (wt.% in electrolyte)	1.00	14.22	0.001
Anodizing time (h)	4.04	7.70	0.012
Type of nanotube (pure or doped)	19.39	9.97	0.005
NH_4F * NH_4F	15.22	19.63	0.000
H_2O * NH4F	1.99	8.40	0.009
NH_4F * Anodizing time	1.50	5.13	0.035
NH_4F * Applied potential (V)	6.85	18.20	0.000
Anodizing time *Applied potential	5.73	9.73	0.005
H_2O * Type of nanotube	12.09	22.65	0.000
Error	10.68		
Lack-of-Fit	10.00	1.65	0.443
Pure Error	0.67		
Total	100.00		

organic-based electrolytes, fluoride species and water content are respectively the controlling agents of these processes [40, 41].

In addition, the expressive contribution of doping elements is consistent with published studies [9, 14, 23], showing that the method effectively increases TNT performance in light-harvesting applications.

Figure 3 shows the main effects plot for mean PC density. A linear relationship is observed for H_2O content (Fig. 3a) and anodizing time (Fig. 3c) versus developed current at 0 V. Regarding the extent of anodization, an increment in synthesis time progressively evolves TNT length and regularity [9, 42]. Similarly, added water in anodizing electrolytes acts as the source of oxygen required for oxide formation and dissolution of F^- ions. A gradual increase in H_2O content leads to broader nanotube diameters and wall thickness [21, 43]. Thus, both parameters translate into better morphological aspects, which enhance TNT properties.

The quadratic effect of NH_4F (Fig. 3b) shows an increase in the applicability of TiO_2 up to 0.5 wt %. The result agrees with the body of the literature, which employs an overall window of around 0.3% NH_4F in organic electrolytes [44]. Also, structural formation is severely impaired when F^- ion content reaches values above 2% [45], as the etching rate of the oxide layer becomes overly aggressive. Relative fluoride concentration is then a rate-limiting factor in anodization processes [40].

As for the type of material (Fig. 3d), dopant addition increases the photocurrent efficiency for TiO_2 nanotubes by about 65% (0.656 $mA.cm^{-2}$ on pure TNTs to 1.082 $mA.cm^{-2}$). Such an outcome reinforces the benefit of doping strategies for performance enhancement on clean energy generation.

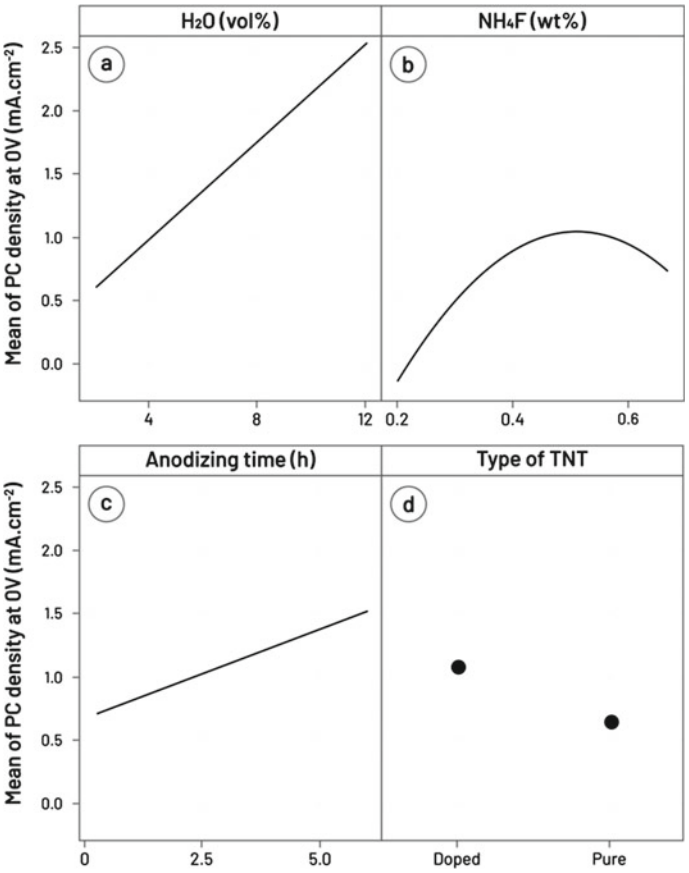

Fig. 3 Main effects plot for photocurrent density measured at 0 V (mA.cm^{-2}). Significant predictors are **a** H_2O and **b** NH_4F content in the electrolyte; **c** anodizing time; and **d** nanotube modification type

The regression model also discloses combined effects on developed current. Ammonium fluoride percentage (Fig. 4a) and the type of TNT (Fig. 4b) are both limiting factors for the suitable concentration of water in the electrolyte. As observed in Fig. 4a, the commonly employed volume of about 2% H_2O maximizes the current density with low amounts of NH_4F [44]. Moreover, higher concentrations of F^- ions require an increased amount of water to prevent corrosion of the Ti substrate [46]. For doped materials, water percentage shows a considerable influence on photocurrent density, which may relate to occurring side reactions. By adding secondary elements, the role of H_2O could be extended beyond oxygen input for oxide layer formation.

Regarding the interaction plot for anodizing time and applied potential (Fig. 4c), the optimal window for well-aligned and progressively longer TNT architectures is reported to be 20–60 V [47, 48]. Accordingly, an increase in current density

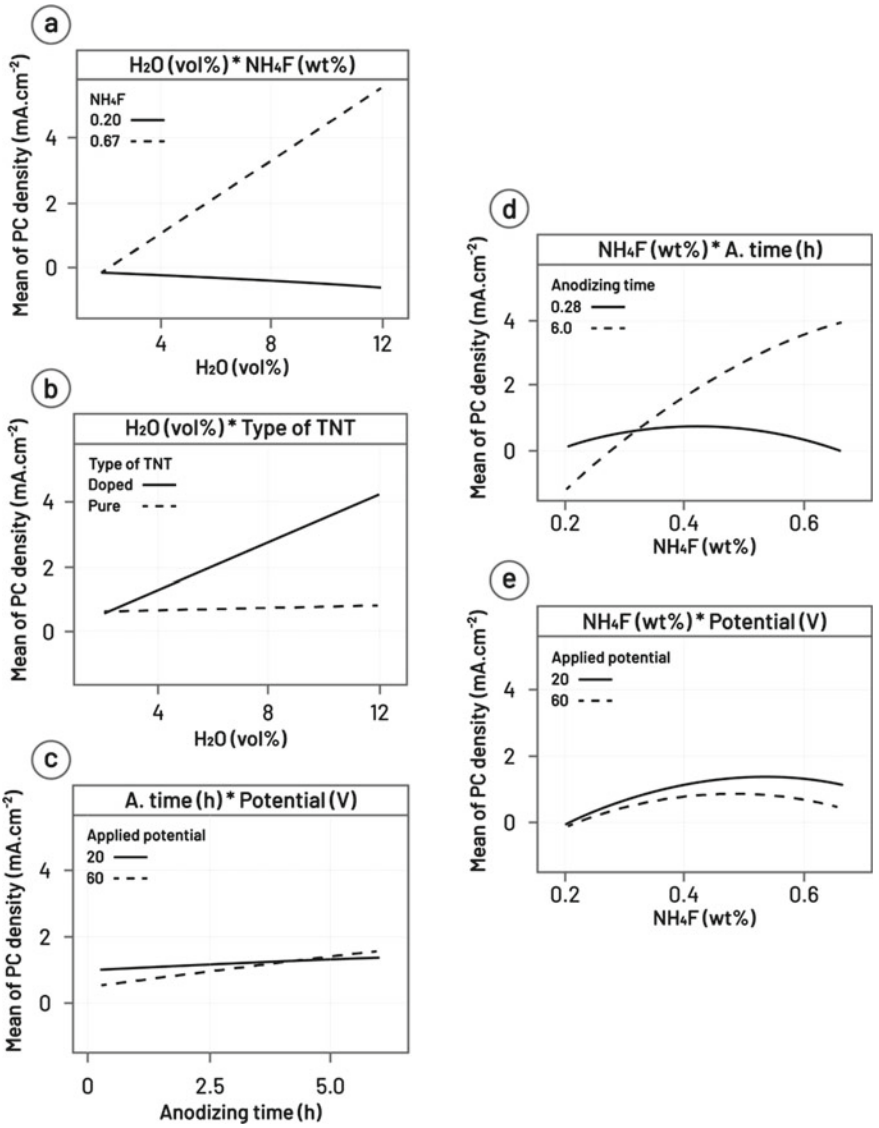

Fig. 4 Interaction plots for photocurrent density measured at 0 V ($mA.cm^{-2}$): **a** H_2O * NH_4F; **b** H_2O * type of TNT; **c** anodizing time * applied potential; **d** NH_4F * anodizing time; and **e** NH_4F * applied potential

is noticed for the regression model with longer anodizing times at both applied potentials. However, as the tendency of higher voltages to increase the randomness of synthesized arrays hamper their mechanical properties [49], the photocatalytic performance observed for tubes anodized at 60 V flattens out after 6 h in the presented model.

On correlations for NH_4F and anodizing time, Fig. 4d points that developed PC density grows for extended processes and more substantial amounts of fluoride species. Concentrations up to 0.3 wt % yielded a negative value of measured current, as the electrolyte may not have enough F^- ions to maintain sustainable etching rates for long periods. Shorter intervals showed that photocurrent density is not notably changed with NH_4F amount, indicating that the processing time was insufficient to cause meaningful variations in the resulting nanotubes. Lastly, as the parabolic behavior of both lower and higher fluoride concentrations suggests, excessive lengthening of anodization processes has no significant effect on morphological features or output properties, as the material is already in the steady-state growth region [21].

Proceeding on the NH_4F combined effects, lower concentrations result in similar PC responses for the evaluated potential window (Fig. 4e). However, a decrease in current density is observed as the percentage of F^- ions increase. A more pronounced effect is perceived at 60 V, as higher anodizing voltage impairs the ability to form well-aligned arrays due to a multi-directional chemical dissolution of the oxide layer derived from the enhanced mobility of fluoride species [50]. Therefore, anodizing with lower potentials and longer times would be more appropriate to maximize both tubular organization and measured photocurrent.

The performed meta-analysis highlights a strong correlation between the evaluated anodizing parameters of TNTs, indicating that their deliberate selection is necessary to improve morphology and applicability in catalytic processes. The observed effectiveness of adding doping agents into the TiO_2 lattice is also backed up by several studies, being one of the most efficient options to promote charge carrier separation and optimize the material response under incident solar irradiation [15].

4 Conclusions

Multiple linear regression was calculated to predict the developed photocurrent density of doped and undoped TiO_2 nanotubes based on the percentages of water (H_2O) and ammonium fluoride (NH_4F) in the electrolyte, anodizing time, and applied voltage. A significant regression equation was found ($F(10, 20) = 3.90$, $p = 0.0000$), with an R^2 of 0.893 and an adjusted R^2 of 0.84. The most significant main effects were H_2O, type of TNT, and NH_4F.

Doping processes are a remarkable modification of TiO_2 nanotubes, as they enhance the suitability for light-harvesting and water splitting techniques. The meta-analysis revealed mean values of PC density 65% higher for doped TNTs. Also, a

secondary element allows greater ranges of water and fluoride to be added to the electrolyte, fundamental variables in enhancing tubular morphology and, consequently, applied performance.

References

1. Ahmad, H., Kamarudin, S.K., Minggu, L.J., Kassim, M.: Hydrogen from photo-catalytic water splitting process: A review. Renew. Sustain. Energy Rev. **43**, 599–610 (2015)
2. Wang, Q., Hisatomi, T., Jia, Q., et al.: Scalable water splitting on particulate photocatalyst sheets with a solar-to-hydrogen energy conversion efficiency exceeding 1%. Nat. Mater. **15**, 611–615 (2016). https://doi.org/10.1038/nmat4589
3. Jang, J.S., Kim, H.G., Lee, J.S.: Heterojunction semiconductors: A strategy to develop efficient photocatalytic materials for visible light water splitting. Catal. Today **185**, 270–277 (2012). https://doi.org/10.1016/j.cattod.2011.07.008
4. Zou, Z., Ye, J., Sayama, K., Arakawa, H.: Direct splitting of water under visible light irradiation with an oxide semiconductor photocatalyst. Nature **414**, 625–627 (2001). https://doi.org/10.1038/414625a
5. Ismail, A.A., Bahnemann, D.W.: Photochemical splitting of water for hydrogen production by photocatalysis: A review. Sol. Energy Mater. Sol. Cells **128**, 85–101 (2014). https://doi.org/10.1016/j.solmat.2014.04.037
6. Fujishima, A., Honda, K.: Electrochemical photolysis of water at a semiconductor electrode. Nature **238**, 37–38 (1972). https://doi.org/10.1038/238037a0
7. Sazali, N.: Emerging technologies by hydrogen: A review. Int. J. Hydrogen Energy **45**, 18753–18771 (2020). https://doi.org/10.1016/j.ijhydene.2020.05.021
8. Lee, J.S.: Photocatalytic water splitting under visible light with particulate semiconductor catalysts. https://doi.org/10.1007/s10563-005-9157-0
9. Roy, P., Berger, S., Schmuki, P.: TiO2 nanotubes: Synthesis and applications. Angew. Chemie Int. Ed. **50**, 2904–2939 (2011)
10. Zhao, Y., Hoivik, N., Wang, K.: Recent advance on engineering titanium dioxide nanotubes for photochemical and photoelectrochemical water splitting. (2016). https://doi.org/10.1016/j.nanoen.2016.09.027
11. Grätzel, M.: Photoelectrochemical cells. Nature **414**, 338–344 (2001)
12. Wang, H., Zhang, L., Chen, Z., et al.: Semiconductor heterojunction photocatalysts: design, construction, and photocatalytic performances. Chem. Soc. Rev. **43**, 5234 (2014). https://doi.org/10.1039/C4CS00126E
13. Ni, M., Leung, M.K.H., Leung, D.Y.C., Sumathy, K.: A review and recent developments in photocatalytic water-splitting using TiO2 for hydrogen production. Renew. Sustain. Energy Rev. **11**, 401–425 (2007). https://doi.org/10.1016/J.RSER.2005.01.009
14. Tahir, M., Amin, N.S.: Advances in visible light responsive titanium oxide-based photocatalysts for CO2 conversion to hydrocarbon fuels. Energy Convers Manag. **76**, 194–214 (2013). https://doi.org/10.1016/j.enconman.2013.07.046
15. Kumaravel, V., Mathew, S., Bartlett, J., Pillai, S.C.: Photocatalytic hydrogen production using metal doped TiO2: A review of recent advances. Appl. Catal. B Environ. **244**, 1021–1064 (2019). https://doi.org/10.1016/j.apcatb.2018.11.080
16. El Ruby, M.A., Rohani, S.: Modified TiO2 nanotube arrays (TNTAs): Progressive strategies towards visible light responsive photoanode, a review. Energy Environ. Sci. **4**, 1065–1086 (2011)
17. Zwilling, V., Aucouturier, M., Darque-Ceretti, E.: Anodic oxidation of titanium and TA6V alloy in chromic media. Electrochem. Approach Electrochim. Acta **45**, 921–929 (1999). https://doi.org/10.1016/S0013-4686(99)00283-2

18. Zwilling, V., Darque-Ceretti, E., Boutry-Forveille, A., et al.: Structure and Physicochemistry of Anodic Oxide Films on Titanium and TA6V Alloy. Surf Interface Anal **27**, 629–637 (1999). https://doi.org/10.1002/(SICI)1096-9918(199907)27:7%3c629::AID-SIA551%3e3.0.CO;2-0
19. Zhang, Z., Wang, P.: Optimization of photoelectrochemical water splitting performance on hierarchical TiO2 nanotube arrays. Energy Environ. Sci **5**, 6506–6512 (2012). https://doi.org/10.1039/c2ee03461a
20. Jarosz, M., Pawlik, A., Kapusta-Kołodziej, J., et al.: Effect of the previous usage of electrolyte on growth of anodic titanium dioxide (ATO) in a glycerol-based electrolyte. Electrochim. Acta **136**, 412–421 (2014). https://doi.org/10.1016/j.electacta.2014.05.077
21. Albu, S.P., Roy, P., Virtanen, S., Schmuki, P.: Self-organized TiO2 nanotube arrays: Critical effects on morphology and growth. Isr. J. Chem. **50**, 453–467 (2010)
22. Regonini, D., Bowen, C.R., Jaroenworaluck, A., Stevens, R.: A review of growth mechanism, structure and crystallinity of anodized TiO2 nanotubes. Mater. Sci. Eng. R Reports **74**, 377–406 (2013). https://doi.org/10.1016/j.mser.2013.10.001
23. Vásquez, G.C., Peche-Herrero, M.A., Maestre, D., et al.: Effects of transition metal doping on the growth and properties of rutile TiO2 nanoparticles. J. Phys. Chem. C **117**, 1941–1947 (2013). https://doi.org/10.1021/jp3101656
24. Marschall, R., Wang, L.: Non-metal doping of transition metal oxides for visible-light photocatalysis. Catal. Today **225**, 111–135 (2014). https://doi.org/10.1016/j.cattod.2013.10.088
25. Liu, J., Dai, M., Wu, J., et al.: Electrochemical hydrogenation of mixed-phase TiO2 nanotube arrays enables remarkably enhanced photoelectrochemical water splitting performance. Sci. Bull. **63**, 194–202 (2018). https://doi.org/10.1016/j.scib.2017.12.023
26. Maggio, G., Nicita, A., Squadrito, G.: How the hydrogen production from RES could change energy and fuel markets: A review of recent literature. Int. J. Hydrogen Energy **44**, 11371–11384 (2019). https://doi.org/10.1016/j.ijhydene.2019.03.121
27. Page, M.J., McKenzie, J.E., Bossuyt, P.M., et al: The PRISMA 2020 statement: an updated guideline for reporting systematic reviews. Syst. Rev. 10:n71 (2021). https://doi.org/10.1186/s13643-021-01626-4
28. Alitabar, M., Yoozbashizadeh, H.: Effect of sodium carbonate as an additive on the morphology and photocatalytic activity of TiO2 nanotubes. Mater. Res. Bull. **95**, 169–176 (2017). https://doi.org/10.1016/j.materresbull.2017.07.013
29. Dong, Z., Ding, D., Li, T., Ning, C.: Facile fabrication of Si-doped TiO2 nanotubes photoanode for enhanced photoelectrochemical hydrogen generation. Appl. Surf. Sci. **436**, 125–133 (2018). https://doi.org/10.1016/j.apsusc.2017.12.030
30. Hejazi, S., Nguyen, N.T., Mazare, A., Schmuki, P.: Aminated TiO 2 nanotubes as a photoelectrochemical water splitting photoanode. Catal. Today **281**, 189–197 (2017). https://doi.org/10.1016/j.cattod.2016.07.009
31. Huo, S., Xu, Z., Yin, M., et al.: Improved growth rate of anodized TiO 2 nanotube arrays under reduced pressure field and light illumination. Sci. Bull. **62**, 332–338 (2017). https://doi.org/10.1016/j.scib.2017.01.036
32. Luo, J., Li, D., Yang, Y., et al.: Preparation of Au/reduced graphene oxide/hydrogenated TiO 2 nanotube arrays ternary composites for visible-light-driven photoelectrochemical water splitting. J. Alloys Compd. **661**, 380–388 (2016). https://doi.org/10.1016/j.jallcom.2015.11.211
33. Passalacqua, R., Perathoner, S., Centi, G.: Use of modified anodization procedures to prepare advanced TiO2 nanostructured catalytic electrodes and thin film materials. Catal. Today **251**, 121–131 (2015). https://doi.org/10.1016/j.cattod.2014.11.003
34. Puga, M.L., Venturini, J., Guaglianoni, W.C., et al.: Aluminium-doped TiO2 nanotubes with enhanced light-harvesting properties. Ceram. Int. (2021). https://doi.org/10.1016/j.ceramint.2021.03.157
35. Regonini, D., Groff, A., Sorarù, G.D., Clemens, F.J.: Photoelectrochemical study of anodized TiO2 Nanotubes prepared using low and high H2O contents. Electrochim. Acta **186**, 101–111 (2015). https://doi.org/10.1016/j.electacta.2015.10.162

36. Regonini, D., Chen, G., Leach, C., Clemens, F.J.: Comparison of photoelectrochemical properties of TiO 2 Nanotubes and sol-gel. Electrochim. Acta **213**, 31–36 (2016). https://doi.org/10.1016/j.electacta.2016.07.097
37. Sánchez-Tovar, R., Fernández-Domene, R.M., Martínez-Sánchez, A., et al.: Synergistic effect between hydrodynamic conditions during Ti anodization and acidic treatment on the photoelectric properties of TiO2 nanotubes. J. Catal. **330**, 434–441 (2015). https://doi.org/10.1016/j.jcat.2015.08.002
38. Dong, Z., Ding, D., Li, T., Ning, C.: Ni-doped TiO2 nanotubes photoanode for enhanced photoelectrochemical water splitting. Appl. Surf. Sci. **443**, 321–328 (2018). https://doi.org/10.1016/j.apsusc.2018.03.031
39. Regonini, D., Schmidt, A., Aneziris, C.G., et al.: Impact of the Anodizing Potential on the Electron Transport Properties of Nb-doped TiO2 Nanotubes. Electrochim. Acta **169**, 210–218 (2015). https://doi.org/10.1016/j.electacta.2015.04.070
40. Kojima, R., Kimura, Y., Bitoh, M., et al.: Investigation of Influence of Electrolyte Composition on Formation of Anodic Titanium Oxide Nanotube Films. J. Electrochem. Soc **159**, D629–D636 (2012). https://doi.org/10.1149/2.003211jes
41. Xie, Z.B., Blackwood, D.J.: Effects of anodization parameters on the formation of titania nanotubes in ethylene glycol. Electrochim. Acta **56**, 905–912 (2010). https://doi.org/10.1016/j.electacta.2010.10.004
42. Macák, J.M., Tsuchiya, H., Schmuki, P.: High-aspect-ratio TiO2 nanotubes by anodization of titanium. Angew Chemie Int. Ed. **44**, 2100–2102 (2005). https://doi.org/10.1002/anie.200462459
43. Berger, S., Kunze, J., Schmuki, P., et al.: Influence of Water Content on the Growth of Anodic TiO2 Nanotubes in Fluoride-Containing Ethylene Glycol Electrolytes. J. Electrochem. Soc. **157**, C18 (2010). https://doi.org/10.1149/1.3251338
44. Paulose, M., Prakasam, H.E., Varghese, O.K., et al.: TiO 2 Nanotube Arrays of 1000 μm Length by Anodization of Titanium Foil: Phenol Red Diffusion. J. Phys. Chem. C **111**, 14992–14997 (2007). https://doi.org/10.1021/jp075258r
45. Li, Y., Ma, Q., Han, J., et al.: Controllable preparation, growth mechanism and the properties research of TiO2 nanotube arrays. Appl. Surf. Sci. **297**, 103–108 (2014). https://doi.org/10.1016/j.apsusc.2014.01.086
46. Prakasam, H.E., Shankar, K., Paulose, M., et al.: A New Benchmark for TiO 2 Nanotube Array Growth by Anodization. J. Phys. Chem. C **111**, 7235–7241 (2007). https://doi.org/10.1021/jp070273h
47. Oh, H.-J., Kim, I.-K., Jang, K.-W., et al.: Influence of electrolyte and anodic potentials on morphology of titania nanotubes. Met. Mater. Int. **18**, 673–677 (2012). https://doi.org/10.1007/s12540-012-4027-6
48. Paulose, M., Shankar, K., Yoriya, S., et al.: Anodic Growth of Highly Ordered TiO 2 Nanotube Arrays to 134 μm in Length. J. Phys. Chem. B **110**, 16179–16184 (2006). https://doi.org/10.1021/jp064020k
49. Durdu, S., Cihan, G., Yalcin, E., Altinkok, A.: Characterization and mechanical properties of TiO2 nanotubes formed on titanium by anodic oxidation. Ceram. Int. (2020). https://doi.org/10.1016/j.ceramint.2020.12.218
50. Yin, H., Liu, H., Shen, W.Z.: The large diameter and fast growth of self-organized TiO2 nanotube arrays achieved via electrochemical anodization. Nanotechnology 21:035601 (2010). https://doi.org/10.1088/0957-4484/21/3/035601

CNT/TiO_2 Hybrid Nanostructured Materials: Synthesis, Properties and Applications

Gustavo da Rosa Cunha, Waleska Campos Guaglianoni, and Carlos Pérez Bergmann

Abstract The study of semiconductor photocatalysts is essential to achieve sustainable solutions for application in energy generation and treatment of environmental pollution. Titanium dioxide (TiO_2) is one of the most researched photocatalysts because of its abundance and non-toxicity, but its low efficiency, when deployed as a photocatalyst, can sometimes hinder its potential for these applications. Combining nanostructured TiO_2 with carbon nanotubes (CNTs) to form hybrid materials can help overcome some of the metal oxide limitations, such as a large band-gap and a high electron–hole recombination rate. This chapter summarizes some of the CNT/TiO_2 nanostructured materials that have been reported in the last years and outlines their morphologies, methods of synthesis, and applications.

Keywords TiO_2 · CNTs · Nanocomposites · Photocatalysts · Semiconductor

Abbreviations

1D	One-dimensional
AC	Alternating current
ALD	Atomic layer deposition
BET	Brunauer-Emmett-Teller
CNT	Carbon nanotube
CO	Carbon monoxide
Co-TiO_2	Cobalt doped titanium dioxide
CVD	Chemical vapor deposition
DMF	Dimethylformamide
DSC	Differential scanning calorimetry
DSSC	Dye-sensitized solar cell
EDL	Electric double-layer capacitor

G. da Rosa Cunha (✉) · W. C. Guaglianoni · C. P. Bergmann
Universidade Federal do Rio Grande do Sul, Porto Alegre, Brazil
e-mail: rosa.cunha@ufrgs.br

A. Kopp Alves (ed.), *Environmental Applications of Nanomaterials*, Engineering Materials, https://doi.org/10.1007/978-3-030-86822-2_11

EDS	Energy dispersive X-ray spectroscopy
FE-SEM	Field emission scanning electron microscopy
FF	Fill factor
FT-IR	Fourier transform infrared spectroscopy
H_2	Hydrogen gas
HCl	Hydrochloric acid
HNO_3	Nitric acid
J_{SC}	Short circuit current density
KOH	Potassium hydroxide
LIB	Lithium-ion battery
MAO	Micro-arc oxidation
MWCNT	Multi-walled carbon nanotube
$Na_2S_2O_3$	Sodium thiosulfate
NO	Nitric oxide
NP	Nanoparticle
PAN	Polyacrylonitrile
PCE	Power conversion efficiency
PP	Plasma polymer
PVP	Poly(vinyl pyrrolidone)
SEM	Scanning electron microscopy
SiO_2	Silicon dioxide
SWCNT	Single-walled carbon nanotube
TBT	Titanium butoxide
TEM	Transmission electronic microscopy
TGA	Thermogravimetric ananalysis
TiO_2	Titanium dioxide
TNR	Titania nanoribbon
TTIP	Titanium isopropoxide
UV	Ultraviolet
V_{OC}	Open circuit voltage
XRD	X-ray diffraction

1 Introduction

Titanium dioxide is the naturally occurring oxide of titanium and can be found in nature in its three primary crystalline forms: anatase, rutile, and brookite [1]. Due to its low cost, non-toxicity, and strong oxidizing power [2, 3], TiO_2 is a promising material to be used in applications such as photocatalysis [4], dye-sensitized solar cells (DSSC) [5], and H_2 production via water splitting [6]. However, its relatively high band-gap (3.2 eV for the anatase phase) and high charge carrier recombination rate limit its solar photoconversion [7]. The three main ways this can be overcome is by band-gap tuning, which can be achieved using dopants [8] or by synthesizing

oxygen-rich titania [9], suppressing the electron–hole recombination [10], and by improving surface reactions [11]. Carbon nanotubes (CNT) present a high surface area, high-quality active sites, and high electronic conductivity [12, 13], therefore allowing it to enhance the photocatalytic activity of TiO_2 through all of these routes.

Since their discovery by Iijima in 1991 [14], CNTs have attracted attention because of their unique properties. They can be either single-walled (SWCNTs), which consists of a single graphite sheet wrapped into a cylindrical tube, or multi-walled (MWCNTs), which are an arrangement of multiple concentrical SWCNTs [7]. The SWCNTs have a surface area of 400–900 $m^2\ g^{-1}$, while MWCNTs have a surface area of 200–400 $m^2\ g^{-1}$, which means that they can provide a large reactive surface area that is comparable to activated carbon. According to Woan et al. [15], TiO_2 and CNTs may form a Schottky barrier similar to metal–semiconductor junctions, which results in the CNTs having an excess negative charge and the TiO_2 an extra positive charge. In addition, they may accept photo-induced electrons in CNT/TiO_2 hybrid materials, thus increasing the recombination time.

The formation of CNT/TiO_2 heterostructures was reported by Banerjee and Wong in the early 2000s [16]. Thenceforth, a variety of TiO_2/CNTs hybrid nanomaterials have been researched [7], including TiO_2 nanoparticles on the CNTs surface [17], TiO_2 coated with CNTs [18], and CNTs grown on TiO_2 nanotubes [19].

2 Synthesis and Morphology

As mentioned above, both the CNTs and the TiO_2 used in the hybrid nanostructures can present different morphologies. The titanium dioxide can be synthesized in the form of nanoparticles [17], nanotubes [19, 20], nanorods [21, 22], nanofibers [23], or thin films [24]. Regarding the methods employed for the synthesis of these hybrid nanostructures, some widely performed techniques can be mentioned: mixture in solution with pre-functionalized surfaces [4, 25], sol–gel [26, 27], hydrothermal [28, 29], chemical vapor deposition (CVD) [19], and atomic layer deposition (ALD) [17]. This section summarizes some of the main synthesis routes and promising nanostructures that have been studied recently.

2.1 CNT/TiO_2 Nanoparticles

Hybrid nanostructures of CNTs and TiO_2 nanoparticles can be obtained through multiple routes, such as hydrothermal synthesis [28], modified microwave method [30], and ALD [17]. However, sol–gel is the most employed technique [7]. Sol–gel is a relatively low-cost method that presents good controllability of the synthesis conditions [31]. In addition, it has the advantage of using precursors in a liquid state, which allows good dispersion of the filler phase when producing composites [32]. However, because CNTs present strong van der Waals interactions, they tend

to form agglomerates, which requires a functionalization step to be dispersed in an aqueous solution [33]. Thus, the synthesis is divided into two significant steps, one organic and one inorganic. The CNTs are functionalized in the organic step, and surfactants are used to disperse them in the inorganic step. The composite materials are formed during the gelification process of the condensed sol, and the porous sol–gel can encapsulate nanoparticles and carbon nanotubes. In addition, sol–gel synthesis provides the prospect of adding CNTs alongside the precursors, allowing for a better connection between the carbon and the nanotubes and providing a uniform mesoporosity throughout the material [31].

Da Dalt et al. [4] produced CNT@TiO_2 composites by a modified sol–gel method using commercial MWCNT (Baytubes®), titanium propoxide, nitric acid, isopropyl alcohol, and deionized water. Different heat treatment temperatures for the obtained sol were evaluated. The authors synthesized spherical-shaped TiO_2 nanoparticles (NPs) aggregated on the CNT surface, as shown in Fig. 1. The TiO_2 NPs presented an average diameter smaller than 30 nm. The photocatalytic activity of the composites was evaluated and compared to commercial TiO_2 (AEROXIDE®—P25) and its combination with MWCNT. The CNT@TiO_2 composites performed better than pure TiO_2 nanoparticles when the catalyst concentration in the dye solution increased. The authors concluded that the CNT/TiO_2 heterojunctions formed reduced the recombination rate of photo-induced electron–hole pairs.

Yao et al. [18] synthesized anatase/CNTs composite materials. Anatase nanoparticles with diameters of 5 and 100 nm were added to different proportions of commercially SWCNTs and MWCNTs. First, the CNTs were functionalized with nitric acid and dispersed in water. Then, they were combined with the composite structures by simple evaporation and drying process. The photocatalytic activity for the degradation of a solution containing phenol was tested. The TiO_2/SWCNTs composites presented a lower electron–hole recombination rate than TiO_2/MWCNTs composites, probably because of the attachment area of the nanotubes on the surface of the nanoparticles.

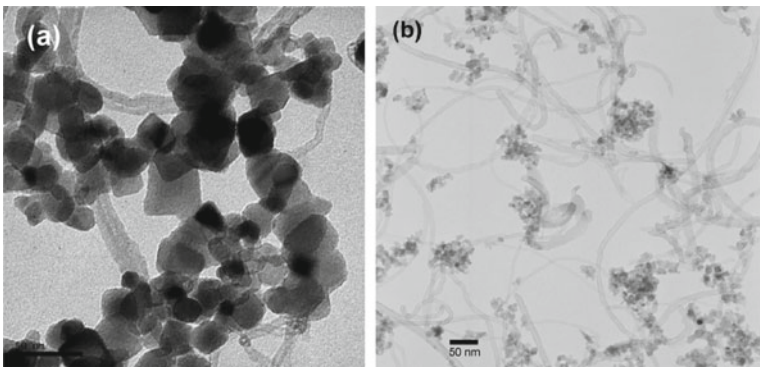

Fig. 1 TEM images of the CNT@TiO2 composites using. **a** P25. **b** Sol–gel obtained nanoparticles. Edited and reprinted with permission of Da Dalt et al. [4]

Banerjee and Wong [16] synthesized heterostructures by oxidizing raw SWCNTs bundles using acidic potassium permanganate solution and hydrochloric acid and then etched the nanotubes using HNO_3. This procedure removed most of the amorphous carbon and the metal catalysts from the nanotubes. Next, the TiO_2 nanoparticles were synthesized by slow hydrolysis of titanium tetraisopropoxide in the presence of an alcoholic solution of 11-aminoundecanoic acid. Finally, in order to achieve TiO_2/CNTs heterostructures, solutions containing the nanoparticles and the oxidized SWCNTs were sonicated for 24 h in a dimethylformamide (DMF) solution. After filtering, washing, and drying, the authors confirmed the formation of the heterostructures by Transmission Electronic Microscopy (TEM), Energy Dispersive X-ray Spectroscopy (EDS), and Fourier Transform Infrared Spectroscopy (FT-IR). In addition, the FT-IR analysis indicated that charge transfer from nanotube to nanoparticles had been achieved.

Zhao et al. [34] deposited TiO_2 on the surface of CNTs by solvothermal reaction. To achieve that, the authors functionalized commercial-grade CNTs with HNO_3, which was later dispersed in an ethanol and glycerol solution. Titanium butoxide (TBT) was added dropwise to this solution, and the formed liquid was heated at 110 ºC for 24 h. Finally, the products were dried and then calcinated at 350 ºC for 2 h. Figure 2a shows a schematic illustration of the experimental procedure adopted and Fig. 2b presents the scanning electron microscopy (SEM) image of the CNT@TiO_2 morphology obtained, in which can be noticed the TiO_2 grains on the surface of CNTs. The SEM analysis showed that composites with a CNT content of 42 wt% maintained the original morphology of tangled CNTs, and EDS analysis showed that the TiO_2 nanoparticles were connected and coated on the surface of the CNTs.

MWCNT forests coated with TiO_2 films via Atomic Layer Deposition (ALD) were obtained by Kaushik et al. [35]. Two types of layer configuration were obtained: (1) MWCNT with TiO_2 films and (2) MWCNT with a coating of carboxyl plasma polymer (PP) and TiO_2 films. Figure 3a presents the SEM image of the lateral view of the MWCNTs forest after 400 cycles of ALD. It can be seen that the tips of the forests are brighter, which means that TiO_2 film was not deposited uniformly on CNTs, only on the surface of the forests. The region selected at TEM analysis (Fig. 3b) shows a uniform TiO_2 film covering a MWCNT. The carboxyl coating created more nucleation sites for the deposition of TiO_2, thereby producing a more uniform layer.

2.2 CNT/TiO_2 Fibers

One-dimensional (1D) nanoarchitectures attract attention because of their length-to-diameter ratio, which can enhance their chemical and optic properties when compared to nanoparticles [36]. That may occur because TiO_2 nanoparticles have reduced electron mobility caused by the contact between the particles, which enhances the scattering of free electrons [5]. Nevertheless, when employed as a photoanode, structures such as nanofibers present some limitations caused by their

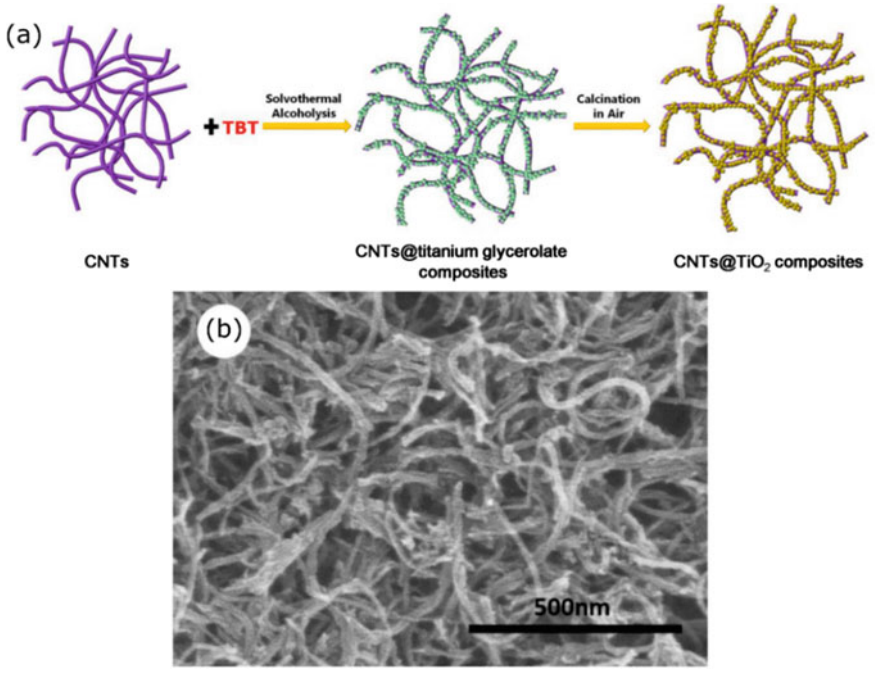

Fig. 2 **a** Schematic illustration of the experimental procedure for the synthesis of CNTs@TiO_2 composites. **b** SEM image of the CNTs@TiO_2 composite with 42 wt%. of CNT. Edited and reprinted with permission of Zhao et al. [34]

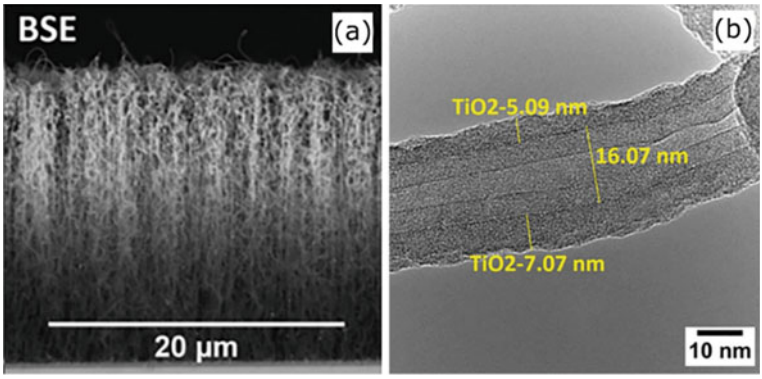

Fig. 3 **a** Backscattered electrons (BSE) SEM image of the lateral view of the MWCNTs forest coated with TiO_2. **b** TEM image of the TiO_2-coated MWCNT. Reprinted with permission of Kaushik et al. [35]

reduced surface area, which can be surpassed by using nanoparticles decorated on their surface [37]. Another innovative way to overcome these limitations is by using CNTs combined with 1D nanostructures.

One versatile and simple method to produce ultrathin TiO_2 fibers is the electrospinning technique [38]. It requires a relatively simple basic setup that involves electrifying a liquid droplet to generate a jet, which is stretched into a fiber. The droplet is deformed into a Taylor cone due to the electrostatic repulsion among the surface. Initially, the formed jet is stretched through a straight line before whipping due to electrostatic instability, and finally, the thinner jet solidifies and is deposited into an electrified collector [39].

Macdonald et al. [40] fabricated a TiO_2 nanofiber-CNTs composite to be applied as a photoanode in a DSSC. To achieve that, the authors synthesized SWCNTs by arc discharge and TiO_2 nanofibers by electrospinning. First, they electrospun a sol–gel containing titanium n-butoxide, poly(vinyl pyrrolidone) (PVP), and glacial acetic acid in absolute ethanol. Next, the fiber mats were subject to pyrolysis at 500 ºC to remove the PVP. The remaining TiO_2 nanofibers were then sonicated in an SWCNT/ethanol solution until a uniform TiO_2 nanofibers/CNTs mixture was formed. Finally, the mixture underwent rotary evaporation to remove the ethanol. The inclusion of CNTs in the mixture was confirmed by Raman spectroscopy, which showed the disorder-induced D-band at 1345 cm^{-1} and the G-band at 1575 cm^{-1} for the samples containing SWCNTs. Following, the authors fabricated DSSC using TiO_2 nanofibers and TiO_2 nanofibers/SWCNT photoanodes and applied J-V curves to characterize the photovoltaic activity. The solar cells composed of TiO_2/CNTs photoanodes presented J_{SC} of 12.65 mA cm^{-2}, V_{OC} of 0.72 V, FF of 0.53, and PCE of 4.83%. The addition of SWCNTs improved the efficiency of the solar cells by 67%, probably due to the CNTs contributing with addition charge-transfer channels which ultimately increased the diffusion coefficient.

Jung et al. [41] synthesized hollow TiO_2 nanofibers with embedded CNTs through electrospinning and impregnation. To achieve that, they electrospun a solution containing polyacrylonitrile (PAN), DMF, and MWCNTs. The as-spun fibers were then impregnated using a solution containing 0, 1, 5, and 10 wt% titanium isopropoxide (TTIP)/ isopropyl alcohol for 5 h, dried, and later calcinated at 550 ºC for 1 h. The characterization was made by field emission scanning electron microscopy (FE-SEM), thermogravimetric analysis (TGA), differential scanning calorimetry (DSC), and the surface area was calculated via Brunauer-Emmett-Teller (BET) method. Finally, the adsorption and photocatalytic capability of the obtained materials were investigated by adding the photocatalyst in a solution containing methylene blue under magnetic stirring in a dark room for 30 min before exposing the solution to UV light at 365 nm for 70 min. For comparison, the authors also prepared hollow TiO_2 nanofibers without the presence of CNTs. A schematic representation of the experimental procedure is shown in Fig. 4. The obtained CNT-embedded hollow TiO_2 fibers (Fig. 5) had a diameter that ranged from 430 to 550 nm, and the CNTs were aligned with the fibers. The authors attributed this variation in diameter to the irregular distribution of CNTs within the nanofiber. They suggested that the alignment of the CNTs could be due to the electric field lines during the injection.

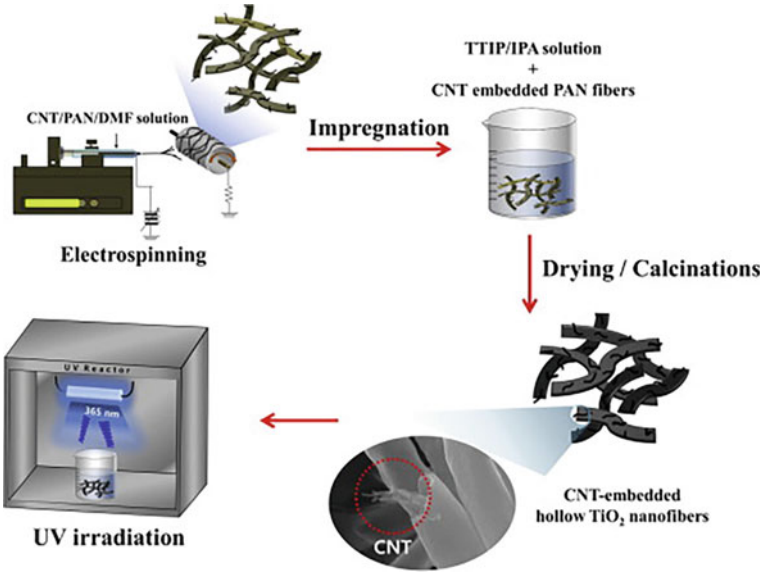

Fig. 4 Schematic representation of the experimental procedure to obtain hollow TiO_2 nanofiber embedded with CNTs. Reprinted with permission of Jung et al. [41]

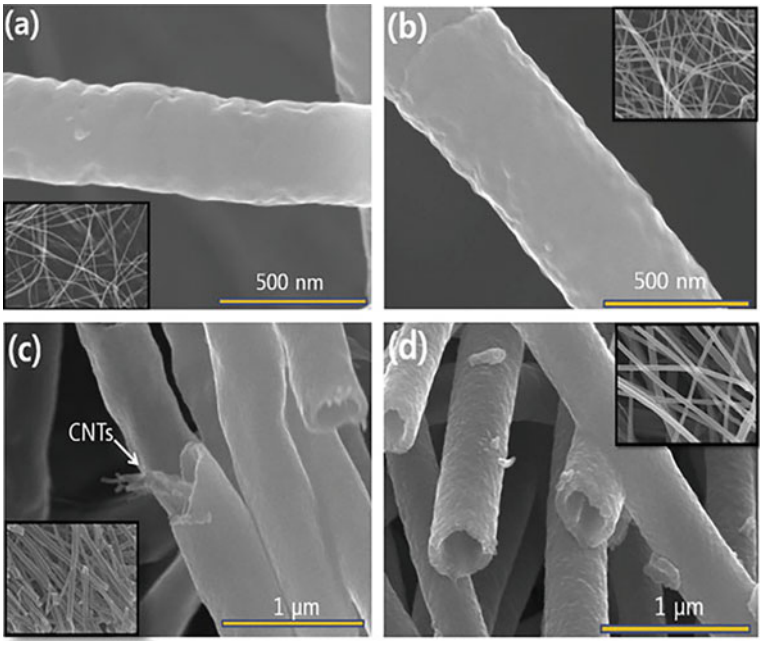

Fig. 5 SEM images of the **a** PAN-CNT fibers, **b** impregnated PAN-CNT fibers, **c** CNT embedded hollow TiO_2 fibers, and **d** hollow TiO_2 fibers. Reprinted with permission of Jung et al. [41]

Furthermore, the addition of CNTs improved the adsorption capability of the TiO_2 nanofibers. The photocatalytic activity was highest for the sample impregnated in the solution containing 5 wt% TTIP concentration, and the CNT-TiO_2 photocatalysts more efficiently degraded the methylene blue compared to the pure TiO_2 nanofibers. The authors proposed that the CNTs might have introduced photogenerated electrons into the conduction band of the TiO_2 fibers, contributing to the enhancement of the photocatalytic capability of the TiO_2 fibers.

2.3 TiO_2 as Catalyst for CNT Synthesis

Carbon nanotubes can be synthesized by three main methods: the laser deposition method, electric arc method, and CVD [42]. The latter is the most employed method to synthesize nanomaterials and to mass-produce CNTs. When employed to synthesize CNTs, CVD has the advantage of requiring a lower temperature (550–1000 ºC). Moreover, the method allows the control of the morphology and structure of the nanotubes and the growth of CNTs with the desired alignment [43].

In order to produce CNTs, the CVD method involves employing a carbon-bearing precursor over a substrate in the presence of a catalyst [43]. This catalyst has the function of decomposing and nucleate the carbon source in the form of nanotubes. The most common catalysts are transition metals such as Fe, Ni, and Co. Hydrocarbons such as methane or acetylene are commonly used as carbon sources. As for the substrates, the most common are Ni, SiO_2, Cu/Ti/Si, glass, and stainless steel [44]. Lately, a particular type of substrate (doped TiO_2) has been researched, where the doping atoms act as a catalyst for the CNTs [19].

Recently, Guaglianoni et al. [45] investigated the influence of CVD parameters on synthesizing CNTs using cobalt doped TiO_2 nanotubes (Co-TiO_2) as catalyst. For that, the authors produced Co-TiO_2 nanotubes via a one-step anodization process using titanium foil as substrate. Instead of performing the traditional heat treatment to transform the amorphous titania to anatase, they used the as-synthesized metal oxide as catalyst to produce MWCNTs. They employed hexane as the carbon source and studied the synthesis temperatures of 700 and 800 ºC, as well as different synthesis times (10, 20, and 30 min). The Co-TiO_2/CNT structures were characterized by X-ray diffraction (XRD), Raman spectroscopy, SEM, and TEM. The Raman spectra showed the characteristic modes for CNTs in all synthesized samples. The presence of CNTs on the surface of the TiO_2 nanotubes was also confirmed by SEM (Fig. 6). By comparing the intensity between the D and the G bands (I_D/I_G), the authors found out that the CNTs obtained in longer synthesis times are more defective. Linear voltammetry essays showed that the combination of CNTs and Co-TiO_2 developed a photocurrent density 65 times greater than the Co-TiO_2 nanotubes.

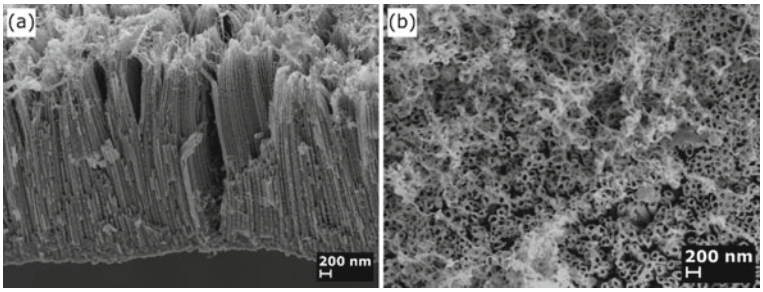

Fig. 6 **a** Lateral, **b** top-view FE-SEM images of connected Co-TiO_2 nanotubes and CNTs obtained by CVD with synthesis temperature of 700 ºC

3 Applications

3.1 Lithium-Ion Batteries

TiO_2 is a promising material to be employed as anode for lithium-ion batteries (LIBs) because of its stability, non-toxicity, low cost, high theoretical capacity and low volume expansion during the charging/discharging processes (<4%) [34, 46]. However, the electrochemical performance of this semiconductor is hindered by its poor electronic conductivity and low lithium-ion diffusivity [25, 34, 47]. A strategy to surpass these limitations is the formation of composites with carbonaceous materials, such as carbon nanotubes (CNTs).

Lo et al. [48] reported the application of TiO_2-CNT layers deposited on titanium thin plate as anodes for LIBs. The composites (Fig. 7a, b) were obtained using a micro-arc oxidation (MAO) process with different CNT quantities in the electrolyte. The charge–discharge behavior (Fig. 7c) was evaluated between 0.1 and 3.0 V (vs. Li/Li^+) at a current rate of 0.2 C. The sample without CNTs ($Ti/nTiO_2$) presented charge–discharge capacities of 176 and 170 mAh g^{-1} in the initial cycle. The formation of the CNT composite greatly increased the charge–discharge capacities. For instance, the capacities were 292/248 mAh g^{-1} for the sample with higher CNT content ($Ti/nTiO_2$-CNT3). Thus, the presence of CNTs provided electrons to the TiO_2 nanostructure and promoted the Li-ion incorporation. Additionally, the discharge capacity of the $Ti/nTiO_2$ decreased to 69 mAh g^{-1} at the 20th cycle (Fig. 7d), probably due to changes in the anode surface generated by the Li-ion insertion/extraction. On the other hand, the TiO_2-CNT composites showed high cycle stability and discharge capacities. The discharge capacities of the $Ti/nTiO_2$-CNT3 sample at discharge rates of 0.2 C, 1 C, and 2 C were 201, 53 and 38 mAh g^{-1}, respectively. The authors attributed the enhancement of electron transport and discharge capacity observed for the composites to the conductive CNT network that supported the TiO_2 nano-flaky structures.

Another interesting TiO_2/CNT configuration that produced outstanding results for application as anode material for LIBs was obtained by Zhao et al. [34]. TiO_2

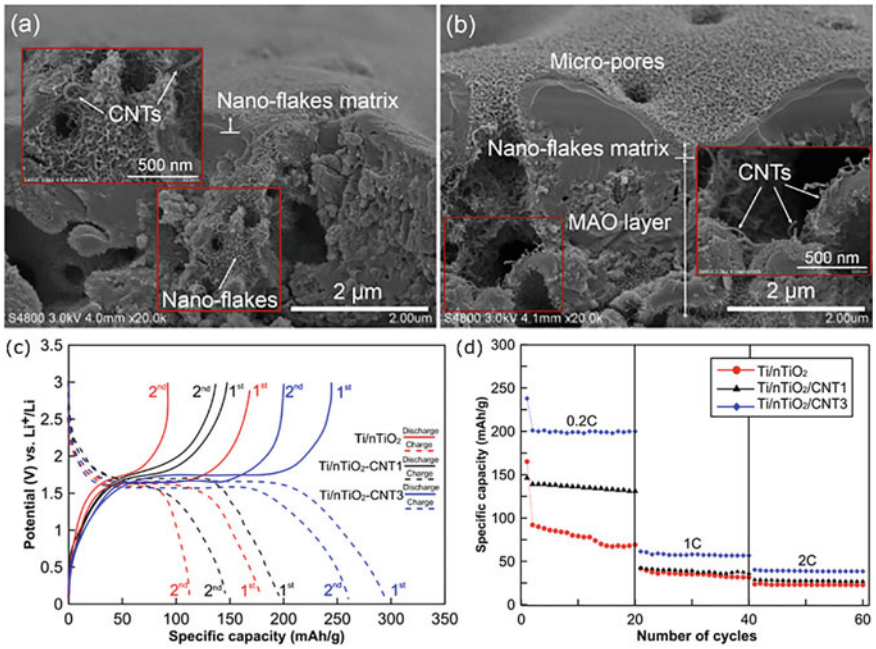

Fig. 7 FE−SEM cross-sectional images of **a** Ti/nTiO_2-CNT1 and **b** Ti/nTiO_2-CNT3 composites. **c** Charge–discharge curves for Ti/nTiO_2, Ti/nTiO_2-CNT1, and Ti/nTiO_2-CNT3 anodes. **d** Cycling performance of Ti/nTiO_2 and Ti/nTiO_2-CNT composites at discharge rates of 0.2 C, 1 C, and 2 C. Edited and reprinted with permission of Lo et al. [48]

nanoparticles connected to the surface of the CNTs were obtained. The samples had their specific capacities tested at different current densities (Fig. 8a) and their cyclic performances were evaluated at 10C (Fig. 8b). The composites exhibited superior performance than the TiO_2 alone for all current densities tested. The sample with

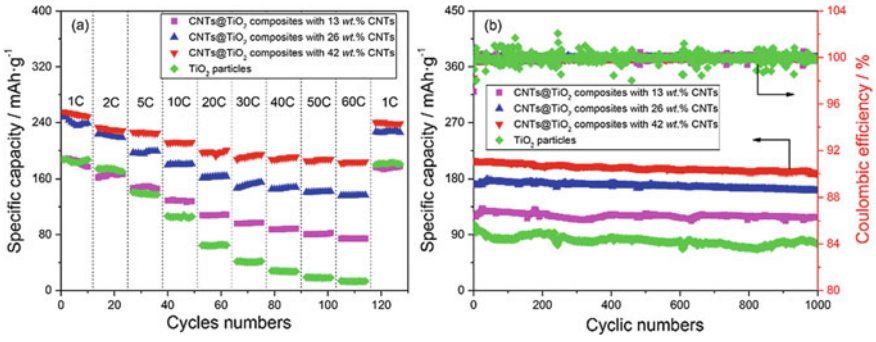

Fig. 8 **a** Specific capacities at different current densities and **b** cyclic performances of the CNTs@TiO_2 composites. Reprinted with permission of Zhao et al. [34]

higher CNT content (i.e., 42 wt%) showed an increased specific capacity (approximately 200 mAh g^{-1}), with a discharge capacity almost 2.5 times that of pure TiO_2 after 1000 cycles (Fig. 8b). These results indicate that the CNTs provided a prompt pathway for the electrons and ions movement throughout the composites.

3.2 Supercapacitors

Originated from the patent applied by Becker in 1954 [49], supercapacitors or ultracapacitors are electrochemical energy storage devices that present high power-density in discharge and recharge, basically combining the capabilities of batteries and capacitors [50, 51]. The supercapacitors can be divided into three categories based on their charge storage mechanism: (1) electric double-layer capacitors (EDL); (2) pseudocapacitors; and (3) hybrid capacitors [52].

Due to their high surface area, high chemical stability, and low electric resistance, CNTs are promising materials to be used as an electrode of supercapacitors [53]. To further enhance the CNTs performance for this application, methods such as modifying the nanotubes with transition metal oxides or conductive polymers are often used [54, 55].

Zhang et al. [56] produced a CNT/TiO_2 composite via hydrothermal method and enhanced its capacitance by pretreating the material with UV light irradiation. To achieve this, the authors placed commercial-grade CNTs, titanium sulfate, and urea in an autoclave and baked it at 150 ºC for two hours. The remaining product was centrifuged and later dried. Electrodes were manufactured with the composite to test the electrochemical properties by cyclic voltammetry, chronopotentiometry, and AC impedance method. Finally, the UV light pretreatment was made by placing the CNT/TiO_2 electrode in a black-box-type analyzer and irradiated it for 1 h under 254 and 365 nm UV light. In addition, pristine CNT electrodes were used for comparison. The SEM analysis (Fig. 9a–b) revealed that the TiO_2 nanoparticles and dispersed evenly and well-mixed with the CNTs. The AC impedance analysis (Fig. 9c) showed that the CNT/TiO_2 electrodes pretreated with UV light presented the largest polarization resistance. The authors attributed the results to the oxygen-containing groups on the TiO_2 surface and its larger Faradic pseudo capacitance from the oxidation–reduction reaction of TiO_2. In addition, the calculated impedance derived from the AC impedance method was 10.7 F g^{-1} for the UV-irradiated CNT/TiO_2 electrode and 4.1 F g^{-1} for the pristine CNT electrode.

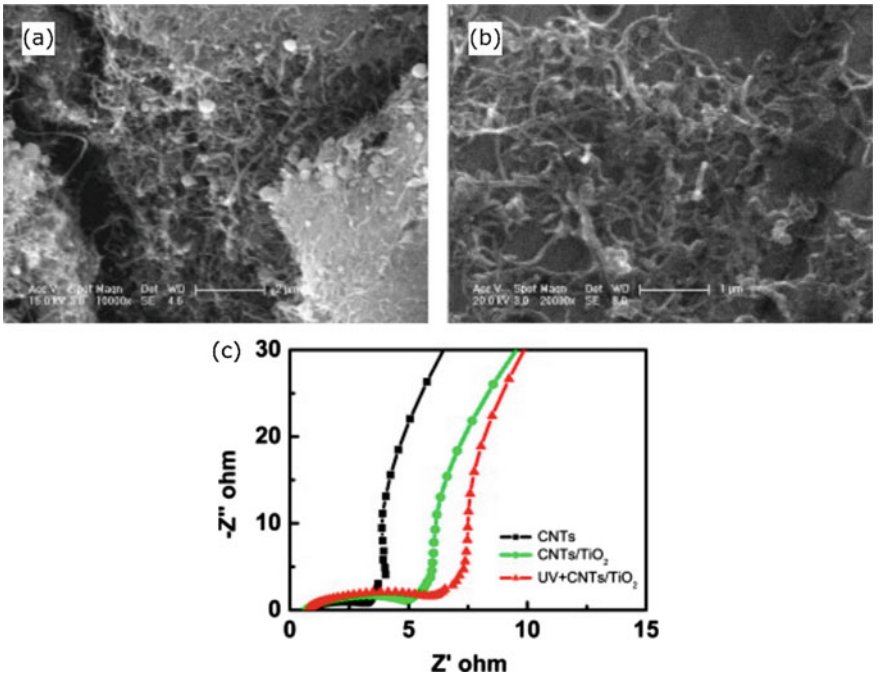

Fig. 9 **a–b** SEM images of the CNT/TiO_2 electrodes. **c** AC impedance analysis performed on the CNT, CNT/TiO_2 and UV-irradiated CNT/TiO_2 electrodes. Reprinted and edited with permission of Zhang et al. [56]

3.3 Gas Sensors

TiO_2/CNT composites have been studied as gas sensors for detection of ammonia, toluene, hydrogen, oxygen, NO, CO, among other gases [35, 57–60]. The TiO2/CNT hybrid materials present enhanced sensing performance, when compared to sensors made by the single constituents, due to the formation of p-n junctions, facilitated electron transfer and increased surface area [61, 62].

MWCNT forests coated with TiO_2 films via ALD were employed as ammonia gas sensors [35]. The samples synthesized were exposed to different concentrations (100, 250, and 500 ppm) of ammonia gas, as shown on Fig. 10. The sensors with the thinnest TiO_2 layers, nominal thickness of 5 nm, presented the best response for ammonia detection. TiO_2 layers with greater thicknesses may have reduced the diffusion of charge carriers, which decreased the sensitivity of the sensor. Regarding the type of layer configuration, the sensors formed by TiO_2-coated MWCNTs with carboxyl PP film had the higher response. According to Kaushik et al. [35], this result can be attributed to the formation of a conduction path for charge carriers that facilitated the charge transfer between the MWCNTs and the TiO_2. The authors proposed that the improved sensing behavior of the TiO_2/CNT composites is due to the formation of

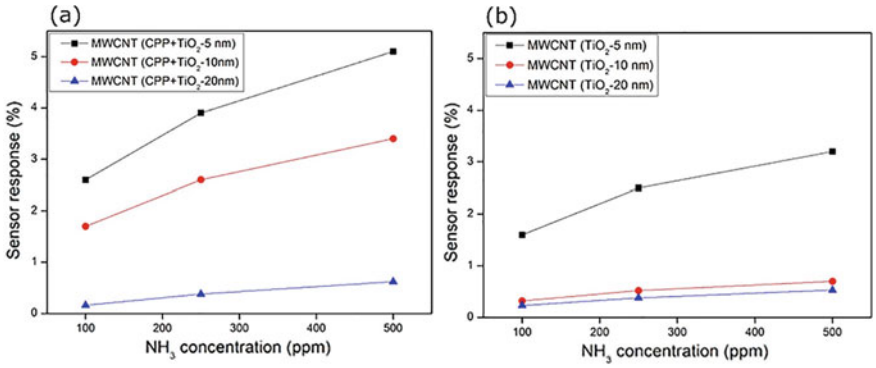

Fig. 10 Sensor response for ammonia detection of the MWCNTs-TiO_2 sensors (**a**) with and (**b**) without carboxyl PP layer. Reprinted with permission of Kaushik et al. [35]

two p-n junctions: (1) between the MWCNTs (p-type semiconductor) and the TiO_2 (n-type semiconductor); (2) the TiO_2 surface.

3.4 H_2 Production via Water Splitting

Hydrogen (H_2) is a promising compound used as an energy source in the replacement of petroleum because of its low molecular weight and high-power density. It can be produced by steam reforming of natural gas; however, it can be harnessed more environmentally friendly way. A greener alternative to using fossil fuels is to reduce water to hydrogen using semiconductor and solar energy, but the high charge carrier recombination of these materials is a limiting factor [63]. Fujishima and Honda [6] were the first to publish a report on splitting water using solar radiation. For that, they used an n-type TiO_2 coupled with a Pt counter electrode. The relatively high band-gap of the TiO_2 (3.2 eV) makes only ultraviolet light excite the semiconductor, hindering the TiO_2 application. Thus, solutions to this limitation have been widely researched.

The photocatalytic activity of TiO_2 can be enhanced in numerous ways. One that is commonly researched is the use of dopants, such as metal ions, to decrease the band-gap and better the optical response to sunlight [64, 65]. The most popular dopants are transition metals since their incorporation in the TiO_2 lattice can form a new energy level near the conduction band [66]. The use of CNTs combined with TiO2 can also increase the photocatalytic activity of the semiconductor. Carbon Nanotubes can promote charge transfer because of their high electrical conductivity and high surface area [67–69].

Recently, Ahmed et al. [70] managed to combine hydrothermal synthesis and CVD to produce a nanoribbon-shaped TiO_2 and CNT hybrid material with a lower band-gap than commercially available TiO_2. They evaluated the hybrid nanomaterial

using different electrolytes (KOH, $Na_2S_2O_3$, and HCl) and prepared two configurations of electrodes, one using the titania nanoribbons (TNRs) and other using CNT@TNRs. They found a substantial increase in current density voltage from the CNT@TNRs electrode compared with the TNRs electrode under the same configuration. The authors concluded that this was probably because of the decrease of electron–hole recombination on the CNT@TNRs electrode. Moreover, its large surface area, nanoporous structure, and high optical absorption in the visible region made the electrode suitable for H_2 production. However, the downside of their method was that a long time was required to synthesize the TNRs.

Another interesting configuration is the usage of TiO_2 in the form of nanotubes in combination with CNTs. Because of their 1D structure, nanotubes can present enhanced optical and chemical properties when compared to nanoparticles [36]. For example, Guaglianoni et al. [19] produced cobalt doped titania nanotubes via one-step anodization followed by CVD treatment to grow CNTs on its surface. The method allowed the production of connected arrays of titania nanotubes and CNT. When tested, the Co-TiO_2/CNT nanotubes presented an improved photocurrent performance compared with the cobalt doped titania nanotubes and CNT and TiO_2 nanoparticles composites reported in literature [71].

4 Conclusion

TiO_2 is a widely employed semiconductor, but some of its applications are hindered due to its relatively high band-gap and recombination rate. The addition of CNTs to form hybrid nanomaterials with TiO_2 has been extensively studied for various applications, from photocatalysts to supercapacitors. The unique properties and high specific surface area of the carbon nanotubes allow them to overcome these limitations. CNTs can enhance the photocatalytic activity of the TiO_2 by decreasing the recombination rate of electron-hole pairs and contributing to adsorptive active sites. In addition, TiO_2 may improve the capacitance of carbon nanotubes, thus making it a more suitable material to be used as an anode in supercapacitors. Novel CNT/TiO_2 nanostructures have been reported in recent years, and a better understanding of the mechanisms that cause this synergic effect and the development of reliable, low-cost synthesis would make these materials more suitable for energy and eco-friendly applications.

Acknowledgements The authors would like to thank the Human Resources Program of the National Agency of Petroleum, Natural Gas and Biofuels (PRH-ANP 13.1; grant number 042319) and the Coordenação de Aperfeiçoamento de Pessoal de Nível Superior – Brasil (CAPES) – Finance Code 001 for the financial support.

References

1. Haider, A.J., Jameel, Z.N., Al-Hussaini, I.H.M.: Review on: Titanium dioxide applications. In: Energy Procedia, pp. 17–29. Elsevier Ltd. (2019). https://doi.org/10.1016/j.egypro.2018.11.159
2. Abdel Messih, M.F., Ahmed, M.A., Soltan, A., Anis, S.S.: Facile approach for homogeneous dispersion of metallic silver nanoparticles on the surface of mesoporous titania for photocatalytic degradation of methylene blue and indigo carmine dyes. J. Photochem. Photobiol. A Chem. **335**, 40–51 (2017). https://doi.org/10.1016/j.jphotochem.2016.11.001
3. Hamaloğlu, K.Ö., Sağ, E., Tuncel, A.: Bare, gold and silver nanoparticle decorated, monodisperse-porous titania microbeads for photocatalytic dye degradation in a newly constructed microfluidic, photocatalytic packed-bed reactor. J. Photochem. Photobiol. A Chem. **332**, 60–65 (2017). https://doi.org/10.1016/j.jphotochem.2016.08.015
4. Da Dalt, S., Alves, A.K., Bergmann, C.P.: Photocatalytic degradation of methyl orange dye in water solutions in the presence of MWCNT/TiO_2 composites. Mater. Res. Bull. **48**, 1845–1850 (2013). https://doi.org/10.1016/j.materresbull.2013.01.022
5. Mor, G.K., Shankar, K., Paulose, M., Varghese, O.K., Grimes, C.A.: Use of highly-ordered TiO_2 nanotube arrays in dye-sensitized solar cells. Nano Lett. **6**, 215–218 (2006). https://doi.org/10.1021/nl052099j
6. Fujishima, A., Honda, K.: Electrochemical photolysis of water at a semiconductor electrode. Nature **238**, 37–38 (1972). https://doi.org/10.1038/238037a0
7. Leary, R., Westwood, A.: Carbonaceous nanomaterials for the enhancement of TiO_2 photocatalysis. Carbon N. Y. **49**, 741–772 (2011). https://doi.org/10.1016/j.carbon.2010.10.010
8. Ullah, I., Haider, A., Khalid, N., Ali, S., Ahmed, S., Khan, Y., Ahmed, N., Zubair, M.: Tuning the band gap of TiO2 by tungsten doping for efficient UV and visible photodegradation of Congo red dye. Spectrochim. Acta—Part A Mol Biomol. Spectrosc. **204**, 150–157 (2018). https://doi.org/10.1016/j.saa.2018.06.046
9. N. G., D.R. A., A.I. A., J. R.L.: Tuning the optical band Gap of pure TiO_2 via photon induced method. Optik (Stuttg). **179**, 889–894 (2019). https://doi.org/10.1016/j.ijleo.2018.11.009.
10. Pesci, F.M., Wang, G., Klug, D.R., Li, Y., Cowan, A.J.: Efficient suppression of electron-hole recombination in oxygen-deficient hydrogen-treated TiO_2 nanowires for photoelectrochemical water splitting. J. Phys. Chem. C. **117**, 25837–25844 (2013). https://doi.org/10.1021/jp4099914
11. Al Jitan, S., Palmisano, G., Garlisi, C.: Synthesis and surface modification of TiO_2-based photocatalysts for the conversion of CO_2. Catalysts (2020)
12. Baughman, R.H., Zakhidov, A.A., De Heer, W.A.: Carbon nanotubes—The route toward applications. Science **297**, 787–792 (2002). https://doi.org/10.1126/science.1060928
13. Serp, P., Figueiredo, J.L.: Carbon Materials for Catalysis. John Wiley & Sons, Inc., Hoboken, NJ, USA (2008). https://doi.org/10.1002/9780470403709
14. Iijima, S.: Helical microtubules of graphitic carbon. Nature **354**, 56–58 (1991). https://doi.org/10.1038/354056a0
15. Woan, K., Pyrgiotakis, G., Sigmund, W.: Photocatalytic Carbon-Nanotube-TiO_2 Composites. Adv. Mater. **21**, 2233–2239 (2009). https://doi.org/10.1002/adma.200802738
16. Banerjee, S., Wong, S.S.: Synthesis and characterization of carbon nanotube-nanocrystal heterostructures. Nano Lett. **2**, 195–200 (2002). https://doi.org/10.1021/nl015651n
17. Acauan, L., Dias, A.C., Pereira, M.B., Horowitz, F., Bergmann, C.P.: Influence of different defects in vertically aligned carbon nanotubes on TiO_2 nanoparticle formation through atomic layer deposition. ACS Appl. Mater. Interfaces. **8**, 16444–16450 (2016). https://doi.org/10.1021/acsami.6b04001
18. Yao, Y., Li, G., Ciston, S., Lueptow, R.M., Gray, K.A.: Photoreactive TiO_2/carbon nanotube composites: synthesis and reactivity. Environ. Sci. Technol. **42**, 4952–4957 (2008). https://doi.org/10.1021/es800191n
19. Guaglianoni, W.C., Florence, C.L., Bonatto, F., Venturini, J., Arcaro, S., Alves, A.K., Bergmann, C.P.: Novel nanoarchitectured cobalt-doped TiO_2 and carbon nanotube arrays:

synthesis and photocurrent performance. Ceram. Int. **45**, 2439–2445 (2019). https://doi.org/10.1016/j.ceramint.2018.10.169
20. Zhu, Z., Zhou, Y., Yu, H., Nomura, T., Fugetsu, B.: Photodegradation of humic substances on MWCNT/nanotubular-TiO_2 composites. Chem. Lett. **35**, 890–891 (2006). https://doi.org/10.1246/cl.2006.890
21. Yang, L., Leung, W.W.F.: Electrospun TiO_2 nanorods with carbon nanotubes for efficient electron collection in dye-sensitized solar cells. Adv. Mater. **25**, 1792–1795 (2013). https://doi.org/10.1002/adma.201204256
22. Zhu, Y.E., Yang, L., Sheng, J., Chen, Y., Gu, H., Wei, J., Zhou, Z.: Fast sodium storage in TiO_2@CNT@C Nanorods for High-Performance Na-Ion Capacitors. Adv. Energy Mater. **7**, 1701222 (2017). https://doi.org/10.1002/aenm.201701222
23. Hieu, N.T., Baik, S.J., Chung, O.H., Park, J.S.: Fabrication and characterization of electrospun carbon nanotubes/titanium dioxide nanofibers used in anodes of dye-sensitized solar cells. Synth. Met. **193**, 125–131 (2014). https://doi.org/10.1016/j.synthmet.2014.04.010
24. Wang, G.J., Lee, M.W., Chen, Y.H.: A TiO_2/CNT coaxial structure and standing CNT array laminated photocatalyst to enhance the photolysis efficiency of TiO_2. Photochem. Photobiol. **84**, 1493–1499 (2008). https://doi.org/10.1111/j.1751-1097.2008.00374.x
25. Liu, J., Feng, H., Jiang, J., Qian, D., Li, J., Peng, S., Liu, Y.: Anatase-TiO_2/CNTs nanocomposite as a superior high-rate anode material for lithium-ion batteries. J. Alloys Compd. **603**, 144–148 (2014). https://doi.org/10.1016/j.jallcom.2014.03.089
26. Koli, V.B., Dhodamani, A.G., Delekar, S.D., Pawar, S.H.: In situ sol-gel synthesis of anatase TiO_2-MWCNTs nanocomposites and their photocatalytic applications. J. Photochem. Photobiol. A Chem. **333**, 40–48 (2017). https://doi.org/10.1016/j.jphotochem.2016.10.008
27. Nguyen, K.C., Ngoc, M.P., Van Nguyen, M.: Enhanced photocatalytic activity of nanohybrids TiO_2/CNTs materials. Mater. Lett. **165**, 247–251 (2016). https://doi.org/10.1016/j.matlet.2015.12.004
28. Naffati, N., Sampaio, M.J., Da Silva, E.S., Nsib, M.F., Arfaoui, Y., Houas, A., Faria, J.L., Silva, C.G.: Carbon-nanotube/TiO_2 materials synthesized by a one-pot oxidation/hydrothermal route for the photocatalytic production of hydrogen from biomass derivatives. Mater. Sci. Semicond. Process. **115**, 105098 (2020). https://doi.org/10.1016/j.mssp.2020.105098
29. Dai, K., Zhang, X., Fan, K., Peng, T., Wei, B.: Hydrothermal synthesis of single-walled carbon nanotube-TiO_2 hybrid and its photocatalytic activity. Appl. Surf. Sci. **270**, 238–244 (2013). https://doi.org/10.1016/j.apsusc.2013.01.010
30. Alosfur, F.K.M., Jumali, M.H.H., Radiman, S., Ridha, N.J., Yarmo, M.A., Umar, A.A.: Modified microwave method for the synthesis of visible light-responsive TiO_2/MWCNTs nanocatalysts. Nanoscale Res. Lett. **8**, 1–6 (2013). https://doi.org/10.1186/1556-276X-8-346
31. Bazli, L., Siavashi, M., Shiravi, A.: A Review of Carbon nanotube/TiO_2 Composite prepared via Sol-Gel method. J Compos. Compd. **1**, 1–12 (2019). https://doi.org/10.29252/jcc.1.1.1
32. De Andrade, M.J., Lima, M.D., Stein, L., Bergmann, C.P., Roth, S.: Single-walled carbon nanotube silica composites obtained by an inorganic sol-gel route. Phys. Status Solidi Basic Res. **244**, 4218–4222 (2007). https://doi.org/10.1002/pssb.200776114
33. de Andrade, M.J., Lima, M.D., Bergmann, C.P., de Ramminger, G.O., Balzaretti, N.M., Costa, T.M.H., Gallas, M.R.: Carbon nanotube/silica composites obtained by sol–gel and high-pressure techniques. Nanotechnology **19**, 265607 (2008). https://doi.org/10.1088/0957-4484/19/26/265607
34. Zhao, S., Ding, H., Chen, J., Yang, C., Xian, X.: Facile synthesis of CNTs@TiO_2 composites by solvothermal reaction for high-rate and long-life lithium-ion batteries. J. Phys. Chem. Solids. **152**, 109950 (2021). https://doi.org/10.1016/j.jpcs.2021.109950
35. Kaushik, P., Eliáš, M., Michalička, J., Hegemann, D., Pytlíček, Z., Nečas, D., Zajíčková, L.: Atomic layer deposition of titanium dioxide on multi-walled carbon nanotubes for ammonia gas sensing. Surf. Coatings Technol. **370**, 235–243 (2019). https://doi.org/10.1016/j.surfcoat.2019.04.031
36. Chen, C., Fan, Y., Gu, J., Wu, L., Passerini, S., Mai, L.: One-dimensional nanomaterials for energy storage. J. Phys. D. Appl. Phys. **51**, 113002 (2018). https://doi.org/10.1088/1361-6463/aaa98d

37. Anjusree, G.S., Deepak, T.G., Pai, K.R.N., Joseph, J., Arun, T.A., Nair, S.V., Nair, A.S.: TiO_2 nanoparticles @ TiO_2 nanofibers-an innovative one-dimensional material for dye-sensitized solar cells. RSC Adv. **4**, 22941–22945 (2014). https://doi.org/10.1039/c4ra03701d
38. Marinho, B.A., de Souza, S.M.A.G.U., de Souza, A.A.U., Hotza, D.: Electrospun TiO_2 nanofibers for water and wastewater treatment: a review. J. Mater. Sci. **56**, 5428–5448 (2021). https://doi.org/10.1007/s10853-020-05610-6
39. Xue, J., Wu, T., Dai, Y., Xia, Y.: Electrospinning and electrospun nanofibers: Methods, materials, and applications. Chem. Rev. **119**, 5298–5415 (2019). https://doi.org/10.1021/acs.chemrev.8b00593
40. MacDonald, T.J., Tune, D.D., Dewi, M.R., Gibson, C.T., Shapter, J.G., Nann, T.: A TiO_2 nanofiber-carbon nanotube-composite photoanode for improved efficiency in dye-sensitized solar cells. Chemsuschem **8**, 3396–3400 (2015). https://doi.org/10.1002/cssc.201500945
41. Jung, J.Y., Lee, D., Lee, Y.S.: CNT-embedded hollow TiO_2 nanofibers with high adsorption and photocatalytic activity under UV irradiation. J. Alloys Compd. **622**, 651–656 (2015). https://doi.org/10.1016/j.jallcom.2014.09.068
42. Anzar, N., Hasan, R., Tyagi, M., Yadav, N., Narang, J.: Carbon nanotube—a review on synthesis properties and plethora of applications in the field of biomedical science. Sensors Int. **1**, 100003 (2020). https://doi.org/10.1016/j.sintl.2020.100003
43. Manawi, Y.M., Ihsanullah, Samara, A., Al-Ansari, T., Atieh, A.: A review of carbon nanomaterials' synthesis via the chemical vapor deposition (CVD) method. Materials (Basel) **11**, 822 (2018). https://doi.org/10.3390/ma11050822
44. Prasek, J., Drbohlavova, J., Chomoucka, J., Hubalek, J., Jasek, O., Adam, V., Kizek, R.: Methods for carbon nanotubes synthesis—review. J. Mater. Chem. **21**, 15872–15884 (2011). https://doi.org/10.1039/c1jm12254a
45. Campos Guaglianoni, W., Garcia, A.P., Basegio, T.M., Arcari Bassani, M.A., Arcaro, S., Pérez Bergmann, C.: Influence of CVD parameters on Co-TiO2 /CNT properties: a route to enhance energy harvesting from sunlight. Int. J. Appl. Ceram. Technol. **18**, 1297–1306 (2021). https://doi.org/10.1111/ijac.13773
46. Roy, P., Srivastava, S.K.: Nanostructured anode materials for lithium ion batteries. J. Mater. Chem. A. **3**, 2454–2484 (2015). https://doi.org/10.1039/c4ta04980b
47. Ventosa, E., Chen, P., Schuhmann, W., Xia, W.: CNTs grown on oxygen-deficient anatase $TiO_{2-\delta}$ as high-rate composite electrode material for lithium ion batteries. Electrochem. Commun. **25**, 132–135 (2012). https://doi.org/10.1016/j.elecom.2012.09.031
48. Lo, W.C., Su, S.H., Chu, H.J., He, J.L.: TiO_2-CNTs grown on titanium as an anode layer for lithium-ion batteries. Surf. Coatings Technol. **337**, 544–551 (2018). https://doi.org/10.1016/j.surfcoat.2018.01.029
49. Becker, H.J.: United States Patent Office Low Voltage Electolytic Capacitor. https://patentimages.storage.googleapis.com/a2/f8/a9/b7d5c04a415c8b/US2800616.pdf (1957). Accessed 31 May 2021
50. Conway, B.E.: Electrochemical Supercapacitors. Springer US, Boston, MA (1999). https://doi.org/10.1007/978-1-4757-3058-6
51. Burke, A.: Ultracapacitors: Why, how, and where is the technology. J. Power Sources. **91**, 37–50 (2000). https://doi.org/10.1016/S0378-7753(00)00485-7
52. Mendoza, R., Al-Sardar, M., Oliva, A.I., Robledo-Trujillo, G., Rodriguez-Gonzalez, V., Zakhidov, A., Oliva, J.: Improving the electrochemical performance of flexible carbon nanotubes based supercapacitors by depositing Ni@TiO_2: W nanoparticles on their anodes. J. Phys. Chem. Solids. **155**, 110128 (2021). https://doi.org/10.1016/j.jpcs.2021.110128
53. Liu, C.G., Liu, M., Li, F., Cheng, H.M.: Frequency response characteristic of single-walled carbon nanotubes as supercapacitor electrode material. Appl. Phys. Lett. **92**, 143108 (2008). https://doi.org/10.1063/1.2907501
54. Xiao, Q., Zhou, X.: The study of multiwalled carbon nanotube deposited with conducting polymer for supercapacitor. Electrochim. Acta. **48**, 575–580 (2003). https://doi.org/10.1016/S0013-4686(02)00727-2

55. Zhou, Y.K., He, B.L., Zhang, F.B., Li, H.L.: Hydrous manganese oxide/carbon nanotube composite electrodes for electrochemical capacitors. J. Solid State Electrochem. **8**, 482–487 (2004). https://doi.org/10.1007/s10008-003-0468-7
56. Zhang, B., Shi, R., Zhang, Y., Pan, C.: CNTs/TiO_2 composites and its electrochemical properties after UV light irradiation. Prog. Nat. Sci. Mater. Int. **23**, 164–169 (2013). https://doi.org/10.1016/j.pnsc.2013.03.002
57. Seekaew, Y., Wisitsoraat, A., Phokharatkul, D., Wongchoosuk, C.: Room temperature toluene gas sensor based on TiO_2 nanoparticles decorated 3D graphene-carbon nanotube nanostructures. Sensors Actuators, B Chem. **279**, 69–78 (2019). https://doi.org/10.1016/j.snb.2018.09.095
58. Khalilian, M., Abdi, Y., Arzi, E.: Formation of well-packed TiO_2 nanoparticles on multiwall carbon nanotubes using CVD method to fabricate high sensitive gas sensors. J. Nanoparticle Res. **13**, 5257–5264 (2011). https://doi.org/10.1007/s11051-011-0511-z
59. Ueda, T., Takahashi, K., Mitsugi, F., Ikegami, T.: Preparation of single-walled carbon nanotube/TiO_2 hybrid atmospheric gas sensor operated at ambient temperature. Diam. Relat. Mater. **18**, 493–496 (2009). https://doi.org/10.1016/j.diamond.2008.08.017
60. Frontera, P., Malara, A., Stelitano, S., Leonardi, S.G., Bonavita, A., Fazio, E., Antonucci, P., Neri, G., Neri, F., Santangelo, S.: Characterisation and H_2O_2 sensing properties of TiO_2-CNTs/Pt electro-catalysts. Mater. Chem. Phys. **170**, 129–137 (2016). https://doi.org/10.1016/j.matchemphys.2015.12.030
61. Nunes Simonetti, E.A., Cardoso de Oliveira, T., Enrico do Carmo Machado, A., Coutinho Silva, A.A., Silva dos Santos, A., de Simone Cividanes L.: TiO_2 as a gas sensor: The novel carbon structures and noble metals as new elements for enhancing sensitivity—a review. Ceram. Int. **47**, 17844–17876 (2021). https://doi.org/10.1016/j.ceramint.2021.03.189
62. Li, Z., Yao, Z.J., Haidry, A.A., Plecenik, T., Xie, L.J., Sun, L.C., Fatima, Q.: Resistive-type hydrogen gas sensor based on TiO_2: a review. Int. J. Hydrogen Energy. **43**, 21114–21132 (2018). https://doi.org/10.1016/j.ijhydene.2018.09.051
63. Moniz, S.J.A., Shevlin, S.A., Martin, D.J., Guo, Z.X., Tang, J.: Visible-light driven heterojunction photocatalysts for water splitting-a critical review. Energy Environ. Sci. **8**, 731–759 (2015). https://doi.org/10.1039/c4ee03271c
64. Venturini, J., Bonatto, F., Guaglianoni, W.C., Lemes, T., Arcaro, S., Alves, A.K., Bergmann, C.P.: Cobalt-doped titanium oxide nanotubes grown via one-step anodization for water splitting applications. Appl. Surf. Sci. **464**, 351–359 (2019). https://doi.org/10.1016/j.apsusc.2018.09.093
65. Dholam, R., Patel, N., Adami, M., Miotello, A.: Hydrogen production by photocatalytic water-splitting using Cr- or Fe-doped TiO_2 composite thin films photocatalyst. Int. J. Hydrogen Energy **34**, 5337–5346 (2009). https://doi.org/10.1016/j.ijhydene.2009.05.011
66. Khlyustova, A., Sirotkin, N., Kusova, T., Kraev, A., Titov, V., Agafonov, A.: Doped TiO2: the effect of doping elements on photocatalytic activity. Mater. Adv. **1**, 1193–1201 (2020). https://doi.org/10.1039/d0ma00171f
67. Yang, H., Wu, S., Duan, Y., Fu, X., Wu, J.: Surface modification of CNTs and enhanced photocatalytic activity of TiO_2 coated on hydrophilically modified CNTs. Appl. Surf. Sci. **258**, 3012–3018 (2012). https://doi.org/10.1016/j.apsusc.2011.11.029
68. Wang, S., Ji, L., Wu, B., Gong, Q., Zhu, Y., Liang, J.: Influence of surface treatment on preparing nanosized TiO_2 supported on carbon nanotubes. Appl. Surf. Sci. **255**, 3263–3266 (2008). https://doi.org/10.1016/j.apsusc.2008.09.031
69. Wang, H., Wang, H.L., Jiang, W.F., Li, Z.Q.: Photocatalytic degradation of 2,4-dinitrophenol (DNP) by multi-walled carbon nanotubes (MWCNTs)/TiO_2 composite in aqueous solution under solar irradiation. Water Res. **43**, 204–210 (2009). https://doi.org/10.1016/j.watres.2008.10.003
70. Ahmed, A.M., Mohamed, F., Ashraf, A.M., Shaban, M., Aslam Parwaz Khan, A., Asiri, A.M.: Enhanced photoelectrochemical water splitting activity of carbon nanotubes@TiO_2 nanoribbons in different electrolytes. Chemosphere **238**, 124554 (2020). https://doi.org/10.1016/j.chemosphere.2019.124554

71. Chaudhary, D., Singh, S., Vankar, V.D., Khare, N.: A ternary Ag/TiO_2/CNT photoanode for efficient photoelectrochemical water splitting under visible light irradiation. Int. J. Hydrogen Energy. **42**, 7826–7835 (2017). https://doi.org/10.1016/j.ijhydene.2016.12.036

Nanostructured Zero-Valent Iron: From Synthesis to Application

Tania Maria Basegio, Ana Paula Garcia, and Carlos Pérez Bergmann

Abstract Iron is one of the most abundant chemical elements in the Earth's crust and is found in nature in the form of ores. Obtaining it in its pure state involves the exploration, extraction and processing of these minerals. The production of iron is of fundamental importance, given the scope of its use, which ranges from the production of steel—its main application—to the most diverse industrial applications. It is due to its physical and chemical properties that iron has such a wide range of industrial uses. Thus, knowing the behavior of iron in different structures and environments is necessary. Currently, one of the forms of iron that has attracted attention because of its most diverse applications is zero-valent iron (ZVI), which is the subject of many studies, especially on its uses in soil remediation and effluent treatment on account of its physical and chemical properties. These properties can be enhanced when it is on a nanoscale, in the form of nanoscale zero-valent iron (nZVI). nZVI—given that it is easily obtainable, affordable, and has a toxic effect that is considered irrelevant—has environmental uses that are accepted by many regulatory agencies, and its applications have deserved attention. Thus, this chapter will provide a general review of the subject of iron ore and, in particular, will analyze the properties and applications of nZVI. It will also discuss its synthesis methods and the treatments that it can be submitted to in order to improve its efficiency in applications of interest.

Keywords ZVI · nZVI · Synthesis · Application · Environmental remediation · Composites · Biochar

Abbreviations

_COOH	Carboxyl group
$2Fe_2O_3 \cdot 3H_2O$	Limonite

T. M. Basegio (✉)
Federal University of Rio Grande Do Sul, Porto Alegre, Brazil

A. P. Garcia · C. P. Bergmann
Federal University of Pampa, Bagé, Brazil

A. Kopp Alves (ed.), *Environmental Applications of Nanomaterials*, Engineering Materials, https://doi.org/10.1007/978-3-030-86822-2_12

aq	Aquous
BC	Biochar
BET	Brunauer-Emmett-Teller method
BJH	Barret, Joyner and Halenda method
cm	Centimeter
CO	Carbon monoxide
CO_2	Carbon dioxide
CPC	Cetylpyridinium chloride,
DDT	Dichlorodiphenyltrichloroethane
EPA	Environmental Protection Agency
Fe	Iron
$Fe_{(1-x)}S$	Pyrrothite
Fe_2O_3	Hematite
$Fe_2O_3 \cdot H_2O$	Goethite
Fe_3O_4	Magnetite
$FeCl_3$	Ferric chloride
$FeCO_3$	Siderite
FeS_2	Pyrite
$FeTiO_3$	Ilmenite
g/cm^3	Gram per cubic centimeter
GO	Graphene
h	Hour
H_2	Hydrogen gas
khz	Kilohertz
ksp	Solubility product constant
m^2/g	Surface area
min	Minute
mL	Milliliter
MO	Methyl orange
Mt	Millions of tonnes
MΩ	Megaohm
N_2	Nitrogen gas
$NaBH_4$	Sodium borohydride
NB	Nitrobenzene
nm	Nanometer
nZVI @ BC	Biochar-supported nZVI for in-situ remediation
nZVI/BC	Biochar-supported nZVI
nZVI	Nanoscale zero-valent iron
nZVI-GO	Graphene-nZVI hybrid composite
O_2	Oxygen gas
°C	Degree Celsius
_OH	Hydroxyl group
PCBs	Polychlorinated biphenyls
PEG-4000	Polyethylene glycol-4000
PEI	Polyethylenimine

PEI-nZVI	Polyethylenimine-modified nZVI nanocomposite
pH	Potential of hydrogen
pKa	Acidity constant
PVP	Polyvinylpyrrolidone
R&D	Research and Development
RHC/Fe	Iron-impregnated rice husk catalyst
S	Sulfate
SA	Surface area
SEM	Scanning electron microscopy
SF-Fe^0	Iron-supported silica
S-nVZI	Sulfate-nZVI hybrid composite
TEM	Transient electromagnetic method
TNT	Trinitrotoluene
W	Watt
WOS	Web of science
XRD	X-ray diffraction
ZVI	Zero-valent iron

1 Introduction

Iron is the fourth most abundant chemical element in the Earth's crust, representing 5% (in mass) of its elements and being surpassed only by oxygen (46.6%), silicon (26.72%) and aluminum (8.13%) [1]. It is found in nature as ores and obtained by their exploration. According to their definition, ores are natural aggregates of minerals and gangue (a material without value, or with secondary value) that, in the current state of technology, can be normally used for the economic extraction of one or more metals [2]. Hence, an iron ore can contain one or more iron minerals. The major iron-bearing minerals and their respective iron contents are shown in Table 1. The greater their iron content is, the more important the mineral is for the exploration of iron.

Table 1 Major iron-bearing minerals: chemical formulae and contents [3]. Edited and reproduced from Carvalho et al. [3]

Mineral	Chemical formula	Theoretical iron content (%)
Magnetite	Fe_3O_4	72.4
Hematite	Fe_2O_3	69.9
Goethite	$Fe_2O_3 \cdot H_2O$	62.9
Pyrrhotite	$Fe_{(1-x)}S$	61.0
Limonite	$2Fe_2O_3 \cdot 3H_2O$	59.8
Siderite	$FeCO_3$	48.2
Pyrite	FeS_2	46.5
Ilmenite	$FeTiO_3$	36.8

With regard to the data on worldwide production and iron ore reserves (Table 2), they can be presented as follows [5]: (i) crude ore: obtained directly by mining, without undergoing any sort of processing; (ii) usable ore: products created after the processing of crude ores, usually with an iron content of 58–65%; (iii) iron content: amount of metal available in a reserve or in crude and processed production.

According to data from the U.S. Geological Survey [4] (shown in Table 2), in 2019 the world reserve of iron ore amounted to 180.000 million tonnes and world production amounted to 2.450 billion tonnes. Australia, Brazil and Russia are the countries with the largest reserves. However, in terms of worldwide iron ore production, Australia produces 919.000 Mt annually and Brazil 405 Mt, maintaining their ranks of first and second major producers, respectively, with China following in the third place with 351 Mt. Remarkably, the three countries are responsible for 68.4% of the iron ore production in the world.

Large-scale production of iron is of the utmost importance, given its wide range of uses. Iron applications range from steel production—its main use—to the most

Table 2 Iron ore: 2019 world production, estimate for 2020 and world reserves in 2019. Edited and reproduced from U. S. Geological Survey [4]

Mine production						
	Usable ore		Iron content		Reserves*	
	2019	2020	2019	2020	Crude ore	Iron content
United States	46,900	37,000	29,800	24,000	3000	1000
Australia	919,000	900,000	569,000	560,000	50,000	24,000
Brazil	405,000	400,000	258,000	252,000	34,000	15,000
Canada	58,500	57,000	35,200	34,000	6000	2300
Chile	13,100	13,000	8430	8000	NA	NA
China	351,000	340,000	219,000	210,000	20,000	6900
India	238,000	230,000	148,000	140,000	5500	3400
Iran	33,100	32,000	21,700	21,000	2700	1500
Kazakhstan	22,000	21,000	6150	5900	2500	900
Peru	15,100	15,000	10,100	10,000	NA	1500
Russia	97,500	95,000	64,300	63,000	25,000	14,000
South Africa	72,400	71,000	41,200	40,000	1000	640
Sweden	35,700	35,000	22,100	22,000	1300	600
Turkey	16,400	16,000	9110	8,900	NA	NA
Ukraine	63,200	62,000	39,500	39,000	6,500	2,300
Other countries	67,700	75,000	39,000	43,000	18,000	9500
World total (rounded)	2,450,000	2,400,000	1,520,000	1,500,000	180,000	84,000

*Value in Mt (million tonnes)

diverse industrial purposes, such as, for instance, in the metalmechanic industry, where it plays a fundamental role. Iron can also be used in agriculture as a fertilizer, in the chemical industry as pigments and catalysts of processes, e.g. the Fischer–Tropsch process, in which iron-based catalysts are employed in the conversion of synthesis gases (hydrogen and carbon monoxide) into liquid fuels [5]. Another important industrial process to which iron is essential is the production of ammonia via the Haber–Bosch process [6].

Naturally, there is a long path that must be followed in order to use iron in industrial processes: a path that involves the research, exploration, extraction and processing of minerals.

As can be seen in Table 1, the minerals that contain major amounts of iron are found in the form of oxides. Thus, it can be inferred that the exploration of these oxides to obtain iron is of great economic significance, considering the high iron content (of over 62%) in their composition.

The primary forms of iron oxides are magnetite (Fe_3O_4) and hematite (Fe_2O_3), substances that, when heated in the presence of a reducing agent, release iron in its metallic form (Fe) [7]. The production of iron with higher purity is important for certain uses and can be achieved by specific methods, such as electrolysis and the reduction of oxides or hydroxides with hydrogen, or the formation of a carbonyl complex—$Fe(CO)_5$—followed by its thermal decomposition [8].

The physical and chemical properties of iron allow it to have such a wide array of applications. Therefore, knowing its behavior in different structures and means is necessary.

According to Duarte [1], in order to better understand the potential roles of iron in many chemical, biological and geochemical processes, its reactivity in an aqueous environment must be analyzed.

Fe has three predominant oxidation states: 0, +2 and +3, in addition to +4, + 5 and +6. Fe^{3+} is a relatively strong acid, with pkAs of 2.2, 3.5, 6.3 and 9.6, and is water-insoluble ($Kps = 2.79 \times 10^{-39}$). On the other hand, the ion Fe^{2+} is a weak acid with a pKa of approximately 9.2 and a solubility of 0.72 g/100 mL ($Kps = 4.87 \times 10^{-17}$) [9, 10].

With regard to the electrochemical potentials of Fe^{3+}, it is known that its standard electrochemical potential is 0.77 V—in other words, $Fe^{3+}(aq)$ tends to be reduced to $Fe^{2+}(aq)$ in standard conditions [1].

Another important property of iron-based compounds is their magnetism, which has been studied by several authors.

The magnetism of these materials potentiates their application in several areas, such as: magnetic fluids, catalysis processes, the acquisition of elements for magnetic storage, compounds with biotechnological potential in biomedicine and magnetic resonance systems [11].

In relation to their use as catalysts, their magnetism facilitates the separation of iron in a reactive environment simply by means of an external magnet. This method renders unnecessary the use of solvents (filtration stage) and additional filtration or centrifugation stages during the separation process of iron-based catalysts [12].

Magnetic iron oxide particles can be easily synthesized from low-cost, accessible reagents; additionally, when secure and controlled, its reaction conditions allow the production of this material to be upscaled in its use in industrial reactions [12]. Currently, one of the most remarkable forms of iron is zero-valent iron (ZVI), which has been the subject of much research, especially regarding its roles in soil remediation and effluent treatment. Due to its physical and chemical properties, iron plays an important role in the efficiency of the degradation of recalcitrant compounds [13].

At the nanoscale, the physical and chemical properties of ZVI can be potentiated. As is well-known, nanostructured materials have a crystallite size of less than 100 nm and distinguished properties compared to conventional materials. Nanostructured materials are defined by the ISO/TS 80004-1:2015 standard as materials with an internal structure or surface structure at the nanoscale, i.e. with an approximate length range of 1–100 nm.

According to Fransciquini [15], nanostructured systems have unique properties that are not found in voluminous or bulk materials. The author also states that, at the nanoscale, the system has a much higher surface area to volume ratio than that of traditional systems, being in many cases treated as an essentially two- or one-dimensional system [15]. It can be inferred that one of the determining factors for the augmentation of the physical and chemical properties of nanostructured materials lies in the fact that their grain size is so reduced an important fraction of their atoms is located in the grain boundaries (or in the surface of the particles of the material). Meanwhile, bulk materials have most of their atoms located in the interior of the grains, i.e. in their volume [16]. The greater the proportion of atoms located in the surface, the greater their tendency toward adsorbing, interacting and reacting with other atoms, molecules and complexes in order to attain charge stabilization [17]. With respect to nanoparticules, in addition to their diminutive size, particle size distribution, specific surface area and surface charge, their morphology and crystallography are also important features for understanding their behavior [18].

In this context, due to the possibility of controlling the property of materials by manipulating particle sizes, nanomaterials are being studied at a growing pace. Alongside them, nanoscale zero-valent iron (nZVI) has also been frequently studied, as it can be obtained easily, has a low cost and a toxic effect that is nonetheless considered irrelevant. It also has environmental uses that are approved by many regulatory agencies, and its applications deserve attention [19].

Thus, this chapter shall do a general review of the features and applications of nZVI, as well as its synthesis methods.

2 Zero-Valent Iron (ZVI) and Zero-Valent Iron Nanoparticles (nZVI)

The intermediate position of ZVI in the reduction potential table indicates that its electrochemical equilibrium can be easily dislodged due to environmental conditions—in other words, due to the pH, concentration and presence of other ions [1]. This chemical equilibrium can be represented by the following reaction: $Fe \rightleftarrows Fe^{2+} + 2\ e^{-}$, where there is a reduction potential and an oxidation potential.

The ability of iron to function as a reducing agent allows it to perform efficiently when reacting with oxidized contaminants. The ZVI transfers electrons to the contaminants, reducing and transforming them into less toxic or even non-toxic species. The most common methods of degrading organic contaminants by using ZVI are hydrogenolysis and dehalogenation [18, 20].

Keane [21] lists a few environmental contaminants that can be transformed via contact with ZVI and nZVI, such as: chlorinated methanes, chlorinated benzenes, chlorinated ethenes, trihalomethanes, organic dyes, pesticides (dichlorodiphenyltrichloroethane—DDT–, lindane), heavy metal ions (mercury, nickel, silver, cadmium), inorganic anions (dichromate, arsenic, perchlorate, nitrate), other polychlorinated hydrocarbons (polychlorinated biphenyls, dioxins, pentachlorophenol), other organic contaminants (N-nitrosodimethylamine, trinitrotoluene—TNT), among others.

The author also remarks that metallic iron oxidizes naturally when exposed to air, with the same occurring when it is exposed to contaminants. When metallic iron is in contact with organic contaminants, the latter decompose into simpler compounds, and when it is in contact with heavy metals, it transforms the soluble saline forms of the latter into water. The behavior displayed by ZVI when degrading contaminants can be illustrated by the reactions shown in Table 3.

At the macroscale, ZVI and nZVI particles are chemically very similar. That is, ZVI—regardless of its particle size—is a good reducing agent and functions efficiently in environmental remediation processes. However, when it is converted into nanoparticles, its effects are amplified, and it becomes a more efficient material due to its reactivity compared with micro ZVI [23, 24].

Table 3 Contaminant degradation: Fe^0 reactions and considerations. Based on Li et al. [22]

$Fe^0 \rightarrow Fe_2{}^+ + 2e^-$ (1)	Fe^0 or ZVI: functions as an electron donor
$RCl + H^+ + 2e^- \rightarrow RH + Cl^-$ (2)	Chlorinated hydrocarbons: accept electrons and undergo reductive dechlorination
$RCl + Fe^0 + H^+ \rightarrow RH + Fe^{2+} + Cl$ (3)	Thermodynamic perspective: coupling of reactions (1) and (2) is highly favorable
$C_2Cl_4 + 5Fe^0 + 6H^+ \rightarrow C_2H_6 + 5Fe^{2+} + 4Cl^-$ (4)	An example: tetrachloroethene (C_2Cl_4), a common solvent, can be completely reduced into ethene by nZVI according to the general Eq. (4)

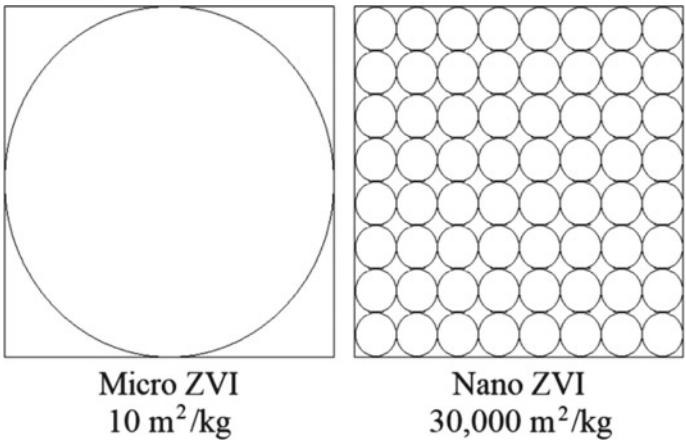

Fig. 1 Comparison of available surface area between micro and nano ZVI. Created by the authors of the present chapter based on Remillard et al. [27]

The augmented efficiency of nZVI can be explained, according to Henry et al. [25], by the fact that it has a greater density of active sites on its surface, allowing its pores to be penetrated by contaminants with greater power when compared to macroscopic ZVI.

Likewise, the higher reactivity displayed by nZVI is a result of its large specific surface area, which yields higher reactivity rates than those of micron-scale ZVI [26].

Figure 1 shows a comparison of available surface areas between micro and nano ZVI. It was created by the authors of the present chapter, based on information from reference [27].

In short, according to Keane [21], the properties that make most nanoparticles qualitatively different from larger particles are their large surface areas in relation to their volumes, and/or the higher natural reactivity of the reactive surface sites. The smaller the particles are, the larger their proportion of surface atoms is, which raises their tendency toward adsorbing, interacting and reacting to other atoms, molecules and complexes to achieve charge stabilization. This relation corroborates the study conducted by Gillham and O'Hannesin [19], which identified the larger specific area of nZVI as the factor responsible for its better efficiency in the dehalogenation of chlorate compounds. In other words, the smaller the particles are, the higher its surface is, which raises its reactivity.

Figure 2 shows how the surface area grows as the diameter of the particles is reduced. It can be noticed that the smaller the size of the particle, the larger its surface area—basically, size and surface area are inversely proportional variables.

With regard to the structure of nZVI particles, many studies suggested a core–shell type of structure [28]. A schematic diagram of a core–shell type zero-valent iron nanoparticle can be seen in Fig. 3. Its core consists of zero-valent iron, while its mixed-valence oxide layer is a result of the oxidation of the metallic iron of

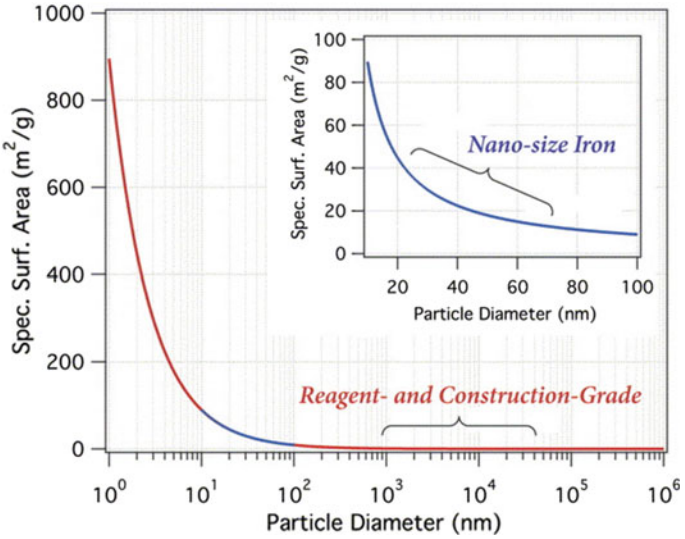

Fig. 2 Particle surface area calculated from diameter assuming spherical geometry and density = 6.7 g/cm^3 (based on the average of densities for pure FeO and Fe_3O_4). Reprinted with permission from Tratnyek et al. [23]

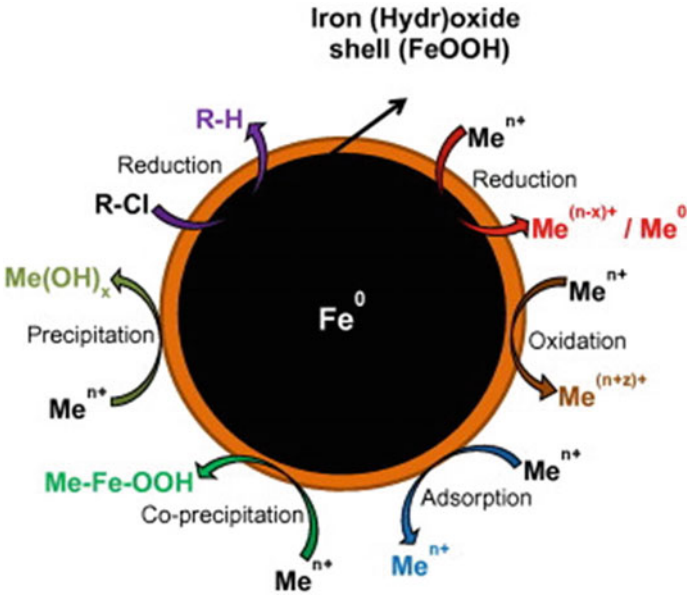

Fig. 3 Schematic diagram of zerovalent iron nanoparticle. Reprinted with permission from O'Carroll et al. [26]

the core [22]. In other words, the iron oxide/hydroxide layer is formed due to the oxidation of the metallic iron core (Fe^0). Nonetheless, even after this crust/fine layer of oxide/hydroxide is formed, it still allows the transference of electrons from the core of the metal, causing this nanoparticle to preserve its reduction capacity. Furthermore, because of this oxide/hydroxide crust, the nanoparticle also becomes able to react with inorganic components, such as metallic anions and metals [29]. Hence, the external oxide/hydroxide layer allows nZVI to function as an efficient adsorbent for several contaminants, including metals.

It has been established that with a smaller particle size comes a larger specific surface area, and consequently more reaction sites on the surface of the nanoparticles—which, in turn, will increase the reaction between contaminants and nZVI particles. However, it must also be known that due to its significant magnetic property, nZVI can create an aggregate of nanoparticles, as seen in Fig. 4. The formation of such aggregate leads to a reduction in surface area, which results in the decrease of the reactivity of nZVI. In order to solve these questions pertaining to the reactivity of nZVI particles, as well as their mobility, many researchers have developed studies

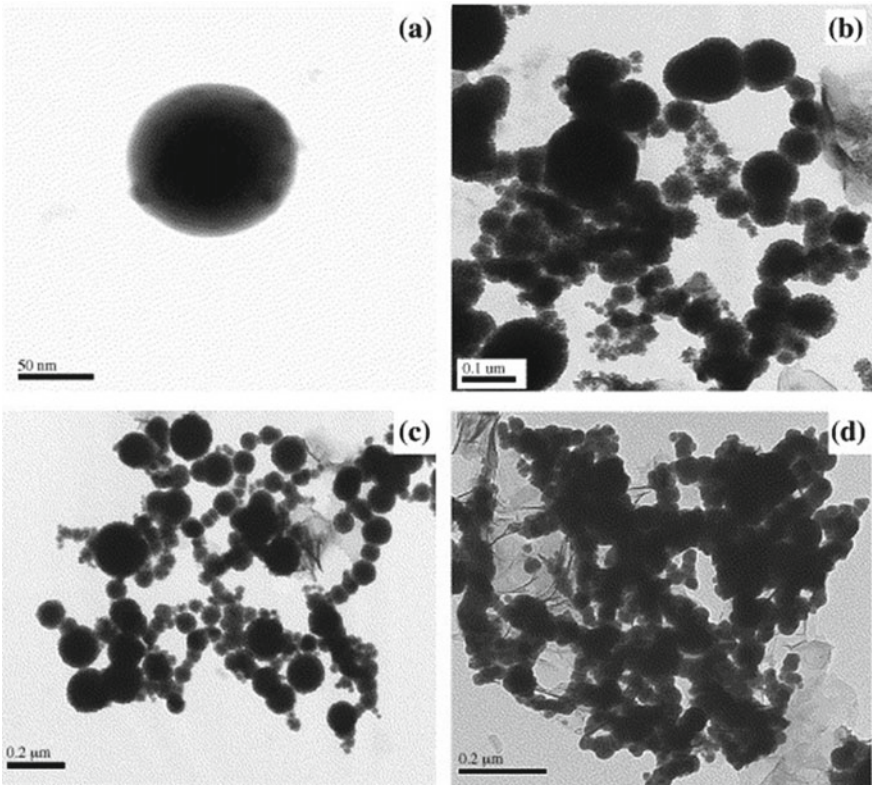

Fig. 4 Micrographs of: **a** a single particle and **b–d** aggregates of iron particles. Reprinted with permission from Suna et al. [30]

on the processing or modification of the synthesis of nZVI, which shall be covered in item 12.5 of this chapter.

3 nZVI Synthesis

There is a wide range of methods that can be used to synthesize metallic nanoparticles. Such as: chemical vapor deposition, inert gas condensation, pulsed laser ablation, spark discharge generation, sputtering gas-aggregation, thermal decomposition, thermal reduction of oxide compounds, hydrogenation of metallic complexes and the aqueous reduction of iron salts, among others [17].

These methods can be divided into two major groups depending on the type of processing they employ to obtain the nanoparticles: top-down and bottom-up [17].

A method belonging to the top-down category obtains nanoparticles from larger materials (granular or microscale), which are submitted to mechanical and/or chemical processes, such as, for instance, mechanical milling, chemical etching, laser ablation and electro-explosion. On the other hand, a bottom-up method "grows" nanostructures, atom by atom or molecule by molecule, and basically consists of a sequence of different physical and chemical processing techniques. A few examples of this approach are methods that employ chemical reducers (e.g. sodium borohydride, lithium borohydride and hydrazine), carbothermic reduction, electrochemical deposition, chemical vapor deposition and reduction with the use of biogenic compounds (green synthesis) [17, 22, 24, 32–34].

According to Li et al. [22], both types of processing were successfully applied to the ZVI nanoparticle preparation process. A typical example of the top-down approach to the production of nZVI is the milling of iron swarf, which reduces the material from a micrometric to a millimetric size until a nanoscale size (below 100 nm) is reached [35]. In this process, iron microparticles are decomposed into nanoparticles by the mechanical forces generated by stainless steel granules inside a high-velocity rotation chamber [34]. It is a method used in the industrial production of nZVI by the US company Golder Associates [35].

With regard to nZVI synthesis methods belonging to the bottom-up classification, a notable example can be cited: the chemical method of reducing nanoscale iron oxides to goethite or hematite using hydrogen as a reducing agent at high temperatures [22]. It was developed for the commercial production of nZVI by the Japanese company Toda Kogyo Ltd. and is still used by the latter currently [17]. Another example of this approach is the method of decomposing iron pentacarbonyl in organic solvents or in argon, which is also used for the commercial production of nZVI, in addition to the iron reduction method [22, 35].

The method of reducing Fe or Fe using sodium borohydride ($NaBH_4$) is the most widely used method in academia due to its simplicity and the high reactivity of the particles it obtains [22]. This method was reported for the first time more than 50 years ago by Oppegard et al. [36]. Nevertheless, it received much attention in 1997, when Wang and Zang [37] described it, singling out its efficiency, and also pioneered the

use of nZVI for contaminant degradation. The nZVI synthesis process was done via the reduction of Fe^{+3} with sodium borohydride. To this end, an aqueous solution of 1.6 M $NaBH_4$ was added dropwise to an aqueous solution of 1.0 M $FeCl_3$. $6H_2O$ at room temperature, in accordance with the following reaction:

$$Fe(H_2O)_6^{3+} + 3BH_4^- + 3H_2O \rightarrow Fe^0 + 3B(OH)_3 + 10.5H_2 \quad (1)$$

Over 90% of the obtained particles had a final size of 1–100 nm. The resulting surface area (obtained by the Brunauer–Emmett–Teller method, BET) was 33.5 m^2/g, approximately 37 times larger than the fine iron powder commercially available at that time.

In the decades after the work of Wang and Zang [37], many other researchers advanced studies on the synthesis of nZVI by reducing Fe^{+3} or Fe^{+2} with $NaBH_4$. The studies done by [38–42] can be cited as examples for each decade.

Sun et al. [38] synthesized ZVI by reducing iron with sodium borohydride. They used a 1:1 volume proportion of $NaBH_4$ (0.2 M) and $FeCl_3 \cdot 6.H_2O$ (0.05 M), which were stirred in a reaction flask during 30 min after titration. 92% of the acquired particles had a size of less than 100 nm, with an average size of around 60 nm, leaving only a small percentage of particles sized between 200 and 250 nm.

Singh et al. [39] also synthesized nZVI using the iron reduction method, employing $FeCl_3.6H_2O$ (0.05 M) and the reducing agent $NaBH_4$ (0.2 M) in the same concentrations proposed by Sun et al. [38]. $NaBH_4$ was added dropwise to the $FeCl_3$ solution, and the resulting mixture was stirred vigorously for 30 min. Afterward, the iron nanoparticles formed were separated by filtration, then washed and stored in ethanol to avoid the oxidation of the zero iron obtained. They were characterized as follows: crystallite size, 15.9 nm, calculated using XRD (X-ray diffraction with Scherrer equation), and average nanoparticle size, 26 nm, evaluated via the transient electromagnetic (TEM) method.

Boparai et al. [40] also bet on the iron reduction method, starting with a solution containing FeCl and using $NaBH_4$ as a reducing agent. $NaBH_4$ was added dropwise to the $FeCl_3$ solution with a 1:1 volume ratio, with constant stirring in an inert environment. An excess of borohydride was added to accelerate the synthesis of nZVI and ensure a uniform formation of particles. The process yielded spherical nZVI particles with sizes between 20 and 200 nm; among these, around 85% had a diameter of less than 120 nm, with an average particle size of 80 nm.

Xiaoyuan Li [41], following the examples set by the previous researchers, also synthesized nZVI using the iron reduction method, employing sodium borohydride as a reducing agent—although with a solution containing $FeSO_4.7H_2O$ instead of $FeCl_3$. Also used was a deoxygenated solution of 30% ethanol–water to dissolve $FeSO_4$ and later add, dropwise, $NaBH_4$ under stirring. The surrounding environment was kept inert in order to accomplish the required reactions (high-purity N_2). As to the characterization of the resulting particles, it was as follows: the scanning electron microscopy (SEM) found sphere-shaped particles, XPS showed that the surface of the acquired iron nanoparticles consisted of 86.9% Fe (II/III) and only 13.1% Fe^0, and the BET result was 23.4 m^2/g.

Mdlovu et al. [42] also used sodium borohydride as a reducing agent for iron and $FeSO_4.7\ H_2O$. However, the synthesis method they employed was slightly modified in comparison with the methods of previous studies. Their coprecipitation method consisted of the dissolution of 10 g of $FeSO_4.7\ H_2O$ in an aqueous solution with 30% ethanol and pH adjusted to 6.8, with NaOH 3.8 N (aq). After that, 1.9 g of powdered $NaBH_4$ was added and the solution remained in stirring for 30 min, followed by filtration using a 0.22 μm filter. The resulting particles were filtered, collected via magnetic filtration and then washed with ethanol 3 to 5 times. The acquired nZVI particles were vacuum-dried for 24 h. As a result of this synthesis, sphere-shaped nZVI particles with sizes between 20 and 60 nm were obtained. The total surface area of the nZVI, per the BET analysis, was 42.6 m^2/g. According to the Barret, Joyner and Halenda (BJH) method, which was used to examine the distribution of the pore sizes of the specimens, the nZVI had a mesoporous structure with an adsorption–desorption hysteresis typical of a Type IV isotherm, representing thus the mesoporous nature of the samples [42].

As can be noted in the studies mentioned in this section, to obtain nZVI using the method of reducing iron ions, different precursors and reducers can be used. It is remarkable that these precursors and reducers have a fundamental role in defining the morphology, size and composition of the acquired nZVI particles, which are important aspects that influence the chemical and physical properties of the nanoparticles. Figure 5 shows the morphology of nZVI variants synthesized by different combinations of precursors (ferrous sulfate and ferric chloride) and reducing agents (sodium dithionite and sodium borohydride) [43].

These were only a few examples to illustrate the many studies done throughout the years on zero iron synthesis by reducing Fe^{+3} or Fe^{+2} with NaBH4. Researchers such as Visentin et al. [44], Wang et al. [45], Li et al. [46], Stefaniuk [47] and Phenrat et al. [35] include in their articles extensive lists of studies on the synthesis of nanoscale zero iron, featuring the most diverse methods and applications. As these lists can be consulted in the articles cited above, it will not be necessary to reproduce them here.

According to Phenrat et al. [35], with regard to the research and development (R&D) on nZVI as a field of study, using the Web of Science (WOS) database as a corpus (consulting data from 2001 to 2018), the number of peer-reviewed articles and citations about the subject has grown quadratically each year. In 2017, there were 262 peer reviews of journal articles and 8094 citations related to research on nZVI.

Stefaniuk et al. [47] cite a few nZVI production methods that, due to their advantages, can become very popular. They are: precision milling, carbothermal reduction, ultrasound-assisted production, electrochemical generation and green synthesis. Thus, a brief report describing these methods shall be done, despite some of them already having been mentioned as examples of top-down and bottom-up approaches earlier in this chapter.

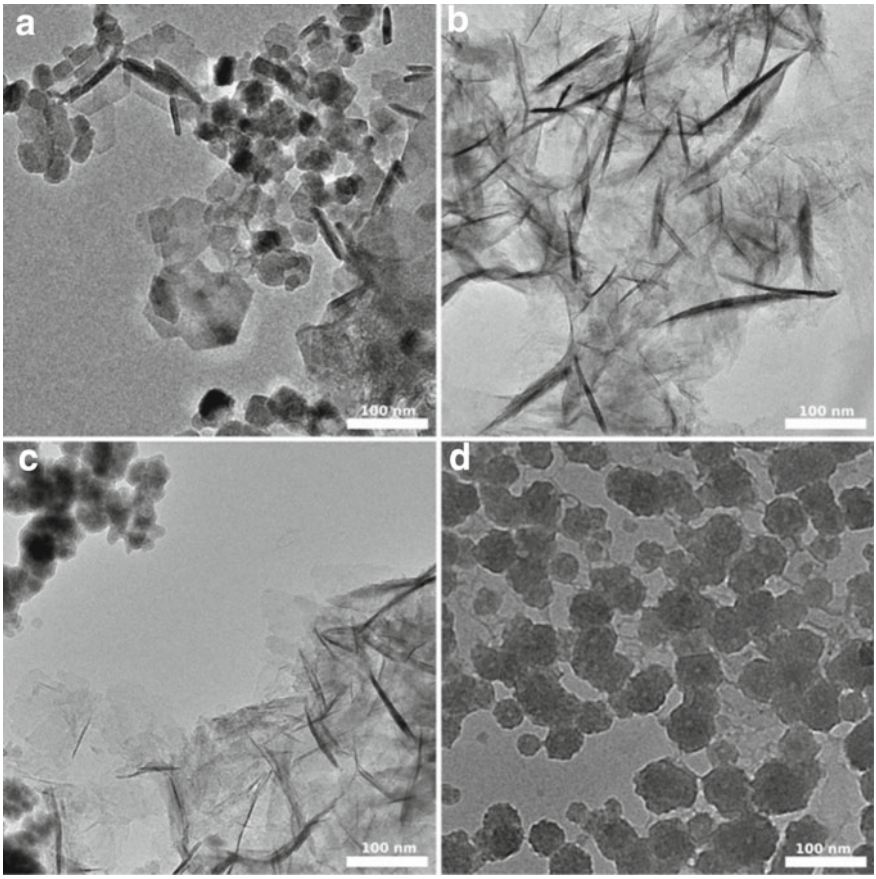

Fig. 5 TEM images of freshly synthesized nZVI samples: **a** and **b** nZVI were synthesized using ferrous sulfate and ferric chloride as precursors and sodium dithionite as reducing agent, respectively, while **c** and **d** were formed by using ferrous sulfate and ferric chloride as precursors and sodium borohydride as reducing agent. Reprinted with permission from Rónavári et al. [43]

3.1 Precision Milling

Li et al. [31] synthesized nZVI by using precision milling. According to the authors, it is an environmentally-friendly and economical method because, in order to break down micrometric iron particles and thus produce nanoparticles, it depends solely on the mechanical impact forces generated by stainless steel granules inside a high-velocity rotating chamber. They performed tests using microscale zero-valent iron (BASF, iron content >99%, d50 = 2 μm). The tests lasted 8 h and yielded particles smaller than 50 nm—with the great majority of the particles having 20 nm—and with a specific surface area of 39 m^2/g. The authors state that the size and superficial area of the particles are easily controllable by the milling time, and that the

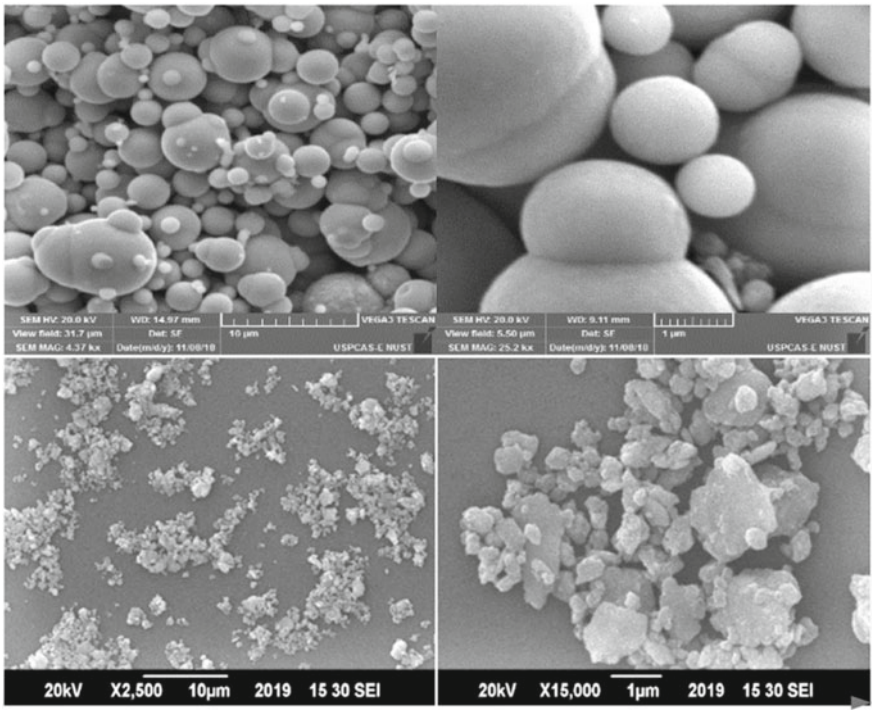

Fig. 6 SEM images of micro iron and iron milled for 30 h. Reprinted with permission from Khayam et al. [48]

system is completely scalable for large-scale production. It does not employ toxic solvents and is thus an attractive synthesis pathway for the ecological creation of iron nanoparticles.

Figure 6 shows the SEM images of micro iron particles, including an image of them after 30 h of milling, which evidences the reduction of the particle size after the milling process [48].

3.2 Carbothermal Reduction

The method of obtaining nZVI by carbothermal reduction consists of reducing nanoparticles of iron oxide or hydrated Fe^{+2} ions under high temperatures (T > 600 °C) using thermal energy and exposing them to gaseous reducing agents (H_2, CO_2 ou CO) in an inert atmosphere. According to Stefaniuk et al. [47], these reducing agents are a result of the thermal decomposition of carbon-based materials (carbon black, biochar, carbon nanoparticles, among others). In other words, this method allows the use of the supporting elements or products from gasification as reducing agents, thus

dispensing the need for the addition of other reducers. It also minimizes monetary costs and the environmental damage that could be caused by certain reducing agents, e.g. sodium borohydride, which is not only expensive but also requires an intense washing process to remove it from the synthesized nZVI when it is used as a reducing agent.

To put it shortly, in the carbothermal reduction process, Fe^0 is formed by a high-temperature endothermic reaction in the presence of gaseous products. This reaction can occur according to Eqs. 1 and 2:

$$Fe(C_2H_3O_2)_2 + C \rightarrow Fe^0 + 2CH_2CO + H_2O \quad (1)$$

$$Fe_3O_4 + 2C \rightarrow 3Fe^0 + 2CO_2 \quad (2)$$

A typical example of nZVI production via carbothermal reduction is the study carried out by Hoch et al. [49], which was also already mentioned by [17, 44, 47].

Hoch and collaborators [49] synthesized nZVI using iron salts with carbon black as a starting material. The carbon black, which had a surface area of 80 m^2/g, was combined with aqueous solutions containing Fe^{+2} or Fe^{+3} salts. 50 g of $Fe(NO3)_3.H_2O$ and 5 g of carbon black were mixed in 200 mL of deionized, nanopure water, with a resistivity of 18.2 MΩ cm. This solution was filtered, and the resulting solid was removed from the filter and placed inside a vacuum oven to dry, with no heating being applied. Afterward, it was heated in accordance with the following conditions: inert atmosphere (argon), heating rate of 4.5 °C/min until 800 °C was reached, followed by the maintenance of the same temperature for 3 h. Under these conditions, the researchers managed to produce Fe^0 with 20–100 nm of fixed diameter, especially in the external surface of the support. The improvement of the necessary properties for the reduction of Cr (VI), which was the object of the aforementioned study, was attained. Furthermore, Hoch et al. [49] remark that the method can be easily scaled to larger reactors, which allows its use in the mass production of nZVI. I.e., it is a cheap and environmentally-compatible method. This carbothermal reduction method was also used by Dai et al. [50] with great success in the synthesis of nZVI composites and ordered mesoporous carbon (OMC) by means of simultaneous carbothermal reduction methods.

3.3 Ultrasound-Assisted Production

Ultrasound-assisted production of nZVI is the application of ultrasonic waves to enhance the efficiency of the physical and/or chemical methods employed in the synthesis of nZVI [47]. These waves act directly on the reduction of particle size, and also increase surface area and particle uniformity [44, 47].

Jamei et al. [33] present the ultrasound-assisted method as a new and innovative way of synthesizing nZVI particles. The method the researchers used in the initial

synthesis of nZVI is the chemical method, i.e. the reduction of Fe^3 based on a $FeSO_4$ and $NaBH_4$ solution. nZVI was synthesized within a reaction flask with three open necks. Nitrogen gas was injected into the two necks of the extremity to remove oxygen and prevent the oxidation of nZVI. The ultrasound was applied to the central neck via the placement of a titanium sonic probe with a diameter of 1 inch. It was adjusted until 2.5 cm of the probe was submerged in the solution. A range of ultrasonic power (0–1000 W) with constant frequency (20 kHz) was used during the experiments, and the sonication device used was a 1000 W-Ultrasonic Processor. The resulting material was filtered and washed with pure ethanol then put in a centrifuge to remove the renascent humidity. Afterward, it was dried in a vacuum oven for a minimum of 24 h in order to proceed to the characterization of its physicochemical properties.

The results demonstrated that the application of the ultrasound wave significantly altered the morphology of the nanoparticles, also reducing their size from 90.3 to 29.9 nm and consequently increasing the specific surface area, from 10 to 42 m^2/g. These results corroborate the argument that the use of ultrasound in the synthesis of nZVI via iron reduction improves the efficiency of this same method, significantly enhancing the properties of interest of these materials.

3.4 Electrochemical Generation

Electrolysis is a well-established industrial method for sequestering metals from an ionic solution. It is an extremely simple, cheap and fast method, which made electrochemical techniques for synthesizing nZVI an object of research [17]. It requires only a solution containing Fe^{+2}/Fe^{+3} salts, electrodes (cathode and anode), an electric current and a method to disperse the electrodeposited nanoparticles [17, 47]. The dispersion method became necessary in light of the iron atoms involved in the process, which are formed by the reduction of ferric chloride (reactions 3 and 4) and are deposited in the cathode, displaying a strong tendency toward aggregating and forming agglomerations [44, 47].

$$\text{Cathode} : Fe^{+3} + 3e^{-} + \text{stabilizer} \rightarrow \text{nZV} \tag{3}$$

$$\text{Anode} : Cl^{-} \rightarrow 1/2Cl_2 + e^{-} \tag{4}$$

Among the dispersion methods studied, Chen et al. [51] combine electrochemical techniques and ultrasonic waves for the dispersion of the particles. To this end, they employed cationic surfactants as stabilizing agents and ultrasonic waves (20 kHz), which are a necessary energy source for the rapid removal of iron nanoparticles from the cathode and thus to avoid their aggregation [47].

According to Chen et al. [51], in order to produce nZVI, a ferric chloride solution must be prepared first. Then an electrogalvanization reactor is used, to which a platinum cathode and anode connected to an energy source are added. The reactor is

then submerged in an ultrasonic vibrator. The ferric chloride solution is transferred to the electrogalvanization reaction together with the stabilizers (e.g. polyvinylpyrrolidone, PVP, and cetylpyridinium chloride, CPC) [44]. The stabilizers and the ultrasonic vibrator are fundamental in order to avoid the clustering of the produced nZVI nanoparticles. The nZVI produced under these conditions has a particle size of 1–20 nm and a specific surface area of 25 m^2/g [47].

In addition to the work of Chen et al. [51], other researchers also studied methods geared toward dispersing the nZVI particles formed in the cathode, such as, for instance, Wang et al. [52], who used ion-exchange in nafion film, and Yoo et al. [53], who electrodeposited thin films and nanowires from an aqueous electrolyte using template-directed electrodeposition methods.

3.5 Green Synthesis

In the last decades, concerns with environmental sustainability began to become the subject of discussions and encourage the search for solutions from all areas of expertise. Naturally, it would not be any different when it comes to the synthesis of materials that satisfy this demand and are many times used for environmental treatment activities.

The traditional nZVI synthesis methods can often involve some toxicity due to the reagents, reducers and stabilizers they use, as well as a high production cost given how expensive these products are [34]. In this regard, green synthesis can be an environmentally and economically viable alternative in the production of nZVI.

The economy offered by the green synthesis methods lies not only in the cost of the products it uses, but also in the different versions of its process, as it does not require the use of high temperatures or pressures and additional energy sockets, being also easy to implement on a large scale [47].

One of the most significant aspects of green synthesis is the production of nZVI using biogenic material such as plants or microorganisms, fungi and bacteria, which can function not just as stabilizing agents but also as reducers for nanoparticles [34]. Microbial enzymes or plant phytochemicals with antioxidant or reducing properties are generally responsible for the reduction and oxidation of metallic compounds [44]. Nevertheless, the microorganism-based green synthesis method is not widely used or studied in the scientific community yet. That is because the use of microorganisms in the nZVI synthesis process requires the obligatory restriction of aseptic conditions, which requires trained personnel and thus raises production costs [47]. Factors such as reaction time are more important in the microorganism-based synthesis method than in the method using plant extracts. Therefore, the use of plants for green synthesis ends up being preferred to the use of microorganisms [47].

According to Hoag et al. (2009) apud Stefaniuk et al. [47], green synthesis was used to produce nZVI for the first time by the US company VeruTEK and the Environmental Protection Agency (EPA). The method in question included the preparation of a polyphenolic solution containing a plant extract (coffee, green tea, black tea,

lemon, balsam, sorghum, grape powder, among others) obtained by heating the plant samples in water at a temperature close to boiling point. The prepared extract is then separated from the plant residues and mixed with a Fe^{2+} solution. The iron ions are reduced to nZVI with the exposure to the polyphenols.

The disadvantage of synthesizing nZVI using plants is that the process requires their destruction. However, this problem can be solved by the use of agroindustrial residues as raw materials, e.g. extracts of various fruit residues (lemon, tangerine, orange or grapevine pomace), in addition to other alternatives [47].

According to Stefaniuk et al. [47], the nZVI obtained via green synthesis has been successfully used as a Fenton catalyst to oxidize monochlorobenzene (to 69%) and carry out the reductive degradation of dyes such as malachite green or bromothymol blue. Similarly, green nZVI can also be used to degrade drugs (e.g. ibuprofen) in soils, Cr (VI) ions, nitrates in aqueous solutions, or to treat swine wastewater.

In spite of the countless advantages of green synthesis for the production of nZVI, both in terms of environment and cost, its disadvantages must also be known. One of them is the diminished reactivity and surface energy of the phytogenic ZVI nanoparticles compared to chemically-prepared ZVI nanoparticles. The slower synthesis process in comparison with that of chemically-synthesized nanoparticles and the incomplete reduction of Fe^{2+} ions in ZVI nanoparticles are also disadvantages of phytogenic nanoparticles [34].

Still, regardless of these disadvantages, studies on the optimization of the synthesis process and the improvement of its desired qualities by the processing of the nanoparticles must be done, since solving these difficulties will result in the availability of a low-cost, highly environment-compatible method of producing nZVI.

4 Considerations on the Synthesis Process of nZVI

After this discussion of the several methods of synthesizing nZVI, it is important to highlight which of them are currently used in industrial-level nZVI production. According to Crane and Scott [17], three methods are used in the industrial production of nZVI: milling, chemical reduction with hydrogen and chemical vapor deposition. Table 4 shows data relative to the industrial production of nZVI.

Furthermore, it is important to identify which factors determine the non-implementation of other methods for the large-scale production of nZVI, and also to bring attention to alternatives indicated by researchers for the production of this material. Such alternatives range from processing techniques to traditional synthesis or modified synthesis methods.

Table 4 nZVI industrial production methods. Created by the authors of the present chapter based on Phenrat et al., Visentin et al. and Stefaniuk et al. [35, 44, 47]

Synthesis method	Producing company (Country)	Particle size (nm)	Specific surface area (m^2/g)
Milling	Golder Assoc. (USA)	12.5	30–50
Chemical reduction with H_2	Toda Kogyo Ltd. (Japan)	100	23
Chemical vapor deposition	Nanoestrutured & Amorphous Materials, Inc. (USA)	25	40–60
*NA	Polyflon (USA)	100–25	37–58
NA	SkySpring Nanomaterials, Inc	20–80	7–60
NA	MKNano (Canada)	25	NA
NA	NC	NA	NA

*(NA): Not available

5 nZVI: Modified Treatments and/or Synthesis and Uses

One of the most studied methods in academia is the synthesis of nZVI via the reduction of Fe^{+3} or Fe^{+2} with $NaBH_4$. However, it is rarely recommended for large-scale production because of a few technical and economical aspects: high cost of reagents for the production process, a great amount of hydrogen generated, the presence of polydisperse particles (with size variation), and a high nanoparticle agglomeration, directly impacting the properties of interest, such as reactivity, which diminishes due to the agglomeration of the particles [38, 54, 55].

With the intent of bettering the properties of nZVI produced by the most diverse methods, studies on its processing have been developed to improve issues such as particle agglomeration, stability, mobility and efficiency in different applications. A few examples of the topics investigated in those studies: sulfatation; the formation of Fe/graphene composites; polymer-modified nZVI; emulsified nZVI; and the creation of bimetallic nZVI compounds supported in other materials.

Examples of a few processing treatments and/or modification procedures to the synthesis process of nZVI, its starting synthesis and intended uses, as well as the properties optimized by these treatments/modifications, are shown in Table 5.

6 ZVI and Supported nZVI—Biochar

There are many processing treatments and/or modification procedures that can be adopted to improve the properties of nZVI. Its small particle size makes it very reactive; nonetheless, it can be a problematic material due to the difficulty of separating

Table 5 Processing treatments/modifications of nZVI and applications. Created by the authors of the present chapter

nZVI synthesis method	Processing treatment applied to nZVI/product	Objectives of the nZVI treatment	Application of the treated nZVI	Results obtained in the application	References
Reduction of $FeSO_4.7H_2O$ using $NaBH_4$	Non-aqueous sulfatation method (in absolute ethanol) – S-nZVI	– To make nZVI more efficient in the reduction of chlorinated contaminants – S-nZVI-H_2S-Ethanol (avoid/limit reaction between Fe^0 and during the sulfatation period)	S-nZVI Dechlorination of organic contaminants	– Significant increase in nZVI surface area, from 23,4 m^2/g to 65,6 m^2/g after it became S-nZVI. Sulfidation method promising for the preparation of S-nZVI with improved reductivity and reactivity for the dechlorination of organic contaminants	[41]

(continued)

Table 5 (continued)

nZVI synthesis method	Processing treatment applied to nZVI/product	Objectives of the nZVI treatment	Application of the treated nZVI	Results obtained in the application	References
Reduction of $FeCl_3$ using $NaBH_4$	Formation of Fe/graphene (GO) composites – nZVI-GO hybrid composite	– The incorporation of nZVI into carbon to prevent aggregation and its susceptible oxidation	nZVI-GO Removal of uranium from aqueous solution in an anoxic atmosphere	nZVI-GO composite materials: – Decrease in size of nanoparticles and prevention of their aggregation, thus increasing their specific surface area for reaction with uranium – In neutral-basic groundwater (pH 6.5) it benefitted uranium reduction – In extremely acid conditions (acid mining water containing uranium) nZVI-GO was dissolved, reducing the efficacy of the uranium removal process, with pure nZI being more efficient in this case	[56]

(continued)

Table 5 (continued)

nZVI synthesis method	Processing treatment applied to nZVI/product	Objectives of the nZVI treatment	Application of the treated nZVI	Results obtained in the application	References
Coprecipitation	Production of polyethylenimine (PEI)-modified nZVI nanocomposites – PEI-nZVI	– To avoid aggregation and oxidation, developing economical applications of nZVI	Degradation of TCE, PCE and 1,2-DCE DNAPLs in contaminated groundwater	– The coating of nZVI particles with PEI reduced the magnetic interactions between the nZVI particles – The nZVI (37 m^2/g) e PEI-nZVI (53 m^2/g) surface areas – The coating of the PEI surface increased the stability, mobility and activity of the nZVI – The laboratory remediation results indicate that both nZVI and PEI-nZVI can remove 99% of TCE, PCE and 1.2-DCE. The reaction rate for pure nZVI was higher in the initial stage. Comparatively, PEI-nZVI had a higher removal rate and efficiency after 2 h	[57]

(continued)

Table 5 (continued)

nZVI synthesis method	Processing treatment applied to nZVI/product	Objectives of the nZVI treatment	Application of the treated nZVI	Results obtained in the application	References
Reduction of $FeSO_4.7H_2O$ using $NaBH_4$	Formation of bimetallic compounds – Bimetallic Pd/Fe nanoparticles were synthesized by the reaction of the fresh zero-valent iron particles with the desired amount of potassium hexachloropalladate (IV) aqueous solution under a stirring condition -Pd/Fe nanoparticle (0.54 mg of Pd per gram of iron)	– To make nZVI more effective in the reduction of chlorinated organic compounds	– To assess the efficiency of Pd/Fe nanoparticles in the removal of pentachlorophenol – To gauge of the effects of copper, nickel and ferric cations on degradation	– An increase in PCP degradation kinetics by the synthesized bimetallic Pd/Fe compound was observed – An increase in PCP degradation was observed due to contact with growing concentrations of Cu^{2+} ions as a result of the formation of zero-valent Cu in the Pd/Fe surfaces - Ni^{2+} presence increased the degradation kinetics and removal efficiency of PCP due to the catalytic effect of the reduced Ni form on the Fe surface - The addition of Fe^{3+} ions caused a reduction in pH, which may explain the increase in the observed PCP degradation process	[58]

(continued)

Table 5 (continued)

nZVI synthesis method	Processing treatment applied to nZVI/product	Objectives of the nZVI treatment	Application of the treated nZVI	Results obtained in the application	References
Reduction of $FeCl_3$ using KBH_4 with active silica as support	Supported nZVI – Fe^0 nanoparticles supported in active silica – SF-Fe^0	– To increase the reactivity of iron particles, in order for them to be used in the remediation of chrome VI	– To examine the ability of prepared SF-Fe^0 in stabilizing Cr(VI) ions from aqueous solution	– The fixing of Fe^0 nanoparticles to the commercial submicrometric active silica prevented aggregation, maintaining the reactivity of the particles – The removal of Cr(VI) by Fe^0 particles supported by active silica (SF-Fe^0) in 120 min was 22.55% greater than that of unsupported Fe^0	[59]

nanoscale iron from the purified matrix. Still, that can be counterbalanced by the use of materials that support nZVI, such as silica, activated carbon, zeolites, polymeric membranes and biochar. These supporting materials immobilize the nZVI by fixing it to the structure or trapping it inside their pores. Such treatment corroborates the modification of the physicochemical properties of nZVI that are of interest for the better accomplishment of its intended application [47].

Among these options, biochar-supported nZVI (nZVI/BC) stands out as an innovative technology for the recuperation of degraded soils and the treatment of contaminated industrial effluents.

Biochar, depending on the pyrolysis conditions and the biomass utilized, has a porous structure and a large surface area with a significant density of functional groups containing oxygen, such as carboxyl (_COOH) and hydroxyl (_OH) [60]. Its porous structure facilitates the mass transfer from contaminants to the surface. Furthermore, the biochar matrix controls the size and dispersion of the particles, as well as the corrosion of nZVI, thus offering a good catalytic, reductive and oxidative resource for the treatment of contaminants. It also increases electron transference from the nZVI to target contaminants due its good electric conductivity, which qualifies it to be used as an adsorbent in the removal of organic contaminants and heavy metals. According to Wang et al. [61], the synergetic effect of the nZVI/BC in the removal of contaminants is related to the greater sorption capacity of biochar, the properties of nZVI and the positive interactions among both materials [61].

Some studies on the use of biochar as a support to ZVI are reviewed below.

Yanmei Zhou et al. [62] developed a simple method of synthesizing ZVI-biochar compounds using chitosan as a dispersing and stabilizing agent. Chitosan was used as an "organic glue" in order to annex fine ZVI particles to the biochar. The commercial chitosan powder used was dissolved in 90 mL of a 2% acetic acid solution. Following that, the commercial ZVI particles were dispersed in the solution, and then the biochar (which was produced by the pyrolysis of bamboo) was added. The mixture was then stirred during 30 min to form a homogenous solution, which was then added dropwise to a 450 mL 1.2% NaOH solution. This solution was left undisturbed for 12 h at room temperature. The solid products were then separated by decanting and washed with de-ionized water to remove the NaOH excess, and dried in an oven for 24 h at 70 °C. The iron-modified biochar demonstrated an excellent capability of removing several contaminants, including heavy metals, phosphate and methylene blue, from aqueous solutions. Furthermore, the modified biochar is ferromagnetic and can be easily collected by a magnet. In short, the acquired material can be used in environmental activities, including water treatment and soil remediation.

Yan et al. [62] synthesized a biochar-supported nZVI composite to be used as a persulfate activator and thus increase the removal of trichloroethylene (TCE) in aqueous solutions. Biochar obtained via the pyrolysis of rice hulls was used. It was added to an aqueous $FeSO_4.7H_2O$ solution with 5.0 pH, then N_2 was purged in the solution during 1 h in order to exclude the O_2 dissolved during the preparation process. Afterward, the obtained material, nZVI/biochar, was filtered, washed with ethanol and vacuum-dried. nZVI/biochar was successfully synthesized and used as efficient activator for persulfate. With the oxygen functional groups in the surface

of the biochar, nZVI/biochar offered more reactive sites to activate the persulfate, allowing an almost complete removal of the TCE in 5 min.

Zhang et al. [64] synthesized an nZVI/BC composite with the aim of assessing its efficiency in activating persulfate to promote the oxidative degradation of atrazine. It was synthesized by a simple one-pot method via oxygen-limited high-temperature co-pyrolysis of the mixture of soybean straw powder and Fe_2O_3. To this end, different formulations were carried out by mixing Fe_2O_3 and soybean stem powder. They were subjected to pyrolysis at temperatures between 600 and 900 °C, with a heating rate of 20 °C, under argon flow, for 1 h. The authors found that the most suitable pyrolysis temperature was 800 °C, at which 75% of Fe_2O_3 can be converted to Fe^0. They also verified that the prepared nZVI/BC can effectively activate the persulfate to promote the oxidative degradation of atrazine. In the representative persulfate-catalyst system, the atrazine removal rate was up to 93.8%.

Wei et al. [65] synthesized an nZVI/BC composite using biochar (BC) produced from oak sawdust. Its purpose was to be used in the efficient reduction of nitrobenzene (NB). Firstly, oak sawdust biochar was acquired with the following pyrolysis conditions: N_2 flow, heating rate of 5 °C/min to 800 °C, with a residence time of 4 h, and a final pause for it cool down to room temperature. With the biochar obtained, the nZVI/BC composite was synthesized using the liquid phase reduction method. First, 0.15 g biochar, 0.25 g polyethylene glycol-4000 (PEG-4000), 0.75 g $FeSO_4.7H_2O$, 15 mL n-pentane and 35 mL distilled water were added to a three-necked flask. For the reduction step, a $NaBH_4$ solution (0.108 mol/L with 0.1 wt.% NaOH, 50 mL) was prepared and added dropwise into the flask, then stirred for 30 min. Based on the X-ray diffraction analyses, a peak of zero-valent iron in the synthesized composite was identified. The BET specific surface area of pure nZVI is 6.4 m^2/g, while that of the nZVI/BC composite is 264.9 m^2/g, showing a significant increase. The removal efficiency of nZVI/BC was higher than the simple summation of bare nZVI and BC. Moreover, nZVI/BC displayed lower Fe leaching and high durability in nitrobenzene removal. The obtained results imply that nZVI/BC would be a promising material for the remediation of a nitroaromatic-contaminated aquatic environment.

Han et al. [66] prepared an nZVI/BC composite in order to verify its effectiveness against organic contaminants by evaluating the discoloration of methyl orange (MO), which was used as a representative organic contaminant. The synthesis of the nZVI/BC composite began with the pyrolysis of rice hulls biochar at 500 °C. The biochar (<100-mesh) was first mixed with 1 M HCl (1/20, v/v) and shaken overnight at room temperature for demineralization, in order to remove elements such as K^+, Na^+, Ca^{2+} and Mg^{2+}. The biochar was then purified using dialysis until the pH solution was close to neutral and dried at 80 °C in an oven. Subsequently, the treated biochar was added to a solution of $FeSO_4.7H_2O$ (0.05 M) in methanol/deionized water (3/7, v/v), and stirred for 1 h to form a homogeneous solution. For the iron reduction process, an equal volume of 0.1 M KBH_4 solution was added dropwise into the slurry under vigorous stirring. The nZVI/BC composite formed was separated from the supernatant and washed several times with deionized water and methanol. The BET surface area (SA) of the nZVI/BC composite increased significantly compared to the area of pure nZVI. The SA of nZVI was 20.89 m^2/g, while that of the composite

in its best formulation was 142.80 m^2/g. A mass ratio of biochar to nZVI of 5:1 seemed to give the best performance, with 98.5% MO decolorization efficiency. The effectiveness of nZVI/BC for MO removal was confirmed.

Liu et al. [67] evaluated the dechlorination of polychlorinated biphenyls (PCBs) using an nZVI/BC composite, which was synthesized alongside an nZVI sample. The biomass used was pinewood sawdust. The biomass sample, previously dried at 105 °C for 24 h, was immersed in a $FeCl_3$ solution and subsequently ultrasonicated for 2 h at room temperature. After being stirred at 60 °C for 12 h, the mixture was separated by vacuum filtration. The recovered residue was dried at 100 °C in vacuum for 2 h. Then, it was submitted to the pyrolysis process using a N_2 flow rate of 30 mL/min and heating rate of 20 °C/min, starting from room temperature until 800 °C. It remained at this temperature for 40 min before its cooling process started. It remained in the oven, with exposure to a flow of N_2 until it reached room temperature. The resulting sample was washed several times with deionized water and ethanol and vacuum-dried for use.

In short, the sawdust was able to be significantly activated by ferric chloride, and subsequently nZVI was formed in the carbonization process, thus originating the nZVI/BC composite. For comparison purposes, the sawdust was subjected to the same test conditions, only without impregnation of ferric chloride. The X-ray diffraction results of the sample that was activated with ferric chloride showed characteristic peaks of ZVI and a crystallite size of 27 nm, which was calculated by the Scherrer equation. I.e., an nZVI/BC composite was formed. Regarding BET, surface area and pore volume, the sawdust that was pyrolized without ferric chloride activation presented values of 20 m^2/g and 0.04 cm^3/g, respectively. Meanwhile, the nZVI/BC composite showed much higher values: 423 m^2/g and 0.23 cm^3/g. Additionally, the synergistic and simultaneous function of adsorption and dechlorination carried out by the nZVI/BC resulted in a mostly complete removal of PCBs from the aqueous solution.

Dong et al. [68] also used biochar as a support for iron in order to produce a nanoscale catalyst for the production of ZVI-based bio-oil. The biomass used was rice hull. The raw rice hull was impregnated with $Fe(NO_3)_3 \bullet 9H_2O$, which was achieved by stirring it in a solution for 12 h. The impregnated biomass was dried at 105 °C for 48 h and then heated in a horizontal oven (electric heating) at 800 °C for 1 h, under a N_2 atmosphere. The resulting material was named RHC/Fe. The mineralogy of the catalyst was characterized by XRD, which showed three peaks indicative of ZVI. The ZVI was formed during biomass pyrolysis due to the reduction of the Fe precursor, which was impregnated in the biomass, using H_2 and CO as reducing agents. The catalyst obtained—RHC/Fe—was tested during the pyrolysis of macroalgae from the *Sargassum* genus, and it was observed that esterification reactions and secondary reactions were were promoted, with the formation of a bio-oil enriched in esters.

Su et al. [69] produced a material with biochar-supported nZVI (nZVI @ BC) designed for in-situ remediation of soil contaminated with hexavalent chromium. Biochar was obtained via the pyrolysis of vegetable waste at 600 °C, with a residence time of 2 h. To produce the nZVI @ BC composite, the resulting biochar was added to a $FeSO_4.7H_2O$ solution and stirred for 60 min, under anaerobic conditions, to form a

homogeneous solution. Following that, $NaBH_4$ was added dropwise to this solution to reduce iron, thus enabling the formation of nZVI @ BC. In characterization terms, the BET results showed that the specific surface area of pure nZVI was 35 m^2/g and that of nZVI @ BC was 71 m^2/g; in other words, it doubled in relation to pure nZVI, due to the large surface area of the biochar (which was 353 m^2/g). Sedimentation tests and column experiments were used to compare the stability and mobility of nZVI @ BC and pure nZVI. Chromium immobilization efficiency, the toxic effect of chromium and the iron content were also evaluated by leaching tests and pot experiments. Sedimentation tests and transport experiments indicated that nZVI @ BC, with an nZVI to BC mass ratio of 1:1, had better stability and mobility than pure nZVI. The efficiency in immobilizing Cr (VI) and total Cr was 100% and 92.9%, respectively, when the soil was treated with 8 g/kg of nZVI @ BC for 15 days. Furthermore, the remediation effectively reduced the Fe leaching caused by pure nZVI, and the pot experiments showed that the remediation reduced the phytotoxicity of Cr and leachable Fe and promoted plant growth.

Lastly, these were just some examples of studies developed using biochar as a support for nZVI, aiming to improve its properties of interest for different uses by producing this new material. A wide list of works involving the development of biochar to support nZVI can be found in reference [61].

7 Conclusions

Minerals that contain mostly iron are found in the form of oxides. Thus, it can be inferred that the exploration of these oxides to obtain iron has great economic significance, considering the high iron content (of above 62%) in their composition.

There is a wide range of methods that can be used for ZVI and/or nZVI synthesis. They can be divided into two large groups depending on the type of processing done in order to obtain the particles. They are: top-down (from top to bottom), where particles are obtained from larger (granular or microscale) materials, and bottom-up (from bottom to top), which involves the "growth" of nanostructures atom by atom or molecule by molecule. The type of method used to produce the particles directly influences their properties.

The Fe^{+3} or Fe^{+2} reduction method for the production of ZVI and/or nZVI is a typical bottom-up method. It can be carried out with different precursors and reducers, which will directly influence the morphology and size of the particles obtained. It is the method most widely used in academia due to its simplicity and the high reactivity of the particles acquired; however, it is not used for large-scale production due to the high cost of its required reagents and some technical aspects, e.g. the resulting agglomeration of nanoparticles, which directly impacts the properties of interest. For the industrial production of nZVI, methods such as grinding, chemical reduction with hydrogen gas and chemical vapor deposition are used.

Many studies have been done in order to improve the properties of nZVI produced by the most diverse methods, with respect to particle agglomeration, stability,

mobility and efficiency in different applications. Among them is the use of other materials as support for nZVI. These support materials provide the immobilization of nZVI by fixing it to their structure or imprisoning it inside their pores. This treatment corroborates the modification of the physicochemical properties of nZVI of interest in order to better accomplish its intended application.

Among many other materials, nZVI supported by biochar (nZVI/BC) is emerging as an innovative technology for the recovery of degraded soils and the treatment of contaminated industrial effluents. Biochar, depending on the pyrolysis conditions and the biomass used, has a porous structure and large surface area with a significant density of functional groups containing oxygen. Its porous structure facilitates the mass transfer from contaminants to its surface. Furthermore, it improves the electron transfer capacity of nZVI to target contaminants due to its good electrical conductivity, which qualifies it to be used as an adsorbent in the removal of organic contaminants and heavy metals.

Acknowledgements The authors would like to thank the Human Resources Program of the National Agency of Petroleum, Natural Gas and Biofuels (PRH-ANP 13.1).

References

1. Duarte, H.D.: Ferro: um elemento químico estratégico que permeia história, economia e sociedade. Quim. Nova **42**(10), 1146–1153 (2019). https://doi.org/10.21577/0100-4042.20170443
2. IBGE: Glossário geológico, p. 214. IBGE (1999)
3. de Carvalho, P.S.L., et al.: Minério de ferro. BNDES Setorial **39**, 197–234 (2014)
4. U.S. Geological Survey: Mineral commodity summaries 2021. U.S. Geological Survey, p. 200 (2021). https://doi.org/10.3133/mcs2021
5. Delbianco, J.V.T., et al.: Análise e otimização das condições operacionais de um reator de leito fixo na síntese de Fischer-Tropsch. J. Eng. Exact Sci. **3**(2), 281–293 (2017). https://doi.org/10.18540/2446941603022017281
6. Ribeiro, D.: Processo de Haber-Bosch. Rev. Ciência Elem. **1**(1), 0029 (2013)
7. Pedrosa-Soares, A.C., et al.: Recursos Minerais de Minas Gerais On Line: Síntese do conhecimento sobre as riquezas minerais, história geológica e meio ambiente e mineração de Minas Gerais. Companhia de Desenvolvimento de Minas Gerais (2018). http://www.codemge.com.br
8. Instituto Superior Técnico de Lisboa. Ferro básico. e-escola (2008). http://e-escola.tecnico.ulisboa.pt/topico.asp?id=466&ordem=4
9. Martell, A.E., et al.: Critically selected stability constants of metal complexes. College Station, 46 (1997)
10. Lide, D.R., et al.: Handbook of Chemistry and Physics, p. 2544. CRC Press (2005)
11. Ahmed, M.A., et al.: Magnetite-hematite nanoparticles prepared by green methods for heavy metal ions removal from water. Mater. Sci. Eng. B **178**(10), 744–751 (2013). https://doi.org/10.1016/j.mseb.2013.03.011
12. Oliveira, L.C.A., et al.: Óxidos de ferro e suas aplicações em processos catalíticos: uma revisão. Quím. Nova **36**(1), 23–130 (2013)
13. Pereira, W.S., et al.: Ferro zero: uma nova abordagem para o tratamento de águas contaminadas com compostos orgânicos poluentes. Quim. Nova **28**(1), 130–136 (2005)

14. International Organization for Standardization. ISO/TS 80004-1:2015: nanotechnologies: vocabulary: part 1: core terms, p. 3. International Organization for Standardization (2015). https://www.iso.org/standard/68058.html
15. Francisquini, E., et al.: Nanopartículas magnéticas e suas aplicações. In: Andrades, W.A., et al. (eds.) Química Supramolecular e Nanotecnologia, p. 269 (2014)
16. Ibiapino, A.L., et al.: Síntese e caracterização de CaZrO3 e BaZrO3 nanoestruturados. Quim. Nova **36**(6), 762–767 (2013). https://doi.org/10.1590/S0100-40422013000600003
17. Crane, R.A., et al.: Nanoscale zero-valent iron: future prospects for an emerging water treatment technology. J. Hazard. Mater. **211–212**, 112–125 (2012). https://doi.org/10.1016/j.jhazmat.2011.11.073
18. Thomé, A., et al.: Review of nanotechnology for soil and groundwater remediation: Brazilian perspectives. Water Air Soil. Pollut. **226**, 121, (2015). https://doi.org/10.1007/s11270-014-2243-z
19. Gillham, R.W., et al.: Enhanced degradation of halogenated aliphatics by zero-valent iron. Ground Water **32**, 958–967 (1994)
20. Fu, F., et al.: The use of zero-valent iron for groundwater remediation and wastewater treatment: a review. J. Hazard. Mater. **267**, 194–205 (2014). https://doi.org/10.1016/j.jhazmat.2013.12.062
21. Keane, E.: Fate, Transport, and Toxicity of Nanoscale Zero-valent Iron (nZVI) Used During Superfund Remediation, p. 38. Duke University (2009)
22. Li, X.-Q., et al.: Zero-valent iron nanoparticles for abatement of environmental pollutants: materials and engineering aspects. Crit. Rev. Solid State Mater. Sci. **31**(4), 111–122 (2006). https://doi.org/10.1080/10408430601057611
23. Tratnyek, P.G., et al.: Nanotechnologies for environmental cleanup. Nano. Today **1**(2), 44–48 (2006). https://doi.org/10.1016/S1748-0132(06)70048-2
24. Mukherjee, R., et al.: A review on synthesis, characterization, and applications of nano zero valent iron (nZVI) for environmental remediation. Crit Rev. Environ. Sci. Technol. **46**(5), 443–466 (2016). https://doi.org/10.1080/10643389.2015.1103832
25. Henry, S.M., et al.: Chlorinated solvent and DNAPL remediation: innovative strategies for subsurface cleanup, p. 346. American Chemical Society (2003)
26. O'Carroll, D., et al.: Nanoscale zero valent iron and bimetallic particles for contaminated site remediation. Adv. Water Resour. **51**, 104–122 (2013). https://doi.org/10.1016/j.advwatres.2012.02.005
27. Remillard, S.C., et al.: The use of nanoscale zero valent iron for environmental remediation: benefits and possible pitfalls. TechConnect Br. **3**, 524–527 (2010)
28. Chekli, L., et al.: Analytical characterisation of nanoscale zero-valent iron: a methodological review. Anal. Chim. Acta **903**, 13–35 (2016). https://doi.org/10.1016/j.aca.2015.10.040
29. Manfrona, S., et al.: Aplicação de nanopartículas de ferro zero-valente (nFeZ) na remediação de solos e águas subterrâneas contaminadas: uma revisão. Quim. Nova **43**(5), 623–631 (2020). https://doi.org/10.21577/0100-4042.20170523
30. Suna, Y.-P., et al.: Characterization of zero-valent iron nanoparticles. Adv. Colloid Interface Sci. **120**(1–3), 47–56 (2006). https://doi.org/10.1016/j.cis.2006.03.001
31. Li, S., et al.: Solvent-free production of nanoscale zero-valent iron (nZVI) with precision milling. Green Chem. **11**(10), 1618–1626 (2009). https://doi.org/10.1039/B913056J
32. Khan, I., et al.: Nanoparticles: properties, applications and toxicities. Arab. J. Chem. **12**(7), 908–931 (2019). https://doi.org/10.1016/j.arabjc.2017.05.011
33. Jamei, M.R., et al.: A novel ultrasound assisted method in synthesis of NZVI particles. Ultrason. Sonochem. **21**(1), 226–233 (2014). https://doi.org/10.1016/j.ultsonch.2013.04.015
34. Puthukkara, A.R., et al.: Plant mediated synthesis of zero valent iron nanoparticles and its application in water treatment. J. Environ. Chem. Eng. **9**(1), 104569 (2021). https://doi.org/10.1016/j.jece.2020.104569
35. Phenrat, T., et al.: Nanoscale zerovalent iron (NZVI) for environmental decontamination: a brief history of 20 years of research and field-scale application. In: Nanoscale Zerovalent Iron Particles for Environmental Restoration: From Fundamental Science to First Scale Engineering Applications, p. 597. Springer (2019). https://doi.org/10.1007/978-3-319-95340-3

36. Oppegard, A.L., et al.: Magnetic properties of single-domain iron and iron-cobalt particles prepared by borohydride reduction. Int. J. Appl. Phys. **32**, S184 (1961)
37. Wang, C.B., et al.: Synthesizing nanoscale iron particles for rapid and complete dechlorination of TCE and PCBs. Environ. Sci. Technol. **31**(7), 2154–2156 (1997). https://doi.org/10.1021/es970039c
38. Sun, Y.-P., et al.: Characterization of zero-valent iron nanoparticles. Adv. Colloid Interface Sci. **120**(1–3), 47–56 (2006). https://doi.org/10.1016/j.cis.2006.03.001
39. Singh, R., et al.: Removal of Cr(VI) by nanoscale zero-valent iron (nZVI) from soil contaminated with tannery wastes. Bull. Environ. Contam. Toxicol. **88**, 210–214 (2012). https://doi.org/10.1007/s00128-011-0425-6
40. Boparai, H.K., et al.: Cadmium (Cd^{2+}) removal by nano zerovalent iron: surface analysis, effects of solution chemistry and surface complexation modeling. Environ. Sci. Pollut. Res. **20**, 6210–6221 (2013). https://doi.org/10.1007/s11356-013-1651-8
41. Xiaoyuan, L., et al.: Critical roles of sulfidation solvent in controlling surface properties and the dechlorination reactivity of S-nZVI. J. Hazard. Mater. **417**, 126014 (2021). https://doi.org/10.1016/j.jhazmat.2021.126014
42. Mdlovu, N.V., et al.: Synthesis, characterization, and application of zero-valent iron nanoparticles for TNT, RDX, and HMX explosives decontamination in wastewater. J. Taiwan Inst. Chem. Eng. **114**, 186–198 (2020). https://doi.org/10.1016/j.jtice.2020.08.036
43. Rónavári, A., et al.: Impact of the morphology and reactivity of nanoscale zero-valent iron (NZVI) on dechlorinating bacteria. Water Res. **95**, 165–173 (2016). https://doi.org/10.1016/j.watres.2016.03.019
44. Visentin, C., et al.: Nano scale zero valent iron production methods applied to contaminated sites remediation: an overview of production and environmental aspects. J. Hazard. Mater. **410**, 124614 (2021). https://doi.org/10.1016/j.jhazmat.2020.124614
45. Wang, W., et al.: Application of weak magnetic field coupling with zero-valent iron for remediation of groundwater and wastewater: a review. J. Clean. Prod. **262**, 121341 (2020). https://doi.org/10.1016/j.jclepro.2020.121341
46. Li, L., et al.: Synthesis, properties, and environmental applications of nanoscale iron based materials: a review. Crit. Rev. Environ. Sci. Technol. **36**(5), 405–431 (2006). https://doi.org/10.1080/10643380600620387
47. Stefaniuk, M., et al.: Review on nano zerovalent iron (nZVI): from synthesis to environmental applications. Crit. Rev. Environ. Sci. Technol. **287**, 618–632 (2016). https://doi.org/10.1016/j.cej.2015.11.046
48. Khayam, S.U., et al.: Development and characterization of a novel hybridmagnetorheological elastomer incorporating micro and nano size iron fillers. Mater. Des. **192**, 108748 (2020). https://doi.org/10.1016/j.matdes.2020.108748
49. Hoch, L.B., et al.: Carbothermal synthesis of carbon-supported nanoscale zero-valent iron particles for the remediation of hexavalent chromium. Environ. Sci. Technol. **42**(7), 2600–2605 (2008). https://doi.org/10.1021/es702589u
50. Dai, Y., et al.: Carbothermal synthesis of ordered mesoporous carbon-supportednano zero-valent iron with enhanced stability and activity for hexavalent chromium reduction. J. Hazardous Mater. **309**, 249–258 (2016). https://doi.org/10.1016/j.jhazmat.2015.04.013
51. Chen, S.-S., et al.: A new method to produce nanoscale iron for nitrate removal. J. Nanopart. Res. **6**(6), 639–647 (2004). https://doi.org/10.1016/j.ultsonch.2013.04.015
52. Wang, Q., et al.: Controllable synthesis, characterization, and magnetic properties of nanoscale zerovalent iron with specific high Brunauer-Emmett-Teller surface area. J. Nanopart. Res. **11**, 749–755 (2009). https://doi.org/10.1007/s11051-008-9524-7
53. Yoo, B.-Y., et al.: Electrochemically fabricated zero-valent iron, iron-nickel, and iron-palladium nanowires for environmental remediation applications. Water Sci. Technol. **55**(1–2), 149–156 (2007). https://doi.org/10.2166/wst.2007.017
54. Scott, T.B., et al.: The effects of vacuum annealing on the structure and surface chemistry of iron nanoparticles. J. Nanopart. Res. **12**, 1765–1775 (2010). https://doi.org/10.1007/s11051-009-9732-9

55. Nurmi, J.T., et al.: Characterization and properties of metallic iron nanoparticles: spectroscopy, electrochemistry, and kinetics. Environ. Sci. Technol. **39**(5), 1221–1230 (2005). https://doi.org/10.1021/es049190u
56. Li, Z.-J., et al.: Efficient removal of uranium from aqueous solution by zero-valentiron nanoparticle and its graphene composite. J. Hazard. Mater. **290**, 26–33 (2015). https://doi.org/10.1016/j.jhazmat.2015.02.028
57. Lin, K.-S., et al.: Degradation of TCE, PCE, and 1,2-DCE DNAPLs in contaminated groundwater using polyethylenimine-modified zero-valent iron nanoparticles. J. Clean. Prod. **175**, 456–466 (2018). https://doi.org/10.1016/j.jclepro.2017.12.074
58. Shih, Y.-H., et al.: Pentachlorophenol reduction by Pd/Fe bimetallic nanoparticles: effects of copper, nickel, and ferric cations. Appl. Catal. B. **105**(1–2), 24–29 (2011). https://doi.org/10.1016/j.apcatb.2011.03.024
59. Li, Y., et al.: Stabilization of Fe^0 nanoparticles with silica fume for enhanced transport and remediation of hexavalent chromium in water and soil. J. Environ. Sci. (China) **23**(7), 1211–1218 (2011). https://doi.org/10.1016/s1001-0742(10)60534-7
60. Chun, Y., et al.: Compositions and sorptive properties of crop residue-derived chars. Environ. Sci. Technol. **38**(17), 4649–4655 (2004). https://doi.org/10.1021/es035034w
61. Wang, S., et al.: Biochar-supported nZVI (nZVI/BC) for contaminant removal from soil and water: a critical review. J. Hazard. Mater. **373**, 820–834 (2019). https://doi.org/10.1016/j.jhazmat.2019.03.080
62. Zhou, Y., et al.: Biochar-supported zerovalent iron for removal of various contaminants from aqueous solutions. Bioresour. Technol. **152**, 538–542 (2014). https://doi.org/10.1016/j.biortech.2013.11.021
63. Yan, J., et al.: Biochar supported nanoscale zerovalent iron composite used as persulfate activator for removing trichloroethylene. Bioresour. Technol. **175**, 269–274 (2015). https://doi.org/10.1016/j.biortech.2014.10.103
64. Zhang, Y., et al.: One-step synthesis of biochar supported nZVI composites for highly efficient activating persulfate to oxidatively degrade atrazine. Chem. Eng. J. **420**(1), 29868 (2021). https://doi.org/10.1016/j.cej.2021.129868
65. Wei, G., et al.: Nanoscale zero-valent iron supported on biochar for the highly efficient removal of nitrobenzene. Environ. Sci. Eng. **13**(4), 61 (2019). https://doi.org/10.1007/s11783-019-1142-3
66. Han, L., et al.: Biochar supported nanoscale iron particles for the efficient removal of methyl orange dye in aqueous solutions. PLoS ONE **10**(7), e0132067 (2015). https://doi.org/10.1371/journal.pone.0132067
67. Liu, Z., et al.: Nano-zerovalent iron contained porous carbons developed from waste biomass for the adsorption and dechlorination of PCBs. Bioresour. Technol. **101**(7), 2562–2564 (2010). https://doi.org/10.1016/j.biortech.2009.11.074
68. Dong, Y., et al.: Application of low-cost Fe-based catalysts in the microwave-assisted pyrolysis of macroalgae and lignocellulosic biomass for the upgradation of bio-oil. Fuel **300**, 20944 (2021). https://doi.org/10.1016/j.fuel.2021.120944
69. Su, H., et al.: Stabilisation of nanoscale zero-valent iron with biochar for enhanced transport and in-situ remediation of hexavalent chromium in soil. Environ. Pollut. **214**, 94–100 (2016). https://doi.org/10.1016/j.envpol.2016.03.072

Nanosensors in Forensic Sciences

Gisele Inês Selli, Anne Esther Targino Bonatto, Fernando Targino Bonatto, Michel Jose Anzanello, and Carlos Pérez Bergmann

Abstract The sensors are powerful tools for the detection of illicit substances. The application and development of sensors have attracted tremendous attention in the last few years. This fever for the development of new detectors can be attributed to the lack of an efficient device that brings to the analyst all the required properties, likewise, low-cost production, portable or on-site analysis, instrumental simplicity, reliability, and accurate results. The present chapter outlines the application of sensors in forensics sciences, bringing to the reader recent reviews and papers. It also reports the main differences among the three big classes of sensors, the chemical, biological, and optical sensor, and offers insights into the future perspectives of these sensing materials

Abbreviations

DNA	Deoxyribonucleic acid
DNT	Dinitrotoluene
IUPAC	International Union of Pure and Applied Chemistry
SERS	Surface-enhanced Raman scattering
SEM	Scanning electron microscope
TEM	Transmission electron microscope
TNT	Trinitrotoluene
UV-vis	Ultraviolet-visible

G. I. Selli (✉) · A. E. T. Bonatto · F. T. Bonatto · M. J. Anzanello · C. P. Bergmann
Av. Osvaldo Aranha, 99 sala 709, Porto Alegre-RS 90035-190, Brazil

A. E. T. Bonatto
e-mail: anne.targino@ufrgs.br

C. P. Bergmann
e-mail: bergmann@ufrgs.br

A. Kopp Alves (ed.), *Environmental Applications of Nanomaterials*, Engineering Materials, https://doi.org/10.1007/978-3-030-86822-2_13

1 Introduction

The sensors are characterized as devices used for the detection of specific substances. These devices can perform detection, measurement of different physical properties (such as mass and temperature), and sensing of electrical or optical properties of materials [1–3]. The sensing is realized by the production of a measurable signal, which depending on the sensor, will be generated and interpreted in different ways [3, 4].

Since the second half of the twentieth century, sensors have become a key part of everyday life [5]. One of the first devices developed with this technology was the glucose test [3] and the pregnancy or fertility test for women [6, 7]. The increasing advancement of technology and miniaturization of materials provide an enhancement of nanosensors' role in the sensing field. Similar in some characteristics to macro sensors, on the other hand, nanosensors should contain at least one of their dimensions smaller than 100 nm. Due to the extremely small size, large surface area, and excellent reactivity, the detection of different materials on the nanoscale becomes possible. The potential application and multi-functionality of these nanomaterials mean that the number of researches and the consequent use of these devices in the sensing field has increased exponentially in the last years [1, 8–13].

Forensic science, due to its judicial importance, is a field that mistakes cannot be tolerated. The materials applied for analysis, likewise, fingerprint detection, biological fluids, DNA, narcotics, poisons, and explosives, must present high specificity and precision [1, 9]. To obtain results with the required accuracy, several laboratories have invested in the use of analytical techniques and nanomaterials [8, 9, 14, 15]. The application of nanosensors allows them to be used in the crime scene, as in the case of fingerprint detection [8, 16], or even the use of biosensors for drug detection [17–19] and explosives [20–22].

This chapter aims to provide a brief literature review on the application of nanosensors in different areas of forensic science. The chapter is divided into classes of sensors starting with chemicals sensors, after that, biological and ends with optical sensors.

2 Definition of Nanosensors

To be classified as a nanosensor, the device must have two main components, the material that will have the detection properties and a transducer that have as aim to receive a measurable signal. The material responsible for the detection interacts with different external stimuli; these include temperature and pressure exchange, electric signal and formation of a chemical bond and/or biological reactions, and others. The different reactions, generally, lead to change in one or more of the intrinsic properties of the material, which are then transformed into measurable signals and sent to the transducer [3, 5]. This is the general operation mechanism of nanosensors. But, each

class of these nanomaterials has its particularities, which will be explored in the following topics.

3 Chemical Sensors

The Chemical sensors are defined by IUPAC as "Devices or instruments capable of performing detection by converting a chemical or physical property of a specific analyte into a measurable signal, whereby the magnitude is directly related to the concentration of the analyte". Figure 1 demonstrates the architecture of a chemical sensor [23].

The nanosensors, next to specific compounds or ions, can provide real-time and online results. The main characteristics are low cost and portability for the analysis field. The potential of these materials allows them to be applicable in different areas of our everyday life, as seen in Fig. 2. Chemical detection has gained a significant role in forensics sciences and allows the detection of various substances in forensics such as poisons, drugs, explosives, gunshot residues, and fingerprints detection [7, 14, 24, 25].

The use of nanomaterials in forensics has been the subject of a lot of researches and the development of new devices. This growing number of studies and patents can

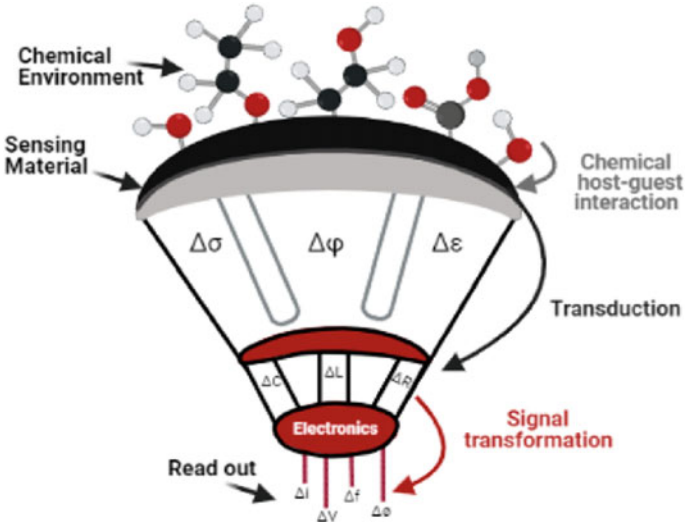

Fig. 1 Chemical structure of sensor. In the first stage, analytes interact with the sensing material changing some of its properties, likewise, temperature (ΔT), mass ΔM, conductivity (Δσ), work function (ΔΦ), refractive index(Δn), permittivity (Δε). In the second stage the transducer make your work, converting some of physical properties into the variation of its electric parameter. In the end, the circuit gives rise to the sensing signal. (Adapted with permission from Ref. [5] Copyright 2021 American Chemical Society)

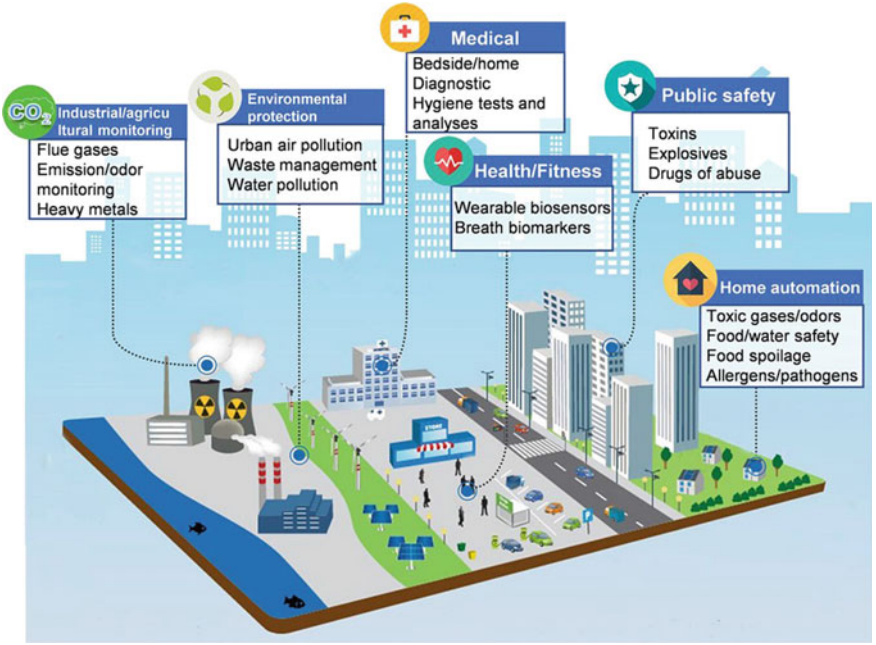

Fig. 2 The application of Chemical sensors in our everyday life (Adapted with permission from Ref. [5] Copyright 2021 American Chemical Society)

be attributed to the versatility of these nanomaterials and the possibility of detection in concentrations that were not even considered. A review about the explosives in trace detection is presented by To, K. C. [13]. According to To, K. C. [13], the use of technologies to detect explosives in trace amounts play a vital role in hold on national security. In this review, the author highlights the use of nanostructured semiconductors as chemical sensors and classifies them according to chemical composition: composites, carbon-based, plasmonic, quantum dots, and semiconductors. Using p-type and n-type semiconductors, such as TiO_2, ZnO, Sn_2O, Cu_2O, the author mentions different studies that attribute the rapid response of these compounds to properties such as improved charge transfer. The presented results are meaningful for the forensic sciences field. Nevertheless, the author reports Qu [26] research, which developed a chemiresistive sensor for detection of trinitrotoluene (TNT), dinitrotoluene (DNT), 2,4,6-trinitrophenol (TNP), 1,3,5-trinitroperhydro-1,3,5-triazine (RDX) and ammonium nitrate (AN).

It is possible to note a large number of references reporting the use of plasmonic materials such as gold (Au) [27] and silver(Ag) [10] for explosives detection. According to Muehlethaler, C. [12], plasmonic materials provide on their surface a large amount of active binding sites that exhibit affinity for the chemical groups present in explosives. The Nitroaromatics TNT or DNT can be cited as examples of explosives with a great affinity for gold. These Nitro compounds, through bonds

with the oxygen atoms (present in their structure), form a bidentate chelate complex with the metal surface.

In the study conducted by Squire [27], it is possible to understand the synthesis of a sensor containing silica and gold in a core–shell structure, applied for detection of vapor DNT. The compound detected trace amounts of the explosive in the order of 100 ppm. Also, according to the author, this detection occurred within 3 min at room temperature [27]. Results like these clearly show the potential application of these materials as sensors for the detection of vapor explosives. Figure 3 outlines the synthesis process and results obtained by Squire, K. J [27].

The use of illicit drugs is a big problem for public health worldwide. Due to the devastating effects of these substances, take action to prevent the transportation, sold, and being able to trace their origin is extremely important. In this context, it is correct to say that the investigation and detection of drugs is one of the main areas for investigators and scientists linked to the forensic sciences [8, 12, 28–31].

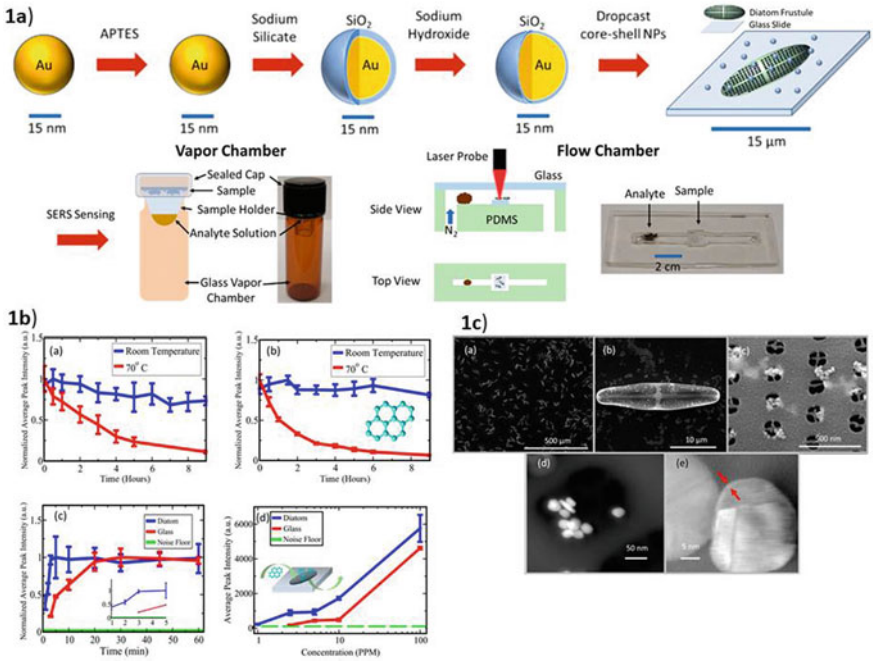

Fig. 3 1**a** Schematic diagram of sensor synthesis containing synthesis Au@SiO_2 core—hell NPs. 1**b** The results of time-dependent desorption analysis **a** with substrate and **b** without substrate at room temperature and at 70 °C. **c**–**d** Average peak intensity in relation to analyte concentration is plotted to show the concentration dependence with a diatom—apor interaction. 1**c** SEM pictures of SERS substrate with core–shell and frustule structure shown at different magnifications **a**–**c**. TEM pictures of NPS in a frustule pore **d** and core—hell structure with arrows highlighting the shell **e**. (Adapted with permission from Ref. [27]. Copyright 2020 American Chemical Society)

The development of sensors that are easy to use, have high-throughput, on-site, and fast has been the focus of the scientific community. Furthermore, Nanomaterials with a chemical affinity for these drugs have been explored in researches, as seen in research conducted by Minhas [29]. The Minhas [29], have demonstrated the detection of illicit performance-enhancing substances in athletes. Using biological matrices and the device compound of nanostructured silicon, the samples were submitted for analysis with a mass spectrometer (SALDI-MS). The results obtained were compared with other analytical methods and showed a better performance. As seen in Fig. 4 (adapted from Ref. [29]), a schematic illustration show the steps for the development of a new device. Also in Fig. 4b is the analysis mechanism for the detection of banned substances in biological samples belonging to athletes.

Other studies that report the detection of illicit drugs using chemical sensors, and it is worth highlighting, are those developed by Akhoundian [30] and Parrilla [31].

The first author [30] developed a method for trace amounts detection of methamphetamine using Fast Fourier Transform Square Wave Voltammetric (FFT-SWV) and a Molecularly Imprinted Polymer (MIP)/multi-walled carbon nanotube (MWCNTs)-Modified Carbon Paste Electrode. The nanopolymer was synthesized using the polymer precipitation method. Furthermore, the sensor was tested with human blood and urine. The results obtained for experimental conditions resulted in a linear response range of 1.0×10^{-8}–1.0×10^{-4} mol L^{-1} and a detection limit of 8.3×10^{-10} mol L^{-1}. According to the author, the detection limit was the lowest ever reported. The development of this sensor provides an important tool to detect methamphetamine in human blood and urine in a quickly and accurately way. On the other hand, Parrilla

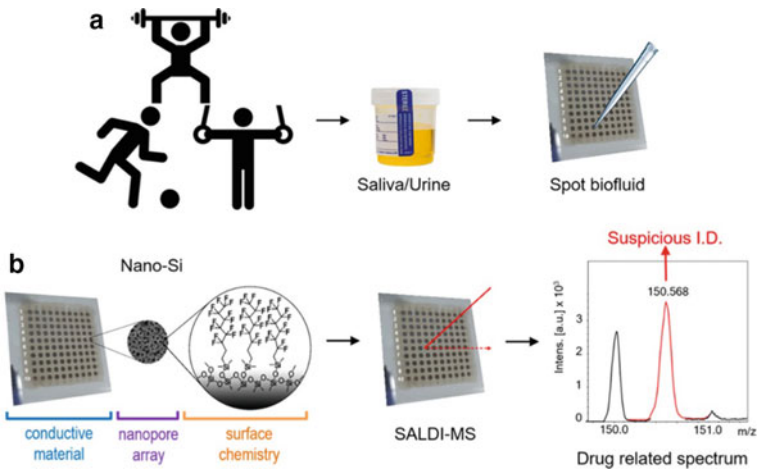

Fig. 4 Scheme of the Testing Procedure for Athlete Doping: **a** The biological samples (Saliva/Urine) are obtained from an Athlete and then spotted onto a Nano-Si Surface, Tailored for Doping Detection. **b** Samples are analyzed with Nano-Si SALDI-MS and the results indicate the presence or no of an Adverse Analytical Finding (AAF). (Adapted with permission from Ref. [29] Copyright 2020 American Chemical Society)

[31] developed a sensor for the detection of amphetamines in samples seized by the police, using voltammetric oxidation of a derivatized compound on a graphite screen-printed electrode. The results exhibit the efficiency of the sensor and its potential to quantify amphetamines in 20 seized samples in approximately 3 min. Figure 6 shows some of the results obtained by analyzing Fig. 5.

The researches presented here explore the development of new chemical devices with some properties, such as high-throughput, real-time analysis, which are essential characteristics for sensors used in the forensic area.

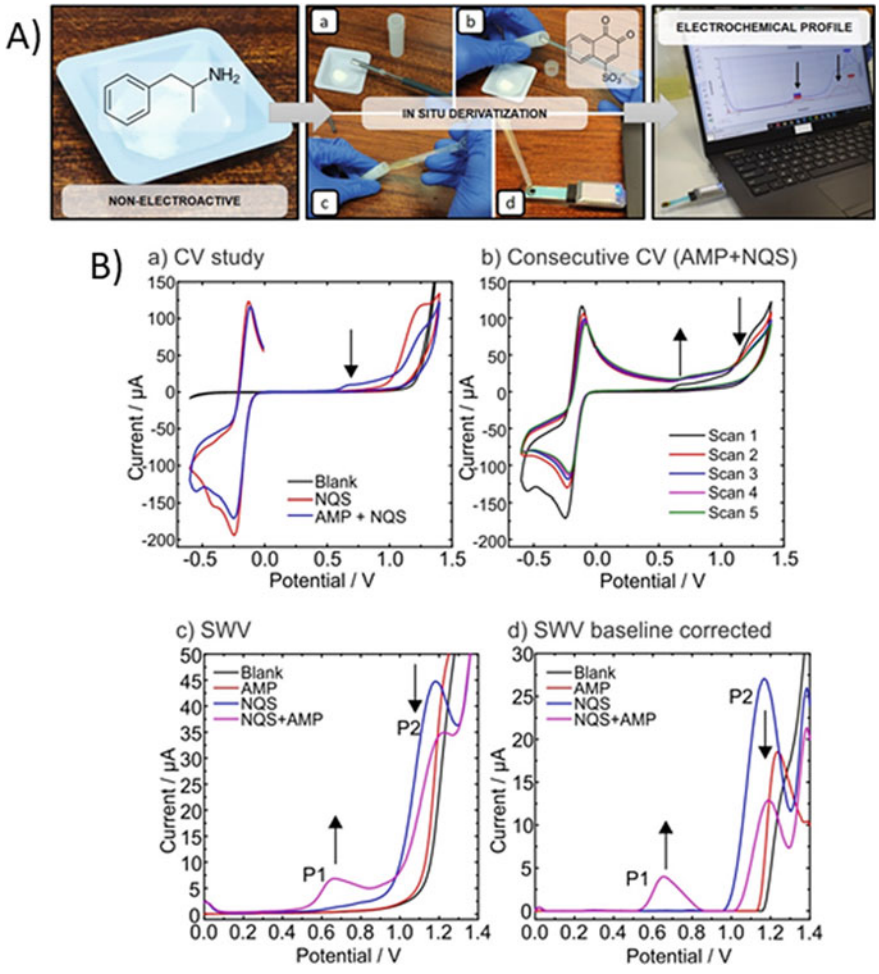

Fig. 5 **a** Schematics of the concept for the on-site screening of Amphetamine. **b** The electrochemical essays of the sensing method to detect Amphetamine at graphite screen-printed electrodes. (Reproduced with permission from Ref. [31])

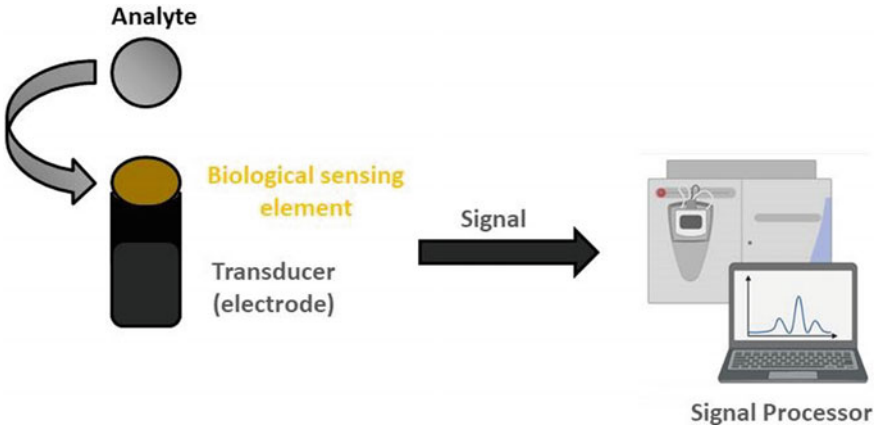

Fig. 6 The schematic structure of biosensor with electrochemical transducer. (Created with biorender. itens)

As seen in this section, there are several studies that address the development of chemical sensors for explosives and illicit drugs detection. Many sensors have multimodal detection properties as a chemical with biological and/or optical. However, when the sensor presents conjugation of biomolecules, antibodies, aptamers, enzymes, and other biological species, the correct classification of sensors is a biosensor that has been widely used.

4 Biosensors

Biosensors are composed of biological sensing receptors (which can be: enzymes, proteins, aptamers, antibodies, nucleic acids, cells, or tissues), a transducer, and a detector (Fig. 6). The target analyte binds to biological receptors and produces a measurable signal that is directly related to the concentration of the target under investigation. Nanostructured biosensors have as an advantage accurate analysis with a minimum amount of sample and the possibility of detection in highly complex matrices such as body fluids and environmental samples [7, 32].

It is possible to cite different references that report the development and application of nanobiosensors as a potential tool for detection of explosives [13, 33]; illicit drugs [32, 34]; body fluids [35, 36] at crime scenes, among others. In this section, we will explore a little more about biosensors and their applications.

Body fluids are complex matrices; however, the amount of relevant information that can be extracted and the abundance of these samples at crime scenes make them the object of many types of research that focus on nanobiosensores synthesis, like the study developed by Li et al. [35] that used human saliva.

Saliva is an important tool at crime scenes because it allows the association between victim and suspect. Based on the quantity of information that can be found in this fluid the author proposes the development of a multimodal sensor for the detection of two classes of bacteria using a smartphone as a platform and human saliva for sampling. This sensor was developed using silicon-carbide quantum dots with blue fluorescence and gold nanoclusters with red fluorescence to develop a series of test strips.

According to the results, when the strips were exposed to a solution of bacteria (of the species S. salivarius and S. sanguinis) was verified the color change under 365 nm UV light. This change of color was collected using a smartphone camera and analyzed by the app. The app idea is collect the color change and generate the result, according to the number of bacteria present in saliva. In Fig. 7 (reproduced with permission of the author), the scheme with procedures performed for simultaneous detection of S. salivarius and S. sanguinis in the saliva is based on the sensing platform using the smartphone [35].

Sweat is an interesting biological fluid that shows as advantages your non—invasive nature. In the study developed by Xue [34], sweat was used to verify the performance of biosensor. The researchers prepared a sensor based on a microfluidic capillary array combine with a competitive enzyme-linked immunosorbent assay (ELISA protocol). This device allows the quantitative, quick, and accurate detection of illicit substances. The results demonstrated the potential of the sensor for detection of 4 drugs of abuse (Methadone, Methamphetamine, Amphetamine, and Tetrahydro-Cannabinol (THC)) in artificial sweat. According to the author, the sensor showed an excellent specificity concerning to cross-reactivity, with values lower than 1%. Furthermore, in approximately 16 min and with only 4 μL of each drug, all the desired results were obtained. The estimated detection limits for the sensor were: 1.6 pg mL^{-1} for Methadone, 142 pg mL^{-1} for Methamphetamine, 35 pg mL^{-1} for

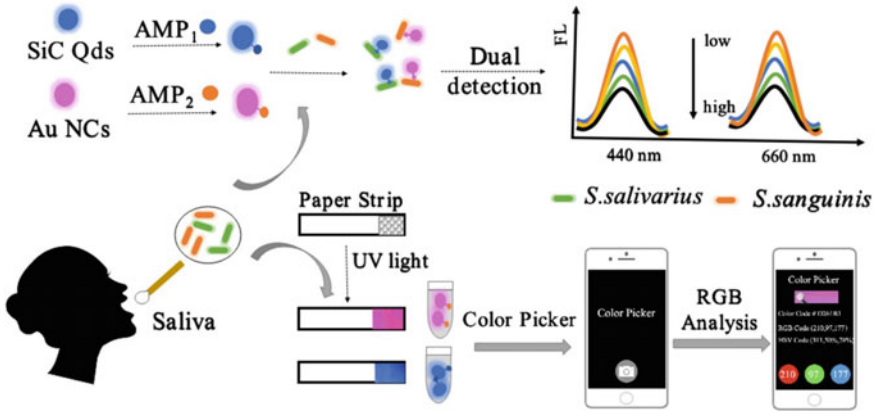

Fig. 7 Scheme showing the working of simultaneous detection of S. salivarius and S. sanguini in saliva, applying the smartphone as sensing platform. (Reproduced with permission from Ref. [35])

Amphetamine, and 20 pg mL^{-1} for THC. The results were excellent, demonstrating the accuracy of the method since others presented in the literature exhibit a range of 100–1000 pg mL^{-1} [34].

The detection of illicit substances is a challenge for border security professionals because many of these compounds have low vapor pressure, and the concentrations in vapor are extremely low. Moreover, in order the organizations hide the substances in boxes with complex odors, confusing the more accurate detection systems. However, one of the main problems related to the existing detection systems is the occurrence of many false—positives results and extremely high maintenance and purchase prices.

In this context, Scorsone [37] has selected several Ligand Binding Proteins (LBPs) and integrated them into a nanodiamond transducer coated with acoustic surface waves with the aim to develop a biosensor array. The biosensor arrays have been used for the detection of explosives and illicit drugs, which exhibit a high affinity for proteins. According to the results, a linear response over the range of ppb—ppm concentrations values was observed. Furthermore, using Principal Component Analysis, the sensor was able to discriminate among different explosives and narcotics. The developed biosensor showed a higher affinity for Nitroaromatic compounds than for narcotics. According to the author, bioelectronics noses are seen as an important tool to overcome existing challenges in current detection systems.

As can be seen, biosensors provide analysis with exceptional specificity and sensitivity for explosives through the use of antibodies, aptamers, and molecularly imprinted polymers. A review that addresses the state of the art and future trends for the development of biosensors for explosives detection is the one prepared by Liu [38]. During the review different studies are referenced; among them, we can mention one that uses aptamer composite sensors for TNT detection. The study developed by Kong [39]., reports the development of a chemiluminescent biosensor composed of magnetic beads incorporating Co^{2+} and N-(4-aminobutyl)-N-ethyl isoluminol with magnetic properties. The TNT aptamer was attached to the composite surface via electrostatic interactions and coordination interactions between the TNT aptamer and Co^{2+}. This interaction resulted in a decrease in the chemiluminescence intensity of the compound. According to the author, this quenching effect may be due to effects in the catalytic site of Co^{2+} being blocked by the TNT-aptamer peptide, thus leading to a reduction in fluorescence intensity. Finally, the biosensor was able to detect TNT in the range of 0.05–25 ng/ mL with a detection limit of 17 pg/mL. We can see in Fig. 8 the schematic diagram of the biosensor and the comparison of the luminescence curves of the compound according to the synthesis steps [38, 39].

From perspectives, the author points out that, unfortunately, there isn't still on the market a sensor that combines all the required properties such as low detection limit, stand-off distance, high selectivity, and portability in a single device. But, the future of these materials is very promising due to the quick development of both technologies that improve the sensing and progress in the biological area [38].

This chapter demonstrates the potential and different applications of biosensors. Furthermore, we present the different characteristics of biosensors and the possibility of enhancing the performance of the devices tunning the properties. It can also be seen

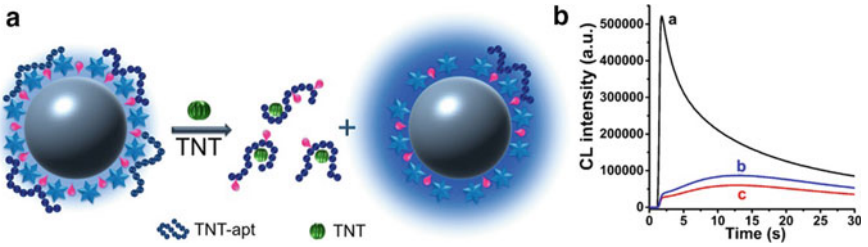

Fig. 8 **a** Scheme illustrating of the proposed label-free aptasensor for TNT. **b** Comparison of kinetic curves in different moments of compound synthesis. (Reproduced with permission from Ref. [38, 39])

that the response of biosensors will be controlled by reaction kinetics, transduction reactions, or mass transfer rates.

In the following sections, we will present a little more about optical sensors. As demonstrated in the other sections of the chapter, combined with different sensors, optical sensors play a vital role in the forensic area.

5 Optical Sensing

Optical sensors have played an important role in forensic science due to their sensitivity, fast detection, and easy operation [40]. Moreover, this sensor exhibits great ease of interaction between substances and elements with sensory properties, providing important information through easy and low-cost processes [41]. There are different methods for detection analysis using optical sensors, such as fluorescence, colorimetry, chemiluminescence, surface-enhanced Raman scattering (SERS), and immune chromatographic assays (ICAs). Its structure is similar to another sensor reported in this chapter, but it consists of a transducer that captures the signal and converts it into different radiations [41].

Optical sensors are mainly obtained with straightforward synthesis methods, as reported by Lantam [42], who developed a sensor employing the Sol–Gel method for promethazine detection in lean cocktail and pharmaceutical dosages. The working process of the sensor is attributed to the oxidation reaction of promethazine caused by potassium persulfate entrapped within a sol–gel polymer network. The reaction leads to a color change to pinkish-red in the aqueous medium. Although the color change is visible, allowing qualitative analysis to obtain more accurate and quantitative data, the sample was analyzed with a portable spectrometer. As related by the author, the device was successful in being developed at low cost, easy to use, and portable. The limits of detection and quantification obtained were 16.5 and 48.9 mg L^{-1}, respectively. The accuracy of the promethazine detection analysis was in the range of 87–105%, and the device showed stability of 90 days. One of the significant advantages of this sensor is that it allows qualitative and quantitative analysis of the

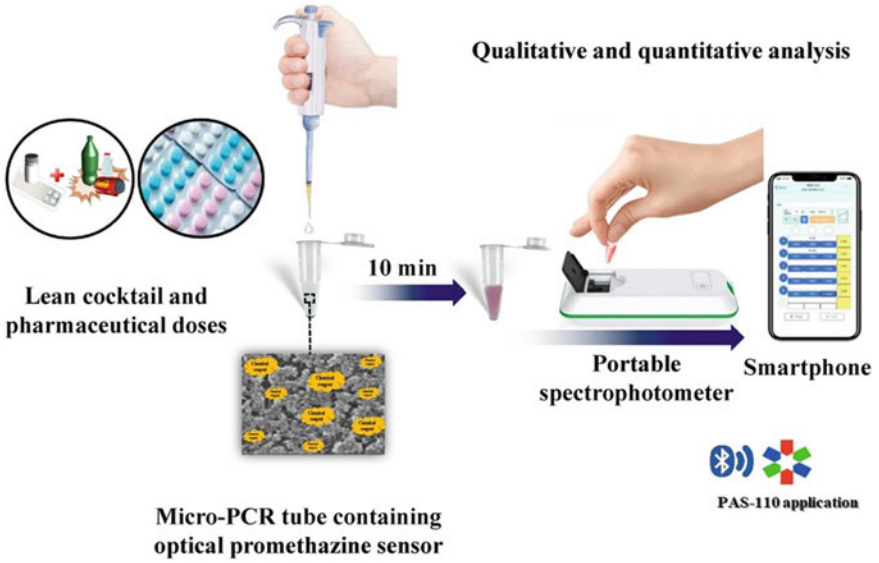

Fig. 9 Schematic illustration of device development for promethazine detection, using a portable spectrometer. (Reproduced with permission of Ref. [42])

target molecule [42]. Figure 9, adapted from Ref. [42] illustrates the method to obtain the presented results.

Another method of analysis using optical sensors that have been widely applied is Surface Enhanced Raman Spectroscopy (SERS). As can be seen in this chapter, they are associated with different sensors, such as chemical and biological. Materials with SERS properties enhance the characteristics of Raman spectroscopy [9]. The enhancement is due to their ability to form a localized plasmonic surface, that's improves the Raman signal by factors [9] of 10^3 to 10^6.

Different researches are presented in the literature reporting about the application of SERS for the detection of illicit substances, mainly drugs, such as methamphetamine [9, 41, 43–45] and explosives [13, 46, 47]. The author Khorablou [41] shows a review, which describes some advances in the development of optical and electrochemical sensors for Methamphetamine detection. The review brings us the main methods to realize detection with optical sensors, likewise: fluorescence, colorimetry, SERS, and ICAs. According to Khorablou [41], sensors that present SERS properties have shown optimal performance in the detection of illicit substances due to ease of sampling and to being a non-destructive method.

Concerning the materials engineering area properties, the author Khorablou, presents important studies, such as, carried out by Hong [44] e Mao [45]. Both studies bring different insights for sensor development.

Optoplasmonic materials are composed of materials with photonic and plasmonic properties. Its main function is to improve plasmonic properties. Based on this factor,

Hong [44], developed a study aiming to apply self-assembled optoplasmonic structures as a substrate for trace detection of methamphetamine. The depositions of microspheres consisting of dielectric material and self-assembly of monolayers of gold nanoparticles were used to obtain the sensor. The synthesis process aims to improve the intensity of electric (E-) field localization and redirect the analyte to areas close to electromagnetic hot-spots. Different simulations and measurements using SERS spectroscopy were performed by the author to verify the reliability of the material. As seen in the study, great results were obtained as the performance of SERS material by using 5 μm diameter SiO_2 spheres. Furthermore, the detection of Methamphetamine in biological fluids and concentrations in the nanomolar range was possible [44].

On the other hand, Mao [45], developed a novel nanosensor based on aligner mediated cleavage (AMC) for methamphetamine detection. The operation is based on several specific breaking sequences of the aptamer bound to gold nanoparticles, causing aggregation of nanoparticles and consequently, generating a plasmonic coupling effect. According to the results obtained, it was possible to enhance the electric field and improve the SERS effect. A detection limit of 7 pM and a linear range of 10 pM–10 nM were obtained. The author also provides a table with the association of existing methods, demonstrating the potential of the presented [45]. Figure 10 shows a schematic illustration with synthesis steps and operation of the developed sensors.

Finally, the author compares the advantages and disadvantages of optical and electrochemical sensors; and highlights some lacks that still need to be overcome in the development of sensors for methamphetamine detection [41].

Optical sensors have been widely used in different analyses, but they present some disadvantages such as susceptibility to environmental interference and complexity depending on the method used. However, it has advantages such as being inert and being portable [41].

6 Conclusions

In summary, reviews of articles have been presented to provide for readers different applications of sensors in forensics science. There are many materials under development, many features that still need to be improved, but this area has a bright future. Through the reading of this chapter, it is possible to note that, to obtain a detector with the necessary reliability for forensic analysis and portable, it must be the blending of materials with different properties (chemical, physical and biological).

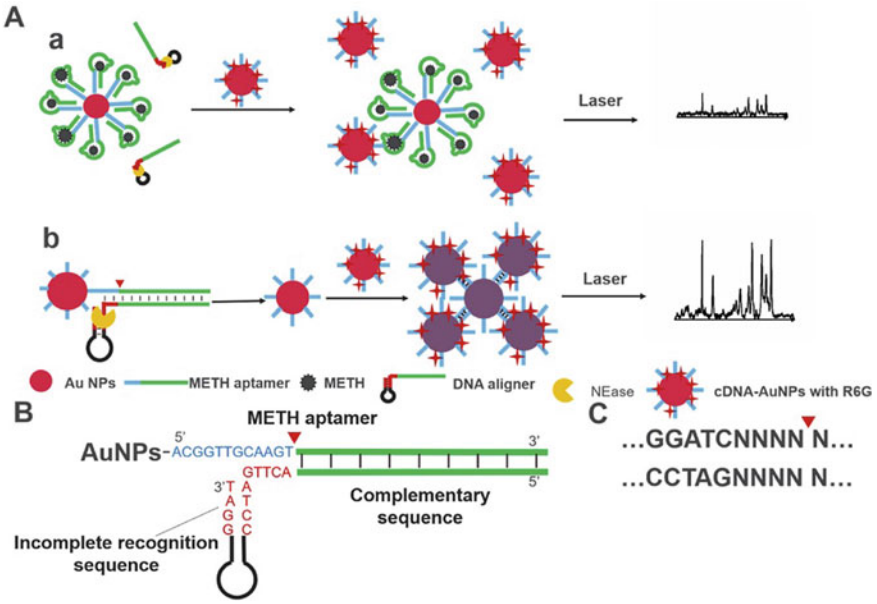

Fig. 10 Scheme illustrating the sensor synthesis and detection of methamphetamine based on AMC method. **a** The AMC unsuccessful process, due to the methamphetamine presence and no enhancement of signal. **b** The formation of DNA-directed self- assembly of Au NPs in the absence of methamphetamine and enhancement of signal. **b** DNA structure aligner hybridized with methamphetamine aptamer. **c** Process of recognition sequence and cleavage of specific site Nt.AlwI. (Reproduced with permission from Ref. [45])

References

1. Mahbub, T., Hoque, M.E.: In: Pal, K., Gomes, F. (eds) Nanofabrication Smart Nanosensor Applications. pp. 1–20. Elsevier (2020)
2. Zhang, S., Geryak, R., Geldmeier, J., Kim, S., Tsukruk, V.V.: Chem. Rev. **117**, 12942–13038 (2017)
3. Wongkaew, N., Simsek, M., Griesche, C., Baeumner, A.J.: Chem. Rev. **119**, 120–194 (2019)
4. Fadel, T.R., Farrell, D.F., Friedersdorf, L.E., Griep, M.H., Hoover, M.D., Meador, M.A., Meyyappan, M.: ACS Sensors **1**, 207–216 (2016)
5. Meng, Z., Stolz, R.M., Mendecki, L., Mirica, K.A.: Chem. Rev. **119**, 478–598 (2019)
6. Bahadır, E.B., Sezgintürk, M.K.: Biosens. Bioelectron. **68**, 62–71 (2015)
7. Ronkainen, N.J., Brian, H., Heineman, W.R.: Chem. Soc. Rev. **39**, 1747–1763 (2010)
8. Rawtani, D., Tharmavaram, M., Pandey, G., Hussain, C.M.: TrAC Trends Anal. Chem. **120**, 115661 (2019)
9. Fikiet, M.A., Khandasammy, S.R., Mistek, E., Ahmed, Y., Halámková, L., Bueno, J., Lednev, I.K.: Spectrochim. Acta Part A Mol. Biomol. Spectrosc. **197**, 255–260 (2018)
10. Ben-Jaber, S., Peveler, W.J., Quesada-Cabrera, R., Sol, C.W.O., Papakonstantinou, I., Parkin, I.P.: Nanoscale **9**, 16459–16466 (2017)
11. Shafiee, H., Lidstone, E.A., Jahangir, M., Inci, F., Hanhauser, E., Henrich, T.J., Kuritzkes, D.R., Cunningham, B.T., Demirci, U.: Sci. Rep. **4**, 1–7 (2014)
12. Muehlethaler, C., Leona, M., Lombardi, J.R.: Anal. Chem. **88**, 152–169 (2016)
13. To, K.C., Ben-Jaber, S., Parkin, I.P.: ACS Nano **14**, 10804–10833 (2020)

14. Shaw, L., Dennany, L.: Curr. Opin. Electrochem. **3**, 23–28 (2017)
15. Raza, A., Saha, B.: Forensic Sci. Int. **233**, 21–27 (2013)
16. Chávez, D., Garcia, C.R., Oliva, J., Diaz-Torres, L.A.: Ceram. Int. **47**, 10–41 (2021)
17. Vidal, J.C., Bertolín, J.R., Bonel, L., Asturias, L., Arcos-Martínez, M.J., Castillo, J.R.: J. Pharm. Biomed. Anal. **125**, 54–61 (2016)
18. Montagner, C., Sodré, F., Acayaba, R., Vidal, C., Campestrini, I., Locatelli, M., Pescara, I., Albuquerque, A., Umbuzeiro, G., Jardim, W.: J. Braz. Chem. Soc. **30**, 614–632 (2018)
19. Teymourian, H., Parrilla, M., Sempionatto, J.R., Montiel, N.F., Barfidokht, A., Van Echelpoel, R., De Wael, K., Wang, J.: ACS Sensors **5**, 2679–2700 (2020)
20. Lefferts, M.J., Castell, M.R.: Anal. Methods **7**, 9005–9017 (2015)
21. Moram, S.S.B., Shaik, A.K., Byram, C., Hamad, S., Soma, V.R.: Anal. Chim. Acta **1101**, 157–168 (2020)
22. Gong, Z., Du, H., Cheng, F., Wang, C., Wang, C., Fan, M., Appl, A.C.S.: Mater. Interfaces **6**(2014), 21931–21932 (1937)
23. Paolesse, R., Nardis, S., Monti, D., Stefanelli, M., Di Natale C.: (2016)
24. Steinegger, A., Wolfbeis, O.S., Borisov, S.M.: Chem. Rev. **120**, 12357–12489 (2020)
25. Ge, L., Li, S.-P., Lisak, G.: J. Pharm. Biomed. Anal. **179**, 112913 (2020)
26. Qu, J., Ge, Y., Zu, B., Li, Y., Dou, X.: Small **12**, 1369–1377 (2016)
27. Squire, K.J., Sivashanmugan, K., Zhang, B., Kraai, J., Rorrer, G., Wang, A.X., Appl, A.C.S.: Nano Mater. **3**, 1656–1665 (2020)
28. Zhao, Y., Xie, Y., Zhou, Q., Wang, P., Chang, Y., Lin, C.: ACS Omega **6**, 2045–2051 (2021)
29. Minhas, R.S., Rudd, D.A., Al Hmoud, H.Z., Guinan, T.M., Kirkbride, K.P., Voelcker, N.H.: ACS Appl. Mater. Interfaces **12**, 31195–31204 (2020)
30. Akhoundian, M., Alizadeh, T., Ganjali, M.R., Norouzi, P.: Talanta **200**, 115–123 (2019)
31. Parrilla, M., Felipe Montiel, N., Van Durme, F., De Wael, K.; Sensors Actuators, B Chem. **337**, 129819 (2021)
32. Mao, K., Zhang, H., Pan, Y., Zhang, K., Cao, H., Li, X., x Yang, X.: TrAC Trends Anal. Chem. **130**, 115975 (2020)
33. Fan, M., Andrade, G.F.S., Brolo, A.G.: Anal. Chim. Acta **1097**, 1–29 (2020)
34. Xue, W., Tan, X., Khaing Oo, M.K., Kulkarni, G., Ilgen, M.A., Fan, X.: Analyst **145**, 1346–1354 (2020)
35. Li, X., Li, J., Ling, J., Wang, C., Ding, Y., Chang, Y., Li, N., Wang, Y., Cai, J.: Sensors Actuators B Chem. **320**, 128303 (2020)
36. Adhikary, R.R., Banerjee, R.: Biosens. Bioelectron. **184**, 113244 (2021)
37. Scorsone, E. Manai, R., Cali, K., Ricatti, M.J., Farno, S., Persaud, K., Mucignat, C.: Sensors Actuators B. Chem. **334**, 129587 (2021)
38. Liu, R., Li, Z., Huang, Z., Li, K., Lv, Y.: TrAC. Trends Anal. Chem. **118**, 123–137 (2019)
39. Kong, W., Zhao, X., Zhu, Q., Gao, L., Cui, H.: Anal. Chem. **89**, 7145–7151 (2017)
40. Majdinasab, M., Mitsubayashi, K., Marty, J.L.: Trends Biotechnol. **37**, 898–915 (2019)
41. Khorablou, Z., Shahdost-fard, F., Razmi, H., Yola, M.L., Karimi-Maleh, H.: Chemosphere **278**, 130393 (2021)
42. Lantam, A., Limbut, W., Thiagchanya, A., Phonchai, A.: Microchem. J. **159**, 105519 (2020)
43. Weng, S., Dong, R., Zhu, Z., Zhang, D., Zhao, J., Huang, L., Liang, D.: Spectrochim. Acta Part A Mol. Biomol. Spectrosc. **189**, 1–7 (2018)
44. Hong, Y., Zhou, X., Xu, B., Huang, Y., He, W., Wang, S., Wang, C., Zhou, G., Chen, Y. Gong.: ACS Appl. Mater. Interfaces **12**, 24192–24200 (2020)
45. Mao, J., Kang, Y., Yu, D., Zhou, J.: Anal. Chim. Acta **1146**, 124–130 (2021)
46. Hakonen, A., Wu, K., Stenbæk Schmidt, M., Andersson, P.O., Boisen, A., Rindzevicius, T.: Talanta **189** 649–652 (2018)
47. Wu, J., Zhang, L., Huang, F., Ji, X., Dai, H., Wu, W.: J. Hazard. Mater. **387**, 121714 (2020)

Perovskite Nanomaterials: Properties and Applications

Anne Esther Targino Bonatto, Gisele Inês Selli, Pedro Tonom Martin, and Fernando Targino Bonatto

Abstract The exceptionally outstanding performances of organometallic perovskites are a result of their unique characteristic properties. Hybrid perovskites exhibit significant optical absorption, a modifiable bandgap, long diffusion lengths, ambipolar charge transport, high charge carrier mobility, and high tolerance to point defects. Besides that, its processing is easy and low cost. This chapter describes the properties of perovskites and their most notable applications.

Keywords Perovskite · Solar cells · Thin films · Stability · Sensors

Abbreviations

DMA	Dimethyl acetamide
DMF	Dimethyl formamide
DMSO	Dimethyl sulfoxide
DSSC	Dye sensitive solar cell
FA	Formamidinium
FAI	Formamidinium iodide
FTO	Fluorine doped tin oxide
IPA	Isopropyl alcohol
ITO	Indium doped tin oxide
MA	Methylammonium
MAI	Methylammonium iodide
$MAPbBr_3$	Methylammonium lead bromide perovskite
mp-TiO_2	Mesoporous TiO_2
PET	Polyethylene terephthalate
PSC	Perovskite solar cell
PV	Photovoltaic
PVc	Photovoltaic cell

A. E. T. Bonatto · G. I. Selli · P. T. Martin · F. T. Bonatto (✉)
Universidade Federal do Rio Grande do Sul, Porto Alegre, Brazil

A. Kopp Alves (ed.), *Environmental Applications of Nanomaterials*, Engineering Materials, https://doi.org/10.1007/978-3-030-86822-2_14

TCO	Transparent conductive oxide
UV	Ultraviolet light

Perovskites are materials with a structure of the ABX3 type, with A and B being cations with different sizes (with A greater than B) and X is an anion. The first perovskite studied was the mineral calcium titanate ($CaTiO_3$), discovered in Russia by Gustav Rose in 1839, which was later named perovskite in honor of Russian mineralogist Lev Perovski [1]. The crystal structure of perovskites mentioned above is typically cubic form, for temperatures above 330 K. However, for temperatures in the range of 160–330 K, the structure undergoes a phase transition, changing to tetragonal, while below 160 K it presents an orthorhombic structure [2]. Perovskites can be divided into two classes, the purely inorganic ($PbTiO_3$, $CaSiO_3$, etc.) and the organic–inorganic hybrids (CH3NH3MX3 - M = Pb or Sn; X = Cl, Br or I, among other configurations) [3].

1 General Perovskites Properties

It is already known that perovskites are causing considerable interest and dedication of various scholars in various science branches, especially in the electrical and renewable energy segment. The reason for that is that perovskites-based materials have a variety of properties that assist them in their applications in several areas.

One of these properties (and probably the most know) is the optical absorption and conductivity property. The perovskite, in this case, absorbs the incident light and turns it into moving electrons, electrons which will compose the electrical current in the photovoltaic cell the perovskite is included in. The fact here is that this property can be tunable by the addition of impurities [4]; this process is called “doping”. Therefore, choosing the correct doper may cause the perovskite to conduce and absorb more electrons, and thus the solar cell will be generating more energy. Depending on the doper, the crystal structure of the perovskite may be changed as well.

Another perovskite’s property is magnetism (especially in Cobalt-based perovskites, explained by the Cobalt’s spin). For example, some perovskites (for example, $LnCoO_3$) may present magnetic characteristics such as paramagnetism and ferromagnetism, depending on their circumstances [5]. As an example, $LnCoO_3$ presents a crescent magnetic susceptibility from 30 to 100 K where it reaches the maximum; then it becomes to decrease till 500 K, where it gets stable in a plateau [5]. So, there will be different parameters for different perovskites, and each one with its magnetic properties. It is relevant to state that magnetic properties may also be improved by doping.

The third property for perovskites material is optical reflectivity. It is quite curious to imagine that a material with one of its mains purposes as absorb light can reflect it. The main reason for a perovskite material to reflect light is that it can degrade

the perovskite just like moisture can [6]. Too much heat on the material can harm its structure and lower its efficiency; therefore, reflect some spectrum of light and absorb another is beneficial once it extends the lifetime of the material.

2 Applications

As seen above, the structure of perovskite has a variety of interesting properties, highlighting magnetoresistance, ferroelectricity, superconductivity, and high dielectric capacity, as described by confirmed by Lozano-Gorrín [7], which allow its use as a sensor, semiconductor, dielectric material, luminescent material, among other applications, which some of the most relevant are discussed below.

2.1 Solar Cells

Perovskites have attracted enormous attention in the area of renewable energies, especially organic–inorganic halide perovskites, because of their exceptional optical properties and can be processed at low temperatures. The type of perovskite most used in solar cells is organic–inorganic hybrid semiconductor materials based on lead halides, with general formula $MPbX_3$ ($M = CH_3NH_3$, X = Br, I), which, in addition to being low cost, present excellent performance when used as sensitizers in photovoltaic devices. The 3D structure of lead methylammonium perovskite can be seen in Fig. 1 [8].

Perovskite solar cells are currently the most prominent among emerging cells. The first perovskite solar cell (PSC) developed in 2009, only 3.8% of the total energy conversion efficiency was achieved by introducing organometallic perovskite

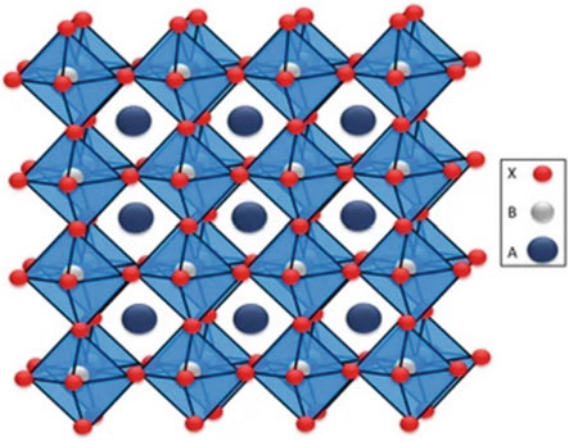

Fig. 1 Structure of 3D perovskites with ABX_3 formula. Reproduced from ref. [8]

$CH_3NH_3PbI_3$ with a liquid-based hole transport layer in a dye-sensitized solar cell. These cells, composed of this photoactive material, already surpass 25% of the energy conversion efficiency, thus surpassing even silicon cells. Among the major challenges related to the research development regarding the application of this material are to achieve high efficiency in the face of instability caused by environmental variations, especially in relation to humidity.

2.1.1 Efficiency of Perovskites Solar Cells

The first researches focused on the application of perovskites in solar cells date back to 2009, carried out by Miyasaka et al. [9], where $CH_3NH_3PbI_3$ was used as a dye-sensitizing material in solar cells. The efficiencies reached low values of 3.8%, and in addition, such devices were unstable due to problems with the liquid electrolyte then used in the hole transport material (HTM), with the aggravation of these devices being sensitive to atmospheric moisture [10]. Park et al. [11] performed similar tests and produced a device with a 6.5% increase in efficiency, but the stability of the HTM layer was still the main problem due to the liquid medium. The most promising results involving the study of perovskite solar cells appeared in 2012, when researchers replaced the liquid electrolyte with a polymeric matrix, making the cells more stable and raising their levels efficiencies to 9.7% [12].

The application of solid-state HTM in the highly crystallized perovskite layer, such as Spiro-OMeTAD, has increased its efficiency over the past few years. Lee et al. [13] reported in 2012 a device efficiency of 10.9% with an open-circuit voltage greater than 1.1 V. Wang et al. [14] have introduced graphene in PSCs, thus acquiring an efficiency of 15.6%. The application of another perovskite material, formamidinium iodide, together with poly-triarylamine (PTAA) as a new HTM brought a remarkable 20.1% efficiency in 2015 [15]. The current record for PHC efficiency was 22.1%, created in 2016 by Seong Sik Shin et al. [16]. They also achieved a long-term and stable efficiency of 21.2% in other work [17]. The perovskite-inserted tandem cell also achieved a promising efficiency of 26.7% when combined with Si cells [18]. The rapid improvement in the efficiency of PSCs makes perovskite comparable to the stable performance of c-Si solar cells, while all other types of non-silicon solar cells have suffered major hurdles in future improvements. According to the theoretical calculation based on the known Shockley-Queisser limit, perovskite devices could reach an efficiency of around 25–27% [19].

2.1.2 Perovskites Stability

The degradation of organometallic perovskites is the main problem in solar cells, requiring further study to improve the stability of this material in the long term. Humidity, oxygen, temperature, and UV radiation are the main factors affecting the stability of organometallic perovskites [20]. As the material is very sensitive

to oxygen and moisture, most manufacturing processes are carried out in an inert atmosphere and controlled temperature, such as in a glove box.

Significant degradation occurs in solar cells during testing under ambient conditions. Seok et al. reported that degradation of the perovskite film begins to occur at a humidity of 55%, exhibiting a color change from dark brown to yellow [21]. This degradation limits perovskite solar cells in outdoor applications, as there is a significant decrease in their efficiency [22].

Several studies are currently being carried out to improve the stability of perovskite solar cells and not to restrict their use in external applications [23–25]. As it is a new technology, the perovskite stabilization process is not fully understood, thus requiring further study for practical applications of the devices [26].

2.2 Perovskite-Based LED

Quantum dots from metallic perovskite (PQD) already play a good role in consumer color display products. However, the excellent properties of PQDs suggest that they should be suitable for these applications. However, injection and charge transport in perovskite nanocrystal films need to be optimized to obtain high-efficiency devices. Some studies emerged from research by Tan et al. [27] in 2014, who demonstrated infrared and visible electroluminescence in lead halide and methylammonium perovskites using a charge-limited diode structure to achieve effective radiative recombination.

However, the use of methylammonium halide, which is a chemical combination of gaseous methylamine and hydrogen halide, substantially limits the thermal stability of these perovskite-based devices. The replacement of methylammonium by inorganic cesium provides extra thermal stability to perovskite up to its melting point at ±500 °C, but makes it more intractable for solution processing, necessitating the manufacture of thin films of PQDs. Song et al. [28] prepared the first device with the structure ITO/PEDOT:PSS/PVK/$CsPbBr_3$/TPBi/LiF/Al to generate LEDs with blue, green, and orange emissions. These materials have narrow emission lines, ideal for these applications. Thus, while the bands were narrow, the brightness of the LEDs was limited (less than 1000 cd/m^2), and the external quantum efficiency (EQE) was limited to 0.1% [28]. Therefore, Li et al. [29], in their studies, cited the importance of the surface chemistry of nanocrystals. As much as ligands are needed to passivate the surface of PQDs and prevent aggregation (leading to high quantum yields and greater stability), the excessive amount of surface ligands blocks the injection and transport of electrons. Thus, by optimizing the charge transport layers and controlling the density of the ligand on the surface, the EQE of the $CsPbBr_3$-based LEDs increased by 50 times more (0.12% to 6.27%) and was obtained if a brightness greater than 15,000 cd/m^2.

Over time, the EQE of perovskite LEDs increased to more than 10%. Yan et al. [30] developed devices that reached a maximum external quantum efficiency of 12.9%. Chiba et al. exhibited red emissive perovskite LEDs with an EQE efficiency of 21.3%.

This contribution demonstrates a significant advance in studies about LEDs based on PQDs [31]. It is noteworthy that despite the rapid advances in Perovskite LEDs in recent years, their commercial applications remain a challenge as the device's efficiency still does not outperform traditional devices, and the long-term stability of perovskite LEDs still requires improvements, in addition to the appeal for the development of environmentally-friendly LEDs.

2.3 Perovskite Sensors

Perovskites are multifunctional materials with an important role in the field of sensors, and that has attracted a lot of attention from the scientific community [32–35]. This great interest in Perovskites can be attributed to its intrinsic optoelectronic properties, such as electro-optic, high carrier mobility, long diffusion length, broadband absorption, photoluminescence quantum yield, photorefractive, and precise tunable bandgaps and emission [32, 33, 36, 37]. Furthermore, perovskite structures allow the coupling of different metallic ions as well as several anions. This characteristic of having different elements in the structure allows the adjustment and improvement of some specific properties.

In addition to having a wide application in solar cells [38–40], light-emitting diodes (LEDs) [41–43], and lasers [44, 45], Perovskites have proven to be a good alternative for application as sensors [32–34, 46].

Due to their chemical structure, Perovskites can show great sensitivity and instability to environmental conditions. However, in the face to the potential that this material has, researchers made this sensitivity an advantage, using Perovskites as optical and electrochemical sensors.[33, 37, 47].

According to Huang [37], perovskites can be used to detect organic compounds, metal ions, gases, and biomolecules, in addition to being used in devices that measure temperature and humidity. These measurements can be performed with different methods such as photoluminescence (PL), photoelectrochemistry (PEC), electrochemiluminescence (ECL), and chemoresistance (CR) [37].

As mentioned above, Perovskites have excellent optical properties but also a high sensitivity to the environment. Therefore, these materials have shown great potential for detecting different analytes among these gases.

We can highlight the study conducted by Guishun [48], which worked developing a fluorescent sensor consisting of $MAPbBr_3$/mesoporous TiO_2 for detection of gases such as NH_3 and amine. According to the author, after the preparation of the compound containing different $MAPbBr_3$/mp-TiO_2 layers, analyzes were carried out to investigate whether there would be an improvement or attenuation of fluorescence when exposed to NH_3 or amine vapors. Among the main results shown by the author, he highlights the increase in fluorescence intensity (72% and 988% at concentrations of 5 and 100 ppm of the analyte, respectively), in the first seconds after sensor exposure to analyte vapors. Subsequently, a decrease in the initial level was noted when complete gas volatilization occurred. During the discussion, the author discusses

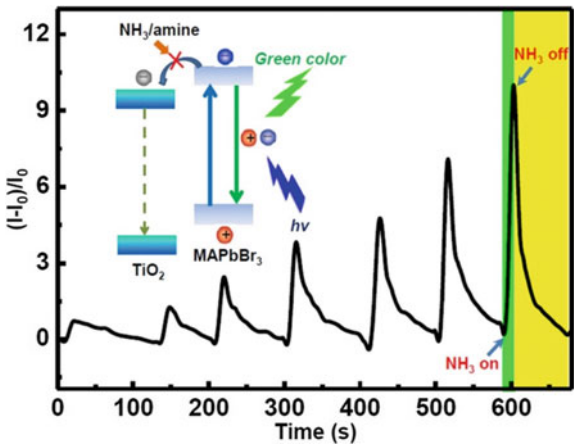

Fig. 2 Graphical abstract of main results obtained for study in the development of perovskite as gas sensing Reproduced with permission from Ref. [48]

and presents the physical phenomena that are related to the increase in fluorescence intensity. The author also reports the successful detection of amine vapors. Finally, properties obtained and properly characterized are highlighted, including favorable reversibility, high gas selectivity, humidity insensitivity, and regeneration [48]. We can see the Graphical Abstract of the article with the main scientific contributions in Fig. 2.

As it is possible to notice, in the study presented above, through a chain of optoelectronic reactions, it was possible to obtain the detection of gases derived from the amine. Through similar references that present gas detection, it was possible to notice a similarity when the detection mechanism is discussed. According to the study by Qin [49], who worked with $LaCoO_3$ (LCO) modified on the ZnO surface; it is possible to study the gas detection mechanism of this compound. The author reports that the optimization of sensory properties can be attributed to the increase in the amount of oxygen adsorbed on the surface and the strong catalytic oxidation activity of LCO. That is, through different optoelectronic reactions, it was possible to obtain a significant improvement in the detection of ethanol vapor.

Other articles present results demonstrating the synthesis of Perovskites and improvement of the properties of this material to be applied as a sensor. A study that presents the synthesis and development of a nanosensor is developed by Moradi [50]. In this study, the authors designed and developed an optical nanosensor using a low-cost deposition process. The nanosensor was synthesized using Methylammonium lead iodide and lead sulfide (PbS) nanoparticles as an active layer. The results demonstrate the potential of the nanocompound, with a little dark current for low applied bias voltages less than 1 V, a very important parameter for optical sensors. Furthermore, the sensors have demonstrated excellent quantum efficiency over a wide range of wavelengths, 370–940 nm.

In order to start the contextualization of different detection mechanisms, we can mention the study developed by Jing [34]. According to the author, there are not many works that present the use of monocrystalline perovskites using flexible devices. The

results presented demonstrate the success of the synthesized device; it was possible to obtain a responsivity (5600 A/W), 2 times greater than that presented in other studies using the polycrystalline material. Furthermore, the extremely thin 20 nm thickness allowed for an improvement in the temporal response, resulting in a broadband photodetection to 0.2 MHz. These results demonstrate the potential for using this photodetector in wearable and cellular devices, artificial eyes, and in areas such as medicine and robotics [34]. We can see the structure of the device and its proper characterization in Fig. 3.

Another research that is based on this context is that developed by Ippili [32]. In the study, a multifunctional sensor consisting of methylammonium lead iodide-polyvinylidene fluoride ($MAPbI_3 - PVDF$) was developed. This device allows the simultaneous detection of light and pressure without the need to use an external power source. The functioning mechanism of this device proves to be extremely interesting since the device collects mechanical energy to feed itself and simultaneously operates

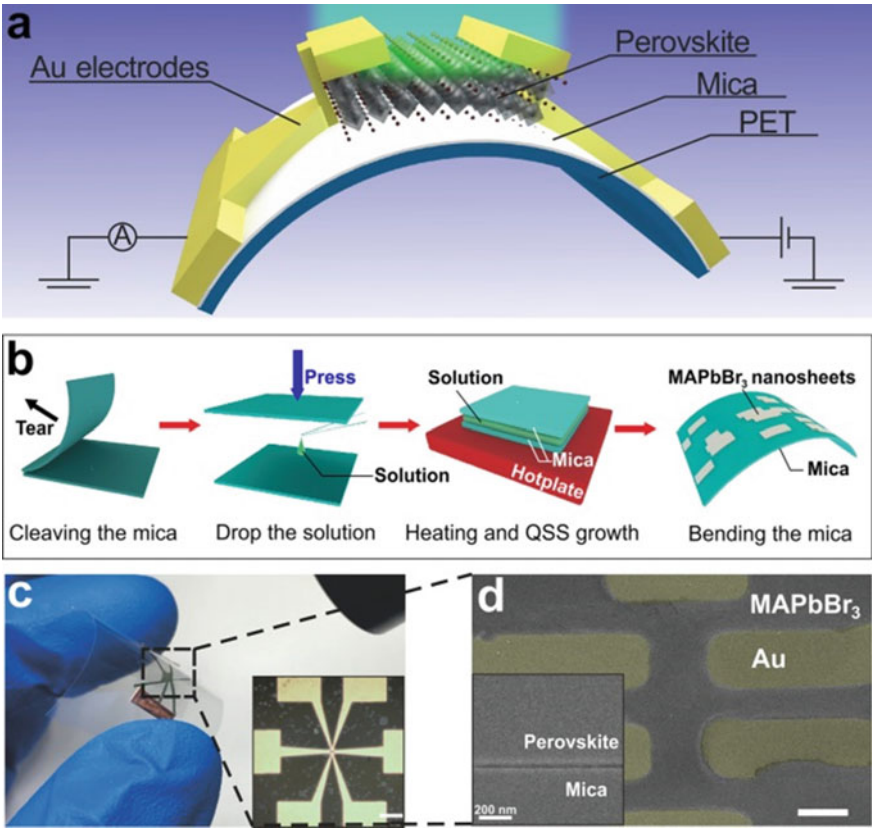

Fig. 3 Scheme exhibiting the architecture and the characterization of flexible photodetector. Reproduced with permission from Ref. [34]

as light and pressure sensor due to the combination of intrinsic photoelectric and piezoelectric/triboelectric properties of the synthesized compound, called by the author as $MAPbI_3$−PVDF. The results show responsiveness (~129.2 V/mW) and a relatively fast response time (~50 ms), excellent data when developing sensors. It was also possible to obtain satisfactory detection in piezoelectric mode ($\sim 1.4 \times 10^{10}$ Jones). Due to the multimodality of the sensor, it was possible to obtain excellent results regarding pressure detection, values in the range of 0.107 and 0.194 V/kPa in the piezoelectric and triboelectric modes respectively. Finally, through the analysis of the results, it is possible to highlight that the sensor had a very fast response time, long-term stability, and excellent mechanical resistance [32].

In addition, the device features a fast response time with long-term on–off properties, excellent mechanical durability, and long-term stability. In Fig. 4, it is possible to see the main results obtained in the study [32].

Other studies that present very interesting topics using electrochemical sensors composed of perovskites are those carried out by He [51] and Anajafi [52].

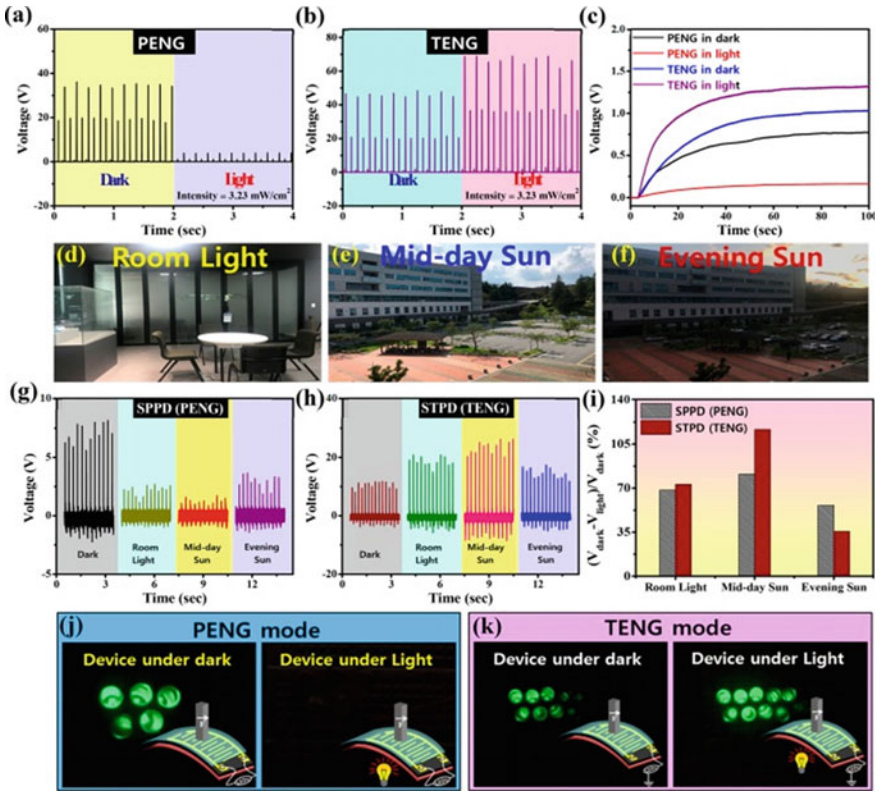

Fig. 4 Scheme exhibiting a brief overview of main results obtained by the research in PENG and TENG mode. Reproduced with permission from Ref.[32]

The first author [51] works with the detection of p-phenylenediamine (PPD), a chemical compound used in hair dyes. The study reports the systematic characterization of a series of oxide perovskites composed of $Pr_{1-x}Sr_xCoO_{3-\delta}$ (x = 0, 0.2, 0.4, 0.6, 0.8, and 1), denominated by the author as PSC82, for detection of PPD in alkaline solution. For the best performance of the sensor properties, the deposition of PSC82 was carried out under a glassy carbon electrode (PSC82/GCE). Through the formation of this composite, it was possible to perceive a correlation between the yields of the intermediate hydrogen peroxide and the bond strength of these oxide perovskites, which was attributed to electronic phenomena that occur in the transport of electrons. The reactions that occurred in the sensor follow amperometric mechanisms. The synthesized composite had a very high sensitivity de 655 and 308 $\mu A\ mM^{-1}\ cm^{-2}$ in a PPD concentration range of 0.5–2900 and 2900–10,400 μM, respectively. Comparing with the traditionally used method, which is ultraviolet–visible (UV–vis) spectrometry, the amperometric sensor provided more accurate results with a detection limit of 0,17 μM and being able to detect trace concentrations of PPD in real paints. Furthermore, the sensor showed greater stability being tested with cyclic voltammetry, resisting for 50 cycles and one month of storage. These properties obtained demonstrate the potential of the sensor to be used in the detection of this and other toxic compounds in hair dyes [51]. We can see the main results and reactions that improved the detector's performance by analyzing Fig. 5.

The other study that presents the development of an electrochemical sensor is the one developed by Anajafi [52]. Using a heat treatment method, he obtained nanoparticles of $NdFeO_3$ perovskite screen-printed carbon electrode for detection of dopamine and uric acid. The characterization and results showed that the composite improved the electrooxidation of dopamine compared to the results obtained for the screen-printed carbon electrode. Regarding the characteristic parameters of the sensors, it presented a detection limit of 0.27 μM (at S/N = 3) and two linear concentration ranges of 5 to 100 μM and 150 to 400 μM. To complement the results, the sensor was used to detect dopamine in real samples. With this, the author points

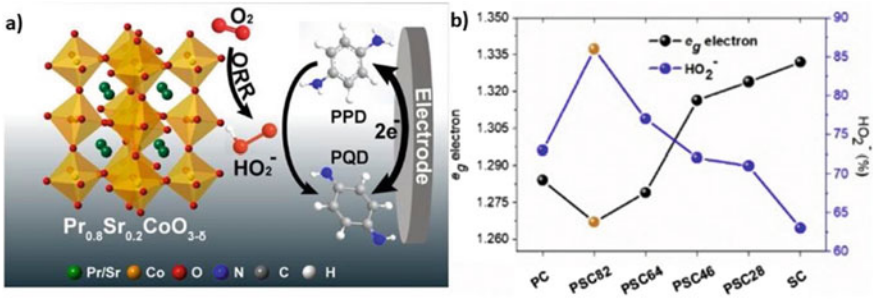

Fig. 5 **a** Scheme illustrating the sensing perovskite reactions and the related redox reaction that converts PPD to PQD on the PSC82/GE electrode, **b** graph of Chronoamperometric responses in the form of current–time (I-t). Reproduced with permission from Ref. [51]

out the originality of the work stating that this is the first sensor that allows the quantification of dopamine.

In these sections, it was possible to understand a little more about the application of perovskites as optical and electrochemical sensors. We saw the main detection mechanisms and checked how wide the range of applications of these materials is.

References

1. De Graef, M., McHenry, M.E.: Structure of materials: an introduction to crystallography, diffraction and symmetry. (2012). https://doi.org/10.1017/CBO9781139051637.
2. Oku, T.:Crystal Structures of $CH_3NH_3PbI_3$ and Related Perovskite Compounds Used for Solar Cells. Sol. Cells - New Approaches Rev. (2015). https://doi.org/10.5772/59284
3. Jung, H.S., Park, N.-G.: Perovskite solar cells: from materials to devices. Small **11**(1), 10–25 (2015). https://doi.org/10.1002/SMLL.201402767
4. Gao, R., et al.: Tunable electronic properties and large optical anisotropy in the CsPbXnY3-n (X, Y = Cl, Br, I) perovskite. Sol. Energy **217**, 165–172 (2021). https://doi.org/10.1016/J.SOLENER.2021.01.053
5. Raveau, B., Seikh, M.M.: Magnetic and physical properties of cobalt perovskites. Handb. Magn. Mater. **23**, 161–289 (2015). https://doi.org/10.1016/B978-0-444-63528-0.00003-6
6. Zhao, Y., et al.: Enhanced optical reflectivity and electrical properties in perovskite functional ceramics by inhibiting oxygen vacancy formation. Ceram. Int. **47**(4), 5549–5558 (2021). https://doi.org/10.1016/J.CERAMINT.2020.10.139
7. Lozano-Gorrín, A.D.: Structural characterization of new perovskites. Polycryst Mater. - Theor. Pract. Asp. (2012). https://doi.org/10.5772/30869
8. Kim, E.-B., Akhtar, M.S., Shin, H.-S., Ameen, S., Nazeeruddin, M.K.: A review on two-dimensional (2D) and 2D-3D multidimensional perovskite solar cells: Perovskites structures, stability, and photovoltaic performances. J. Photochem. Photobiol. C Photochem. Rev. **48**, 100405 (2021). https://doi.org/10.1016/j.jphotochemrev.2021.100405
9. Kojima, A., Teshima, K., Shirai, Y., Miyasaka, T.: Organometal halide perovskites as visible-light sensitizers for photovoltaic cells. J. Am. Chem. Soc. **131**(17), 6050–6051 (2009). https://doi.org/10.1021/JA809598R
10. Mishra, A.K., Shukla, R.K.: Effect of humidity in the perovskite solar cell. Mater. Today Proc. **29**, 836–838 (2020). https://doi.org/10.1016/J.MATPR.2020.04.872
11. Im, J.-H., Lee, C.-R., Lee, J.-W., Park, S.-W., Park, N.-G.: 6.5% efficient perovskite quantum-dot-sensitized solar cell. Nanoscale **3**(10), 4088–4093 (2011). https://doi.org/10.1039/C1NR10867K
12. Kim, H.-S. et al.: Lead iodide perovskite sensitized all-solid-state submicron thin film mesoscopic solar cell with efficiency exceeding 9%. Sci. Reports **2**(1), 1–7 (2012). https://doi.org/10.1038/srep00591
13. Lee, M.M., Teuscher, J., Miyasaka, T., Murakami, T.N., Snaith, H.J.: Efficient hybrid solar cells based on meso-superstructured organometal halide perovskites. Science **338**(6107), 643–647 (2012). https://doi.org/10.1126/SCIENCE.1228604
14. Wang, J.T.-W., et al.: Low-Temperature processed electron collection layers of graphene/TiO_2 nanocomposites in thin film perovskite solar cells. Nano Lett. **14**(2), 724–730 (2013). https://doi.org/10.1021/NL403997A
15. Yang, W.S. et al.: High-performance photovoltaic perovskite layers fabricated through intramolecular exchange. Science **348**(6240), 1234–1237 (2015). https://doi.org/10.1126/SCIENCE.AAA9272
16. Yang, W., Park, B., Jung, E., Jeon, N., Kim, Y., Lee, D.U., Shin, S.S., Seo, J., Kim, E.K., Noh, J.H. Seok, S.I.: Iodide management in formamidinium-lead-halide–based perovskite layers for

efficient solar cells. science.sciencemag.org, Accessed 12 July 2021. Online. Available: https://science.sciencemag.org/content/356/6345/1376.abstract.
17. Cao, J., et al.: Efficient, hysteresis-free, and stable perovskite solar cells with ZnO as electron-transport layer: effect of surface passivation. Adv. Mater. **30**(11), 1705596 (2018). https://doi.org/10.1002/ADMA.201705596
18. Rohatgi, A., et al.: 26.7% Efficient 4-Terminal perovskite-silicon tandem solar cell composed of a high-performance semitransparent perovskite cell and a doped Poly-Si/SiOx passivating contact silicon cell. IEEE J. Photovoltaics **10**(2), 417–422 (2020). https://doi.org/10.1109/JPHOTOV.2019.2963564
19. Hossain, M.I., Qarony, W., Ma, S., Zeng, L., Knipp, D., Tsang, Y.H.: Perovskite/Silicon tandem solar cells: from detailed balance limit calculations to photon management. Nano-Micro Lett. **11**(1), 1–24 (2019). https://doi.org/10.1007/S40820-019-0287-8
20. Li, J., Wang, Q., Abate, A.: Perovskite solar cells. Nanomater. Sol. Cell Appl. 417–446 (2019). https://doi.org/10.1016/B978-0-12-813337-8.00012-6
21. Noh, J.H., Im, S.H., Heo, J.H., Mandal, T.N., Il Seok, S.: Chemical management for colorful, efficient, and stable inorganic–organic hybrid nanostructured solar cells. Nano Lett. **13**(4), 1764–1769 (2013). https://doi.org/10.1021/NL400349B
22. Niu, G., Guo, X., Wang, L.: Review of recent progress in chemical stability of perovskite solar cells. J. Mater. Chem. A **3**(17), 8970–8980 (2015). https://doi.org/10.1039/C4TA04994B
23. Jiang, Q., Rebollar, D., Gong, J., Piacentino, E.L., Zheng, C., Xu, T.: Pseudohalide-induced moisture tolerance in perovskite $CH_3NH_3Pb(SCN)2I$ Thin Films. Angew. Chemie Int. Ed. **54**(26), 7617–7620 (2015). https://doi.org/10.1002/ANIE.201503038
24. Cao, J., Yin, J., Yuan, S., Zhao, Y., Li, J., Zheng, N.: Thiols as interfacial modifiers to enhance the performance and stability of perovskite solar cells. Nanoscale **7**(21), 9443–9447 (2015). https://doi.org/10.1039/C5NR01820J
25. Chen, W., et al.: Efficient and stable large-area perovskite solar cells with inorganic charge extraction layers. Science **350**(6263), 944–948 (2015). https://doi.org/10.1126/SCIENCE.AAD1015
26. Song, T.-B., et al.: Perovskite solar cells: film formation and properties. J. Mater. Chem. A **3**(17), 9032–9050 (2015). https://doi.org/10.1039/C4TA05246C
27. Li, G., et al.: Highly efficient perovskite nanocrystal light-emitting diodes enabled by a universal crosslinking method. Adv. Mater. **28**(18), 3528–3534 (2016). https://doi.org/10.1002/ADMA.201600064
28. Song, J., Li, J., Li, X., Xu, L., Dong, Y., Zeng, H.: Quantum dot light-emitting diodes based on inorganic perovskite cesium lead halides (CsPbX3). Adv. Mater. **27**(44), 7162–7167 (2015). https://doi.org/10.1002/ADMA.201502567
29. Li, J. et al.: 50-Fold EQE Improvement up to 6.27% of solution-processed All-Inorganic perovskite CsPbBr3 QLEDs via surface ligand density control. Adv. Mater. **29**(5), 1603885 (2017). https://doi.org/10.1002/ADMA.201603885.
30. Yan, F., et al.: Highly efficient visible colloidal lead-halide perovskite nanocrystal light-emitting diodes. Nano Lett. **18**(5), 3157–3164 (2018). https://doi.org/10.1021/ACS.NANOLETT.8B00789
31. Chiba, T., et al.: Anion-exchange red perovskite quantum dots with ammonium iodine salts for highly efficient light-emitting devices. Nat. Photonics **12**(11), 681–687 (2018). https://doi.org/10.1038/s41566-018-0260-y
32. Ippili, S., Jella, V., Eom, S., Hong, S., Yoon, S.-G.: Light-Driven Piezo- and triboelectricity in organic-inorganic metal trihalide perovskite toward mechanical energy harvesting and self-powered sensor application. ACS Appl. Mater. Interfaces **12**(45), 50472–50483 (2020). https://doi.org/10.1021/acsami.0c15009
33. George, J., Halali, K,V.V., Suvina, S.C.G.V., Sakar, M., Balakrishna, R.G.: Perovskite nanomaterials as optical and electrochemical sensors. Inorg. Chem. Front. **7**(14), 2702–2725 (2020). https://doi.org/10.1039/D0QI00306A
34. Jing, H., et al.: Flexible ultrathin single-crystalline perovskite photodetector. Nano Lett. **20**(10), 7144–7151 (2020). https://doi.org/10.1021/acs.nanolett.0c02468

35. Rahimi, F., Jafari, A.K., Hsu, C.A., Ferekides, C.S., Hoff, A.M.: Selective sensing in perovskite-based image sensors. Org. Electron. **75**(July), 105397 (2019). https://doi.org/10.1016/j.orgel.2019.105397
36. Rao, C.N., Dua, P., Kuchhal, P., Lu, Y., Kale, S.N., Cao, P.: Enhanced sensitivity of magneto-optical sensor using defect induced perovskite metal oxide nanomaterial. J. Alloys Compd. **797**, 896–901 (2019). https://doi.org/10.1016/j.jallcom.2019.05.118
37. Huang, Y., et al.: Sensing studies and applications based on metal halide perovskite materials: current advances and future perspectives. TrAC Trends Anal. Chem. **134**, 116127 (2021). https://doi.org/10.1016/j.trac.2020.116127
38. Idígoras, J., Todinova, A., Sánchez-Valencia, J.R., Barranco, A., Borrás, A., Anta, J.A.: The interaction between hybrid organic–inorganic halide perovskite and selective contacts in perovskite solar cells: an infrared spectroscopy study. Phys. Chem. Chem. Phys. **18**(19), 13583–13590 (2016). https://doi.org/10.1039/C6CP01265E
39. Bhooshan Kumar, V., Gouda, L., Porat, Z., Gedanken, A.: Sonochemical synthesis of $CH_3NH_3PbI_3$ perovskite ultrafine nanocrystal sensitizers for solar energy applications. Ultrason. Sonochem. **32**, 54–59 (2016). https://doi.org/10.1016/j.ultsonch.2016.02.012
40. de Oliveira, A.E.R.T.P., Alves, A.K.: Organic-inorganic hybrid perovskites for solar cells applications. 89–101 (2019)
41. Pacchioni, G.: Highly efficient perovskite LEDs. Nat. Rev. Mater. **6**(2), 108 (2021). https://doi.org/10.1038/s41578-021-00280-5
42. Matsushima, T., et al.: High performance from extraordinarily thick organic light-emitting diodes. Nature **572**(7770), 502–506 (2019). https://doi.org/10.1038/s41586-019-1435-5
43. Xu, W., et al.: Rational molecular passivation for high-performance perovskite light-emitting diodes. Nat. Photonics **13**(6), 418–424 (2019). https://doi.org/10.1038/s41566-019-0390-x
44. Das, S., Gholipour, S., Saliba, M.: Perovskites for laser and detector applications. Energy Environ. Mater. **2**(2), 146–153 (2019). https://doi.org/10.1002/eem2.12044
45. Lei, L., Dong, Q., Gundogdu, K., So, F.: Metal Halide Perovskites for Laser Applications. Adv. Funct. Mater. **31**(16), 2010144 (2021). https://doi.org/10.1002/adfm.202010144
46. Qi, F., et al.: Improving the performance through SPR effect by employing Au@SiO_2 core-shell nanoparticles incorporated TiO_2 scaffold in efficient hole transport material free perovskite solar cells. Electrochim. Acta **282**, 10–15 (2018). https://doi.org/10.1016/j.electacta.2018.06.015
47. Zhu, Z., et al.: Metal halide perovskites: stability and sensing-ability. J. Mater. Chem. C **6**(38), 10121–10137 (2018). https://doi.org/10.1039/C8TC03164A
48. Li, G., et al.: A 'Turn-on' fluorescence perovskite sensor based on $MAPbBr_3$/mesoporous TiO_2 for NH_3 and amine vapor detections. Sensors Actuators B Chem. **327**(September 2020), 128918 (2021). https://doi.org/10.1016/j.snb.2020.128918
49. Qin, W., Yuan, Z., Gao, H., Zhang, R., Meng, F.: Perovskite-structured $LaCoO_3$ modified ZnO gas sensor and investigation on its gas sensing mechanism by first principle. Sensors Actuators B Chem. **341**(March), 130015 (2021). https://doi.org/10.1016/j.snb.2021.130015
50. Moradi, Z., Fallah, H., Hajimahmoodzadeh, M.: Nanocomposite perovskite based optical sensor with broadband absorption spectrum. Sensors Actuators, A Phys. **280**, 47–51 (2018). https://doi.org/10.1016/j.sna.2018.07.033
51. He, J., et al.: A highly sensitive perovskite oxide sensor for detection of p-phenylenediamine in hair dyes. J. Hazard. Mater. **369**, 699–706 (2019). https://doi.org/10.1016/j.jhazmat.2019.02.070
52. Anajafi, Z., et al.: $NdFeO_3$ as a new electrocatalytic material for the electrochemical monitoring of dopamine. Anal. Bioanal. Chem. **411**(29), 7681–7688 (2019). https://doi.org/10.1007/s00216-019-01975-z